ALMA MATER STUDIORUM
UNIVERSITÀ DI BOLOGNA

DOTTORATO DI RICERCA IN

IL FUTURO DELLA TERRA, CAMBIAMENTI CLIMATICI E SFIDE SOCIALI

Ciclo 36

Settore Concorsuale: ASTRONOMIA, ASTROFISICA, FISICA DELLA TERRA E DEI PIANETI

Settore Scientifico Disciplinare: FISICA PER IL SISTEMA TERRA E IL MEZZO CIRCUMTERRESTRE

Understanding the metrology challenges and variability of black carbon properties from urban to remote environments

Presentata da: Laura Renzi

Supervisore
Angela Marinoni

Coordinatore Dottorato
Silvana Di Sabatino

Co-supervisori
Marco Zanatta
Federico Porcù

Esame finale anno 2024

ABSTRACT

Black carbon (BC) is an important short-lived climate forcer, which overall impact is still uncertain in climate models. A better estimate requires the accurate characterization of fundamental properties such as BC size and mixing state, and climate-relevant properties (i.e. BC mass concentration and mass absorption cross-section) in different environments. Here, we integrated field observations from European and South American urban and remote sites with chamber experiments in the CESAM simulation chamber to assess the metrology limits of widely used measurement techniques and the variability of BC properties, both at the emission and after ageing in the atmosphere.

We found that metrology limitations, and the use of different correction methods, in the measurement of mass concentration and absorption coefficient are site and technique dependent. The combination of biases from mass concentration and absorption coefficient can induce a potential increase in the estimate of the MAC up to 90%. In urban environments BC properties were observed to quickly react to the diurnal changes in emissions (type, intensity, vicinity) and meteorology (dilution induced by atmospheric dynamic). BC in the Po Valley urban sites was mainly emitted by traffic sources in summer (71-83%), with a secondary contribution from biomass burning in the colder months (46-56%) when heating systems are extensively used. Mass concentration varied significantly with the intensity of traffic emission, resulting in a sudden increase of BC mass concentration from the baseline to daily maximum during rush hours in both European (+160%) and Bolivian (+450%) cities. Simultaneous measurements showed an increase in BC particle size from the traffic site of La Paz (85 nm) to the urban background site of El Alto (187 nm), reflecting the proximity of direct sources and the rapid BC modification. The establishment of ventilated conditions was observed to promote dispersion of traffic emission and dilution with regional background, resulting in a change of concentration (-80%), diameter (+8%), mixing state (+80%) and absorption (+24%) of BC compared to stagnating periods in urban coastal site (Barcelona). Contrary to the urban sites, the variability of BC properties at the mountain site of Chacaltaya was found to be influenced by long range transport. The injection of pollution from the boundary layer appeared to systematically modify the climate-relevant properties of BC such as mass

concentration (+550%) and absorption cross-section (-23%) compared to free-tropospheric conditions, having instead a negligible impact on particle size.

This study contributes to reducing uncertainty in BC observations, offering insights into fundamental and climate-relevant BC properties in urban and remote environments essential for refining BC direct radiative forcing estimates in models.

TABLE OF CONTENTS

LIST OF FIGURES

LIST OF TABLES

1 INTRODUCTION

1.1 ATMOSPHERIC AEROSOLS

Atmospheric aerosols are defined as a population of solid or liquid particles suspended in a gas (Hinds and Zhu, 2022). Despite constituting a minority of atmospheric mass, these particles play a crucial role in climate and biogeochemical systems, with repercussions on human well-being and ecosystems. As a function of their sources, which can be both natural and anthropogenic, aerosol particles are characterized by a wide variety of physical and chemical properties. Hence, they interact differently with solar radiation and clouds, and can have a more or less pronounced impact on human health and ecosystems.

Aerosol science has developed significantly since the end of the Second World War, drawing on contributions from a variety of scientific disciplines including meteorology, physics, engineering, chemistry and mathematics. The historical origins of aerosol studies are linked to the history of air pollution, dating back to Ancient Rome times when complaints about dirty air were documented (Jacobson, 2012). As early as the 13th century, regulations and measures were introduced in London in response to high concentrations of particulate matter (PM), emphasising the harmful effects of emissions from coal burning (Spurny, 1998). The term 'aerosol' was coined by E.G. Donnan in 1918 and from this time until the mid-20th century, this field of science saw the development of measurement techniques and the publication of milestones such as 'The Mechanics of Aerosols' by Fuchs and Fuks (1964). By the second half of the 20th century, aerosol science had become a recognised discipline, characterised by advances in measurement methods and instrumentation. Progress continued with innovations in sampling methods, laboratory analysis and modelling, making aerosol science an integral part of climate research, with a surge in publications reflecting the growing interest in the field (Spurny, 1998; Flagan, 1998; McMurry, 2000). Recent areas of research focus on the optical properties of aerosols, their radiative effects and their role in climate variability, highlighting the dynamic and expanding nature of aerosol science (Park et al., 2010; Skeie et al., 2011). The remarkable increase in

publications containing the term 'aerosols' from nearly 16,800 in the 1980s to over 53,500 in the first decade of the 21st century reflects the increased interest and importance of aerosol studies within the scientific community.

Despite recent progress, understanding aerosol impacts on the atmosphere lags behind that of gaseous species, primarily due to challenges in characterizing different chemical components that tend to mix in the atmosphere. Ongoing efforts focus on developing measurement methods and models to effectively quantify and represent the properties and effects of individual aerosol components, addressing a key source of uncertainty in atmospheric science.

1.1.1 Aerosol sources and life cycle

Aerosol particles may originate from many different sources and are generally classified as natural or anthropogenic and as primary or secondary (Figure 1-1). Anthropogenic sources include fuel combustion, industrial processes, transport and land use, while natural sources include volcanic eruption, sea spray, dust resuspension, biological processes and biomass burning. Primary aerosols are emitted directly into the atmosphere by combustion sources, resuspension or erosion. Among these are mineral dust, sea salt, black carbon, metals, and primary organics. Secondary particles are formed through vapor nucleation of precursor gases and rapid growth of molecular clusters. Homogeneous nucleation involves the aggregation of molecules of the same type to form solid particles, while heterogeneous nucleation occurs when gas phase molecules condense on existing surfaces. Secondary aerosols predominantly consist of secondary organics, sulphate, nitrate, and ammonium. Depending on the source and formation mechanism, aerosols are remarkably diverse in terms of their physical and chemical properties.

The properties of aerosols evolve dynamically after emission during their suspension time as a result of physicochemical processing until wet or dry deposition occur (Figure 1-1). During this time, called lifetime, aerosol travel from their source region and undergo changes in size, mass, morphology and composition. These changes, usually called atmospheric ageing, in turn affect

other climate relevant properties such as hygroscopicity and their ability to interact with radiation.

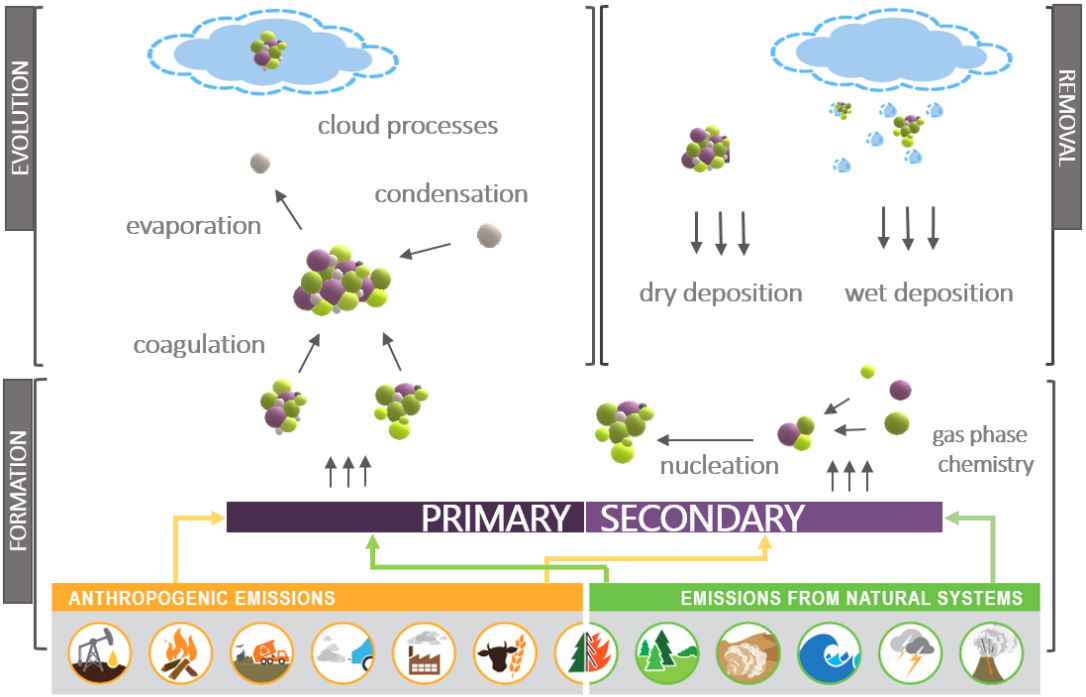

Figure 1-1: Schematic description of aerosol sources and their classification (adapted from IPCC, 2021), and synthetic graphical description of aerosol life cycle.

Several processes shape the evolution of aerosols, including coagulation, condensation, photochemical reactions, and heterogeneous chemistry. Coagulation occurs when particles collide and stick together, while condensation occurs when vapors condense on existing particles. Both coagulation and condensation increase size and contribute to change particle composition. During their lifetime, aerosols may decrease in number or mass as some material returns to the gas phase, through evaporation. Depending on ambient humidity and particle composition, water vapor may condense on their surface, leading to the formation of cloud droplets. Conversely, their mass may decrease as they dry out due to decreasing humidity. Inside clouds, aerosols undergo further changes and may be released after evaporation. These changes affect their number concentration, composition, size and mixing state. Aerosols, driven by atmospheric circulation, often travel long distances,

sometimes for days, from one continent to another. The further they travel, the more the physico-chemical processes mentioned above occur.

Finally, removal from the atmosphere occurs through two main pathways: wet and dry deposition. Dry deposition involves the transport of particulate species from the atmosphere to surfaces without precipitation. It is influenced by particle properties such as size, density, shape and composition, as well as the roughness of the surface. Wet deposition is the process by which particles are transported to the surface by precipitation. Wet deposition might involve two different processes. Nucleation scavenging involves the formation of liquid droplets or ice crystal on the aerosol surface at cloud level and their eventual delivery to the Earth's surface upon rain or snow precipitation. Impaction scavenging involves the capture of an aerosol particles by a precipitating hydrometeor inside or below cloud level. Both wet and dry deposition mechanisms play an important role in controlling aerosol concentration and shaping aerosol dynamics and environmental impacts.

1.1.2 Aerosol physico-chemical properties

1.1.2.1 *Chemical composition and morphology*

If we define a chemical species as an ensemble of identical molecules, by chemical composition of an aerosol particle we mean the mass of each chemical species present within the particle. Considering that a single 100 nm particle can consist of millions of molecules, and can contain hundreds to thousands of distinct chemical species within an attoliter (10^{-18} L) volume, the measurement or modeling of each chemical species in numerous atmospheric particles becomes impractical. For this reason, we usually simplify the description of the composition by referring to aerosol species. That is, groups of similar molecules determined by a specific measurement technique or by the level of detail available in aerosol models. As main constituents of atmospheric aerosol, we can mention inorganic salts, mineral species and carbonaceous aerosol. The main inorganic species are sulphate, nitrate, ammonium, sea salt and mineral dust. Sulphate aerosols form in the atmosphere mainly through secondary formation processes involving sulfur dioxide (SO_2), emitted during volcanic eruptions or from anthropogenic sources (linked to power production or industrial processes), or dimethyl

sulphide (DMS) produced by phytoplankton in the ocean. They consist of droplets of a solution of sulphate or sulphuric acid, or can be found as a suspension of solid sulphate particles ($SO^{2}_{4}^{-}$). Nitrate (NO_3) can be produced from the reaction of gas-phase nitrate (nitric acid; HNO^3) and ammonia (NH^3) or from the reaction of gas-phase nitric acid with pre-existing coarse particles (Kim et al., 2019). The sources of gaseous precursors are fossil fuel combustion (e.g. in car engine or industrial processes), soils (agricultural practices, bacterial activity), biomass burning, and lightning. Ammonium nitrate and ammonium sulphate are formed from the reaction of ammonia NH^3 with nitric and sulfuric acid. NH^3 is produced by coal combustion, biomass burning, fertilizer application, naturally release by soils or emitted as a result of the decay of waste products from domestic animals, wild animals, seas and oceans (Wang et al., 2010). Sea spray and mineral dust are primary particles emitted from natural sources. Sea spray originates from sea surface due to bubble bursting in breaking waves, with an emission rate influenced by sea condition, wind speed at the surface and atmospheric stability. On the other hand, mineral dust results from disintegration of aggregates during movement of large soil particles.

Carbonaceous aerosols are an important aerosol component that accounts for 10 - 70 % of atmospheric particulate matter (Monteiro Dos Santos et al., 2016; Chen et al., 2017; Mikhailov et al., 2017; Sharma et al., 2022). Carbonaceous aerosols are usually divided in black carbon (BC), made of almost pure carbon and organic aerosols (OA), which also contain hydrogen and oxygen. Organic species are characterized by a variety of chemical compounds. They can be subdivided into primary organic aerosol (POA) or secondary organic aerosol (SOA). Natural POAs are emitted from forest fires, suspension of biogenic material (e.g. plant and animal debris, microorganisms, pollen, spores, etc.), also known as primary biogenic aerosol particles (PBAPs; Fröhlich-Nowoisky et al., 2016) and spray from surface waters with dissolved organic compounds (Sciare et al., 2009). Anthropogenic sources are represented by biomass burning (e.g. domestic heating), fossil-fuel combustion (domestic, industrial, traffic), and traffic-related suspension of road dust (Jiang et al., 2019). SOA are instead the product of reactions involving volatile organic compounds (VOCs). These gaseous precursors can nucleate

and grow, be adsorbed or absorbed by pre-existing aerosols or cloud droplets, and be involved in heterogeneous and multiphase reactions. Sources of VOCs can be both natural and anthropogenic. The main natural compounds are isoprene, monoterpenes and sesquiterpenes (Laothawornkitkul et al., 2009; Panopoulou et al., 2020), the main anthropogenic are alkanes (40%), followed by aromatics (20%) and alkenes (10%) (Srivastava et al., 2022).

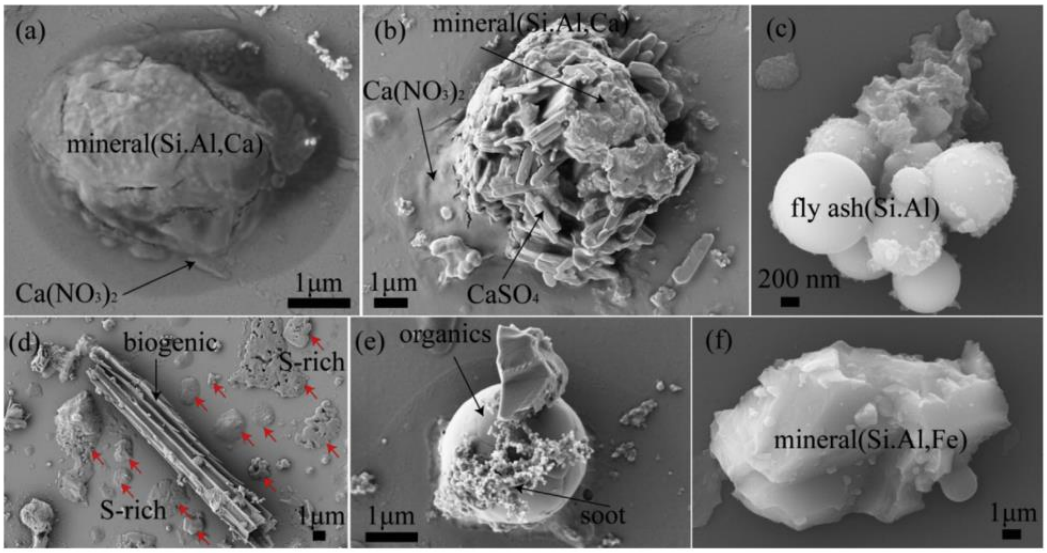

Figure 1-2: Aerosol particles collected on Si wafer, during haze episodes in Jinan city (North China), from (Li et al., 2016). (a) Mineral particles mixed with Ca(NO3)2; (b) Mixture of aggregation of many regular CaSO4 rods and mineral together coated by Ca(NO3)2 (c) An aggregate of fly ash (d) One giant biogenic particle and many secondary S-rich particles (indicated by red arrows). (e) A black carbon (soot) particle associated with a spherical primary organic particle. (f) One irregular mineral particle.

Usually, different chemical species coexist together within the same particle, which is then a mixture of different components. The way these chemical species are arranged spatially within the particle is defined as particle morphology. In the atmosphere, we can find a great variety of particle shapes, from the cubic shape of a sodium chloride crystal to the long branched chains of small spherules of carbon atoms characterizing BC particles. Figure 1-2 gives an idea of the complexity of shapes and mixing states that can be found in the atmosphere.

1.1.2.2 ***Size and size distribution***

Size is another fundamental aerosol property. Aerosol particles can range in size from few nanometres to tens or even hundreds of micrometres.

Usually, the aerosol size is defined through the particle diameter (D_p), which would be the physical diameter if the particles were spherical. The size of the particles represents, then, an alternative speciation of the aerosol population as shown in Figure 1-3. Aerosol particles are usually classified in four main size modes named *nucleation mode* (diameters < 10 nm), *Aitken mode* (diameters ~10 nm – 100 nm), *accumulation mode* (diameters ~0.1 – 2.5 µm), and *coarse mode* (diameters ~2.5 - ~50 µm). Depending on their emission source, aerosol particles can be found in different modes. Freshly formed particles via nucleation are the smallest (nucleation mode), while the Aitken and accumulation is populated by soot and ammonium sulphate. Natural emission dominates the larger modes with mineral dust, sea salt and pollens.

Considering that ambient particles have a variety of morphologies (Figure 1-2), the concept of '*equivalent diameter*' is used. The equivalent diameter is defined as the diameter of a sphere, which with a given instrument, would yield the same size measurement as the particle under consideration. There exist many different definitions depending on the physical property used to measure it (e.g. aerodynamic diameter, diffusion diameter, optical diameter). In this thesis the definition we will encounter are the mass equivalent diameter, the electrical mobility diameter and the optical diameter. The mass equivalent diameter (D_{me}) is defined as the diameter of a spherical particle with the same mass as the one measured. It can be derived by measuring the mass of the particle (m_p) and assuming or measuring its material density (ρ_m) as follows:

$$D_{me}^3 = \frac{6m_p}{\pi\rho_m} \tag{1-1}$$

The electrical mobility diameter (D_m) is instead defined as the diameter of a spherical particle with unit density which has the same electrical mobility (Zp) as the particle in question. The optical diameter (D_{opt}) is instead based on the scattering signal produced by particles when illuminated by a laser beam.

If D_m, D_{me} and D_{opt} define the size of a single particle, size distributions fully describe the properties of a population of aerosol particles. A particle size distribution can be represented by a histogram showing the number of particles per unit volume over specific size intervals. As the size intervals approach infinitesimally small values, a continuous function known as the diameter number density distribution $N(D_p)$ is formed. This function

characterises the number of particles with diameters ranging from D_p to D_p + ΔD_p per unit volume. The differential diameter number size distribution, denoted as $n_N(D_p)$, is precisely defined as:

$$n_N(D_p) = \frac{dN(D_p)}{dD_p} \tag{1-2}$$

so that the total number of particles per unit volume N is obtained by:

$$N = \int_0^\infty n_N(D_p) dD_p \tag{1-3}$$

Many climate-relevant properties depend on the particle mass distributions with respect to particle size more than on the number size distribution. It is than important to define also the aerosol mass size distribution as:

$$n_M(D_p) = \frac{\pi}{6} D_p^3 \, \rho_p n_N(D_p) \tag{1-4}$$

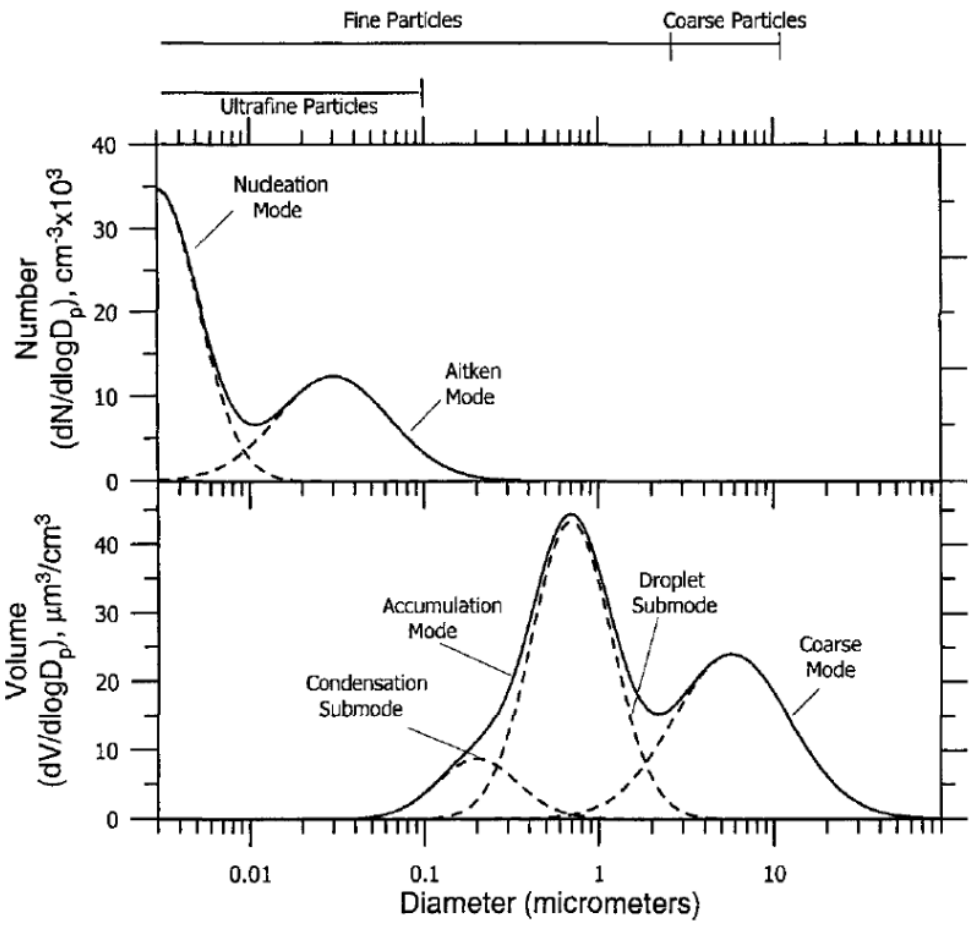

Figure 1-3: Example of number and volume size distributions of atmospheric aerosol particles (Seinfeld and Pandis, 2016). The different modes in which these can be divided are also represented.

From observations it was found that these size distributions can be usually well fitted using a combination of log-normal functions defined as follows:

$$n_N(logD_p) = \sum_{i=1}^{n} \frac{N_{0,1}}{\sqrt{2\pi} log\sigma_{g,i}} exp\left(-\frac{1}{2}\frac{\left(logD_p - log\overline{D_{pg,\iota}}\right)^2}{log^2\,\sigma_{g,i}}\right) \quad (1\text{-}5)$$

where $N_{0,i}$ is the integral of the ith lognormal function, $D_{pg,i}$ is the mean geometric diameter, and $\sigma_{g,i}$ is the geometric standard deviation of the ith log-normal mode. The number size distribution is dominated by the Aitken and nucleation modes, while the volume (and mass) size distribution is dominated by the coarse and the accumulation modes (Figure 1-3).

1.1.2.3 ***Mixing state***

Aerosol chemical and physical properties are not constant in the atmosphere but are highly variable depending on location and lifetime. This variability is described by the aerosol mixing state, which is defined as the distribution of a combination of properties across the particles in a population (Riemer et al., 2019). It can be referred only to the particle composition, so that the mixing state represent the amount of each chemical component in a particle. Or it can be defined in a more general way, including not only the particle composition but a combination of particle properties defining a particle type (e.g. size, composition, optical properties).

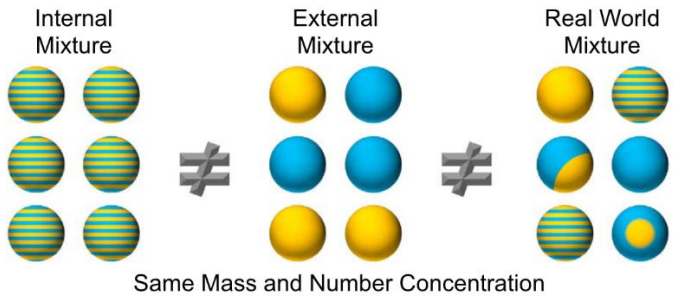

Figure 1-4: Graphical description of the mixing state in an aerosol population (Riemer et al., 2019), showing both the extreme cases of full internal and external mixing, as well as the a real world mixture.

Historically, the mixing state refers to the composition and is divided in external and internal mixing (Winkler, 1973), as described in Figure 1-4. Fully

internal mixtures are populations of particles with the same aerosol type in the same mass fraction, while fully external mixtures are populations of particles with different types in each particle. In the real world we never find these two extremes but more intermediate situations. Different matrixes can be used to define if the population is more internally or externally mixed depending on the properties to be taken into account, the techniques available for measuring or the modelling approach.

1.1.3 Aerosol variability in the atmosphere

The spatial and temporal variability of atmospheric aerosols is a complex and dynamic phenomenon influenced by a multitude of factors. Aerosol concentrations exhibit significant spatial variability due to the inhomogeneous spatial distribution of natural and anthropogenic emissions. As a consequence, different regions or environments are affected by a variable presence of aerosol (Figure 1-5).

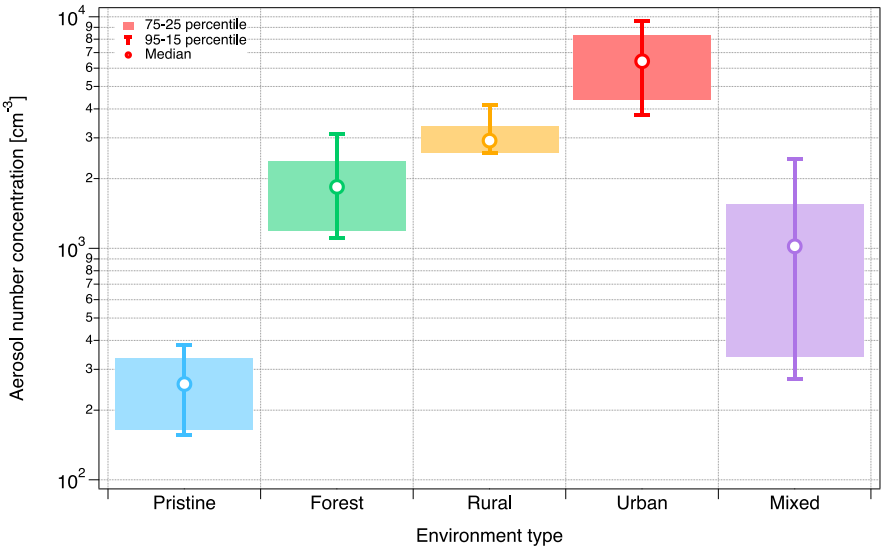

Figure 1-5: Number concentration of aerosol particles in different environments. Data collected at 37 globally distributed stations and representative of four environmental conditions. Adapted from Laj et al. (2020).

Urban areas tend to experience higher concentrations compared to rural backgrounds, reflecting anthropogenic influences, while natural emissions in forest environments can also significantly contribute to aerosol concentration. With increasing distance from emission regions, due to dilution

and removal mechanisms, the concentration of aerosol drastically decreases in pristine regions such as the pole (Figure 1-5). Furthermore, local meteorological conditions, topography, and local atmospheric dynamics control the concentration at specific locations (defined as mixed), which might experience high pollution levels as well as pristine conditions.

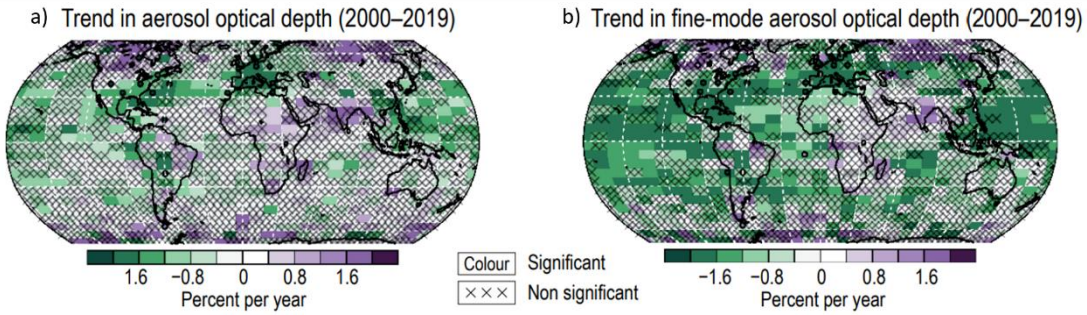

Figure 1-6: Average trend from MODerate Resolution Imaging Spectroradiometer (MODIS) and Multi-Angle Imaging Spectroradiometer (MISR). a) Linear trend in annual mean AOD retrieved from satellite data for the 2000–2019 period (%yr^{-1}). (b) Linear trend in 2000–2019 as in (a), but for fine-mode AOD, AODf, and using only MISR over land.

Temporally, aerosol concentrations vary on different timescales, ranging from diurnal to seasonal and long-term trends. Diurnal variations often result from daily human activities, such as increased traffic during rush hours. Seasonal changes are influenced by factors like meteorological conditions and specific emission patterns associated with different seasons. Long-term trends may be affected by changes in anthropogenic emissions and subsequent regulations, and climate change feedbacks. Hence, there is great uncertainty about multi-decadal trends. As reported by the last IPCC report (2021), there is little confidence in the possibility of a global trend. Most likely there has been a decline since 1990 in Europe and the US (East) and growth since 2000 in East and South Asia. In particular, sulphates increased between up 800 and 1950-70 in Europe, to Svalbard and Russia by a factor 3 to 8, and then decreased by a factor of 2. As for BC, this grew in the 20th century in Europe, Russia, Greenland, the Arctic, saw a slight positive trend in South America, and remained constant at very low concentrations in Antarctica. While a decrease in ground absorption has been observed since the first decade of the 21st century. The study of aerosol optical depth of fine particles (Figure 1-6), related

to anthropogenic aerosol, between 2000 and 2019 shows a decrease (1.5 % per year) in Europe and North America and an increase (1.5 % per year) in South Asia and East Africa.

1.1.4 Aerosol role as short-lived climate forcers (SLCF)

Aerosols have both direct and indirect effects on climate and due to their relatively short suspension time in the atmosphere are important short-lived climate forcers (SLCFs). Their effect is to alter the Earth's radiative balance by scattering and absorbing solar radiation, but also by interacting with clouds. In contrast to well-mixed greenhouse gases, which have more a global effect, SLCFs primarily induce regional-scale radiative forcing effects. They affect climate within weeks after emission. The radiative forcing is proportional to emissions, and change soon after the emissions reach zero. Despite this regional influence, changes in emissions can produce long-term climate effects.

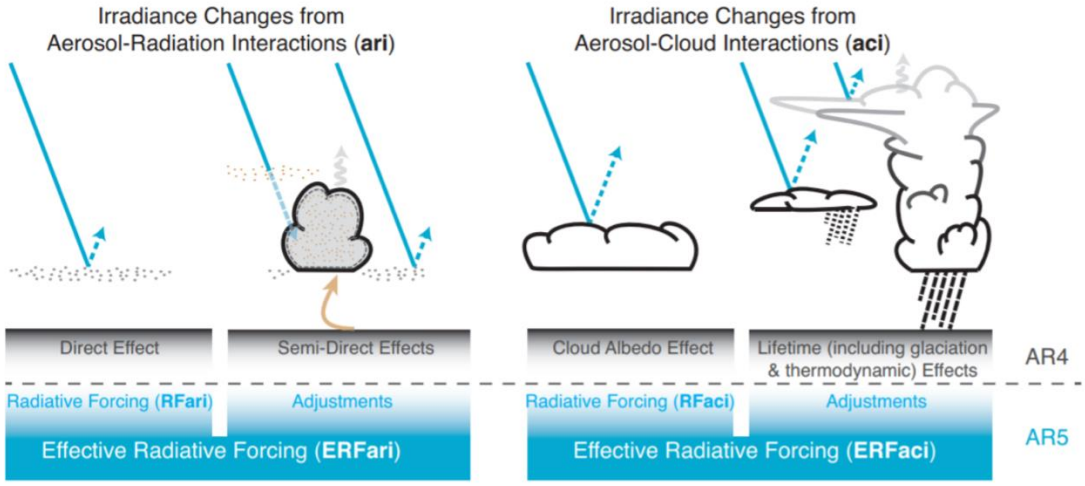

Figure 1-7: Scheme of the new terminology used in the Fifth Assessment Report (AR5) for aerosol-radiation and aerosol-cloud interactions and its relation to the terminology used in the Fourth Assessment Report (AR4), (IPCC, 2013).

Throughout this thesis we adopted the terminology established in the Fifth Assessment Report (AR5) of the Intergovernmental Panel on Climate Change, graphically described in Figure 1-7. This document introduces the distinction between traditional radiative forcing (RF) and effective radiative forcing (ERF), which incorporates rapid adjustments. RF, measured in Wm^{-2}, is

the instantaneous perturbation of the net radiative flux at the top of the atmosphere (TOA) due to changes in the radiative budget with respect to the pre-industrial era (1850), while maintaining the surface temperature and tropospheric state in their unperturbed state.

Negative RFs indicate a decrease in net radiative flux (atmospheric cooling) while positive RFs indicate an energy gain (atmospheric warming). The ERF reflects the change in the net downward radiative flux at the top of the atmosphere, taking into account adjustments in atmospheric temperature, water vapour and clouds, with the global mean surface temperature or part of the surface state unchanged. Essentially, ERF encompasses RF and its rapid adjustments, and has been shown to be a more accurate predictor of subsequent long-term surface temperature changes than instantaneous RF (Bellouin, 2014).

In addition, the IPCC report (2013) distinguishes between aerosol-radiation interactions (ERFari) and aerosol-cloud interactions (ERFaci) as components of the effective radiative forcing, which includes both radiative forcing and adjustments (Figure 1-7). These distinctions are essential for understanding the complex processes of aerosol-induced climate forcing (IPCC, 2013), and are discussed in detail in the following sections.

1.1.4.1 *Aerosol-radiation interaction*

When aerosol particles encounter radiation, their charges are excited. This leads to the re-emission of energy in different directions (scattering) or to its conversion into other forms, such as heat (absorption). The intensity of these interactions vary with the wavelength of the incident radiation, and the aerosol composition, mixing state, size and shape. All atmospheric aerosols have the ability to scatter solar radiation, with only a subset, including black carbon (BC), mineral dust and certain organic matter, that have the additional ability to absorb it. The absorbing components of aerosols contribute to atmospheric warming, while the scattering components contribute to cooling. Therefore, for an accurate assessment of the influence of each chemical species on the planetary energy budget, it is essential to have an estimate of both the scattering and absorption effects.

Mie theory is used to model the radiation-particle interaction. When dealing with submicron aerosols (<1 μm), traditional geometric optics and Rayleigh scattering are not suitable for studying optical properties in the visible spectrum. A theoretical relationship between the microphysical properties of a particle to the absorbed and scattered light was established by Mie (1908) based on Maxwell's equations. The scattering cross-section for a particle of diameter D_p is defined as the amount of light dispersed per unit time in a unit solid angle for a unit of incident light. The scattering cross-section (σ_s) is then determined by integration over the entire surface of a unit sphere. It quantifies the scattered energy (F_s) in all directions relative to the intensity of the incident light (F_0), which is expressed mathematically as follows:

$$\sigma_s = \frac{F_s}{F_0} \tag{1-6}$$

In the same way, the absorption cross-section (σ_a) represents the energy absorbed (F_a) from all directions with respect to F_0, given by:

$$\sigma_a = \frac{F_a}{F_0} \tag{1-7}$$

The conservation of energy leads to the concept of extinction, where the extinction cross-section (σ_e) is defined as the sum of the scattering cross-section and the absorption cross-section, expressed as follows:

$$\sigma_e = \sigma_a + \sigma_s \tag{1-8}$$

The scattering and absorption phenomena are influenced by key parameters such as the wavelength of the incident radiation (λ) and the diameter of the particle (D_p), assuming it is spherical. These parameters are summarised in the dimensionless size parameter (χ), given by $\chi = (\pi D_p)/\lambda$. The size parameter delineates the optical domains, with the Mie domain characterised by χ values close to unity, meaning that the wavelength of incident light is comparable to the size of the particle. Another crucial factor is the refractive index ($m(\lambda) = n + ik$), a complex number with a real part (n) describing scattering and an imaginary part (k) related to absorption. In atmospheric science, the refractive index is normalised to the refractive index of air.

The optical coefficients, including scattering (b_{sca}), absorption (b_{abs}) and extinction (b_{ext}) coefficients, are widely used in atmospheric science. These

coefficients are functions of particle size, refractive index and wavelength of incident light and are expressed in inverse metres (m^{-1}). They are defined by integrals involving the aerosol mass distribution (n_M), particle diameter (D_p) and density (ρ_p) and efficiency factors (Q). Specifically, the coefficients are given by:

$$b_{sca}(\lambda) = \int_0^{D_p^{max}} \frac{3}{2\,\rho_p D_p} Q_s(m,\chi) n_M(D_p) dD_p \tag{1-9}$$

$$b_{abs}(\lambda) = \int_0^{D_p^{max}} \frac{3}{2\,\rho_p D_p} Q_a(m,\chi) n_M(D_p) dD_p \tag{1-10}$$

$$b_{ext}(\lambda) = \int_0^{D_p^{max}} \frac{3}{2\,\rho_p D_p} Q_e(m,\chi) n_M(D_p) dD_p \tag{1-11}$$

Efficiencies (Q) are defined as the ratio of scattering, absorption or extinction cross-section to the geometric cross-sectional area of the particle.

The comprehensive nature of these optical coefficients implies that they are proportional to the amount of aerosol present and that they can be measured by instrumentation. Furthermore, the mass scattering cross-section (MSC), mass absorption cross-section (MAC) and mass extinction cross-section (MEC) can be calculated from observations, representing the amount of scattered, absorbed or extinguished light per unit mass of non-absorbing, absorbing or total aerosol material, respectively. These parameters are given as:

$$MSC(\lambda)[m^2/g] = \frac{b_{sca}(\lambda)[Mm^{-1}]}{m_s[\mu g/m^3]} \tag{1-12}$$

$$MAC(\lambda)[m^2/g] = \frac{b_{abs}(\lambda)[Mm^{-1}]}{m_a[\mu g/m^3]} \tag{1-13}$$

$$MEC(\lambda)[m^2/g] = \frac{b_{ext}(\lambda)[Mm^{-1}]}{m_{tot}[\mu g/m^3]} \tag{1-14}$$

where m_s, m_a, and m_{tot} denote the mass concentrations of the non-absorbing, absorbing, and total aerosol masses, respectively.

Scattering, absorption and extinction depend on the wavelength of the incident light with a power law. The wavelength dependent variation in scattering, absorption and extinction coefficients can be quantified with the Scattering Ångström Exponent (SAE; Equation 1-15), the Absorption Ångström Exponent (AAE; Equation 1-16) Extinction Ångström Exponent (EAE; 1-17), respectively.

$$\frac{b_{sca}(\lambda)}{b_{sca}(\lambda_0)} = \left(\frac{\lambda}{\lambda_0}\right)^{-SAE} \tag{1-15}$$

$$\frac{b_{abs}(\lambda)}{b_{abs}(\lambda_0)} = \left(\frac{\lambda}{\lambda_0}\right)^{-AAE} \tag{1-16}$$

$$\frac{b_{ext}(\lambda)}{b_{ext}(\lambda_0)} = \left(\frac{\lambda}{\lambda_0}\right)^{-EAE} \tag{1-17}$$

These exponents are valuable parameters for deriving aerosol properties from optical measurements. The AAE is related to the colour of the particle and is therefore useful in distinguishing between the three primary absorbing components (BC, dust and OA). Several studies (Rosen et al., 1978; Bergstrom et al., 2002, 2007; Kirchstetter et al., 2004; Clarke et al., 2007) confirm values close to unity for BC, which can vary between 1.9 and 0.8 when BC is internally mixed with other compounds (Lack and Cappa, 2010; Liu et al., 2018). Observed OA AAE ranges from 3.5 to 7 (e.g. Kirchstetter et al., 2004; Sun et al., 2007; Lewis et al., 2008; Yang et al., 2009), while that of dust is typically around 2 to 3, but can be higher for very red dusts (e.g. Alfaro et al., 2004; Bergstrom et al., 2007).

On the other hand, SAE depends primarily on the dominant size mode in an aerosol mixture, with higher values associated with the smallest particles of the fine mode and lower values indicating the predominance of larger particles. Other intensive properties can be calculated by combining b_{abs} and b_{sca}. The single scattering albedo (SSA) defines the dominant light-aerosol interaction and is defined as:

$$SSA(\lambda) = \frac{b_{sca}(\lambda)}{b_{ext}(\lambda)} = \frac{b_{sca}(\lambda)}{b_{sca}(\lambda) + b_{abs}(\lambda)} \tag{1-18}$$

Values close to unity indicate that the aerosol scatters predominantly, while values below 0.8 indicate that the particles could have a net warming effect (Haywood and Shine, 1995).

After having defined the main parameters that are necessary to define the optical properties of a population of particles, let us see how the RFari is then evaluated. RFari depends on the spatial distribution of aerosol concentrations in both the horizontal and vertical dimensions, as well as the scattering and absorption properties. The latter are influenced by aerosol size and chemical composition. In addition, environmental factors contribute significantly to the variability of RFari, such as the zenith angle of the sun and the reflectivity of the underlying surface or cloud beneath the aerosol layer. Several approximate formulae have been developed for the quantification of RFari at the top of the atmosphere in cloud-free conditions. One such formula (Bellouin, 2014) applicable to both scattering and absorbing aerosols is:

$$RFari \sim ST^2\,\overline{SSA}\,\beta\,\Delta\tau\left[(1-R_s)^2 - 2R_s\left(1-\ \overline{SSA}/\left(\overline{SSA}\,\beta\right)\right)\right] \qquad (1\text{-}19)$$

The formula expresses RFari as a function of the solar constant (S) in Wm^{-2}, the dimensionless atmospheric transmittance above the aerosol layer (T) and the dimensionless surface reflectance (R_s). Aerosols are characterised by three dimensionless parameters: the change in optical thickness (Δτ), the single scattering albedo (SSA) and the up-scatter fraction (β), which is the fraction of radiation scattered upward for the horizontal plane of the particle. Equation 1-19 emphasises that the sign of RFari depends on both the aerosol absorption properties and the surface reflectance. For a given set of optical properties, it also illustrates the linear dependence of RFari on the change in aerosol optical thickness or, equivalently, aerosol concentration. Aerosol-radiation interactions induce rapid adjustments. This is particularly noticeable for absorbing aerosols such as BC. Highly absorbing aerosols such as BC can affect cloudiness and liquid water content by heating the cloud and its surroundings. This is known as the semi-direct effect. This effect was identified by Hansen et al. (1997). It results from the direct interaction of aerosols with radiation and indirectly influences climate by changing cloud properties.

1.1.4.2 *Aerosol-cloud interactions*

Clouds play a crucial role in regulating the Earth's radiative budget, nearly doubling the planet's albedo. This results in the reflection of incoming shortwave solar radiation and the re-emission of longwave terrestrial radiation (Ramanathan et al., 1989). Aerosols and clouds are linked through a series of intricate feedback mechanisms, collectively referred to as aerosol-cloud interaction (RFaci).

The radiative forcing resulting from aerosol-cloud interactions is driven by the critical role that aerosols play in the life cycle of clouds as cloud condensation nuclei (CCN) and ice nucleating particles (INP). Condensation of water vapour on pre-existing aerosol particles, specifically CCNs, forms cloud droplets. The super saturation required for water droplet formation, and hence cloud formation, is significantly reduced by the presence of suitable aerosol particles (e.g. Pruppacher et al., (1998)). The effectiveness of a particle to act as a nucleus for the formation of water droplets is dependent on its size, its chemical composition and the local super saturation. Hygroscopic materials such as sulphates and sea salts are highly effective as CCNs. Mineral dust and combustion products can also be effective, particularly if they are wet or have hygroscopic coatings. Hence, CCNs promote the formation of numerous and yet small droplets (Twomey, 1959). This phenomenon, known as the Twomey effect, is responsible for the elevated albedo of liquid droplets in an aerosol-rich atmosphere. Subsequent adjustments tend to delay or suppress rainfall, prolonging the lifetime of clouds and increasing cloud coverage (Albrecht, 1989).

Pure water and solution droplets freeze at temperatures lower than -35 °C. This ice formation mechanism does not require the presence of any impurities such as aerosol particles and it is generally known as homogeneous ice nucleation (Koop et al., 2000). A small subset of aerosols also serves as ice nucleating particles (INPs), triggering the formation of ice crystals and promoting the glaciation of clouds at subzero temperatures and above -35°C (DeMott et al., 2010). These INPs are responsible of the formation of ice via heterogeneous ice nucleation (e.g. Seinfeld and Pandis, 2016). The formation of ice crystals depends directly on the properties of the INP particle such as diameter and composition, but also on super saturation of water with respect

to the ice phase. Overall, biogenic aerosol (spores, pollen and viruses) are very efficient INP at high temperatures (-10°C < T < -5°C; Diehl et al., 2001)) while mineral dust is an efficient INP at slightly colder regime (-15°C < T < -35°C; Atkinson et al., 2013). The transition from a purely liquid cloud to a mixed-phase cloud results in an increase of large ice crystals, leading to reduced sunlight reflection and increased precipitation, thereby shortening cloud lifetime and reducing cloud coverage (Murray et al., 2021). Nevertheless, the incorporation of INPs into climatic models remains rudimentary (Vergara-Temprado et al., 2018), and its impact on the radiative forcing of aerosol-cloud interaction, as outlined in the most recent IPCC report, remains largely unaccounted for. Hence, we here focus on the role of CCN as climatic forcer.

The Twomey effect, as described in studies such as Feingold (2003), means that an increase in the number of CCNs results in more cloud droplets and a simultaneous reduction in droplet size. The relationship between aerosol concentrations and raindrops is non-linear and can be expressed as:

$$N_d \sim N_a^b \tag{1-20}$$

where N_d is the concentration of the droplet, N_a is the concentration of the total particle, and b varies widely depending on the properties of the aerosol. Taking into account the solar constant (S), fractional cloud cover (f), changes in cloud condensation nuclei due to anthropogenic activities (δN_a), the sensitivity of cloud droplet number to changes in cloud condensation nuclei ($\delta N_d/\delta N_a$), and the sensitivity of cloud albedo to changes in cloud droplet number ($\delta\alpha/\delta N_d$), an approximate formula (Bellouin, 2014) for calculating RFaci is:

$$RFaci = -S \cdot f \cdot \frac{\delta\alpha}{\delta N_d} \cdot \frac{\delta N_d}{\delta N_a} \cdot dN_a \tag{1-21}$$

The understanding of the cloud adjustment component of the ERFaci, which includes both albedo and lifetime effects, is still uncertain. The influence of aerosols on the cloud albedo is associated with multiple light scattering within the cloud, which leads to an increase at higher CCN numbers. Models suggest that aerosols also affect the distribution of liquid water within the

cloud. This affects cloud lifetime, precipitation, and extent. The response of the cloud to the adjustment depends on the state of the cloud and the environmental conditions, which influence factors such as precipitation and vertical motion within the cloud. Observational evidence for rapid adjustments varies, showing either reduced or increased precipitation in regions with high anthropogenic aerosol loading, depending on the cloud regime. The influence of aerosol-driven rapid adjustments is probably limited to specific cloud regimes or situations where changes in condensation nuclei force cloud regime transitions.

1.1.4.3 *Estimate and variability of effective radiative forcing*

The last IPCC report AR6 (2021) provides the most updated estimates of ERF and its trend, derived based on the Coupled Model Intercomparison Project (CMIP6). These estimates are valid for 2014 relative to 1850. According to these results the average ERF is -1.11 ± 0.38 Wm^{-2}, with ERFari at -0.25 ± 0.40 Wm^{-2} and ERFaci at -0.86 ± 0.57 Wm^{-2}. This estimate depends on all the different aerosol components as illustrated in Figure 1-8b and is still largely uncertain.

The ensemble-mean aerosol Effective Radiative Forcing (ERF) exhibits significant regional variability over the 1850–2014 period (Figure 1-8a). Negative ERF is most pronounced over and downwind of industrialized regions in the Northern Hemisphere, particularly Eastern Asia and Southern Asia, reflecting changes in anthropogenic aerosol emissions. Europe and North America also show substantial negative forcing. Conversely, positive ERF over high albedo areas, such as cryosphere, deserts, and clouds, attributed to absorbing aerosols, lacks robustness across the applied CMIP6 ensemble.

Regional net aerosol ERF trends demonstrate a division into two groups based on whether the mean ERF reaches its negative peak value in the 1970s–1980s (e.g., Europe, North America) or in the late 1990s–2000s (e.g., Asia, South America). This shift aligns with regional long-term trends in aerosol precursor emissions. However, finer regional scales reveal some areas where sulphate aerosols are still increasing, suggesting persistence in ERF trends for these regions. Global mean ERF experiences a maximum negative value in the mid-1970s, gradually decreasing thereafter, consistent with reduced global mean

SO_2 emissions and increased global BC since 1990. Despite these trends, uncertainties persist due to inter-model variations in aerosol-cloud interactions and microphysical processes, highlighting the complexity of accurately simulating aerosol ERF distribution and trends. In summary, the spatial and temporal distribution of the net aerosol ERF from 1850-2014 is highly heterogeneous, with a global shift from increasing to decreasing negative net aerosol ERF, driven by trends in aerosol and precursor emissions, although with temporal variations at different regional scales.

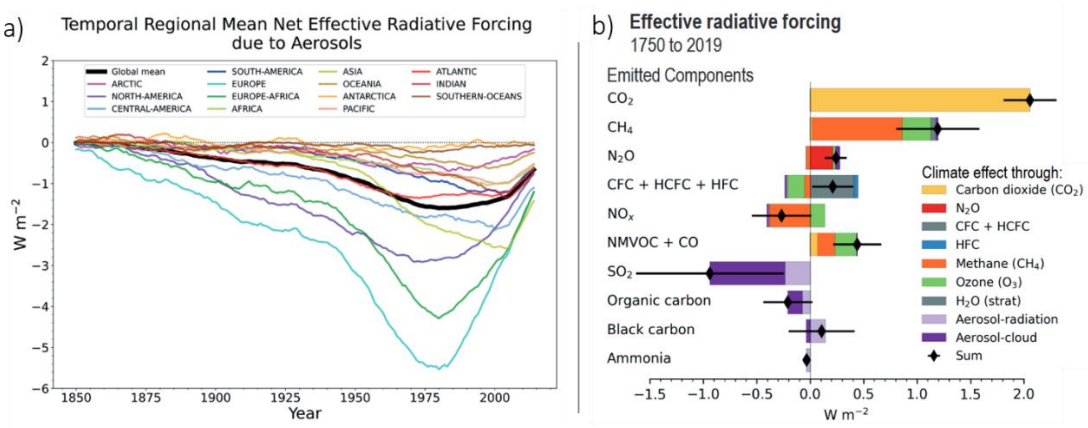

Figure 1-8: a) Temporal variability of mean net radiative forcing due to aerosol in different regions of the globe; b) Description of Effective radiative forcing due to SLCF and specifically to aerosols (purple boxes). Adapted from IPCC (2021).

1.1.5 Observations of aerosol climate-relevant properties

Understanding the spatial and temporal variability of atmospheric aerosols is crucial for assessing their impact on air quality and climate. Monitoring and analyzing these variations provide valuable insights into the complex interplay between natural and anthropogenic factors shaping the atmospheric aerosol composition and distribution. However, there are still notable limitations in accurately assessing the spatial and temporal variability of atmospheric aerosols. One significant challenge arises from the spatial and temporal coverage constraints associated with in situ techniques. While these methods provide accurate measurements, their deployment is often limited to specific locations and short durations, hindering a comprehensive understanding of global aerosol dynamics. There is considerable variation from place to place in the current availability and accessibility of ground-based

datasets. Satellite measurements, while offering extensive spatial coverage, face challenges related to the vertical distribution of aerosols and the difficulty in distinguishing between different aerosol types. Additionally, inconsistencies persist between aerosol models and measurements, highlighting the complexity of simulating the intricate interactions within the atmosphere accurately. Clearly, neither a single approach to atmospheric aerosol observations nor a limited set of instruments can provide the necessary data to quantify the aerosol forcing on climate in all its relevant dimensions and space-time scales (Anderson et al., 2005). A climate aerosol observing system requires combining all types of observations with models to extrapolate large geographical scales to compare satellite measurements (e.g. Anderson et al., 2005 and Kahn et al., 2023).

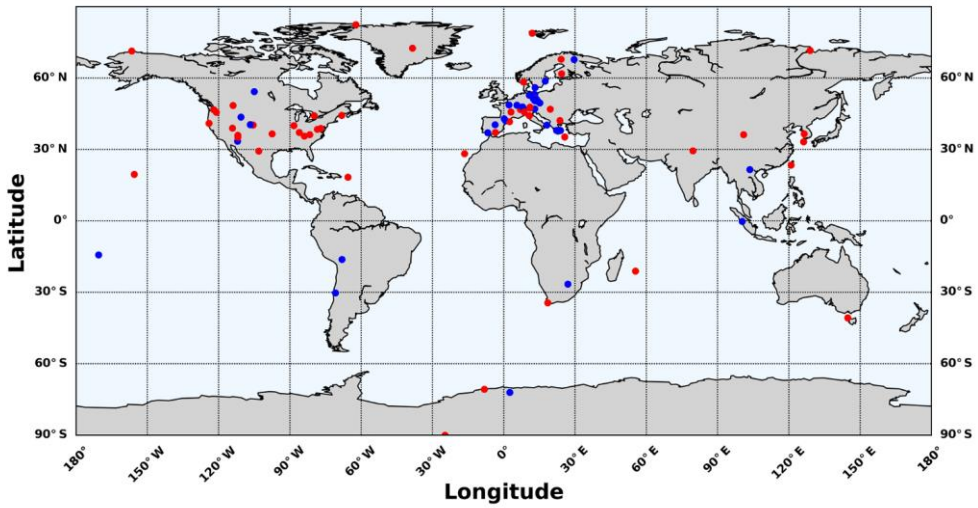

Figure 1-9: Location of major global in situ sites with measurements of aerosol optical properties. In blue, sites active in the year 2017 and in red, sites with at least > 10-year time series (Laj et al., 2020).

The in situ segment of atmospheric observations is very complex, with several networks, operating at regional or global scales, that support consistent, long-term measurements of atmospheric variables. The World Meteorological Organisation's (WMO) GAW programme was established in 1989 and the GAW aerosol programme in 1997, with the specific aim to monitor the background atmospheric conditions, evaluate the polluted air mass transports, evaluate trends of pollutant and essential climate variables, study the interactions between environment and climate. The main networks providing in situ aerosol

properties, are the NOAA's Federated Aerosol Network (NFAN), comprising sites mainly in North America, but also including sites in Europe, Asia and the Southern Hemisphere, including Antarctic sites, and the Clouds and Trace Gases Research Infra Structure (ACTRIS) operating mainly in Europe, but also including sites in other WMO regions. In the last decades, European Community established the ESFRI Research Infrastructures, in order to provide a long term, sustainable, reliable, traceable and high quality data for many actual research investigations. ACTRIS is the Research Infrastructure regarding the short live atmospheric species. Figure 1-9 summarizes the main global stations with in-situ observations of climate relevant properties.

1.2 BLACK CARBON

1.2.1 Definition based on unique properties

Black carbon (BC) is a distinct type of carbonaceous aerosol formed in flames by the incomplete combustion of liquid and solid fuels. Historically labelled as "soot" to describe the black material emitted from wood and coal fires, it has no universally accepted definition yet. The wide variety of nomenclatures and definitions that have proliferated over the past decades have been carefully collected and organised by Petzold et al. (2013), and will be detailed in Section 1.2.4. BC is characterized by unique physical, chemical, and optical properties, encompassing morphology, microstructure, thermal stability, solubility, and light absorption (Bond et al., 2013; Petzold et al., 2013; Corbin et al., 2019).

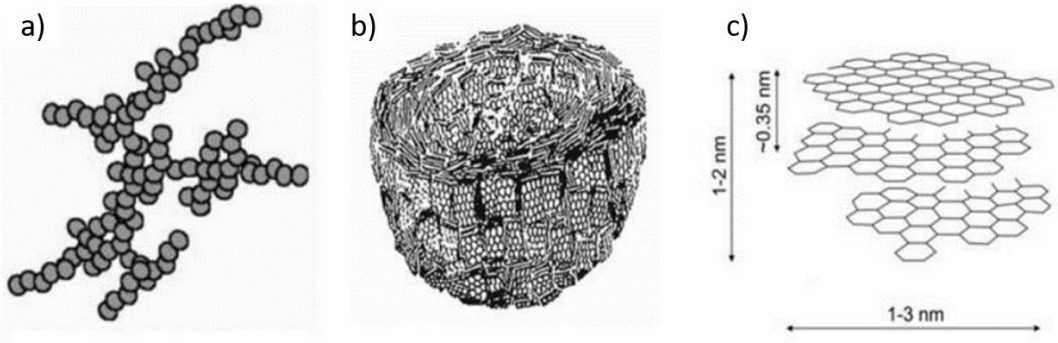

Figure 1-10: Schematic of BC structure in different scales: a) fractal-like soot aggregate consisting of primary spherule; b) inner structure of a primary spherule; c) ordered domain composed of small, parallel carbon layers. From Pawlyta and Hercman (2016).

In terms of morphology, the typical structure of BC involves a fractal-like aggregate formed through rapid coagulation of primary spherules during combustion (Figure 1-10a) (Medalia and Heckman, 1969; Haynes and Wagner, 1981). These primary spherules, exhibit diameters ranging from less than 10 to approximately 50 nm, varying with source type and combustion conditions. The typical morphology of fresh particles is thus well described as a fractal cluster by the following law:

$$N_S = k_0 \left(\frac{R_g}{a}\right)^{D_f}, \tag{1-22}$$

where a is the mean monomer radius, k_0 is the fractal pre-factor, D_f is the fractal dimension, N_S is the number of monomers (primary spherules) in the cluster, and R_g, called the radius of gyration, is a measure of the total cluster radius. In terms of microstructure, each primary spherule comprises disordered graphite layers (Figure 1-10b) predominantly composed of carbon (90% in mass), with a minor presence of hydrogen. The graphite layer is characterized by a significant fraction of sp2-bonded carbon atoms (Figure 1-10c; Ogren and Charlson, 1983; Smith, 1981). Recent classifications by Corbin et al. (2019) introduce the distinction between "soot BC" (predominant type) and "char BC," the latter produced through the pyrolysis of low-volatility fuel droplets, that undergo surface graphitization. Char BC particles are bigger than soot BC particles and more spherical. In terms of thermal stability, both soot BC and char BC display extreme refractoriness in an inert atmosphere, with a sublimation temperature exceeding 4000 K (Schwarz et al., 2006). Gasification occurs solely through oxidation at temperatures above 340 °C (Cachier et al., 1989).

Pure BC exhibits robust light absorption, with a higher mass absorption cross-section (MAC) compared to other light absorbing aerosol species such as dust and brown carbon (BrC), as described in Figure 1-11. A MAC value of 7.5 ± 1.2 m^2g^{-1} at a wavelength of 550 nm is generally accepted as typical for freshly emitted BC. This was proposed by Bond and Bergstrom (2006) and confirmed in a recent review by Liu et al. (2020), where an average of 8.0 ± 0.7 m^2g^{-1} was found. However, ambient measurements show higher variability, reflecting the dependence of this parameter on the compaction of fractal aggregates and the mixing state of the particle. In particular, Zanatta et al.

(2016) found a mean value of 10 m^2g^{-1} at 637 nm for European boundary layer, and values in the range of 10-15 m^2g^{-1} at 550 nm were derived in different sites in the Arctic (Ohata et al., 2021). These values are one to two order of magnitude higher than those measured for dust or BrC. Samset et al. (2018) clearly discuss differences in absorption by these aerosol components. At a wavelength of about 600 nm he calculated a MAC of 8-9 for BC, 0.02-0.05 for dust and 0.1-0.7 for BrC (Figure 1-11).

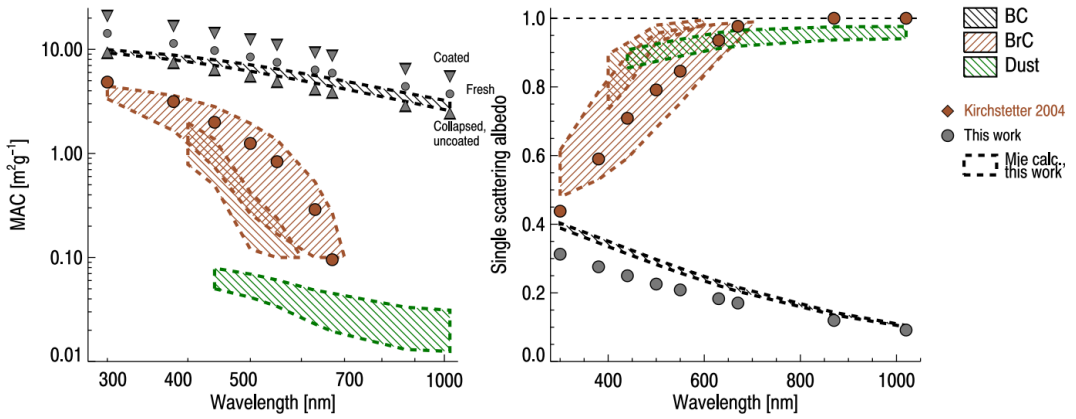

Figure 1-11: Values of Mass Absorption Cross-section (MAC) and Single Scattering Albedo (SSA), and their spectral dependence, for different aerosol species BC, BrC and dust (Samset et al., 2018).

These values in turn lead to marked differences in the values of the single scattering albedo, a parameter that, as discussed in Section 1.1.4.1, determines the nature of the radiative impact caused by an aerosol population. Values of 0.2-0.3, >0.9, >0.8 for BC, dust and BrC respectively are reported by Samset et al. (2018) and shown in Figure 1-11. BC is therefore the only aerosol that causes heating of the atmosphere, while scattering remains dominant for the other absorbing components. In addition, the wavelength dependence of BC absorption differs significantly from that of dust and BrC, as detailed in Section 1.1.4.1.

Notably, BC remains insoluble in any solvent and in water (Fung, 1990). In turns, this means that pure and fresh BC is not hydrophilic and does not behave as cloud condensation nuclei (Dalirian et al., 2018).

1.2.2 Emissions from different sources and regions

Over the centuries, global black carbon (BC) emissions have undergone significant changes. If BC emissions were dominated by biomass burning in the pre-industrial era (before 1750), there was a notable increase in anthropogenic emissions attributed to coal and biomass consumption in the residential sector from 1850 onwards (Lamarque et al., 2010; Bond et al., 2013). By 2000, BC emissions had increased to about five times the background level of 1750, mainly driven by energy consumption. During this period, biomass burning and energy-related activities were the main contributors, with energy-related emissions accounting for 59% and biomass burning for 41% (Bond et al., 2013).

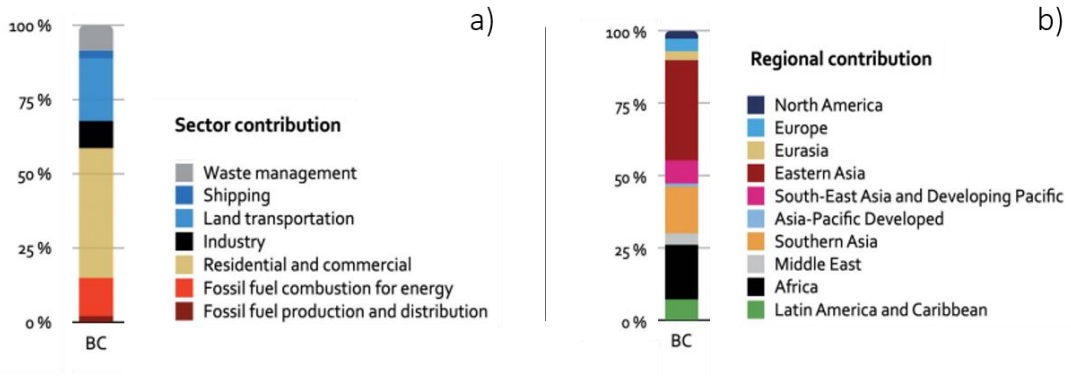

Figure 1-12: Black carbon emission contributions by sector (a) and region of the world (b), adapted from IPCC (2021).

Historically, North America and Europe contributed around half of global BC emissions. However, technological advancement in industrial processing, renewable energy and transport, and global policies to improve air quality have led to significant BC emission reduction in these regions. Nowadays, due to industrial development and the absence of emission reduction policies, Asia and Africa contribute about 80% of global carbonaceous aerosol emissions (Figure 1-12b). Residential solid fuels are a major contributor, accounting for 60-80% of emissions in Asia and Africa, while diesel engines play a significant role in Europe and North America, contributing around 70% (IPCC, 2021) of BC emission in these two areas. Globally, the residential and commercial sectors are the main contributors, followed by land transportation, fossil fuel combustion for energy production, waste

management, and industry. Minor contributions derive from shipping, and fossil fuel production and distribution (Figure 1-12a).

Despite progress, uncertainties remain, particularly in Asia and Africa, that weakens our confidence in emission estimates and trends. Overall, there is a factor of two uncertainties in global BC emission estimates, with post-2005 emissions in Asia (high confidence) and Africa (medium confidence) likely to be overestimated. This highlights the need for continued refinement of emission estimates to improve the quantification of climatic impacts associated with BC (IPCC, 2021).

1.2.3 Formation and evolution

The exact formation mechanism of black carbon particles is not yet fully understood, but involves several steps: i) fuel pyrolysis and thermal degradation; ii) formation of polycyclic aromatic hydrocarbons; iii) growth of polycyclic aromatic hydrocarbon structures; iv) conversion of gas into particles; v) surface growth and coagulation to form the new particles (Masiello, 2004; Moosmüller et al., 2009; Bond et al., 2013).

After emission, during their suspension and transport in the atmosphere, BC particles undergo complex chemical and physical transformations, collectively referred to as atmospheric ageing. Overall, the ageing process promotes the transition from external to internal mixing. The latter, as better defined in Section 1.1.2.3, characterises a diverse population of heterogeneous agglomerates, where black carbon and other materials are combined within the same single-particle volume. This process involves the dynamic interaction of BC with various atmospheric components and it is schematized in Figure 1-13. Within hours to days from emission, condensation of gases, coagulation with other atmospheric aerosol and oxidation result in an internal mixture of BC with other coating material (Jacobson, 2001; Fierce et al., 2015). While condensation dominates during the day, coagulation is more likely to be the driving mixing process at night (Riemer et al., 2010). This first stage of ageing leads to the formation of thin or partial coatings on the BC surface, which maintains a complex geometry (He et al., 2015). On a longer timescale (days, Figure 1-13), the process of coagulation causes an increase in coating thickness (Matsui et al., 2013; Matsui, 2016), which may fully envelop

the BC core resulting in an almost spherical shape (He et al., 2015). As shown in Figure 1-13, depending on the availability of coating material and its precursors, thin coatings form on a local scale, while thick coating may be observed after the regional transport (He et al., 2015; Matsui et al., 2013; Matsui, 2016).

Although there is consensus on the occurrence of internal mixing, there is still debate on the geometry of BC-containing particles. Considering the fractal-like morphology of fresh BC particles (Figure 1-14a), the most common simplification includes the assumption of a complete and symmetrical encapsulation of BC by non-BC material, referred to as concentric core-shell geometry assuming a fully spherical particle shape. An alternative simplified mixing configuration, such as partial and non-concentric shells and BC cores attached to other non-BC particles, have also been proposed (Sedlacek et al., 2012; Adachi et al., 2010; China et al., 2013; Dahlkötter et al., 2014). Figure 1-14 provides examples of the existing geometry found in ambient samples.

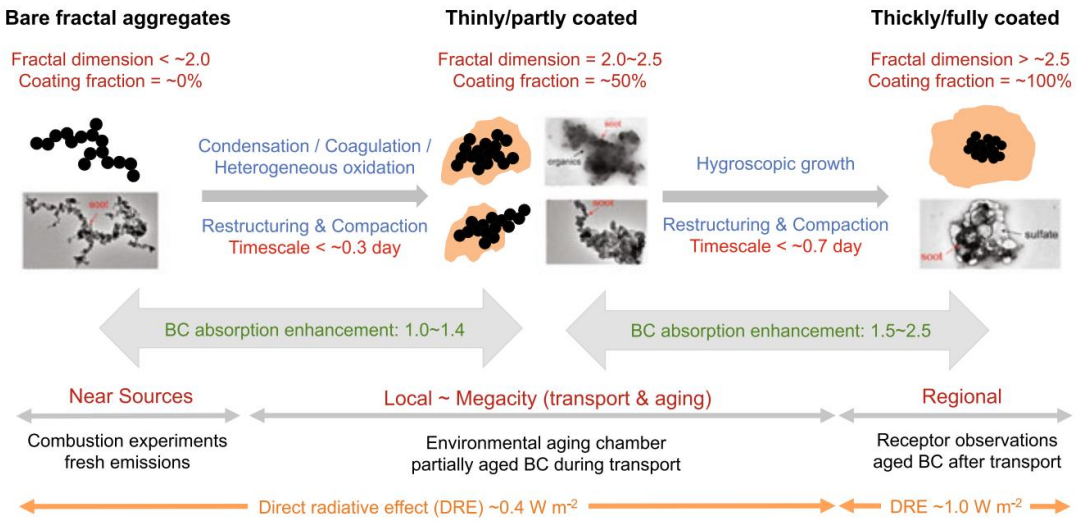

Figure 1-13: Schematic description of black carbon ageing in the atmosphere and main changes in its properties (He et al., 2015).

Ageing processes induce changes in the hygroscopic properties of BC. Freshly released BC is predominantly hydrophobic (Weingartner et al., 1997). However, its hygroscopicity increases (Schwarz et al., 2015; Ohata et al., 2016) during ageing due to changes in the particle diameter (Motos et al., 2019) and

the formation of inorganic and organic coatings (Dalirian et al., 2018; Motos et al., 2019). It is recognised that BC can acquire hydrophilic properties within 1-2 days in the atmosphere, making it capable of acting as cloud condensation nuclei (Koch et al., 2009). Hence, aged and coated BC may be activated in the cloud phase and be removed via nucleation scavenging during precipitation events (Bond 2013). This makes the ageing process to be one of the factors controlling the atmospheric residence time of BC (i.e. the time between emission and deposition). The so-called wet deposition contributes to 66% of the total removal of BC (Chung and Seinfeld, 2002). Models indicate that wet removal is three times more efficient in removing BC from the atmosphere than dry deposition processes (Bauer et al., 2013). BC particles deposited on surfaces such as soils, snow and ice, water and sediments can ultimately be preserved (Bisiaux et al., 2011).

As BC aggregates during ageing, they can collapse to form less fractal and more compact particles (Figure 1-13). Consequently, the size distribution of the BC population gradually changes during transport and ageing. The change in morphology and size coupled with the uptake of a coating, also alters the optical properties of BC, which will be discussed in detail as it follows.

1.2.3.1 *Variability of BC size distribution with sources and ageing*

The size and mass and number size distributions of BC, are crucial parameters in defining its optical properties and lifetime in the atmosphere. Usually in literature, we can find the description of the size distribution of BC derived from the mass equivalent diameter, from which the mass median diameter (MMD) and number median diameter (NMD) are derived. Size distributions, and consequently the MMD or NMD, show great atmospheric variability, influenced by both sources and ageing processes.

In particular, the size varies with the type of source. Traffic emissions produce smaller particles compared to emissions from biomass burning (Schwarz et al., 2008). The number size distribution of traffic emissions peaks around 60-80 nm, while that of biomass burning peaks around 80-130 nm (Gong et al., 2016). MMD measurements in urban areas in summer (mostly related to traffic) range from 119 to 124 nm, while in winter (mixed sources) they range from 135 to 167 nm (Liu et al., 2014). The diameter also differs for

different fuel types; traditional coal combustion shows BC diameters around 200-250 nm (Yuan et al., 2021; Liu et al., 2019). Diesel and gasoline-powered vehicles produce emissions with smaller BC particles than coal, with gasoline-powered vehicles producing more diverse and smaller BC particles than diesel (Krecl et al., 2017; Han et al., 2019). Combustion conditions also contribute to the variability, with studies on petrol vehicles showing high variability in concentrations and sizes (Karjalainen et al., 2014). This variability may be due to a varying number of primary spheres (for a fixed primary sphere size), or a fixed number of spheres of different sizes, or a combination of both.

During atmospheric ageing, the BC core can increase in size due to intra-coagulation. This process occurs between freshly emitted BC particles and between fresh and aged BC. Considering that the coagulation rate is proportional to the square of the particle number concentration, in highly polluted environments, there is a rapid shift of the size distribution towards to larger diameters soon after emission (Krasowsky et al., 2018). On the contrary, in background and cleaner environments the coagulation process becomes less effective. Freshly emitted particles also have a lacy, branched structure, which becomes more compact and almost spherical as the coating causes the core to shrink due to capillary forces (China et al., 2015). In the transition from background to remote regions, and from the boundary layer to higher altitudes, the dominant mechanism changing the size distribution is selective removal. Wet removal is more effective for large and water-soluble BC-containing particles (Moteki et al., 2012; Ohata et al., 2016), leading to a shift towards smaller diameters of the distribution peak (Miyakawa et al., 2017).

1.2.3.2 *Variability of optical properties with ageing*

Becoming internally mixed, the optical properties of BC evolves with the degree of internal mixing, change in morphology, and size. First, each of the chemical species present in the BC-containing particle interacts differently with radiation, with inorganic components being mainly non-absorbing and some organic components being slightly absorbing. Second, with the formation of thin coatings around the BC core, the initial branched fractal-like structure collapses, resulting in a change in the cross-section of scattering and absorption. Third, with the growth of coating, the diameter and cross-section of the total particles increases. The result is a significant change in the intensive

optical properties of the particle, with an increase of its ability to absorb radiation through the so-called 'lensing effect'.

In particular, the MAC, crucial parameter in the assessment of the direct radiative forcing of BC, changes. This change is quantified through a parameter called absorption enhancement (E_{abs}), obtained from the MAC of bare BC compared to that of a coated BC-containing particle as follow:

$$E_{abs} = \frac{MAC_{BC}^{coated}}{MAC_{BC}^{bare}} \tag{1-23}$$

The variability of E_{abs} can be estimated using different approaches: field measurements, laboratory studies and modelling.

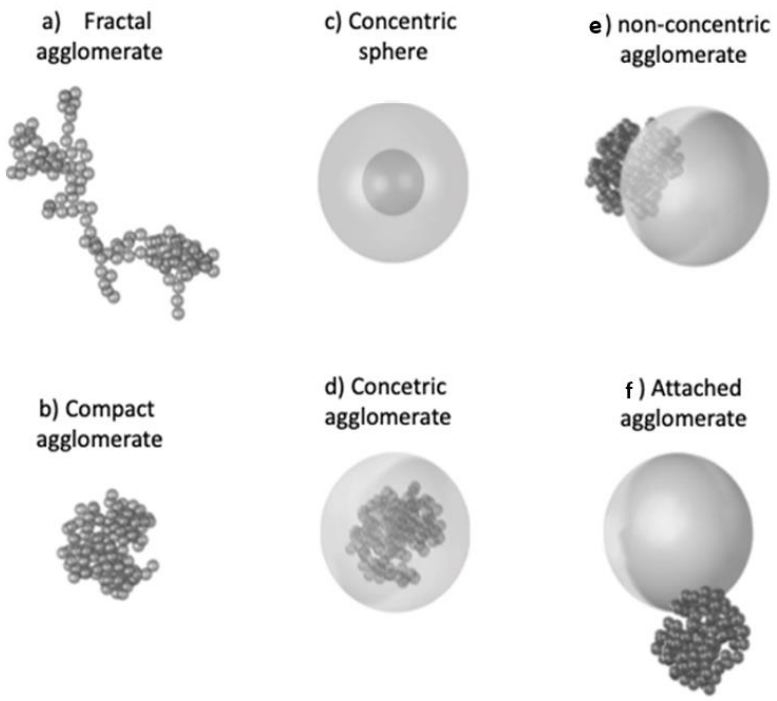

Figure 1-14: Examples of 6 morphological models of BC and BC-containing aerosols, ranging from bare BC to completely embedded BC mixtures (Liu and Mishchenko, 2018). Models a-b represent bare BC particles, c-d different concentric agglomerates, e-f non concentric agglomerates.

Morphology, size and mixing evolution can be mathematically interpreted and the resulting E_{abs} can be theoretically estimated. Mathematical

solutions depend on the assumption of morphology and relative mixing geometry between BC-core and coating material. However, there is still debate on the geometry of BC-containing particles. Considering the complexity of fractal or collapsed BC agglomerates (Figure 1-14a-b), some solutions need a geometrical simplification. Among these, Mie theory provides an analytical solution to determine optical properties for coated BC having concentric spheres core-shell morphologies as shown in Figure 1-14b (Bohren and Huffman, 1998). Alternative mixing configuration including agglomerate core embedded by a spherical coating (Figure 1-14d), non-concentric partial shells (Figure 1-14e), and BC agglomerate attached to other non-BC particles (Figure 1-14f) have also been proposed (Sedlacek et al., 2012; Adachi et al., 2010; China et al., 2013; Dahlkötter et al., 2014).

Both the morphology of the BC core and the relative position of the core within the particle were found to affect the absorption enhancement (China et al., 2013; Adachi and Buseck, 2013; Scarnato et al., 2013; Moffet et al., 2016). Jacobson (2001) estimated an E_{abs} value of 3 using an early model based on Mie theory. Bond et al. (2006) applied Mie theory with varying core/shell relationships and proposed E_{abs} values of 1.5 for fresh BC aerosols (urban already slightly coated) to aged, and 1.9 for uncoated to aged BC aerosols. Adachi et al. (2010) used the discrete dipole approximation model and found E_{abs} values up to 1.9 with increasing coating volume fraction, noting a 30% decrease for off-centre BC nuclei. He also observed a 30% decrease for fractal morphology compared to compact sphere. He et al. (2015) developed a BC aging model, showing E_{abs} values ranging from 1.02 to 3.5 based on coating morphology (embedded, partly encapsulated and partly coated) and aging stages (three steps including uncoated BC, BC coated with soluble material and with soluble material and water). Fierce et al., (2016) observed E_{abs} values between 1 and 1.5 at low relative humidity, and underlined its dependence on coating composition. Wu et al. (2018) constrained BC core morphology, indicating E_{abs} values from close to 1 for fresh BC to 3.5 for heavily coated particles. Chakrabarty and Heinson (2018) proposed a power law with exponent 1/3 for absorption enhancement with internal mixing ratio, consistent with numerical simulations (Wu et al., 2018) and previous experiments. Romshoo et al. (2022) stressed the importance of properly

include the size characterization with morphological information for obtaining more reliable results.

Laboratory experiments shown variable results. He et al. (2015) summarized previous studies and found E_{abs} values ranging from less than 1.1 to around 2. The variability depends on coating type, thickness and BC particle size. However, only a limited number of studies have quantitatively investigated E_{abs} variations alongside coating amount or particle morphology. If formation of mixed diesel soot and dry ammonium sulphate particles by coagulation has only a minor effect on the soot absorption cross-section, coating with secondary organic material amplifies the MAC up to 2.1 factor at a wavelength of 700 nm compared to externally mixed conditions. Similarly, Shiraiwa et al. (2010) coated colloidal graphite particles with volatile organic species and observed that E_{abs} values (at 532 nm wavelength) increased from 1.3 to 2 with an increase in coating volume fraction from 42% to 88%. In contrast, Qiu et al. (2012) observed a negligible lensing effect when coating 150 nm diameter soot particles, with E_{abs} values up to 1.1 for volume equivalent coating fractions from 54% to 70%. Considering the variability of BC proxies, coating materials and mixing mechanisms (condensation, coagulation, photo oxidations), experimental details play a crucial role in making meaningful and appropriate comparisons between these studies (He et al., 2015).

Field studies show variable and often contradictory results, with E_{abs} values from 1 to 3. This variability is partially due to variable methods used to derive the E_{abs} and to account for the coating thickness or the ratio between non-refractory and refractory material in the BC containing particle ($R_{coat\text{-}rBC}$) and to differences in the particle mixing state, which is uncharacterized in many studies. Studies such as that by Samset et al. (2018), highlight the importance of specifying the baseline in E_{abs} calculations, noting differences between studies using freshly emitted BC and uncoated BC as references. Some of this studies report an E_{abs} very close to unity. $E_{abs} < 1.1$ at 532 nm is observed by Cappa et al. (2012) in a coastal region in California during summertime even at significant $R_{coat\text{-}rBC}$ of 12. Healy et al. (2015) observed negligible enhancement at 781 nm in Toronto, and McMeeking et al. (2014) low enhancement up to a $R_{coat\text{-}rBC}$ of 4-5. A limited dependence of the absorption on the ratio between the non-refractory and refractory material, attributed to a non-uniform coating

distribution in the population of particles, was also observed in two different campaigns in different seasons in Fresno (summer) and Fontana (winter) (Cappa et al., 2019). On the other hand, some studies reported an increase of the absorption with the coating thickness, but with variable magnitudes between 1.4 and 3 (Lack et al., 2009; Liu et al., 2015; Peng et al., 2016; Cui et al., 2016; Ueda et al., 2016). Values around 1.5 and up to 3 were observed more recently in long datasets measured in urban environments, where the higher increase was associated to availability of organic material (Zhang et al., 2018; Yus-Díez et al., 2022). Some of the works reported here are summarized in Figure 1-15, where the high variability of these results is evident.

One of the current main issues is the discrepancy between field and laboratory modeling studies. As discussed in recent papers this is probably due to mixing state heterogeneity in the coating thickness within a population of particles (Zhai et al., 2022; Zeng et al., 2024).

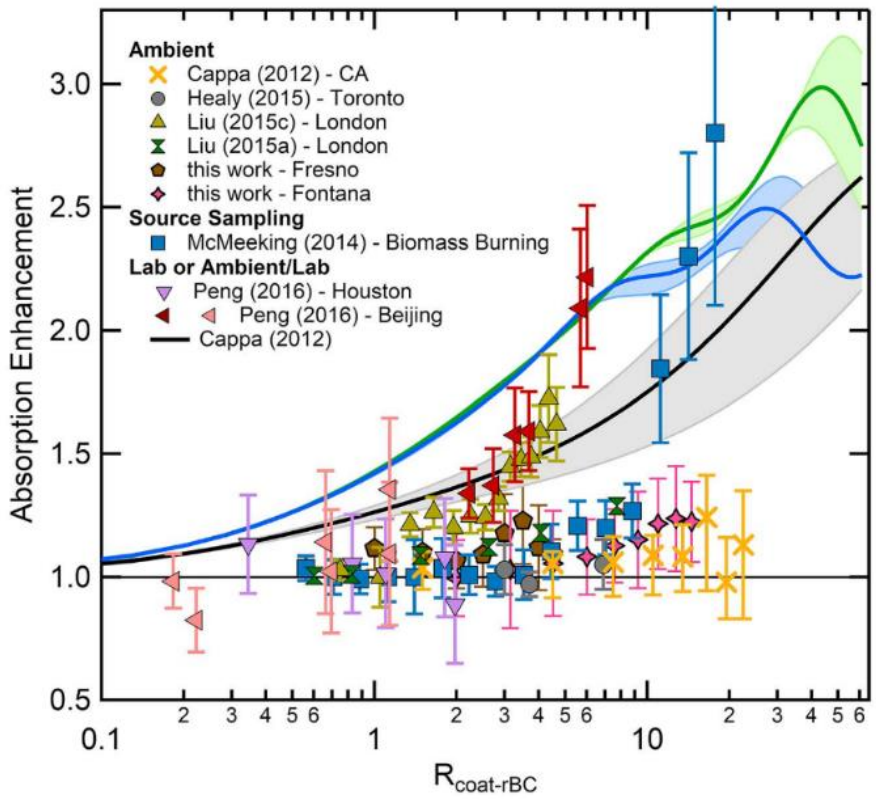

Figure 1-15: Variability of absorption enhancement measured in different ambient studies (Cappa et al., 2019).

1.2.4 BC role in the climate system

Aerosol particles are important players in the Earth's climate system, contributing primarily to a cooling effect. Among the different types of aerosols, black carbon stands out as a distinct component that exerts a warming influence. In the latest IPCC (2021) report, the estimated BC radiative forcing due to direct aerosol-radiation (RFari) was 0.14 Wm^{-2} and that due to aerosol-cloud interaction (RFaci) was -0.037 Wm^{-2}.

1.2.4.1 *BC-radiation interaction*

To assess the global mean direct radiative forcing of black carbon (DRF, measured in Wm^{-2}), it is necessary to integrate different inputs from different models (Schulz et al., 2006):

$$DRF = ER \cdot L \cdot MAC \cdot AFE \tag{1-24}$$

In this equation ER ($gm^{-2}s^{-1}$) is the global mean black carbon emission rate derived from black carbon emission inventories. Gliß et al. (2021) using an ensamble of 14 models included in the AeroCom initiative derived that the median for global annual ER is 9.7 Tg yr^{-1}, with a standard deviation of 3.8 %. L is the global mean lifetime of BC. It is mainly controlled by its removal from the atmosphere, which depends on factors such as location (altitude), season and scavenging processes, and depends on BC properties such as the size and the degree of internal mixing of BC with hygroscopic aerosol constituents. L was found to be 5.5 days on average with a standard deviation of 35%. MAC (m^2g^{-1}) is the global mean mass absorption cross-section at a given wavelength (λ). Observational constraints on MAC at different wavelengths, locations, seasons and states of black carbon atmospheric ageing can be obtained from surface measurements or laboratory experiments. The estimated values of MAC show significant variability (3.1 to 15 m^2g^{-1} at 550 nm, Gliß et al., 2021) due to the complicated properties of BC particles, such as mixing state and internal mixing degree with non-black carbon components, as better detailed in Section 1.2.3.2. Finally, AFE (Wm^{-2} $AAOD^{-1}$) is the global mean absorption forcing efficiency (forcing per aerosol absorption optical depth) determined by radiative transfer models. This factor varies between 90 and 270 Wm^{-2} per AAOD (Bond et al., 2013).

Each of these four parameters affecting the DRF introduces its own uncertainties and complexities. Equation 1-24 clearly shows how the global forcing of BC actually depends on its intrinsic properties, which might in turn varies as function of emission type and atmospheric ageing.

1.2.4.2 *BC-cloud interactions*

The contribution of black carbon (BC) to the formation of cloud and resulting cooling of the atmosphere is firstly controlled by the ability of BC to act as a cloud condensation nucleus (CCN) or ice-nucleating particle (INP).

Fresh and externally mixed BC show limited activation because intrinsic of BC insolubility (Weingartner et al., 1997; Dusek et al., 2006). Condensation of hydrophilic or water-soluble organic matter and inorganic salts on BC cores, combined with coagulation, increase the ability of BC to act as a CCN by altering its solubility (Dusek et al., 2006; Kuwata et al., 2009) and total diameter (Moteki et al., 2012; Motos et al., 2019). More controversial and debated is the ability of BC to promote the formation of ice crystals, hence to act as an (INP). Nowadays, there is generalized consensus on the inability of BC particles to trigger ice formation in mixed-phased cloud regimes (Kanji et al., 2020) and on the efficient role of BC as INP at temperatures below -38°C (Ullrich et al., 2017; Mahrt et al., 2018). Although recent studies have made improvements in assessing the role of BC as CCN and INP, variations in observational metrics and scarcity of observations lead to a lack of robustness in the results. If on one side BC can promote cloud formation, it may lead to cloud dissipation through droplet evaporation and a reduction in cloud cover due to the warming of the atmospheric cloud layer, via the semi-direct effect (Koren et al., 2004; Tosca et al., 2015). Hence, effective forcing of BC-cloud interaction is extremely variable and strongly depends on local and vertically resolved processes (Solomon et al., 2015; Ding et al., 2019; Zanatta et al., 2023).

1.2.5 Modelling improvement through better parameterisation of BC processes and properties

Estimation of the radiative forcing of BC has experienced substantial variation over the decades. In the past, this component was considered as a minority, only gaining climate relevance after the 1960s, when its presence in the Arctic was detected (Novakov et al., 2003; Sharma et al., 2004). At the same

time as a major revision of the literature on this subject was done by Bond et al. (2013), the IPCC that came out in the same years re-evaluated the impact of BC, giving it an importance second only to CO_2. In the 2013 report, the IPCC assessed its radiative forcing at 0.6 Wm^{-2}, considering only its direct impact due to aerosol-radiation interaction and neglecting that due to interaction with clouds.

However, many of the models used in deriving these estimates relied on limited and approximate parameterisation of both the processes and properties of BC. Taking the models included in the AeroCom initiative and CAMS (Copernicus Atmosphere Monitoring Service) as an example, the less up-to-date versions of these models had assumptions about the size distribution and mixing state of BC that were not always in line with observations or able to represent only a small part of the global variability. In fact, the median diameter of the number size distribution at emission assumed in these models could change from 24 to 80 nm (Mann et al., 2014, Bozzo et al., 2017), while the mixing state of newly emitted particles was assumed to be zero or not parameterised. Various subsequent studies have shown how incorrect assumptions or limited parameterisation impact the final values of the radiative forcing derived from the models (Matsui, 2016b, Matsui and Mahowald, 2017, Matsui et al. 2018). In particular, the underestimation of the coating leads to an increased estimate of BC lifetime in the atmosphere due to fewer particles being recognized as cloud condensation nuclei. Simultaneously, it results in an underestimated absorption efficiency because the potential 'lensing effect' is not fully accounted for. A change in the size distribution assumed at emission, taking the lowest and highest diameter values used in the AeroCom models, can lead to a shift of up to 0.20 Wm^{-2} in the estimate of the radiative forcing.

The last estimate derived by the IPCC in 2021 was thus very different from the previous one. The impact is now about 77% lower than estimated in 2013, and this is mainly due to the inclusion of a parameterisation for cloud interaction, the updating of emission inventories, and the updating or improvement of many parameterisations concerning BC properties and processes.

The most recent models base the input parameters on results obtained from in situ observations and are able to give a much more complex representation of the mixing state of BC, and its condensation core activation and 'lensing effect' during atmospheric ageing (Chen et al., 2023). Although models are making great efforts to improve their representations, direct observation of BC properties and processes remains crucial for improving and updating input parameters.

1.2.6 BC measuring techniques and nomenclature

This section summarize the nomenclature used to describe black carbon and the main measurement techniques from which it is derived, which are described in more detail in Sections 2.1 and 2.2. Each of these techniques quantifies BC indirectly by measuring a specific BC property; thus, the use of a specific technique generates a specific BC name. The lack of a universally accepted technique for quantifying BC in the atmosphere is one of the current limitations to a proper study of black carbon and also has created ambiguity in the scientific literature. In this work we will refer to the nomenclature detailed in Petzold et al. (2013) and described schematically in Figure 1-16.

'Soot' is a useful qualitative description when referring to carbonaceous particles that are formed as a result of incomplete combustion. 'Black carbon' (BC) is a useful qualitative description of light-absorbing carbon-containing substances in atmospheric aerosols, but the term needs to be clarified for quantitative applications. Mixed particles that contain a fraction of BC should be referred to as 'BC-containing' particles. Here the main specific nomenclature used in this work:

- Elemental carbon (EC) was used for methods that address the amount of carbon atoms present in the sample of particulate matter being analysed.
- Equivalent black carbon (eBC) was used for data derived from optical absorption methods.
- Refractory black carbon (rBC) was used for measurements derived from incandescence methods.

Elemental carbon (EC) refers to the carbonaceous fraction of particulate matter, being thermally stable in an inert atmosphere up to temperatures above 4000 K. This volatilizes only at temperatures above 340°C by oxidation. Moreover, it is also assumed to be insoluble in any solvent. The thermos-optical method is the main method used to measure particulate matter with these properties. The equivalent black carbon (eBC) is derived from the absorption coefficient by assuming a proper MAC using equation 1-13. The two main method used to quantify the absorption are: filter-based photometers and photoacoustic methods. Finally, the refractory black carbon (rBC), is again the fraction of particulate matter which is refractory and volatilizes at very high temperatures, but measured with laser induced incandescence methods.

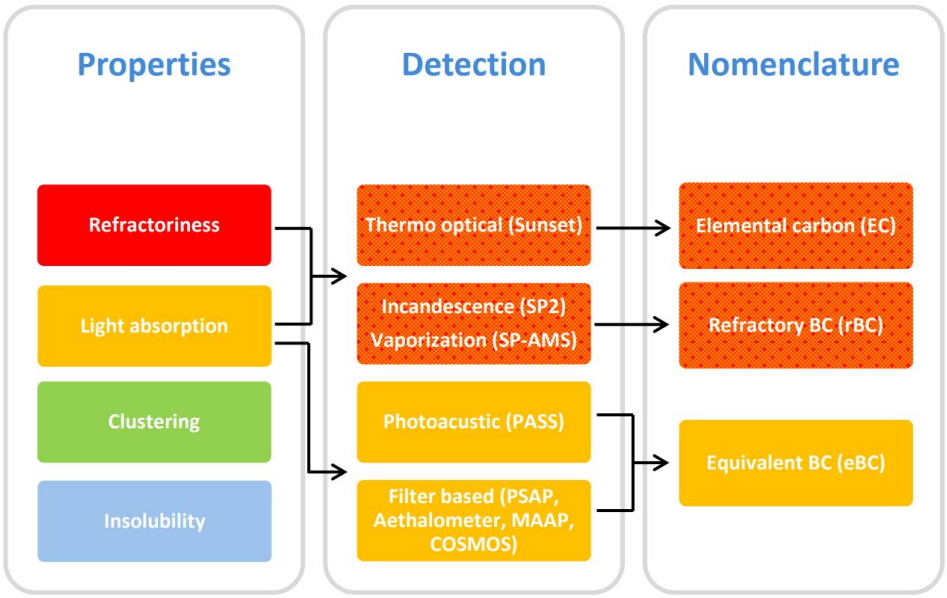

Figure 1-16: Schematic description of main properties and techniques, as well as the nomenclature used to refer to atmospheric black carbon.

1.3 OBJECTIVES OF THE PRESENT STUDY AND OVERVIEW OF THE THESIS

The introduction showed that, although black carbon is not a major component of the atmospheric aerosol, it plays an important role as a positive short-lived climate forcer. Estimates of the radiative forcing of BC still remain largely uncertain due to the numerous and complex mechanisms through which BC affects the radiation balance of our atmosphere. Indeed, BC is emitted into the atmosphere by various combustion sources partially controlling its climate-relevant properties, which undergo additional

modifications during its short life time, further affecting its climatic impacts of on a variable degree on both the temporal and spatial scale.

The overarching objective of the present work is to bring new insights in the observational aerosol community to decrease the instrumental uncertainty and deepen the understanding of the atmospheric processes in which BC is involved. This would provide also additional knowledge to reduce the uncertainty on the BC radiative forcing estimate, representing an important contribution to the modelling community.

Considering the dramatic changes that the physical, chemical and optical properties undergo after emission due to atmospheric ageing, the present study aims to answer to these main research questions:

• How can we reduce the uncertainty of the most commonly used measurement techniques for deriving the absorption coefficient and mass concentration of BC?

• Which are the BC properties and sources in the urban environment, near emissions, both in Europe and South America?

• How do the properties of black carbon change during aging and transport from large urban centres into the free troposphere?

To adequately answer these questions, the present work was organized to reach two specific objectives: 1) quantify the instrumental uncertainties affecting the quantification of absorption coefficient and BC mass concentration; 2) quantify the impact of ageing on BC climate relevant properties in urban and remote environment.

The *first objective* concerns the reduction of uncertainty in measuring BC with filter-based photometry, where BC concentration is derived from the measurement of the aerosol absorption coefficient. This technique is the most widely adopted to observe ambient variability of black carbon concentrations over monitoring infrastructures such as ACTRIS. We thus quantified the variability of the main correction factor C for the multiple scattering effect and studied its variability over time and space, and as a function of aerosol properties. Improving the accuracy of in situ measurements of the aerosol

absorption coefficient contribute to a reproducible quantification of equivalent black carbon mass concentration across the European monitoring system but also to a robust quantification of BC optical properties, namely the mass absorption cross-section. To reach this goal I compared the aethalometer measurements (the unique recommended instruments available on the actual market) with other independent measurements, by taking advantage of long-term measurements and simulation chamber experiments, both within ACTRIS RI.

The *second objective* regards the study of BC properties at the emission and after evolution with aging. Considering the short lifetime of BC, its concentration and fundamental properties can present a large variability at regional scale. To add a contribution to this topic I first studied sources of BC by applying source apportionment methods and characterized the its properties such as size and mixing state, in different urban environments in Europe, where significant reductions were experienced in the last twenty years, and South America, where BC emissions are still significant. Second, I investigated the variability of fundamental and climate relevant properties of BC as function of long-term ageing and transport mechanism in a remote location in the Andes.

The analytical and interpretative process developed/applied to answer the scientific questions and achieve the main objectives of the present work is organized in seven chapters.

CHAPTER 1 provides a general context of the aerosol science and an overview of BC characteristics in the atmosphere and climatic role at global scale

CHAPTER 2-3 describe the methodology and dataset used for answering the main research questions.

Chapter four to six describe the main results obtained.

CHAPTER 4 investigates one of the main artefacts of the aethalometer, currently the most widely used instrument for measuring the aerosol absorption coefficient, by comparing this technique with others that are considered to be independent. Here, I used two datasets from long term stations within ACTRIS observational network (Monte Cimone and ISPRA) and

simulation chamber experiments at the CESAM simulation chamber in Paris, to derive the aerosol absorption coefficient from different measuring techniques. Then, I quantified the correction factor C for the multiple scattering effect affecting aethalometer measurements and studied its variability during BC aging and as a function of certain aerosol properties.

CHAPTER 5 focuses on the study of the role and properties of BC in different urban sites. Measurements at sites in the Po Valley (Milan and Bologna), carried out as part of the RI-Urbans project, were used to assess the role of BC in pollution in this region and to study the variability of the main sources throughout the year. Additional data from short-term measurement campaigns were also used to analyse the main characteristics of BC in two different large urban areas where BC is mainly emitted from traffic sources. One in Europe in Barcelona and one in South America in the Bolivian Andes within to different cities in the same metropolitan region, La Paz and El Alto.

CHAPTER 6 investigates the transport of BC from an urban region into the free troposphere, and the variation of its properties across this transition. Here, I used data from a campaign within the SALTENA project in the Bolivian Andes, using El Alto as a representative of the urban background of a large metropolitan region and the Chacaltaya mountain site at 5200 m above the sea level as representative of the free troposphere.

CHAPTER 7 discusses the main conclusions derived from the work.

2 METHODOLOGY: INSTRUMENTS

2.1 ABSORPTION MEASUREMENT TECHNIQUES

2.1.1 Filter based photometers

Filter-based photometers widely used to measure aerosol light absorption include the Aethalometer (Hansen et al., 1984; Magee Scientific, Berkeley, CA), the multi-angle absorption photometer (MAAP; Petzold and Schönlinner, 2004; Thermo Scientific, Franklin, MA), the multi-wavelength absorption analyser (MWAA; Massabò et al., 2013) the particle soot absorption photometer (PSAP; Bond et al., 1999; Radiance Research, Seattle, WA) and the continuous soot monitoring system (COSMOS; Miyazaki et al., 2008; Kanomax, Osaka, Japan).

In these techniques, aerosol particles are collected on-line on a filter matrix and the transmitted or transmitted and scattered light are detected simultaneously. The amount of aerosol deposited on the filter should be inversely proportional to the transmittance. However, the use of a filter introduces biases in the quantification of the absorption coefficient due to the interaction of the sampled particles with the filter matrix and with other particles. Major effects on a filter matrix include multiple scattering effects caused by filter fibres and aerosol particles (Liousse et al., 1993; Petzold et al., 1997) and the filter loading effect related to the shadowing of deposited aerosol particles (Bond et al., 1999; Weingartner et al., 2003). The MAAP, measuring also the scattered light at different wavelengths, and using a radiative transfer model to derive the absorption is less affected by these biases. The same is done but off-line by the MWAA. Various correction procedures have been developed for aethalometer, PSAP and COSMOS photometers to account for these optical effects.

2.1.1.1 *Aethalometer*

The aethalometer relies on the measurement of attenuation to assess the absorption coefficient of aerosols at different wavelengths (370, 470, 520, 590, 660, 880, 950 nm). Attenuation (ATN) is mathematically defined as the natural logarithm of the ratio of the intensity of light passing through a loaded

filter (I) to the intensity of light passing through an unloaded portion of the filter (I_0), as expressed by the equation:

$$ATN(\lambda) = ln\left(\frac{I}{I_0}\right) \tag{2-1}$$

Consequently, the absorption coefficient or an approximation of it named the attenuation coefficient (b_{atn}), at a given wavelength (λ) is proportional to the change in attenuation over time:

$$b_{atn} \propto \frac{ATN(\lambda, t + \Delta t) - ATN(\lambda, t)}{\Delta t} \tag{2-2}$$

Although this approach is commonly used, and the aethalometer is currently the most widely used instrument in the world for measuring the absorption coefficient, the use of a filter introduces inherent biases in the quantification of the absorption coefficient. Theoretically, a positive change in attenuation (ATN) should be directly proportional to the amount of absorbing material embedded in the filter (Figure 2-1a). However, in practice, the optical properties of the filter matrix, the presence of non-absorbing particles and the loading of absorbing particles introduce complexities that affect ATN measurements. The filter matrix has its own characteristic optical depth, and multiple scattering occurs within the filter fibres, consistently attenuating light passing through the pristine filter layer (Figure 2-1b). The light intensity used as a reference is not the source intensity, but the signal already attenuated by the presence of the filter. In addition, the loading of non-absorbing material will increase the amount of backscattered light, resulting in an apparent increase in the reflectance of the filter (Figure 2-1c). Although the percentage of scattering interpreted as absorption is typically negligible (less than 5%), it depends on the asymmetry parameter of the deposited particles, which is a function of particle diameter and incident light wavelength.

The presence of non-absorbing particles becomes significant when absorbing material is loaded on the filter and is parameterised in terms of the single scattering albedo. Scattering by particles increases the optical path of the light, thereby increasing the probability of encountering embedded absorbing particles (Figure 2-1d). Multiple scattering from the filter matrix has a similar effect.

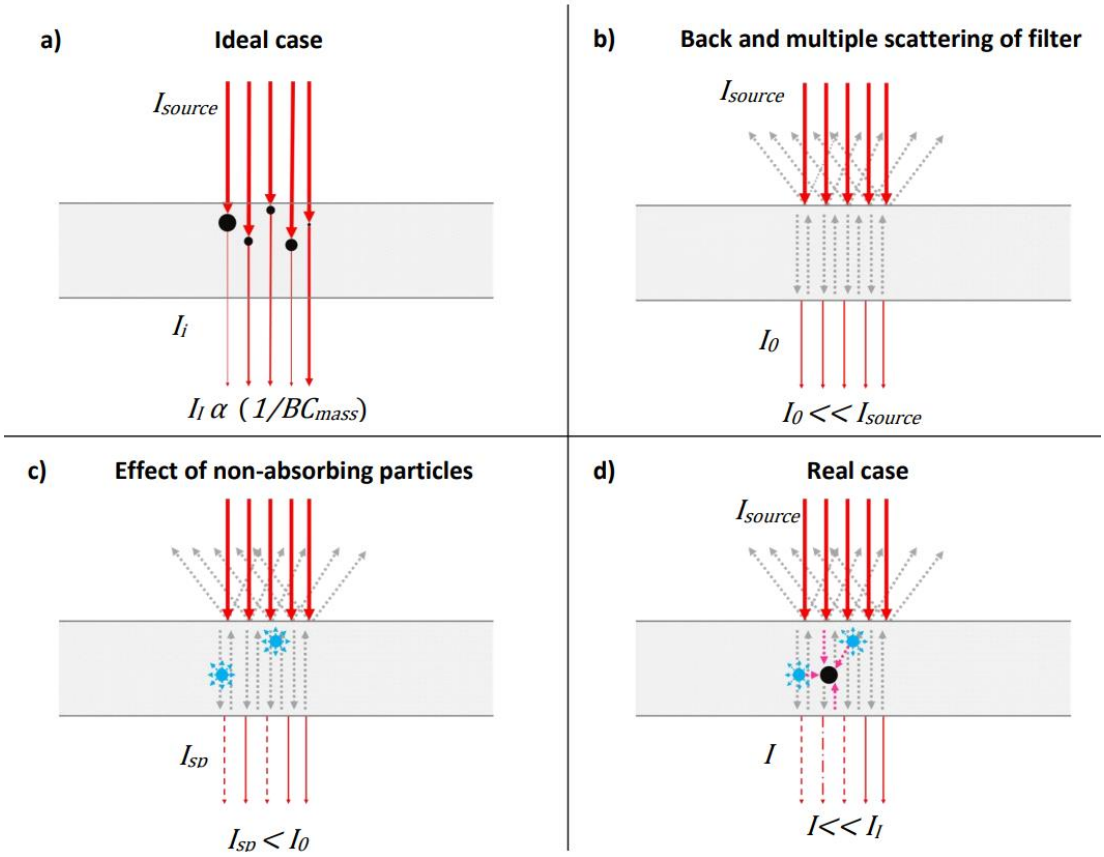

Figure 2-1: Schematic description of the optical processes occurring in a filter matrix. a) Ideal case: the variation of ATN is proportional only to the amount of absorbing material loaded on the filter. b) Effective backscattering and multiple scattering (grey dotted lines) of the filter matrix, no aerosol collected. c) Presence of non-absorbing particles (blue spheres) induces additional scattering (blue dotted lines). d) Filter loaded with absorbing and scattering aerosol. Multiple scattering induced by the filter matrix and non-absorbing particles increases the optical path of light, increasing the probability of light absorption (pink dotted line) by absorbing particles (black spheres).

This increase in optical path leads to an overestimation of absorption, which can be partially compensated by the 'shadowing' effect induced by the loading of absorbing aerosol on the filter. The last loaded particles absorb light, reducing the optical path for a loaded filter and decreasing the probability of absorption by previously loaded particles. The vertical distribution of particles within the filter, determined by particle size, plays a critical role in this process. Larger particles with lower mobility are more likely to be embedded in the surface layer of the filter, where backscattering and absorption are dominated by surface non-absorbing and absorbing particles. These optical effects introduce non-linearity into the attenuation-concentration relationship of the BC in the filter, making the attenuation coefficient an approximation of the true

absorption. To correct for these artefacts and improve the reliability of the results, correction algorithms must be introduced to compensate for them.

Concerning the loading effect, there are numerous algorithms that can be applied after the measurement, which may or may not depend on the properties of the sampled aerosol, such as the single scattering albedo (Weingartner et al., 2003; Schmid et al., 2006; Collaud Coen et al., 2010; Virkkula et al., 2015). These algorithms are typically applied to older aethalometer models such as the AE31. The more recent AE33 model, however, has a more complex internal algorithm and measurement approach known as the DualSpot™ method that provides real-time correction for this artefact. This method involves making two simultaneous measurements of b_{atn}, derived at two different spots with different levels of loading, designated ATN1 and ATN2:

$$\begin{cases} b_{atn,1} = b_{atn}^{LC} \cdot (1 - k \cdot ATN1) \\ b_{atn,2} = b_{atn}^{LC} \cdot (1 - k \cdot ATN2) \end{cases} \quad (2\text{-}3)$$

These equations, derived from an empirical relation describing ATN relation with the surface loading of BC by Gundel et al. (1984) and further developed by Drinovec et al. (2015), allow the determination of a parameter called 'loading compensation' (k) and the loading corrected attenuation coefficient (b_{atn}^{LC}).

For multiple scattering effects, on the other hand, it is necessary to use a correction parameter, typically referred to as 'C' in the literature. This parameter relates the absorption coefficient to the attenuation coefficient, as shown by this simple relationship:

$$b_{abs} = \frac{b_{atn}^{LC}}{C} \quad (2\text{-}4)$$

To date, estimates of C have been made for both the AE31 and the AE33 models from a variety of field and laboratory studies. Aerosols of different types and properties, and under different ambient conditions, have been studied. (Weingartner et al., 2003; Arnott et al., 2006; Bond and Bergstrom, 2006; Collaud Coen et al., 2010; Segura et al., 2014; Backman et al., 2017; Di Biagio et al., 2017; Saturno et al., 2017; Corbin et al., 2018; Kim et al., 2019; Laing et al., 2020; Valentini et al., 2020; Moschos et al., 2021; Yus-Díez et al.,

2021; Bernardoni et al., 2021; Kalbermatter et al., 2022). However, consensus is still missing on the absolute value of C, its dependence on the filter material used in the aethalometer to deposit aerosols, and its possible changes with varying aerosol properties, such as its absorption represented by the SSA or its chemical composition and on the wavelength of the incident light. The evaluation of the impact of this artefact on the absorption coefficient estimate is the main objective of Chapter 4.

2.1.1.2 *Multi-angle absorption photometer*

The multi-angle absorption photometer (MAAP), as described by Petzold and Schönlinner (2004), is used to measure the absorption coefficient at 637 nm. This instrument employs a glass-fibre filter to collect particles and, during the loading process, simultaneously detects the orthogonally transmitted light and the backscattered light at two different angles. Firmware based on a two-stream radiative transfer model is then applied to derive the absorption coefficient (b_{abs}). The firmware treats the particle-loaded filter as a two-layer system (see Figure 2-2), consisting of an aerosol-loaded layer and a particle-free filter matrix. Radiative processes within the deposited aerosol layer and interactions between this layer and the particle-free filter matrix are treated independently. This modelling approach, originally formulated by Hänel (1987) and adapted by Petzold and Schönlinner (2004) for this specific purpose, deals with multiple reflections between the aerosol-loaded filter layer and the particle-free filter matrix using the adding method (Van de Hulst, 1980).

The radiation that has passed through the filter is completely diffuse and can be described by a cosine law:

$$S(\theta) \propto cos(\theta) \tag{2-5}$$

where θ is the angle of the scattered light with respect to the incident radiation. On the other hand, the light scattered back from the filter is better described by combining a function proportional to cos(θ-π) with a Gaussian law:

$$S(\theta) \propto acos(\theta - \pi) + (1 - \alpha)e^{\left[-\frac{\frac{1}{2}(\theta-\pi)^2}{\rho^2}\right]} \tag{2-6}$$

where ρ is a measure of the surface roughness of the aerosol layer collected on the filter and α the fraction of diffusely scattered radiation. The Gaussian part of the law represent the radiation reflected from a rough surface. The way the backscattered radiation is divided in these two components depends on the properties of the sampled aerosol. Measuring the radiation passing through the filter at the scattering angle θ = 0° and simultaneously measuring the radiation scattered back from the filter at two angles θ = 130° and 165°, allows the complete determination of the irradiance in the front and back hemispheres relative to the incident light beam. The exact position of the detection angles has been chosen so that the separation between diffuse and Gaussian types can be determined with the highest resolution.

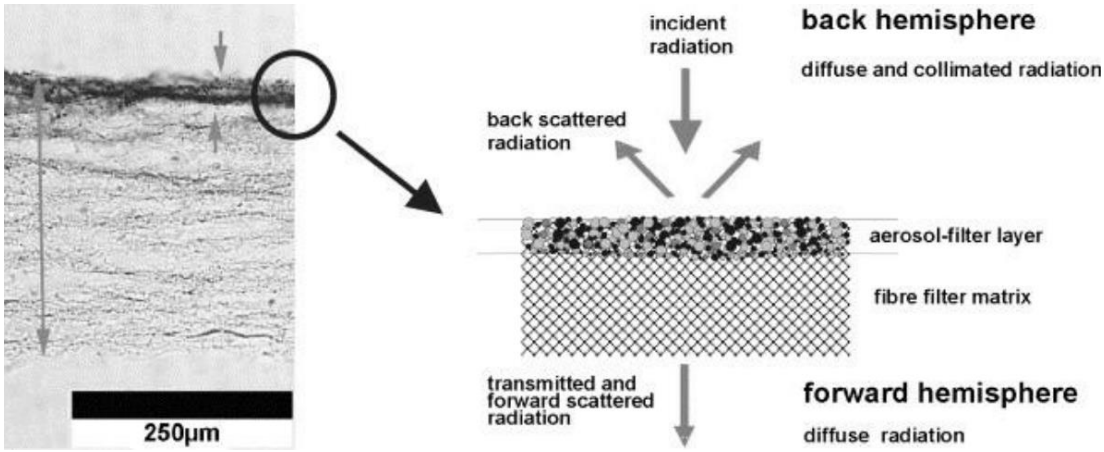

Figure 2-2: Schematic description of a particle loaded filter modelled as a two-layer system (Petzold and Schönlinner, 2004), composed by the filter matrix, and the filter matrix with collected particles.

On the basis of directly measurable quantities, the resolution of the model gives the two parameters necessary for the calculation of the absorbance ABS (fraction of light absorbed in a filter sample):

$$ABS(\lambda) = (1 - SSA)\tau(\lambda) \tag{2-7}$$

τ(λ) is the optical depth of the particle loaded filter and SSA the single scattering albedo defined in equation 1-18. From this the absorption coefficient is calculated as:

$$b_{abs} = ABS(\lambda) \cdot \frac{A}{V} \tag{2-8}$$

where A is the area of the filter spot with the sample collected, and V the volume of the air sampled.

It is important to highlight a historical discrepancy in the operating wavelength of the MAAP. Originally thought to operate at 670 nm as stated by Petzold et al. (2005), subsequent investigations have shown that the correct wavelength is 637 ± 1 nm. Consequently, to derive the correct aerosol absorption coefficient at 637 nm using the MAAP firmware, an adjustment of 5% is required, assuming an absorption Ångström exponent of 1. This correction is made in accordance with the findings of Müller et al. (2011).

2.1.1.3 *Multi-Wavelength Absorption Analyser*

The Multi-Wavelength Absorption Analyser (MWAA) is an off-line absorption photometer that measures aerosol absorption coefficients ($b_{abs}(\lambda)$) over a range of wavelengths (375, 407, 532, 635 and 850 nm). MWAA works by assessing both total light transmission and diffusion through filters, with data collected in both the anterior and posterior hemispheres. The methodology uses the same radiative transfer model developed by Hänel (1987) and adapted for fibre filters by Petzold and Schönlinner (2004) described for the MAAP.

In the MWAA approach, the aerosol-loaded filter is conceptualised as a two-layer system, consisting of an aerosol-loaded layer and a particle-free filter matrix. The outputs of this model include the single scattering albedo and the optical depth (τ) of the aerosol-laden layer, which are crucial for determining the absorbance (ABS) of the deposited aerosol. As in MAAP, the aerosol absorption coefficient is then derived from equation 2.8. As in MAAP, the scattered and transmitted radiation is measured at fixed angles (0°, 125°, 165°). The model then relies on an analytical function to provide the total scattered light. Unlike instruments based solely on transmitted light, MWAA's simultaneous measurement of transmitted and scattered light eliminates the need for complex correction algorithms to account for aerosol scattering properties. Differently from the MAAP it provides the b_{abs} at different wavelengths but measuring collected filters off-line.

2.1.2 Extinction minus scattering

The absorption coefficient can be also derived from the so called extinction minus scattering technique (EMS). We know from the theory described in Section 1.1.4.1 that:

$$b_{abs} = b_{ext} - b_{sca} \tag{2-1}$$

so the absorption coefficient can easily be calculated if scattering and extinction coefficients are measured simultaneously. Since the absorption coefficient is generally much smaller than the scattering coefficient, this calculation is subject to very high uncertainties, when applied in the field to predominantly scattering samples (Modini et al., 2021). However, it can be used successfully in laboratory studies with highly absorbing aerosols. High values of the absorption coefficient reduce the uncertainty resulting from the subtraction of the two contributions.

Various techniques can be used to measure the scattering and extinction coefficients. In the next section, we will briefly describe only the two used in this work. Namely, a CAPS PMex instrument (Aerodyne, Massoli et al., 2010) to measure the extinction coefficient and the integrating nephelometer (TSI Inc., model 3563, Anderson et al., 1996; Massoli et al., 2009) to measure the multispectral scattering coefficient.

2.1.2.1 *Cavity Attenuated Phase Shift monitor*

The Cavity Attenuated Phase Shift monitor CAPS PM_{ex} is one of the main instrument used in aerosol science to measure the extinction coefficient b_{ext}. It consists of a near-confocal optical cavity with highly reflective mirrors (high reflectivity (R>99.98%)) at each end. These mirrors, maintained under a constant flow of particle-free air, create an effective optical path of approximately 2 km. The aerosol sample flows through the cavity at a controlled rate of 0.85 liters per minutes. Square-wave modulated light from a broadband LED enters the optical domain and encounters a phase shift of 35°-40° as it exits the cavity. The light is detected by a photodiode detector with a 10 nm band-pass filter. Regular switching between aerosol and particle-free air ensures stable performance. The relationship between the measured phase shift and the light extinction is:

$$cot(\theta) = cot(\theta_0) + \left(\frac{c}{2\pi \cdot f}\right) \cdot b_{ext} \quad (2\text{-}2)$$

where θ is the phase shift measured, θ_0 is the phase shift under particle-free air conditions, c is the speed of light, and f is the modulation frequency.

Baseline drift and the contribution of gas phase absorption to the total extinction can cause variations in instrument response (i.e. $cot(\theta_0)$). Typically, baseline drift is minimal and related to changes in the temperature of the sampling cell. However, gas-phase absorption, mainly due to NO_2 in the visible, can be significant in polluted environments (Baynard et al., 2007). The instrument operates at ambient pressure and monitors pressure and temperature for accuracy. In this study, a single cavity CAPS instrument was used at 630 nm.

2.1.2.2 *Integrating nephelometer*

The integrating nephelometer (TSI Inc., model 3563, Anderson et al., 1996; Massoli et al., 2009), measures the amount of light scattered by an air sample collected in a measuring chamber, at three different wavelengths (450, 550, 700 nm). The integral structure consists of a dark aluminium tube with aperture plates along its axis. Illumination is provided by a quartz halogen lamp emitting a near Lambertian intensity profile in the visible spectrum. Aperture plates restrict light integration between 7° and 170°, and a backscatter shutter selectively captures light between 7° and 90° for exclusive backscatter measurements. Receiving optics are positioned at one end of the tube, containing three photomultipliers - one for each measured wavelength - while the opposite end houses a light trap for a dark reference against which the scattered light is evaluated. The light from the tube passes through a chopper, allowing separate measurements of the photomultiplier background noise, lamp stability and the effective signal from the measurement volume. After interacting with particles and gases, the light passes through lenses and filters that split it into three wavelengths before reaching the photomultiplier tubes. The signal is then converted to the scattering coefficient value using a model based on Mie theory.

Calibration procedures involve the introduction of filtered air to establish an aerosol zero reference and a gas with a known scattering coefficient,

typically CO_2, to establish the span. The instrument effectively separates the fraction of scattering due to particles from that due to air. During instrument zeroing in particle-free air, where only Rayleigh scattering is dominant, the scattering coefficient component due to gases is accurately measured and subtracted to derive the b_{sca} parameter only due to particles.

The derivation makes several assumptions about the functionality of the nephelometer. It is assumed that the nephelometer is sensitive to radiation scattered in the range 0° to 180°. The model assumes that each volume of air behaves as a point source of scatter and that the lamp acts as an isotropic light source. It also assumes that the scattering response at each wavelength (λ) represents the interaction of the aerosol with a monochromatic light source at that specific wavelength. However, the values of b_{sca} measured by the nephelometer are not free from uncertainties arising from calibration procedures and systematic errors inherent in its operation. Anderson et al., (1996) discuss and estimate in detail the uncertainties associated with the non-idealities of the instrument, mainly related to wavelength and angular sensitivity. The wavelength non-ideality is due to the fact that the scattering coefficient is measured against a narrow but finite range of wavelengths that are not perfectly centred on the nominal wavelength. The angular non-ideality is attributed to two main factors: the light intensity from the source should ideally be isotropic, which may not be the case, and the integration angles are between 7° and 170° instead of the ideal range of 0° to 180° (truncation error). Errors in the nephelometer b_{sca} due to truncation and wavelength non-idealities are reported to range from a few to 10% for submicron particles, signal levels above 10 Mm^{-1} and averaging intervals of 60 seconds or more, as reported by Anderson et al., (1996). However, these errors may be more pronounced for coarser particles and for particles for which the spherical shape assumption made by the Mie theory is not valid. In these work the Anderson and Ogren, (1998) corrections were applied for field measurements and the Massoli et al., (2009) correction was applied in laboratory studies.

2.2 MASS CONCENTRATION MEASUREMENTS

2.2.1 Absorption based

The absorption coefficient, measured with absorption photometers including the required corrections, can be converted to an equivalent black carbon mass concentration (m_{eBC}) using an appropriate mass absorption cross-section, MAC_{eBC}:

$$m_{eBC} = MAC_{eBC} \cdot b_{abs}(\lambda). \quad (2\text{-}9)$$

It is important to note that absorption is not a direct proxy for black carbon mass concentration, and the assumption of a constant relationship between absorption and BC concentration is only valid if there is no interference from light-absorbing materials other than BC (Bond and Bergstrom, 2006).

Both the MAAP and the two model of aethalometer presented (AE31 and AE33), provide as output the eBC mass concentration calculated from the absorption or attenuation coefficients with specific assumed MAC_{eBC} values. In the MAAP this value is set to 6.6 m^2g^{-1}, derived by the manufacturer, optimized towards fresh BC particles measured in urban areas for comparison with EC values (Petzold and Schönlinner, 2004).

In the aethalometer AE31 the eBC mass concentration is derived from the attenuation coefficient at all the seven wavelengths using these MAC(λ) values: 39.5, 31.1, 28.1, 24.8, 22.2, 16.6, 15.4 m^2g^{-1} at 370, 470, 520, 590, 660, 880, 950 nm, respectively.

In the aethalometer AE33 the eBC mass concentration corrected is the main output of the instrument, calculated using the following relation:

$$m_{eBC}(\lambda) = \frac{S \cdot \Delta ATN1(\lambda)}{F1 \cdot (1-\zeta) \cdot MAC_{eBC}(\lambda) \cdot C_{inst} \cdot \left(1 - k(\lambda) \cdot \Delta ATN1(\lambda)\right) \cdot \Delta t}, \quad (2\text{-}10)$$

where S is the filter spot area, F1 is the flow rate in one of the two filter spot, ζ accounts for flow leaks, C_{inst} is the corrective parameter for scattering artefacts deriving from the filter, k is the corrective parameter for the loading effect, described in Section 2.1.1.1, ATN1 is the attenuation in the first filter spot and Δt the time interval considered (1min). MAC_{eBC} are the wavelength dependent

mass absorption cross-section assumed in the instrument: 18.47, 14.54, 13.14, 11.58, 10.35, 7.77, 7.19 m^2g^{-1} at 370, 470, 520, 590, 660, 880, 950 nm, respectively.

2.2.1.1 *Source apportionment based on the aethalometer model*

As described in Section 1.1.4.1, the spectral dependence of the absorption coefficient (represented by the AAE), is related to the aerosol composition. The contribution of the different aerosol components responsible for absorption can thus be separated using this dependence. The main absorbing aerosols are BC, BrC (brown carbon, consisting of organic material) and dust. Outside of specific transport times and proximity to specific sources, dust has a minor contribution in urban environments and the first two will dominate. We know that BC absorbs effectively at all wavelengths in the visible with only a weak wavelength dependence (AAE ~ 1), whereas the organic component absorbs much more effectively in the UV than in the IR with AAE > 1. These two components are mainly associated with emissions from liquid fuels (related to traffic emissions) for BC, and from solid fuels (related to biomass burning such as forest fires, wood-fired heating systems, waste incineration) for BrC. The aethalometer based source apportionment model therefore allows to distinguish two components: absorption from liquid fuel sources ($b_{abs,lf}$) and absorption from solid fuel sources ($b_{abs,sf}$), as expressed by the following equation:

$$b_{abs}(\lambda) = b_{abs,lf}(\lambda) + b_{abs,sf}(\lambda). \tag{2-11}$$

The most widely used model for this derivation is the one developed by Sandradewi et al., (2008). Below are the relationships that allow the derivation of the two contributions.

$$\begin{cases} \dfrac{b_{abs,lf}(\lambda_1)}{b_{abs,lf}(\lambda_2)} = \left(\dfrac{\lambda_1}{\lambda_2}\right)^{-AAE_{lf}} \\ \dfrac{b_{abs,sf}(\lambda_1)}{b_{abs,sf}(\lambda_2)} = \left(\dfrac{\lambda_1}{\lambda_2}\right)^{-AAE_{sf}} \end{cases} \tag{2-12}$$

$$\begin{cases} b_{abs,lf}(\lambda_2) = \dfrac{b_{abs}(\lambda_1) - b_{abs}(\lambda_2) \cdot \left(\frac{\lambda_1}{\lambda_2}\right)^{-AAE_{sf}}}{\left(\frac{\lambda_1}{\lambda_2}\right)^{-AAE_{lf}} \cdot \left(\frac{\lambda_1}{\lambda_2}\right)^{-AAE_{sf}}} \\ b_{abs,sf}(\lambda_2) = \dfrac{b_{abs}(\lambda_1) - b_{abs}(\lambda_2) \cdot \left(\frac{\lambda_1}{\lambda_2}\right)^{-AAE_{lf}}}{\left(\frac{\lambda_1}{\lambda_2}\right)^{-AAE_{sf}} \cdot \left(\frac{\lambda_1}{\lambda_2}\right)^{-AAE_{lf}}} \end{cases} \quad (2\text{-}13)$$

This model allows the calculation of the contributions in terms of b_{abs}, and from these, using a proper $MAC_{eBC}(\lambda)$ it is possible to derive the contributions in terms of BC: BClf and BCsf. These equations are based on a good choice of the two parameter AAE_{lf} and AAE_{sf}, representing the absorption dependence for liquid fuel and solid fuel aerosols. This choice is not trivial and should at best be made with the help of other independent measurements of traffic tracers or biomass burning (e.g. NOx, Levoglucosan, C^{14}). In the absence of these, Zotter et al., (2017) through a sensitivity study done analysing data from different field campaigns across Switzerland found the best combination of values to be used (AAE_{lf} = 0.9 and AAE_{sf} = 1.68). However, the use of fixed values is problematic. From previous studies we can see a significant spatial heterogeneity in the optimal combination. For example, values of 0.9 and 1.82 were reported for Milan (Mousavi et al., 2019), and values in the ranges AAE_{lf} = 0.97-1.12 and AAE_{sf} = 1.63-1.74, were found in urban and rural areas of Spain (Becerril-Valle et al., 2017).

2.2.2 The thermal-optical technique

The thermal-optical technique is a fundamental method for the quantification of total carbon (TC) mass concentration in atmospheric aerosols, separating the organic carbon component (OC) from the elemental carbon component (EC) by relying on their distinct thermal behavior. This employs an OC/EC analyzer and specific thermal protocols. This paragraph explains the underlying principles of the OC/EC analyzer and looks at the specificities of the thermal protocols available.

2.2.2.1 *Measuring principle and biases*

As described in detail by Chow et al. (1993), the preeminent instrument for thermo-optical analysis of the carbonaceous fraction of particulate matter (PM) samples is the Sunset EC/OC analyzer, manufactured by Sunset Laboratory Inc. of Tigard, OR.

This instrument is the most widely used in the scientific community for measuring the carbonaceous fraction of aerosols. The analytical principle is based on the different response of elemental carbon (EC) and organic carbon (OC) to variations in temperature and atmospheric conditions. Figure 2-3 shows a schematic diagram of the Sunset Laboratory OC/EC analyzer, including a front furnace, a manganese oxide oxidation furnace, a methanator and a flame ionization detector (FID).

The process for the quantification of carbonaceous aerosol is based on the thermal desorption of carbonaceous from a quartz filter in a first hoven, where a red light diode laser and a thermocouple monitor, respectively, the filter transmittance and temperature throughout the analysis. Second, carbon species released during the heating enter the oxidizer to form carbon dioxide. Finally, the carbon dioxide is then reduced to methane before entering a flame ionization detector (FID). The concentration of methane (CH_4) is proportional to the carbonaceous mass deposited on the sample filter. A widely used technique for the thermal quantification of OC and EC is the thermal-optical transmittance (TOT) method, described by Birch and Cary (1996). This method involves two thermal cycles. First, carbonaceous particles undergo thermal desorption in a pure helium atmosphere (inert atmosphere), and the measured components in this cycle are designated as organic carbon. After the first heating phase, the furnace cools down and the carrier gas changes to a mixture of helium and oxygen (2% oxygen/helium mixture: oxidizing atmosphere). As the temperature rises again, the refractory components oxidase and volatilize in the second cycle.

This technique is, however, not free from bias. In the helium atmosphere, some of the OC undergoes pyrolysis, producing thermally stable and light-absorbing pyrolytic carbon. Hence, not all of the OC is desorbed in the first heating cycle. In the second cycle pyrolytic carbon is oxidized and miss-quantified as EC. To correct for the underestimation of OC and

overestimation of OC, the transmission signal is continuously monitored in the sample hoven. As the transmission decreases in the helium cycle and increases in the oxygen cycle, the "split point" in the second cycle where the optical signal returns to its initial value is pinpointed.

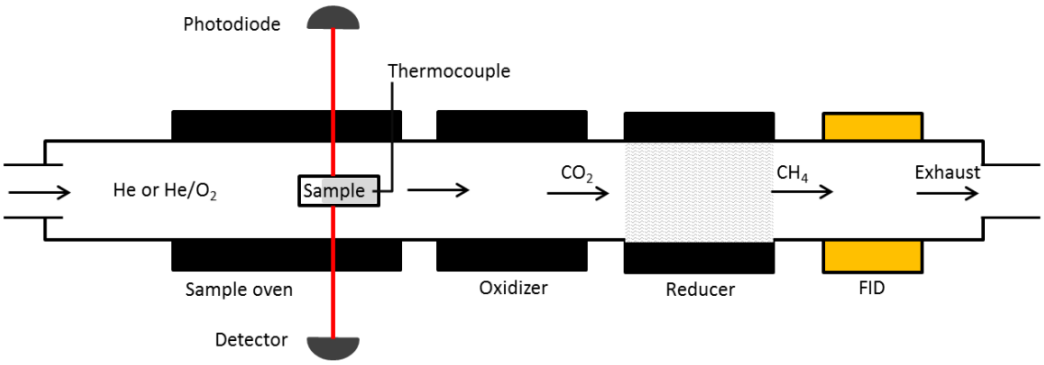

Figure 2-3: Schematic representation of the Sunset Laboratory OC/EC analyzer, and of the main processes required for carbonaceous aerosol measurement.

This defines the pyrolytic carbon component measured before the split point in the oxygen phase and attributes it to the organic carbon phase. This correction, known as the "charring correction", can be made by using the thermo-optical reflectance method (TOR) instead of the transmittance. However, it's important to note that the assumptions described above for optical charring correction are only partially fulfilled, so that charring artefacts often remain a dominant source of bias even for optically corrected EC mass data.

2.2.2.2 ***Existing thermal protocols***

To date, the thermal-optical protocols used in atmospheric science have predominantly centered on the IMPROVE (Interagency Monitoring of PROtected Visual Environments; Chow et al., 1993), NIOSH (National Institute for Occupational Safety and Health; Birch and Cary, 1996), and EUSAAR-2 (European Supersites for Atmospheric Aerosol Research; Cavalli et al., 2010) standards.

Table 2-1: Existing thermal protocols for deriving EC and OC concentrations using the Sunset technique: temperature set points and temperatures listed.

	NIOSH	**NIOSH 5040**	**IMPROVE**	**IMPROVE-A**	**EUSAAR-2**
Step	T, duration [°C, s]	T, duration [°C, s]	T, duration [°C, s]	T, duration [°C, s]	T, duration [°C, s]
He1	310, 60	250, 60	120, 150-580	140, 150-580	200, 120
He2	475, 60	500, 60	250, 150-580	280, 150-580	300, 150
He3	615, 60	650, 60	450, 150-580	480, 150-580	450, 180
He4	900, 90	850, 90	550, 150-580	580, 150-580	650, 180
He/$O_2$1	600, 45	650, 30	550, 150-580	580, 150-580	500, 120
He/$O_2$2	675, 45	750, 30	700, 150-580	740, 150-580	550, 120
He/$O_2$3	750, 45	850, 30	800, 150-580	840, 150-580	700, 70
He/$O_2$4	825, 45	940, 120			850, 80
He/$O_2$5	920, 120				

Historically, the IMPROVE protocol has been the first choice for samples taken at non-urban background sites within the U.S. IMPROVE network. In particular, in 2005, the IMPROVE network transitioned to the use of the IMPROVE-A protocol, which is a slightly modified iteration of the IMPROVE protocol that incorporates refined temperature measurements for improved accuracy (Chow et al., 2007). On the other hand, the NIOSH protocol was applied to samples collected from urban sites as part of the USA-EPA Speciation Trends Network. The subsequent introduction of the NIOSH-5040 protocol addressed the specific determination of elemental carbon (EC) in diesel exhaust. These protocols differ in terms of temperature set points, with NIOSH having higher temperatures, up to 900°C in helium, compared to IMPROVE, which peaks at 550/580°C in helium. In addition, there are variations in dwell times at each temperature step, generally favoring longer dwell times for IMPROVE over NIOSH, as shown in Table 2-1. Furthermore, the reflective method is the cornerstone of the charring correction in the IMPROVE protocol,

whereas the NIOSH protocol has opted for the transmittance method. Throughout Europe, the EUSAAR-2 protocol has emerged as the designated standard for thermal methods in air quality networks. This protocol, which conforms to the European Committee for Standardization Ambient air (2017; EN16909:2017), is tailored for the measurement of total carbon (TC), organic carbon (OC) and elemental carbon (EC) in samples of particulate matter in the size range below 2.5 µm (PM2.5).

2.2.3 Single particle soot photometer

Description of LII

As described in details by Michelsen et al. (2015), incandescence is a form of thermal radiation, which is emitted when a body reaches its sublimation point (Figure 2-4). The so called laser-induced incandescence (LII) is obtained when a laser beam is used to heat a material enough to produce an incandescence emission. Thanks to the refractory nature (vaporization temperature above 4000 K) and strong absorption of light in the visible spectrum of BC particles, LII is an effective technique to detect BC aerosol particles (Stephens et al., 2003). In fact, when heated by a laser beam, BC emits an incandescence signal, proportional to its mass.

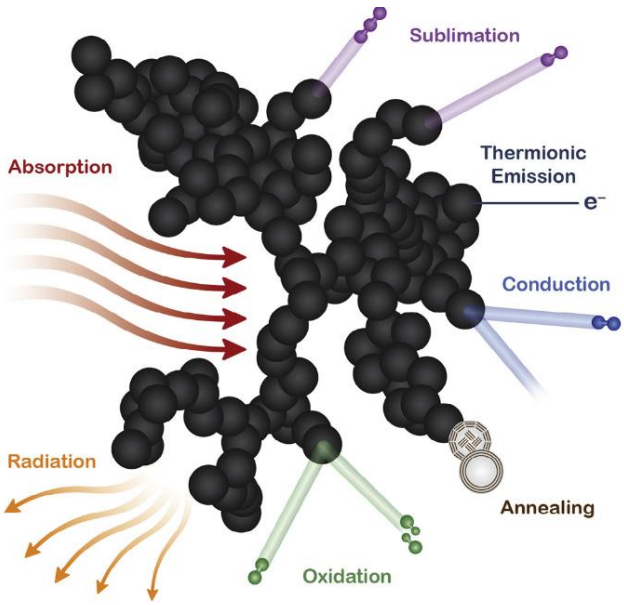

Figure 2-4: Illustration of processes involved in particle interaction with laser beam radiation during LII-signal collection (Michelsen et al., 2015).

Hence, LII has been exploited to derive the mass of BC particles in the atmosphere in the last two decades with the development of the single particle soot photometer (e.g. Stephens et al., 2003; Schwarz et al., 2006, 2010; Moteki and Kondo, 2007). As described in Section 1.2.4, we refer to the particles measured with this technique as rBC particles.

Description of the SP2 system

The single particle soot photometer (SP2, Droplet Measurement Technologies, CO, USA) is a commercial instrument based on laser-induced incandescence, which allows measuring the mass (m_{rBC}) and number concentration of rBC particles, the mass equivalent diameter (D_{rBC}) of rBC cores, and the coating thickness of non-refractory and non-absorbing material (CT_{rBC}). The design of the SP2 allows the continuous sampling of single aerosol particles, which are exposed to a high-intensity continuous intra-cavity laser beam (Figure 2-5).

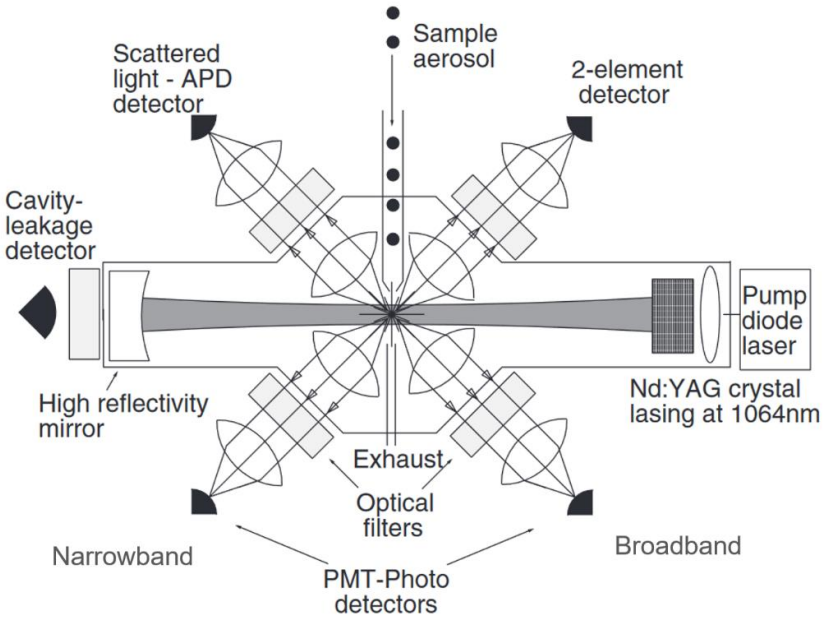

Figure 2-5: Schematic description of the SP2 (adapted from Schwarz et al., 2010).

The laser beam is generated by a Nd:YAG crystal excited by a solid-state pump laser at 808 nm. The resulting intra-cavity beam has a Gaussian shape and a nominal wavelength of 1064 nm. As shown in Figure 2-5, the thermal radiation emitted by refractive and absorbing particles in the visible spectrum is detected by two photomultiplier tubes (PMTs). Each of these photomultiplier

tubes is coupled to an optical band-pass filter to narrow the measured radiation in specific wavelength ranges. One allows measurement in a broad range between 350 nm and 800 nm (broadband detector), the second one (narrowband detector) in a narrow range between 630 nm and 800 nm.

The measurement of the light scattered by all particles is done by avalanche photodiodes (APDs; Figure 2-5) placed at different viewing angles: 13°-77° and 103°-167° relative to the laser. Finally, a two-element APD beam configured as described in Gao et al. (2007), is used to assess the position of the particle in the beam. Each segment of the avalanche photodiode has a distinct polarity, with one half inverted relative to the other. It is oriented so that as particles containing refractory black carbon (rBC) pass through the laser beam, the scattered light is shifted from one detector element to the other. As the particles pass through the central region of the detector, the scattered signal is evenly split, resulting in a measured scatter signal of zero. This mechanism produces a distinct notch in the signal, providing information about the location of rBC-containing particles within the laser beam.

Short description of the SP2-XR system

The Single Particle Soot Photometer Extended Range (SP2-XR, Droplet Measurement Technologies, DMT, Longmont, CO, USA) is the smaller, simpler and newer version of the SP2. It is based on the same physical principles and allows the users to obtain a real-time output of rBC mass and particle size for individual particles as well as some information on the particle mixing state. Moreover, the software provides real-time results for BC particle number/mass concentration and size distribution by automatically processing the raw data. The SP2-XR has a distinct optical cavity with respect to the SP2 and is not equipped with the two-element APD, used in the SP2 to evaluate the position of the particles in the laser beam. Nevertheless, the results provided by this instrument are nicely comparable to those provided by SP2, as described in Modini et al. (in preparation).

2.2.3.1 *Quantification of rBC properties*

Calibration of incandescence signal

The intensity of the thermal radiation emitted by the incandescent particle is parameterized as the peak-height of the incandescence signal as detected by the photomultiplier tubes ($PkHt_{INC}$ in Figure 2-6). $PkHt_{INC}$ is proportional to the mass of refractory and absorbing material (Moteki and Kondo, 2010).

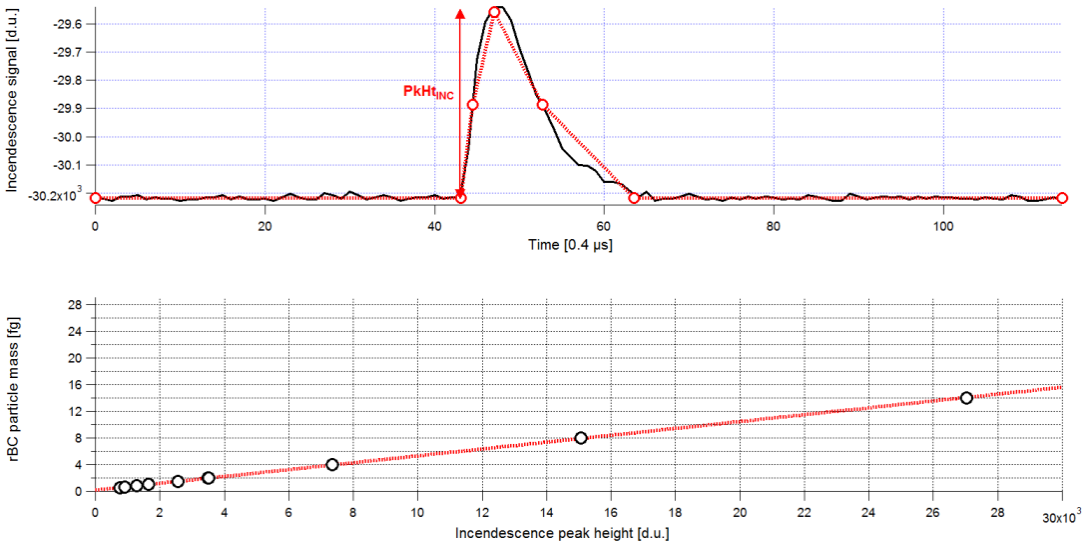

Figure 2-6: Representation of the incandescence signal produced by the SP2 (black line), measure of the $PkHt_{INC}$ (red arrow). Fitting procedure for mass calibration (bottom panel).

The instrumental-specific proportionality between $PkHt_{INC}$ and mass is established by a calibration procedure. Since mainly BC particles remain intact at temperatures above 4000K, the signal can therefore be related to the mass of BC present in the collected particles. The calibration is done by measuring rBC standard material with known mass, and characterized by properties as similar as possible to the ambient BC. Although a NIST standard for refractory BC does not yet exists (Baumgardner et al., 2012), the sensitivity of the SP2 to different calibration materials was investigated in Laborde et al. (2012a).

All the rBC mass observations reported in this thesis were based on the use of fullerene soot as calibration material. The calibration process involved nebulizing a suspension of fullerene soot, selecting particles by size using a

Differential Mobility Analyzer (DMA) and then measuring them with the SP2, similar to Laborde et al. (2012b). The selected diameter values were then converted to mass values using the effective density value specific to fullerene soot (Gysel et al., 2011).

Properties derived

Once that the calibration has been performed, the incandescence signal is used to measure and calculate:

- the mass of each rBC particle passing through the laser beam,
- the rBC mass concentration m_{rBC} (corrected as detailed in Section 2.2.3.4),
- the mass-equivalent diameter (D_{rBC}) of each particle (assuming a particle density of 1800 kg m^{-3}),
- the mass (MSD) and number (NSD) size distributions (as described in Section 1.1.2.2),
- the mass median diameter (MMD), derived as the diameter that divide the fitted size distribution between 10 and 1000 nm, in parts with the same total mass.

2.2.3.2 *Quantification of rBC-free properties*

Calibration

The size of non-absorbing particles, quantified as optical diameter D_p, can be determined using the scattering signal of the SP2. Regardless of their composition, all aerosol particles produce a scattering signal when exposed to radiation. If they are non-absorbing, they will not heat up as they pass through the laser beam, remaining intact and producing a signal proportional to their scattering cross-section $\sigma_{meas}(D_p, m)$ and the beam intensity I_{beam}. Assuming that the particles are spherical and assuming a value for the refractive index of the material, the scattering cross-section can then be related to a diameter D_p value via Mie theory.

As described in the Figure 2-7, the raw signal from the scattering detector s(t), which depends on the cross-section of the particle and the profile of the laser beam $I_{beam}(t)$, assumes the Gaussian shape of the beam, since the cross-section is constant over time. It therefore reaches a maximum value,

defined as PkHt, when the particle is at the center of the beam. This maximum value is proportional to the cross-section of the material according to the following
relationship:

$$\sigma(D_p, m) = \frac{PkHt_{scat}(D_p,m)}{I_{beam} \cdot CF_{scat}(D_p,m)} \quad (2\text{-}3)$$

where CF_{scat} is a calibration factor that can be determined by measuring particles of known size and refractive index (e.g. m = 1.59 and D_p = 220 nm for polystyrene latex spheres, PSL), and deriving their cross-section using the Mie theory. To increase the accuracy of the procedure, it is then possible to average the calibration coefficients obtained by using particles of different sizes or by varying the intensity of the laser beam. Once that the calibration coefficient has been determined it is than possible to derive the cross-section from the $PkHt_{scat}$ produced by each particle measured, using the relation 2-3.

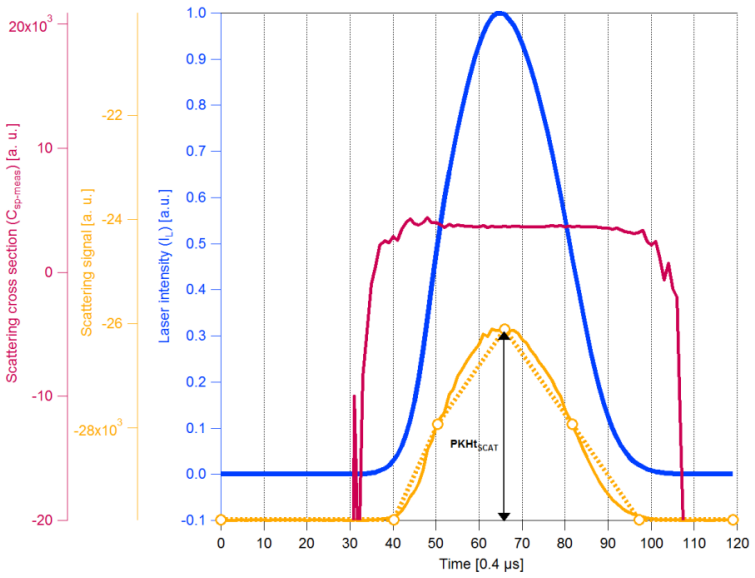

Figure 2-7: Example of scattering signal (orange line) and scattering cross-section (red line) for a rBC-free particle measured by the SP2. Dotted orange line represents the Gaussian fit applied to determine the scattering peak height for every particle. Blue line represents the distribution of laser beam intensity. All properties are expressed in arbitrary unit [a. u.].

In all the measurement campaigns presented in this thesis, the calibration of the scattering detector was performed using 220 nm diameter PSL size standard particles (Thermo Scientific, formerly Duke Scientific), and varying the laser beam intensity. The good reproducibility of the values obtained for the

coefficients over time was checked, as well as the comparability of the size distribution obtained for non-absorbing particles with that obtained from the SMPS. The refractive indexes used in this thesis for calculating the size of non-absorbing particles were 1.50-1.59 for campaigns in Bolivia, 1.48 for the campaign in Barcelona.

2.2.3.3 *Estimation of mixing state*

Several methods, based on different measurement techniques, have been used to derive information on the mixing state of BC (Riemer et al., 2019). Of these, those based on SP2 measurements are the most promising in terms of time-resolved and size-resolved information, although they are still subject to significant uncertainties. There are three in particular: (i) scattering to incandescence lag time, (ii) leading edge only (LEO), (iii) normalised derivative. The second, developed by Gao et al. (2007), is the one implemented in this thesis.

In the assumption of spherical particles with core shell geometry, the quantity derived by this method is the coating thickness, i.e. the thickness of non-incandescent material present around the rBC core. This is calculated from the comparison of scattered and incandescent signals using the following relationship:

$$CT = \frac{D_p - D_{rBC}}{2} \tag{2-4}$$

where D_p is the total optical diameter of the particle containing rBC derived from the scattering signal, D_{rBC} is the mass-equivalent diameter derived from the mass measurement. In the previous section we described how to derive the size of BC-free particles. If the particles contain rBC, the quantification of the particle size is particularly complex, due to the volatility of coating material. While passing thorough the laser beam, the increasing temperature of the rBC core causes the evaporation of coatings, so that the diameter of the total particles decreases with the time spent within the laser edges. Hence, the optical diameter of the rBC-containing particle has to be reconstructed from the first part of the scattering signal before evaporation onset. This is what is done by the leading edge only method described by Gao et al. (2007). To apply this method, it is then necessary to know the shape of the laser profile and the position of the particle in the beam.

The actual shape of the laser can be obtained by analysing the scattered signals from the non-absorbing particles (Laborde et al., 2012a). The laser profile is fitted over the part of the scattered signal produced by the particles, that is within 3% of the maximum laser intensity (Figure 2-8c). This is the very first edge of the signal, where evaporation of coatings did not occur yet. The position of the particle in the beam is derived from the split detector (Figure 2-8b). The distance between the inversion point of the split detector signal and the scattering peak, which is determined during the optical alignment of the sensors, remains unchanged during the measurement. To check the success and quality of this fit, it is then useful to evaluate the scatter plot of the results obtained on scattering only particles with the actually measured scatter signals (Figure 2-9a). Once the scattering cross-section has been evaluated using the reconstructed peak, the total particle diameter is derived assuming a spherical core shell and refractive indices for both the refractory interior and the outer coating.

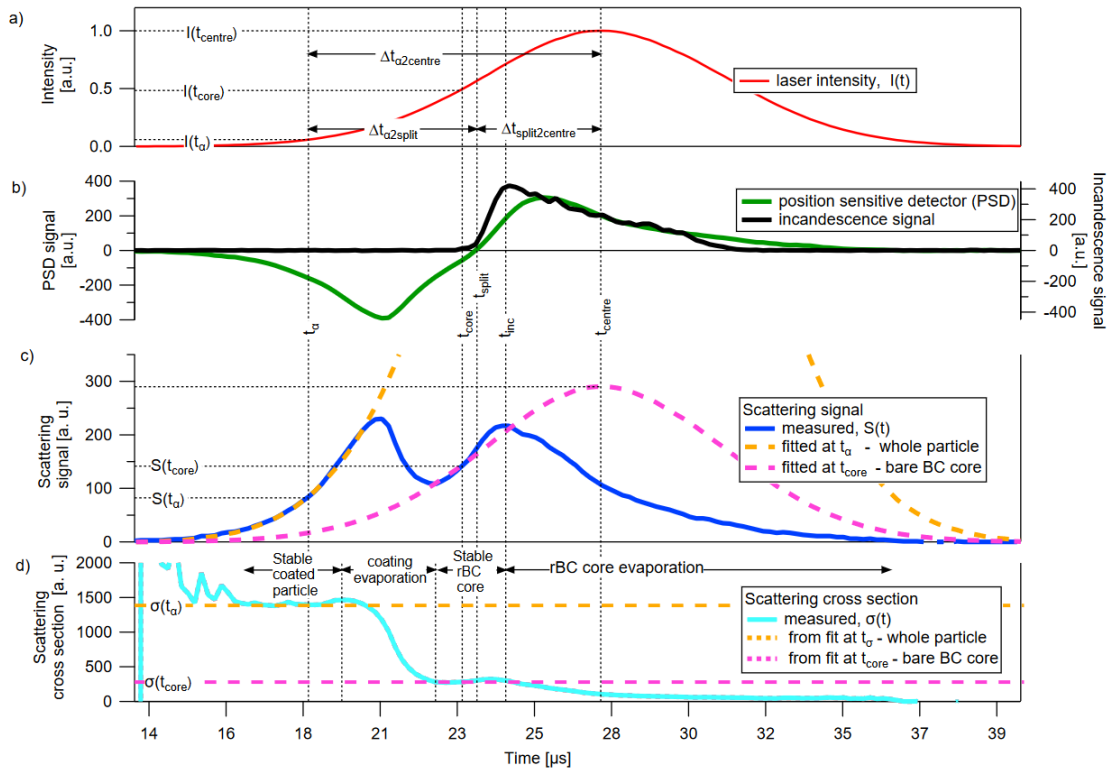

Figure 2-8: Example of SP2 signals over time passed within the laser beam for a rBC containing particle. (a) Laser beam intensity profile (b) incandescence and position sensitive (split) signals (c) scattering signals (d) scattering cross-section (Laborde et al., 2012a).

As a final check, the ability of the method to reproduce the diameter of the inner core is assessed with a scatterplot by comparing its estimate from LEO-fit with its measurement from the incandescence signal (Figure 2-9b). By checking the impact on these comparisons, values of m=2.0+1.0i, m=1.75+0.43i, were selected as refractive indexes for the rBC core and m=1.50, m=1.48 for the coating material in Chacaltaya and Barcelona respectively.

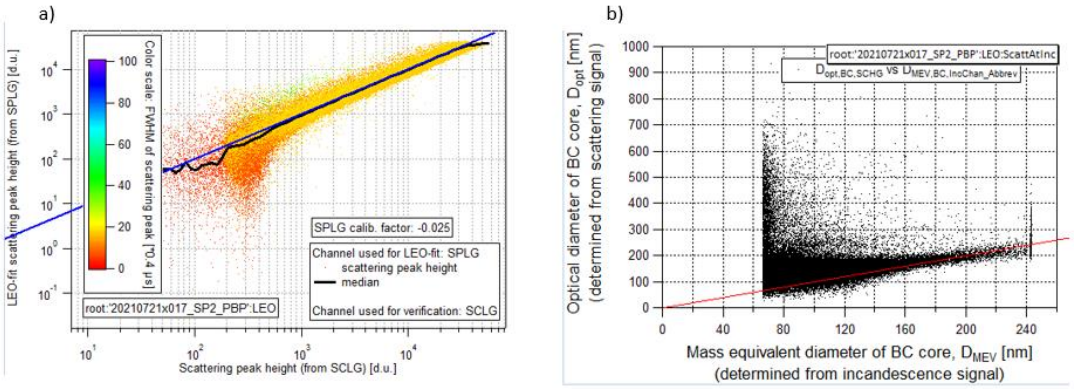

Figure 2-9: Examples of test performed to check the quality of the LEO-fit analysis. A) scatterplot of the LEO-fit derived peak height to the actual scattering peak height. B) Scatterplot of the optical diameter of rBC cores derived from the scattering signal assuming a refractive index to the mass equivalent diameter derived from the incandescence signal.

2.2.3.4 ***Uncertainties and corrections***

Unit to unit variability

During the SOOT11 initiative at the AIDA chamber, six SP2s from different research institutions were examined (Laborde et al., 2012b). The agreement in the number and mass size distributions was within a narrow range of 5% and 10%, respectively. However, a more pronounced variance was observed for rBC cores lighter than 1fg. Discrepancies in rBC mass concentration are commonly attributed to differences in mass calibration accuracy (Laborde et al., 2012b). The number size distribution of rBC-free particles was in agreement within 15%. In addition, all six instruments measured coating thickness within a 17% tolerance. Notably, the accuracy of the mass concentration measurement of the SP2 is dependent on the calibration material, justifying the use of a fullerene soot standard during calibration procedures. Laborde et al. (2012b) emphasised that while the SP2

provides accurate and reproducible data, achieving high quality results requires careful tuning and calibration of the instrument. The main adjustments and calibration steps listed in Laborde et al. (2012b) where always performed in the campaigns presented in this thesis to achieve optimum performance of an SP2.

Mass concentration correction

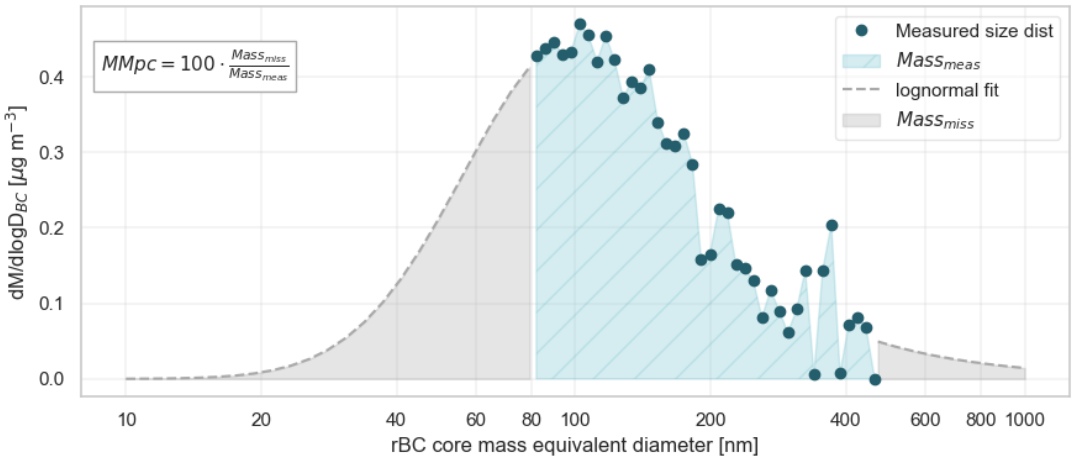

Figure 2-10: Graphical description of the method applied to correct the mass concentration for the missing mass in the SP2.

Having determined the mass of each particle, and knowing the flow sampled, it is possible to derive the mass concentration of rBC. However, the range of diameters over which measurements can be done is limited. This can vary from instrument to instrument and, in the case of the instruments used in this work, is between 80 and 500 nm. If a large proportion of the particles fall below or above this range, the concentration is subject to a major bias. For this reason, in many sites a correction method is needed to account for the missing mass. This correction can vary from one campaign to the other depending on the dataset. Here we describe the methods used in each of the datasets analysed in this thesis (Table 2-2).

Specifically, we introduced an hourly percentage missing mass correction coefficient (MMpc) or a scaling factor. Two different approaches were used to calculate them: (i) one involving the evaluation of the mass lost from the hourly size distribution, (ii) one obtained comparing the mass with an independent technique such as the thermo-optical technique described in section 2.2.2 (e.g. rBC – EC comparison). In the first approach, illustrated in Figure 2-10 a log-normal fit is applied to the hourly measured size distribution.

The total mass is derived integrating the curve obtained in the diameter range 10 to 1000 nm.

Table 2-2: Summary of missing mass correction factors used through the thesis, in each site where an SP2 was used to measure the rBC mass concentration. A percentage correction has been derived when the method used was based on fitting the size distribution, while a scaling factor have been derived when the measurements have been corrected scaling the m_{rBC} on the m_{EC}.

SITE	METHOD	MM_{cp} [%] MEAN	(MIN-MAX)	SCALING FACTOR
BCN	SizeDist - fit	20 %	-2.4 – 96 %	
LP	SizeDist – fit	10.7 %	2.9 – 22 %	
	Scaling to EC			7.7
EA	SizeDist - fit	7.2 %	3.3 – 17 %	
CHC	SizeDist - fit	1.2 %	-14 – 30 %	

The missing mass is estimated from the difference between the total and the measured mass. The correction coefficient MMpc is finally obtained as the ratio of the missing mass to the mass measured, multiplied by 100. In the second approach, the correction coefficient (Scaling factor) was derived from the ratio, between m_{EC} and m_{rBC}.

Limitation to LEO-fit method

The LEO-fit method has limitations connected with the various assumptions and detection limits of the instrument. In particular, the spherical core-shell model with a void-free interior is not entirely realistic; the particles in the environment have a wide variety of shapes (Adachi et al., 2010; Adachi and Buseck, 2013; Liu et al., 2017). The assumed density of 1800 kg/m^3 is close to reality, but it is an approximation in the environment (Ouf et al., 2019). The choice of refractive indices is quite complex.

The variability of the results is significant as the parameters used vary (Taylor et al., 2015). Moreover, both the scatter and incandescence detectors have detection limits, meaning that only particles within a certain size range

can be measured. This can vary from instrument to instrument depending on the condition of the sensors.

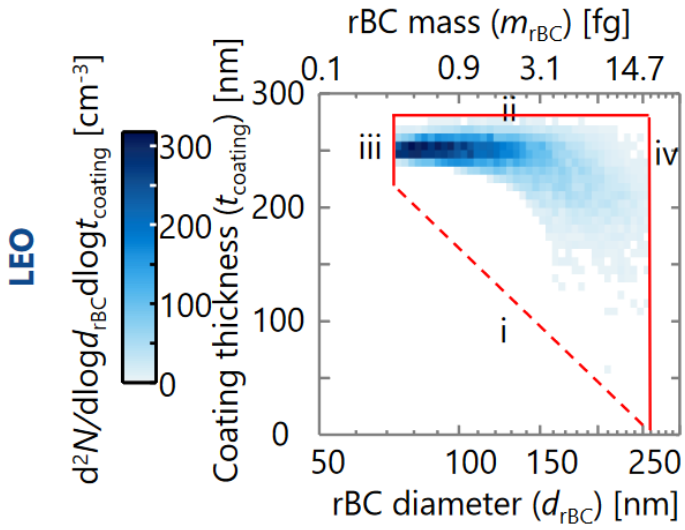

Figure 2-11: Distributions of rBC diameter and coating thickness. Red lines indicate the detection limits, with iii and iv showing the low and high broadband incandescence detection limits, respectively, i and ii showing the LEO lower and higher coating detection limits (Naseri et al., 2023).

As discussed in previous papers (Naseri et al., 2023) and shown in the Figure 2-11, this implies limitations in the coating that can be measured for rBC cores of different sizes. In the case of very small cores, it will only be possible to calculate the coating if it is sufficiently large, in the case of very large particles it will only be possible to calculate the smallest coatings. In the case of the instrument used in this thesis, the limits are set at rBC particles between 180 and 220 nm.

3 METHODOLOGY: FIELD CAMPAIGNS AND EXPERIMENTS

3.1 LONG TERM MEASUREMENTS AT MONTE CIMONE AND ISPRA

The first scientific goal of my work has been investigated by comparing aethalometer measurement and an independent reference technique both in environmental conditions, by using the long term National Facilities in the frame of ACTRIS RI, and with specific experiments in a simulation chamber (in the frame of EUROCHAMPS/ACTRIS). In particular, I studied the ambient variability of the correction coefficient C for the aethalometer's multiple scattering effect (that was described in Section 2.1.1.1) through measurements carried out at two sites being part of international monitoring networks ACTRIS and WMO-GAW.

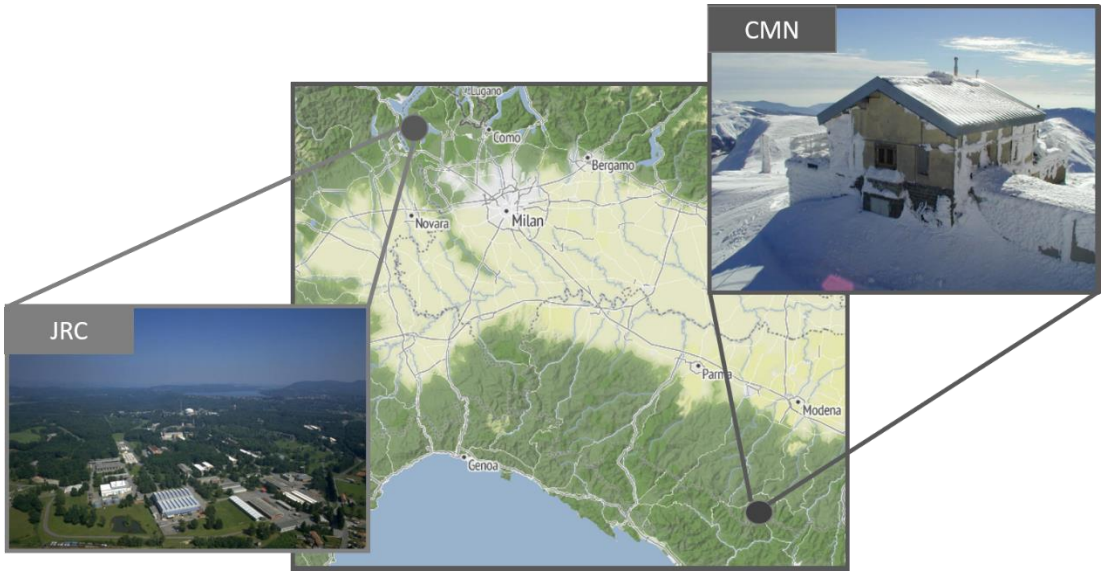

Figure 3-1: Graphical representation of the areas where the Monte Cimone (CMN) and Ispra (JRC) measurement sites are located.

The Monte Cimone observatory (CMN) and the Joint Research Centre Ispra station (JRC) both located in northern Italy (Figure 3-1), provide long-term measurements performed following the standard operation procedures of the ACTRIS network and are representative of different atmospheric conditions. For on-line aerosol measurements, ACTRIS Standard Operating

Procedures and Quality Assurance (QA) and Quality Control (QC) requirements are followed at both stations. Those involve station audits, side by side instrument comparisons at the world calibration center for aerosol physics (WCCAP) in Leipzig (DE), and specific QC measurements.

3.1.1 Sites description

The 'Ottavio Vittori' Climate Observatory, is situated on Monte Cimone, the highest peak in the northern Apennines (44.1933°N, 10.7011°E) at an altitude of 2165 meters above the sea level (m a.s.l.). It is the only GAW-WMO global station on Italian territory and south of the Alps managed by the National Research Council of Italy (CNR), and an essential component of ACTRIS-RI. Located about 40 km from the nearest industrial areas and surrounded by small towns 15 km away and 1100 m below, Monte Cimone is immersed in a pristine environment characterised by grassland and rocky terrain, with coniferous and beech forests ending at an altitude of 1600 m. The absence of major pollution sources, combined with its high altitude, makes Monte Cimone an ideal platform to study the background conditions of the Mediterranean troposphere and the direct influence of surface emissions on it (Cristofanelli et al., 2017).

The site of Ispra (45.8046°N, 8.6287°E, 209 m a.s.l.) is managed by the Climate Change Unit of the Joint Research Centre's (JRC) Institute for Environment and Sustainability of the European Commission. Its aim is to monitor atmospheric variables to contribute in assessing the impact of European policies on air pollution and climate change. It is located in a semi-rural area on the north-western edge of the Po Valley (see Figure 3-1). The station is tens of kilometres away from major emission sources such as heavy road traffic, large factories and major metropolitan areas such as Milan (60 km to the south-east). In particular, four significant industrial sources emitting more than 1000 tonnes of CO per year are located between 20 and 50 km east to southeast of Ispra. The closest source, located 20 km south-southeast, emits more than 2000 tonnes of NOx per year. Overall, JRC is considered to be representative of continental polluted background.

3.1.2 Methodology applied

The main objective of these field observations was the analysis of the C factor in ambient conditions for correcting the aethalometer at CMN and JRC. More in detail, different instrumental setups were used to quantify the spatial-temporal variability of C and its model-to-model variability, and the spectral dependency of C. The specific setups, used for the investigation of the various C dependencies at different sites and during different periods are summarised in Table 3-1.

3.1.2.1 *Spatial-temporal variability of C at CMN and JRC*

At both sites, to quantify the spatial and temporal variability of C, the absorption coefficient (b_{abs}) used as a reference at 637 nm was measured with a MAAP (model 5012, Thermo Sci.). The attenuation coefficient corrected for the loading effect $b_{atn}^{LC}(\lambda)$ was instead measured using two different aethalometer models (AE33 and AE31, Magee Sci.). For the AE33, the internal loading correction algorithm described in Section 2.1.1.1 was used to correct the loading effect. In particular, we obtained $b_{atn}^{LC}(\lambda)$ from BC(λ) as follows:

$$b_{atn}^{LC}(\lambda) = BC(\lambda) \cdot MAC_{eBC}(\lambda) \cdot C_{inst} \quad (3\text{-}1)$$

For the AE31, we instead calculated $b_{atn}^{LC}(\lambda)$ using the output value of BC(λ), multiplied by the spectral $MAC_{eBC}(\lambda)$ assumed in the instrument and reported in Section 2.2.1 and applying the correction by Collaud Coen et al. (2010). The multiple scattering correction factor C at 637 nm was then derived using hourly averaged b_{abs} from the MAAP and $b_{atn}^{LC}(\lambda)$ from both aethalometer models, and applying equation 2-4. The b_{atn}^{LC} at 660 nm was interpolated to 637 nm using equation 1-16, and an AAE calculated from uncorrected $b_{atn}^{LC}(\lambda)$ values (on average ~1.3 for both sites and aethalometer models).

3.1.2.2 *Spectral dependency of C at CMN*

To investigate the spectral dependency, the reference absorption coefficient $b_{abs}(\lambda)$ was measured off-line by the MWAA at five wavelengths (375, 407, 532, 635 and 850 nm), during a specific field campaign. The C(λ), at

the aethalometer wavelengths, was obtained from the ratio of the averaged $b_{atn}^{LC}(\lambda)$ (on the time periods of each filter analysed with the MWAA) and the MWAA $b_{abs}(\lambda)$, which was adjusted to the aethalometer wavelengths with an AAE calculated from $b_{abs}(\lambda)$ values (on average ~1.3). For correcting the aethalometer AE31 measurements with the Collaud Coen et al. (2010) correction and for deriving the SSA needed for discussing C variability, we used scattering coefficient measurements performed by an integrating nephelometer (model 3563, TSI Inc.).

3.1.3 Temporal coverage of observations

At CMN, the measurements performed by the AE31 covered only one-month period (July 2017), those with the AE33 a two-years period (2020-2022). MAAP and nephelometer measurements were always available when both aethalometer models were running. Moreover, at CMN, the spectral analysis with the MWAA covered two months in October-November 2022. At JRC, we analysed data from January to June 2022 when AE31, AE33 and MAAP were simultaneously running.

Table 3-1: Summary of measurement periods for each technique used in the sites of CMN and JRC.

C VARIABILITY	AETHELOMETER MODEL	REFERENCE ABSORPTION	C WAVELENGTH [NM]	SITE AND PERIOD
Spatial-Temporal	AE33	MAAP	637	CMN: 2020-2022 JRC: Jan-Jun 2022
Spectral	AE33	MWWA	370, 470, 520, 590, 660, 880, 950	CMN: Oct-Nov 2022
Model-to-model	AE33 AE31	MAAP	637	CMN: Jul 2017 JRC: Jan-Jun 2022

3.2 RI-URBANS CAMPAIGN IN THE PO VALLEY

I took advantage of the RI-URBANS H2020 and CAIAC projects to study part of my second objective, that is the study and characterization of BC near the sources in urban environments. One of the pilot study of H2020 RI-URBANS project focused on the pollution hot spot of Po Valley, where two sites were instrumented in different regions: Milan and Bologna. Both sites were equipped with instruments for the online source apportionment (ACSM and AE33 aethalometer). The campaign started in January 2023 with one-year duration in 9 cities of Europe. The RI-URBANS project aims to showcase the adaptability and enhancement of Service Tools (STs) from atmospheric Research Infrastructures (RIs) for improved air quality monitoring in European cities and pollution hotspots. Addressing the pressing need to reduce air pollution and assess its health impacts, the project develops synergies between Air Quality Monitoring Networks (AQMNs) and RIs to advance policy assessments.

By analyzing the annual measurement at the two sites of the Po Valley (Milan and Bologna), we explored the role of eBC in total PM1 in urban areas and studied the variability of eBC sources over the year.

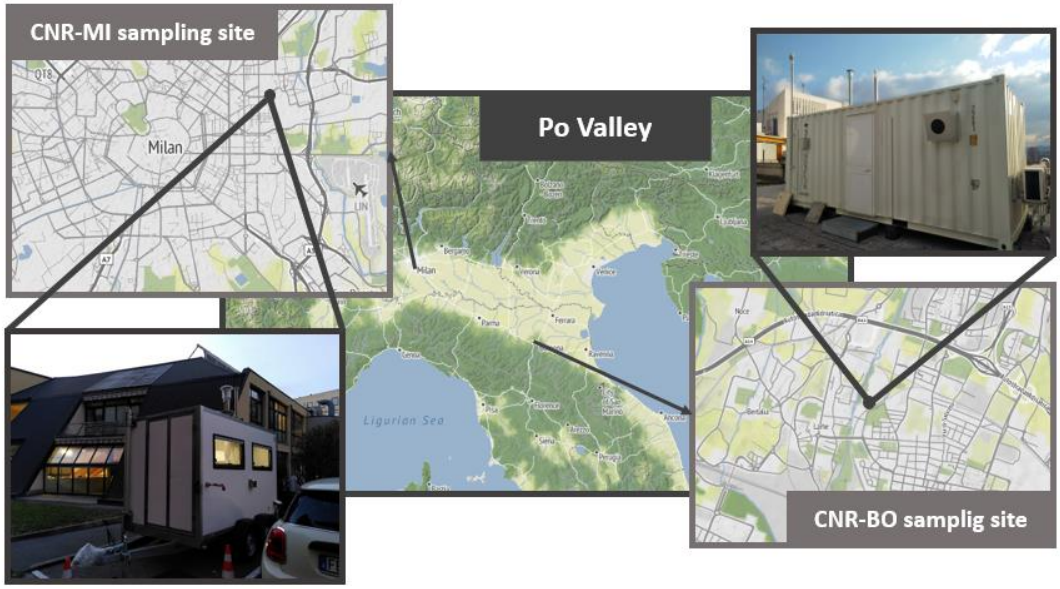

Figure 3-2: Sampling sites in the Po Valley, Bologna and Milan.

3.2.1 Bologna

3.2.1.1 *Description of the site*

The site in Bologna (BO), located within the CNR research area (44.5237°N, 11.3386°E) in a residential suburban site just outside the city center, consists of a container placed on the roof of the building, about 25 m above ground. It is unaffected by direct pollution sources and focuses on the analysis of urban background conditions in Bologna. It serves as a representative site for a densely populated and highly urbanized environment with major roads and an airport.

3.2.1.2 *Methodology applied*

At this site, an aethalometer (model AE33, Magee Sci.) and a Quadrupole Aerosol Chemical Speciation Monitor (Q-ACSM), measured simultaneously for six months from the end of December 2022 to July 2023.

The ACSM provided a chemical characterization of total particulate matter (size cut-off < 1μm). The aethalometer was used to measure the mass concentration of eBC as described in Section 2.2.1.

In addition, the source apportionment model of the aethalometer was used to separate the total eBC into its components from solid (BCsf) and liquid (BClf) fules, as described in Section 2.2.1.1. In the absence of specific measurements to quantify the contribution of dust to the absorption, it was assumed to be small and negligible compared to the contribution of BC and organic aerosol at this site. Waiting for more detailed analyses (i.e. comparisons with traffic and biomass burning tracers such as NOx, m/z 60 of ACSM), the extremes (1%-99%) of the distribution (summer-winter) of AAE values were used for an approximate determination of the Ångström exponents AAE_{sf}, AAE_{lf}. In this case AAE_{lf} = 1.0, AAE_{sf} = 1.8.

3.2.2 Milan

3.2.2.1 *Description of the site*

The site in Milan (MI) is instead located in the internal courtyard surrounded by the buildings of the CNR research area (45.4807°N, 9.2322°E) in a residential area in the eastern part of the city. It consists of a van specifically

designed to perform aerosol and reactive gas measurements in accordance with ACTRIS recommendations and standard operating procedures. Being located in a cohort within buildings, even if at less than 150 m from big roads, it is not subject to any particular direct sources other than the occasional car parked nearby, and is more representative of background conditions, where the aerosol is more aged and diluted than in areas close to roads. It is located less than 100 m from the regional environmental agency station "Milano Pascal", that can provide ancillary measurements useful to compare or integrate the measurements.

3.2.2.2 ***Methodology applied***

At this site, an aethalometer (model AE33, Magee Sci.) and a Time-of-flight Aerosol Chemical Speciation Monitor (Tof-ACSM), measured simultaneously for one year from January 2023 to January 2024.

The ACSM provided a chemical speciation of non-refractory particulate matter (size cut-off < 1 μm), while the aethalometer was used to measure the mass concentration of eBC as described in Section 2.2.1.

In addition, the source apportionment model of the aethalometer was used to separate the total eBC into its components BCsf and BClf as described in Section 2.2.1.1. The same assumptions as for Bologna and the same method to derive AAE_{lf}, AAE_{sf} were used. For this site AAE_{lf} = 1.0, AAE_{sf} = 1.8.

3.3 SUMMER FIELD CAMPAIGN IN BARCELONA

A second field campaign in an urban environment, was devoted to investigate the microphysical properties and mixing of BC particles near emissions. This was carried out from July 19th until July 31st 2021 at an ACTRIS site in Barcelona (BCN), as part of the CAIAC project (Changes on Aerosol composition and their Implications for Air quality and Climate in NE Spain). This project involved many different techniques to characterize the influence of human activities on the physical and chemical properties of aerosols particles.

3.3.1 Description of the site

Barcelona is located in the Western Mediterranean Basin, in a narrow corridor between the sea to the south-east and a mountain range to the north-west. It is the second biggest city in Spain with a population of around 4.5 million people. The metropolitan region is characterized by major highways, densely urbanized areas, industrial zones, power plants, ports and airports. This means a large number of anthropogenic sources of atmospheric aerosols, including BC.

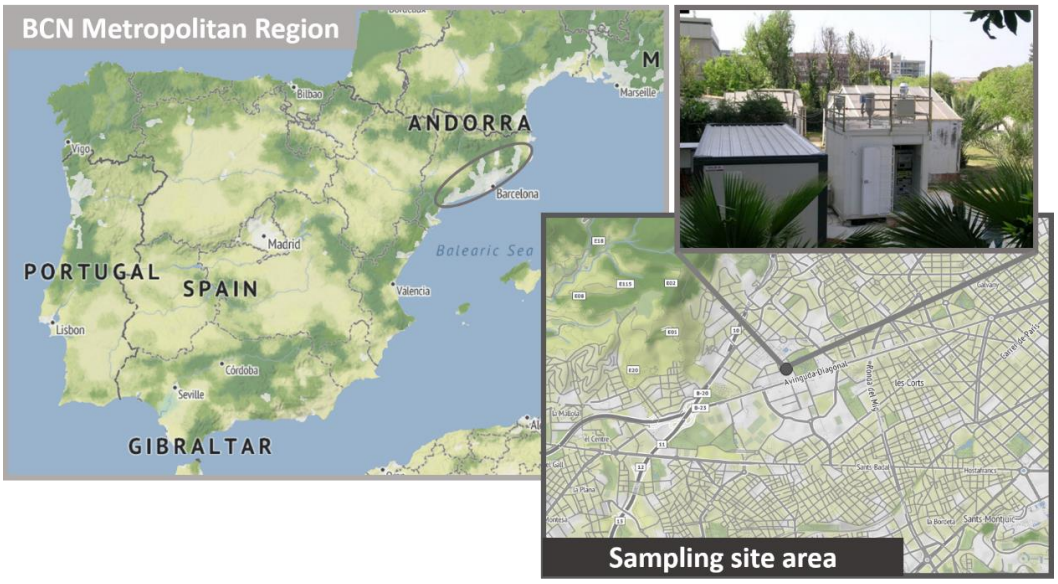

Figure 3-3: *Map of the sampling site at IDAEA CSIC, the Institut de Diagnòstic Ambiental i Estudis de l'Aigua in Barcelona (BCN), where the campaign in July 2021 was performed.*

The sampling site is placed in the western part of the city in the inner courtyard of the IDAEA CSIC, the Institut de Diagnòstic Ambiental i Estudis de l'Aigua (41.3876° N, 2.1146° E; 68 m a.s.l.). As we can see from the Figure 3-4, the area near the measurement site is surrounded by parks, residential blocks and highly trafficked streets. The nearest street but lightly trafficked is about 25 m away. The two largest heavily trafficked roads, Avinguda Diagonal and Ronda de Dalt are located approximately 250 and 680 m west-southeast respectively. The emissions from the city are mainly traffic, domestic heating, cooking, construction with inputs of harbor, airport and industrial emissions. Given its location this site is representative of urban background conditions.

BCN site is equipped with the state-of-the-art systems for both remote-sensing and in-situ measurements of atmospheric aerosol.

3.3.2 Methodology applied

In order to characterize the microphysical properties of BC, we deployed in BCN an SP2-D (Single Particle Soot Photometer, Droplet Measurement Technologies, CO, USA) corrected and calibrated as detailed in Section 2.2.3, for measuring rBC mass concentration, size distribution and coating thickness.

An aethalometer (model AE33, Magee Sci.; corrected with a C factor of 2.44, Yus-Díez et al., 2021) was deployed to derive the absorption coefficient at seven wavelengths.

The rBC mass concentration was compared at this site with the EC mass concentration measured with a semi-continuous OC:EC aerosol analyzer (Sunset Laboratory Inc.). The measurements followed the EUSAAR-2 protocol with a 3 hours measuring interval and a measurement error of 10 % (Karanasiou et al., 2020). This instrument was installed with a PM2.5 inlet cut-off and at a flow rate of 8.0 L min^{-1}. A comparison of this technique with the off-line OC:EC method at this site can be found in Yus-Díez et al. (2022), and demonstrate a strong agreement. The offline EC concentrations in the PM10 fraction were 26 % higher than online EC concentrations in the PM2.5 fraction.

Table 3-2: Summary of variables measured during the field campaign in Barcelona (BCN), including the measurement period and the techniques used.

OBJECTIVE	BC PROPERTIES	TECHNIQUES	PERIOD
Black carbon characterization	Mass concentration Diameter Coating thickness	SP2	19-31 July
Optical properties characterization	Mass absorption cross-section Absorption enhancement	SP2 Aethalometer	19-31 July
Characterization of case events	Mass concentration Diameter Coating thickness Mass absorption cross-section Absorption enhancement	SP2 Aethalometer	Pollution case: 20,23 July Clean case: 24, 25 July
BC mass concentration comparison	Refractory BC Elemental carbon	SP2 OC:EC analyzer	19-31 July

3.4 SALTENA EXPERIMENT IN THE BOLIVIAN ANDES

The last field campaign has been carried out during the Southern Hemisphere High Altitude Experiment on Particle Nucleation and Growth (SALTENA) experiment, that took place between December 2017 and June 2018 (wet to dry season) at Chacaltaya (CHC), El Alto (EA) and La Paz (LP), in the Bolivian Andes. This thesis includes the results of this extensive measurement campaign, with the aim to explore the variability of rBC properties both in special high altitude urban environments and after ageing during transport from urban areas to a remote site. The aim of the campaign was to identify the sources, understand the formation mechanisms and transport, and characterize the properties of the atmospheric aerosol (Bianchi et al., 2022). Three SP2s (one C model and two SP2-XRs) were used for this purpose, with a particular focus on characterizing BC properties in unique urban and remote environments.

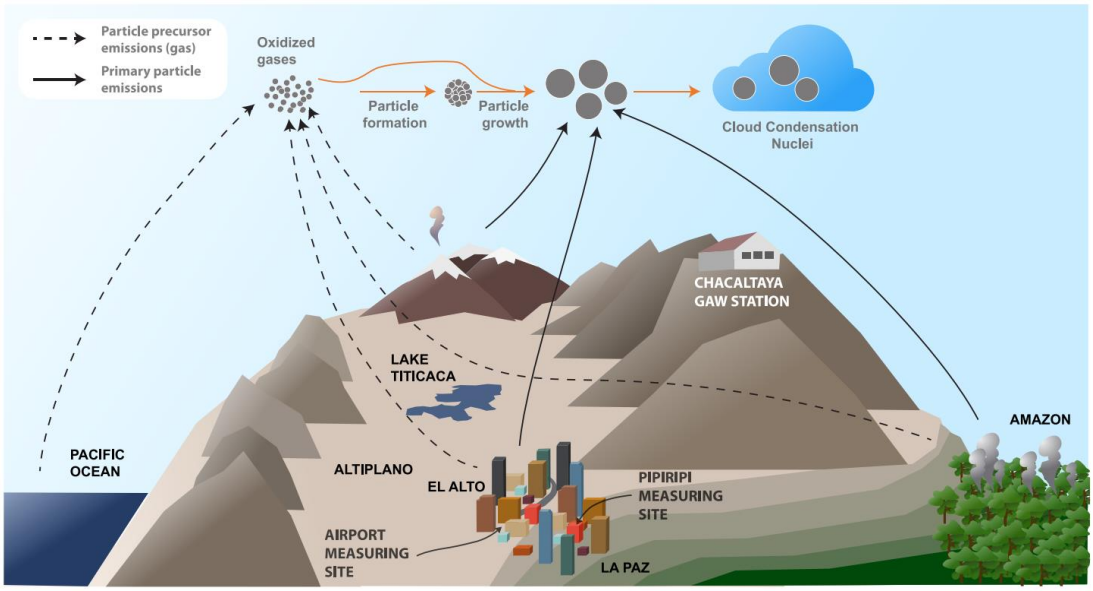

Figure 3-4: Map of the Bolivia region where the three sites involved in this campaign are situated. La Paz (LP) in a valley, El Alto (EA) on the Altiplano and Chacaltaya (CHC) on a mountain top (Bianchi et al., 2022).

Figure 3-4 describes graphically the area were the experiment was conducted. The chosen urban sites are part of a huge metropolitan region, including the cities of LP and EA, with a population of 1.8 million at an altitude of more than 3000 m a.s.l. Here the concentrations of pollutants can be very high and the

properties very special, as combustion processes change in such low-oxygen environments. We used these data for comparing rBC properties in different urban environments. Additionally, measurements were conducted in the global WMO-GAW CHC station (5240 m a.s.l.), located nearly 20 km away from the urban metropolitan area. This sampling configuration allowed the unique opportunity of studying the properties of BC in exceptional urban background conditions as well as free tropospheric conditions, and to study the variability of given properties during transport. To our knowledge, this campaign marked the first instance of conducting such detailed measurements in these distinct environments. The description that follows provides an overview of the three sites where the campaign took place.

3.4.1 Urban sites

3.4.1.1 *Description of urban background sampling sites*

One of the two urban background stations was situated in the city of La Paz (LP; 16.5013°S, 68.1259°W, 3600 m a.s.l.), on the roof of the Pipiripi Municipal Museum (Espacio Interactivo Memoria y Futuro Pipiripi). The building is located in the centre of the city, on a small hill in a central park. It is approximately 70 m horizontally and 45 m vertically from the nearest road. Despite its proximity to a green area (approximately 100 metres), it is in the middle of a densely populated residential district within a 1km radius, characterised by the presence of several busy roads.

The other urban background site was located at El Alto city (EA; 16.5100° S, 68.1987° W, 4025 m a.s.l.), within the facilities of the meteorological observatory of the El Alto International Airport. The station was located in an area closed to the public and at a sufficient distance from the runway (approximately 250 m) to avoid being directly affected by aircrafts landing and departing. The surrounding area of the sampling site was an empty and very dry terrain nearly 600 m from the closest main road.

The two sites are characterized by different topographical features. The city of El Alto is located on the vast and flat Altiplano at around 4000 m a.s.l, while La Paz is distributed along the mountain valleys which lie below the Altiplano, with steep and rough terrain. The meteorological conditions, mostly affected by the transition between the dry and wet seasons typical of tropical

regions, vary considerably between the two cities due to the differences in altitude and local topography (Wiedensohler et al., 2018).

Air pollution emissions in these two sites can be affected by contrasting urban dynamics, due to marked economic and social disparities and persistent inequalities between the respective population, and by daily movement of a significant portion of El Alto's population to La Paz. In addition, most of industrial activities are concentrated near El Alto. Vehicle traffic is also different in the two cities with a higher density of heavy vehicles such as trucks and buses in El Alto (Mardoñez et al., 2023). While La Paz seemed to be more influenced by direct traffic emissions, El Alto station was more representative of urban background conditions.

3.4.1.2 *Methodology applied*

At the urban sites (LP, EA), measurements were taken over a one-month period, starting at the end of April until the end of May. Two SP2-XR (Droplet Measurement Technologies, DMT, Longmont, CO, USA) were used to measure rBC mass concentration and size distribution. The calibration procedures and correction methods applied to SP2 are described in section 2.2.3.1 and are the same applied in Modini et al. (in preparation).

The absorption coefficients needed to calculate the MAC at 660 nm were measured using an aethalometer (model AE31, Magee Sci.), corrected with a C value of 3.0. The latter was obtained from the comparison of the attenuation coefficients measured by the AE31 (interpolated to 637 nm) and the absorption coefficients measured by a MAAP (at 637 nm), both located at the CHC GAW station, as detailed in Mardoñez et al. (2024).

3.4.2 Mountain site

3.4.2.1 *Description of the site*

The mountain site is located on Mount Chacaltaya (CHC; 16.3505°S, 68.1314°W, 5240 m a.s.l.), which is part of the World Meteorological Organisation (WMO) GAW network and has been operational since December 2011 (Andrade et al., 2015). The station is located approximately 140 m below the summit of the mountain, on the north western slope, with a direct view of the metropolitan region below. Due to its high altitude over an area of complex

topography, it receives air masses from different regions: from the Altiplano highlands (3800 m) and the Pacific Ocean to the northwest and west, from the lowlands and the Amazon rainforest to the east and northeast, and from the metropolitan area of LP-EA to the south and south-west.

It experiencies the annual alternation of wet (from November to March, with a transition period in April) and dry (from May to September) seasons. the seasonal meteorological condition affects the source region of air masses. Mainly arriving from west during the dry season and from north-east and south-east during the wet season (Chauvigné et al., 2019). It is regularly affected by pollution transport from the metropolitan area, in particular during daytime as a consequence of the increase in the boundary layer height and thermally-induced winds (Wiedensohler et al., 2018). It can be affected by the influence of volcanic eruptions from an active region in Perù (Bianchi et al., 2022, Moreno et al., 2024), and by biomass burning events from the Amazon Basin during the biomass burning season in August-September (Chauvigné et al., 2019).

3.4.2.2 ***Methodology applied***

At this site the measurements were carried out over a two-month period from the beginning of April to the beginning of June 2018. These periods are the transition between the rainy and dry seasons and the beginning of the dry season.

The rBC properties (mass concentration, size distribution, MMD, coating thickness), were derived at this site using a SP2 (C, Droplet Measurement Technologies, CO, USA). The correction method is detailed in Section 2.2.3.1. The absorption coefficient was measured at 637 nm with a MAAP (model 5012, Thermo Sci.).

Table 3-3: Instruments used in each of the three sites of the Bolivian Andes, where the campaign was performed in April-May 2018, for measuring rBC microphysical properties and absorption coefficient.

Site	rBC Microphysical properties (rBC mass concentration, mass size distribution, MMD, coating thickness)	Abs. Coefficient (b_{abs})
La Paz	SP2-XR, Droplet Measurement Technologies, DMT, Longmont, CO, USA	Aethalometer (model AE31, Magee Sci.)
El Alto	SP2-XR, Droplet Measurement Technologies, DMT, Longmont, CO, USA	Aethalometer (model AE31, Magee Sci.)
Chacaltaya	SP2 (C, Droplet Measurement Technologies, CO, USA)	Multi–Angle Absorption Photometer MAAP (model 5012, Thermo Sci.)

3.5 CHAMBER EXPERIMENTS

By participating to simulation chamber experiments at CESAM chamber (Experimental Multiphasic Atmospheric Simulation Chamber; Wang et al., 2011), we investigated the comparability of absorption measurement techniques for various types of black carbon aerosol under controlled conditions. Four campaigns were conducted during 2021 and 2022.

3.5.1 Description of the chamber

The CESAM chamber is a 4.2 m^3 stainless–steel, multi–instrumented platform allowing the study of aerosol ageing under controlled conditions of temperature, light and chemical composition (Wang et al., 2011). In our case, the aerosol generation was provided by the mini-CAST burner (model 6204C, Jing Ltd., Switzerland), a co-flow diffusion flame generator, producing cast soot (CS) from the combustion of propane (Moore et al., 2014). The procedure for injecting soot into CESAM involves a brief stabilization period of the miniCAST flame. Following this, the miniCAST exhaust is connected to a two-way splitter. This splitter divides the miniCAST output, with one part entering CESAM through a charcoal denuder (custom-made, with a flow rate of 3 to 6 LPM and filled with cut activated carbon, reference: LABO moderne fs99ff6060) to eliminate any potentially present volatile organic compounds (VOCs) in the aerosol flow. The other portion is directed towards an external exhaust. The duration of the injection varied according to the target concentration inside CESAM chamber.

3.5.2 Description of the experiments

The generation process allows control over particle size, composition, and morphology. Five mini-CAST operation points were examined, representing different burning conditions and resulting in particles with varying EC/TC ratios and sizes (Table 3-4).

The CS aerosol was injected into the CESAM chamber, aged under controlled conditions for 2 to 26 hours, and subjected to various experiments, including physical aging (CS as only component in the chamber) and chemical ageing (injection of inorganic and organic species), in dry/wet and light/dark conditions. The chamber underwent thorough cleaning and evacuation

between experiments, maintaining background aerosol concentrations below 10 ng m^{-3}. Multiple repetitions were conducted to ensure result reproducibility. More detailed information is available in Heuser et al. (in preparation).

Table 3-4: Summary of aerosol composition (EC/OC) of freshly emitted particles, generated with the mini-CAST at different operational points.

AEROSOL TYPE	EC/OC RATIO
CS1	3.8
CS2	2.7
CS3	2.0
CS4	1.1
CS5	0

3.5.3 Methodology applied

The objective was to investigate the variability of the C factor with microphysical properties of the particles in controlled conditions. The C factor was derived at 630 nm from the equation 2-4. The absorption coefficient b_{abs} considered as reference here, was derived at 630 nm by using the EMS technique, involving a Cavity Attenuated Phase Shift Extinction (CAPS PMex, Aerodyne) to measure the extinction coefficient and a nephelometer (model 3563, TSI Inc.) to measure the scattering coefficient as detailed Section 2.1.2. The attenuation coefficient loading corrected was then measured by an aethalometer (model AE33, Magee Sci.) using the internal algorithm to correct the loading. Both quantities were averaged over periods of about 30 min where the aerosol properties were almost stable, before calculating the C factor.

The EC/OC fractions for the five combustion sources investigated in this study were determined through thermo-optical analyses following the EUSAAR-2 protocol (Cavalli et al., 2010). These analyses were conducted on aerosol samples collected on quartz filters (47mm diameter, Pall TissuquartzTM, 2500 QAT-UP). The quartz filters were installed in a custom-

made stainless-steel sample holder and directly sampled from the miniCAST exhaust. To ensure accuracy, a charcoal denuder was positioned in front of the filter sampler. The results of the thermo-optical analyses are presented in Table 3-4, revealing a decreasing EC/OC ratio from CS1 to CS5. The particle size was evaluated as the NMD of the distribution derived with a scanning mobility particle sizer, (SMPS, DMA Model 3080, CPC Model 3772, TSI Inc.).

4 RESULTS: INVESTIGATION OF METROLOGY LIMITS

One of the uncertainties associated with BC radiative forcing estimates is due to the lack of reference techniques and calibration materials for accurate measurement of BC absorption coefficient and mass concentration. As described in Chapter 2, many different techniques are currently available to measure both quantities, but each is subject to specific and different uncertainties. In particular, the aethalometer is the most widely used technique for measuring the absorption coefficient worldwide in international networks such as GAW and ACTRIS, but it suffers from numerous biases as described in Section 2.1.1.1. In this chapter, we present a study of one of these biases, the multiple scattering effect, by comparing results from field and simulation chamber studies with results from the existing literature. We also evaluated the comparability of mass concentration measurements derived from the SP2 and the Sunset techniques from a field campaign in Barcelona. Details on the methods applied in the various contexts are described for field studies in Section 3.1 and 3.3, and chamber studies in Section 3.5.

4.1 CHARACTERIZATION OF REFERENCE ABSORPTION TECHNIQUES

To quantify the performances of various absorption measuring techniques, it is fundamental to first identify reference measuring approaches with a minimal influence of systematic artefacts. In this section we compare the results obtained with techniques that measure the absorption coefficient without the use of a filter (EMS) or that automatically correct for the multiple scattering effect (MAAP and MWAA). In particular, the MAAP is the most widely used as reference for deriving the correction values (Collaud Coen et al., 2010; Segura et al., 2014; Saturno et al., 2017; Yus-Díez et al., 2021) and, in general normalize absorption measurements in laboratory experiments (Müller et al., 2011) and field observations (Zanatta et al., 2016). Thanks to its design MWAA is capable to account automatically for multiple scattering effect, and it was already used as a reference measurement (Ferrero et al., 2021; Bernardoni et al., 2021). Although derived by the simultaneous measurements of extinction and scattering coefficient with two distinct instruments, the extinction minus

scattering (EMS) is not a filter-based technique. Hence, although it has other limitations (Modini et al., 2021), it is free from multiple scattering bias.

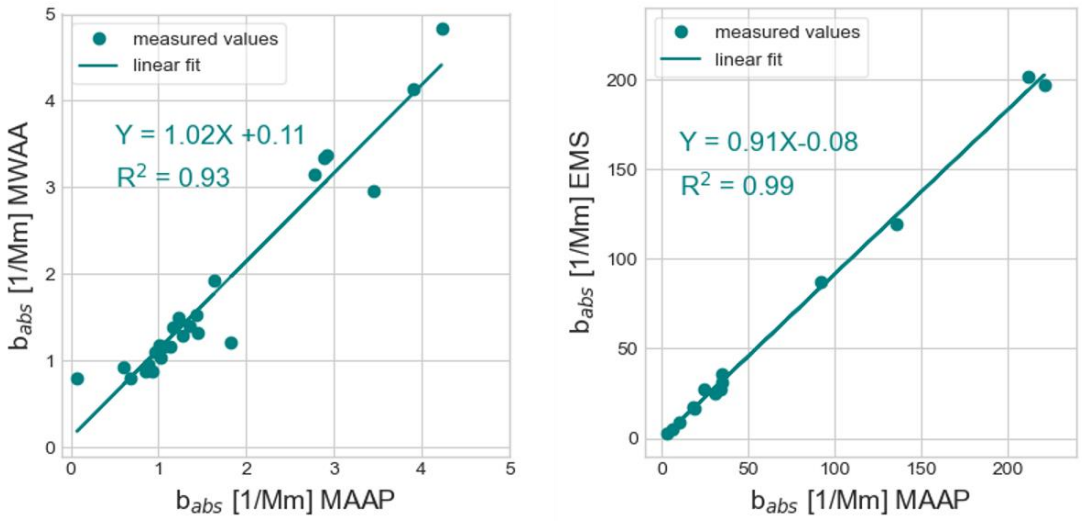

Figure 4-1: Scatterplot of the absorption coefficient measured at 637 nm with the MAAP with those measured with other reference techniques (MWAA at 635 nm and EMS at 630 nm). On the left the MAAP compared with the MWAA during ambient observations at CMN. On the right the MAAP compared with the EMS during chamber experiments.

Since the MWAA was used specifically at the CMN site to study the spectral dependence of C (Section 3.1.2.2), its absorption coefficient was compared with MAAP. As we can see from Figure 4-1, this technique was well correlated linearly with the MAAP (R^2 = 0.93), the intercept of the applied linear fit was low (~0.1 1/Mm) and the slope was 1.02. Generally, we can argue that for Monte Cimone aerosol, the absorption coefficient measured with the MWAA well compared with MAAP, with an overall difference of 2% being well within the accuracy of the MAAP, estimated to be 15% (Petzold et al., 2005; Müller et al., 2011). It must be noted that previous studies reported a much higher discrepancy between the MAAP and the MWAA, which was observed to underestimate absorption coefficient at 637 nm by 16% compared with the MAAP (Saturno et al., 2017). This may partly be due to small differences in the two techniques, input values to the internal radiative transfer model that are assumed in the MAAP are measured by the MWAA instead. Partly in the procedure of collecting the sample on a filter, in the storage and transport

required for the off-line measurement at locations other than the acquisition site required by the MWAA, there may be contamination of the sample.

EMS was used as a reference absorption technique in chamber experiments, where it is subject to lower uncertainties than in the field, and where MAAP showed some limitations due to high BC accumulation rates on the filter as described by Hyvärinen et al. (2013). We used data collected during chamber experiments with propane soot to compare the EMS technique to the MAAP, as shown in the scatterplot of Figure 4-1. Despite the low number of observational points over a much wider range of values, a linear fit well represented the EMS-MAAP relation with a correlation coefficient of $R^2 = 0.99$, a very low intercept (-0.08 1/Mm), and a slope of (0.91). Overall, the low offset and the slight underestimation by the 9% by EMS techniques compared to the MAAP, fell within the MAAP uncertainty (±15%; (Petzold et al., 2005; Müller et al., 2011) and, especially the high variability of errors for EMS-derived absorption (10-100%; Modini et al., 2021)

This comparison is important to show that the results obtained in Section 4.2 and Section 4.3 using EMS and MWAA instead of MAAP as reference technique are non-susceptible to additional source of uncertainties.

4.2 AMBIENT VARIABILITY OF C FACTOR

Here we present the variability of C values in ambient conditions at two different sites, one representative of continental background conditions (JRC) and the second representative of more clean mid-troposphere (CMN). C values were calculated at both sites with two aethalometer models (AE31 and AE33, Magee Sci.) and the MAAP from hourly averaged data.

4.2.1 Site to site variability

The distributions of the site dependent C values for the AE33 (C_{AE33}) are shown in Figure 4-2, while means and standard deviations listed in Table 4-1. C_{AE33} increased from a mean value of 2.3 ± 0.5 (SD) at the mountain site of CMN to a mean value of 3.1 ± 0.4 (SD) at the background site of JRC. Errors resulting from sampling flow uncertainties (7-16%) and signal-to-noise errors (1-10%) might have non-negligible contribution (Cuesta-Mosquera et al., 2021) to the increase of approximately 35% between the C_{AE33} measured at JRC

compared to CMN. Overall, the instrumental error of C_{AE33} was estimated to be 27% by the propagation of the unit-to-unit variability of the MAAP instrument (15%; Muller) and AE33 instrument (23%; Cuesta-Mosquera et al., 2021, estimated from the maximum difference between the considered instruments), being smaller than the range of the site-to-site variability.

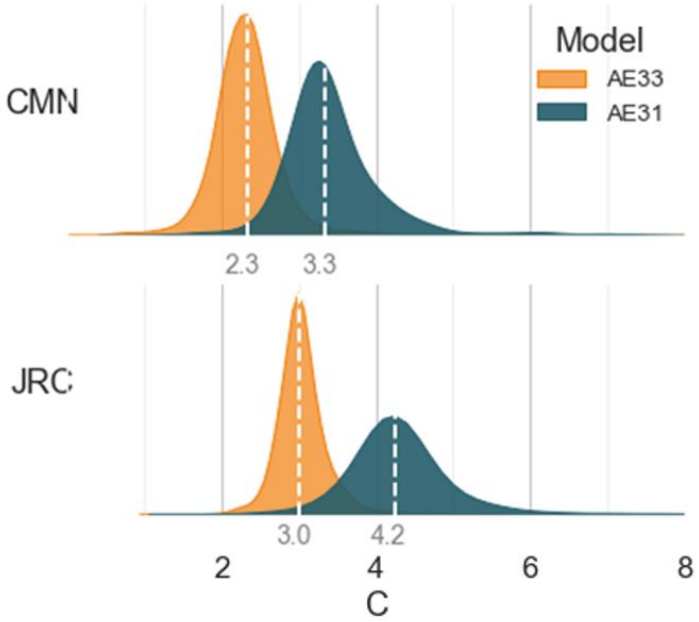

Figure 4-2: Density plots summarizing C at 637 nm variability in all sites (CMN, JRC) for both aethalometer models (AE33 in orange, AE31 in blue). Reference absorption technique: MAAP.

Considering that both CMN and JRC stations comply with the standard operation procedures for aerosol absorption coefficient observation issued by the ACTRIS network, we considered as negligible the errors associated with sampling lines (e.g. tube lengths, air drying systems, particle losses, etc..). Finally, the statistical test t-Student indicated a significant difference ($p << 0.05$) between the CMN and JRC, C_{AE33} values population. Hence, it is fair to consider the C_{AE33} changes shown in Figure 4-2 to be related to the properties of the sampled aerosol rather to instrumental uncertainties. The C_{AE33} calculated at CMN and JRC are in the same range of previous studies (Collaud Coen et al., 2010; Yus-Díez et al., 2021); however, these studies showed different trends between mountain and background sites. While Yus-Díez et al. (2021) showed relatively constant C_{AE33} urban, background and mountain top sites in Spain ($2.44 < C_{AE33} < 2.51$), Collaud Coen et al. (2010) showed a net

increase (+33%) from mountain top in Switzerland to regional background in the Netherlands. It must be noted that here we report only the relative variation since the latter results were obtained at different sites using an AE31. To identify the driving force of C_{AE33}, its variability is investigated in more details.

Table 4-1: Summary of average C values at 637 nm and their standard deviation (SD) in the two sites. Reference absorption instrument: MAAP

SITE	C (637 nm) MEAN (SD)	
	AE31	AE33
CMN	3.2 (0.8)	2.3 (0.5)
JRC	4.1 (1.1)	3.1 (0.4)

Some studies rely the different values at different sites with different mean SSA values, but contrasting results are observed. For example, for the AE31 Collaud Coen et al. (2010), observed higher values in urban sites with lower SSA values compared to mountain sites. Concerning the AE33, Yus-Díez et al. (2021) observed instead a clear relation with the SSA with higher values for mountain than urban background site where 70% and 57% of the data were associated to SSA values higher than 0.9 respectively.

4.2.2 Seasonal variability

The monthly time series of C_{AE33} (Figure 4-3) observed at each site allowed to investigate potential differences of C_{AE33} connected with seasonal variability at both CMN (all seasons) and JRC (winter-spring-summer). At JRC, C_{AE33} remained fundamentally stable from January till May with values raising from approximately 3.0 to a maximum of 3.40 in June.

This summer increase might be correlated with the monotonic decrease of black carbon concentration from winter to summer observed at the site (Zanatta et al., 2016), which might control the type of dominant aerosol at JRC or increase the influence of instrumental noise on the AE33 performance, representing approximately 10% (Cuesta-Mosquera et al., 2021) of summer absorption coefficient at JRC. At CMN it was possible to investigate the full

seasonality of C_{AE33}. Similar to JRC, the C_{AE33} values showed little to no seasonality at CMN with values remaining substantially constant throughout the year, from a minimum of 2.28 in summer, to a maximum of 2.5 in winter.

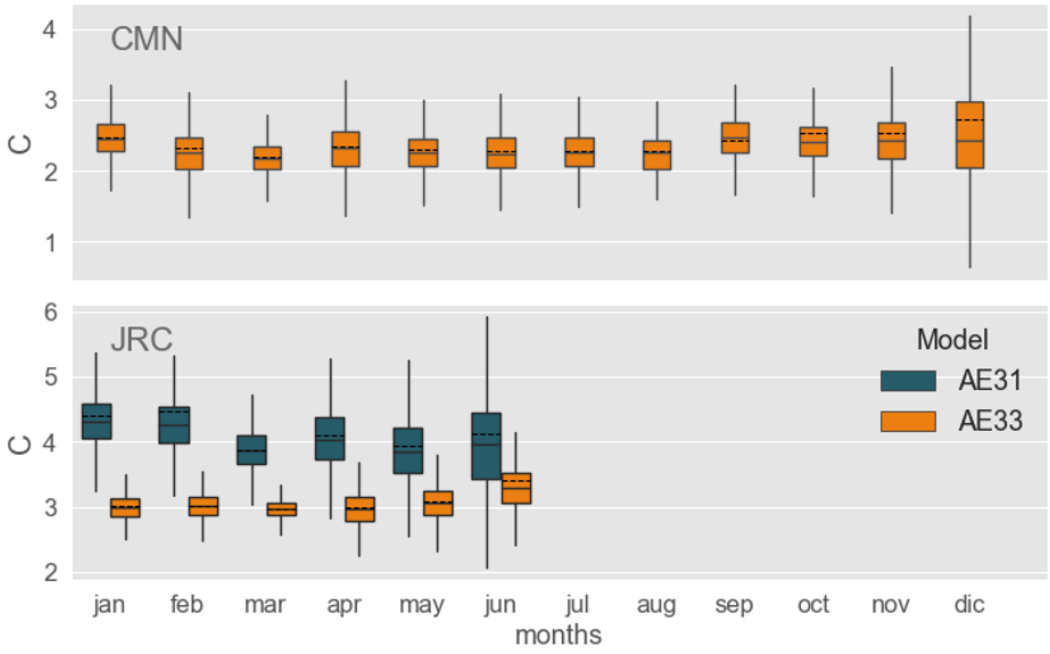

Figure 4-3: Monthly boxplot, describing the seasonal variability of C values at 637 nm at JRC and CMN, for both models of aethalometer (AE31 in blue and AE33 in orange). Reference absorption technique: MAAP.

This slight increase of C_{AE33} is inversely proportional to the concentration of BC at CMN (Marinoni et al., 2008) and consequently absorption coefficient. As in the case of JRC, the slight increase of C_{AE33} in the cleanest month might be attributed to a change in optical and physical properties of the aerosol at both sites but also an increased influence of instrumental noise on the AE33 performances, as shown by (Cuesta-Mosquera et al., 2021). Overall, the seasonal variability at both sites was minimal. Especially compared to other biogenic dominated site of SMEAR II in the Finnish boreal forest, where C value was observed to increase from late winter to summer by approximately 30% (Luoma et al., 2021). Although the factor controlling the seasonality of C factors remains largely unknown, Figure 4-3, clearly shows that the baseline of C_{AE33} is significantly different at the two sites

in any season. Hence the site-to-site variability might be influenced by the completely different properties, such as the single scattering albedo.

4.2.3 Dependence on aerosol optical properties

Pervious works showed that optical properties such as SSA may directly influence the correction factor for the multiple scattering effect (Schmid et al., 2006; Backman et al., 2017; Yus-Díez et al., 2021). In this section the variability of C_{AE33} with the aerosol optical properties is investigated more in details. We compared hourly averaged C_{AE33} values with the corresponding SSA. For this purpose, hourly averaged SSA have been derived at 637 nm using the absorption coefficient measured by the MAAP and the scattering coefficient measured by the nephelometer at both CMN and JRC sites.

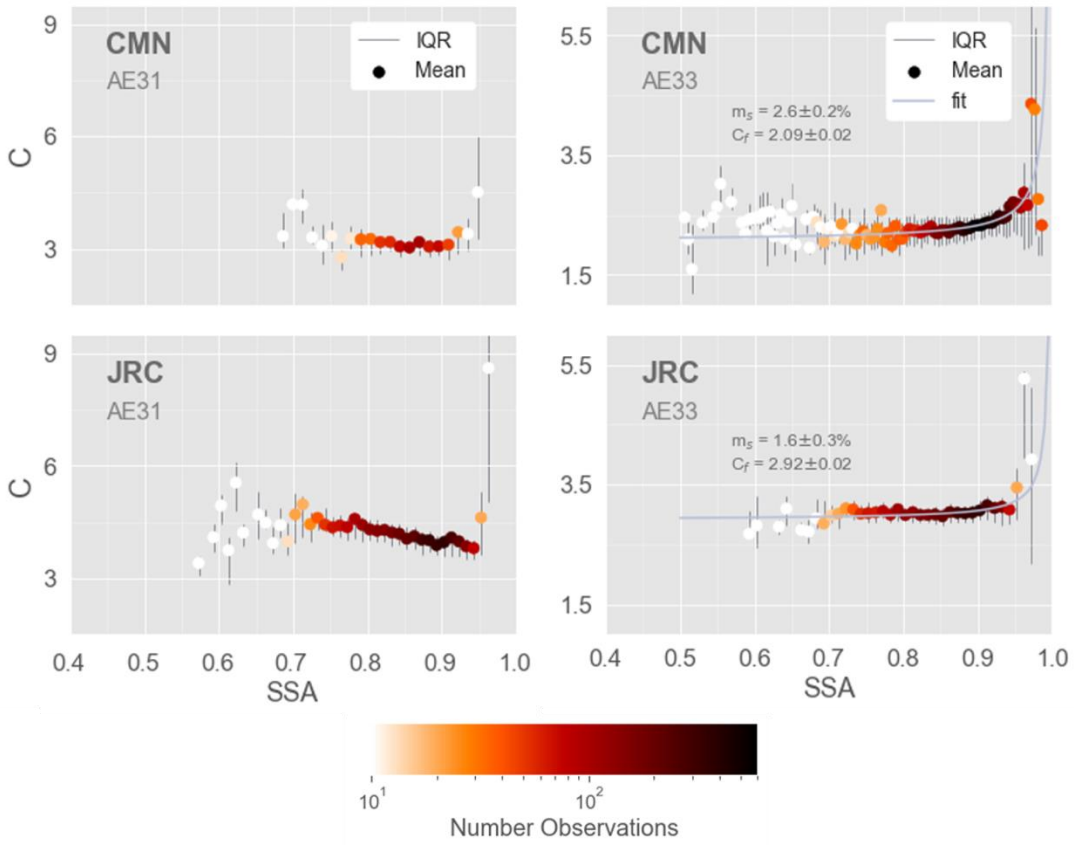

Figure 4-4: C (637 nm) dependence on the SSA (derived at 637 nm combining MAAP and nephelometer) in each site (CMN, JRC) and for both models of aethalometer (AE31 on the left, AE33 on the right). Reference absorption instrument: MAAP. Dots represent the mean values in each SSA bin, the gray lines the 25th and 75th percentile. The dots colors represent the number of observations used in each bin for calculating the mean and the curves are the fitted curves using Yus-Díez et al. (2021) relation.

The C_{AE33} values were then binned to the SSA values, ranging from 0.5 to 0.98. The number of bins was chosen using the 'auto' mode of the numpy histogram_bin_edge function (python). This function selects as best number of bins, the highest value between those obtained with the Freedman and Diaconis, (1981) or the Sturges, (1926) criteria. For each SSA bin, the mean C_{AE33} and the corresponding IQR were derived (Figure 4-4). The mean values derived for the AE33 were then fitted according to the cross sensitivity to scattering law proposed by (Schmid et al., 2006) and used in Yus-Díez et al. (2021), to derive useful parameters to describe and eventually predict this dependence.

For both the CMN and JRC sites, C_{AE33} remains relatively constant up to an SSA of 0.85. It experiences a slight increase in the SSA range of 0.85 to 0.95, particularly at CMN compared to JRC. However, for SSA values higher than 0.95, the SSA-C_{AE33} relationship varied. Both at CMN and JRC an increase was observed but the C values became more scattered in this region. The fitting curve provided by the chosen law aligns with the data up to an SSA equal to 0.95, is more uncertain at higher SSA values where we have few and more scattered observations. Compared to the results obtained in Yus-Díez et al. (2021), these curves are more flat and strongly increase only at higher SSA values, both at the mountain top and the regional background sites. This is probably related to the different data treatment and the lack of measurements at very high SSA values. From these findings, it is essential to thoughtfully choose the right correction factors, especially when applying them to situations with high SSA values. The variations observed in the fitted curves across different sites underscore the potential difficulties and uncertainties linked to deriving accurate corrective factors, particularly for high SSA values where absorption is typically minimal and near the detection limits of the instruments. Further research is necessary to delve into this dependence, utilizing extensive in situ datasets and chamber studies.

4.2.4 Spectral dependence

We assessed the wavelength dependence of the C_{AE33} by comparing the attenuation coefficient measured by the aethalometer with the absorption coefficient measured using the MWAA across all aethalometer wavelengths. This comparison was done in a specific period of one month (September-October 2022) with 43 filters collected at CMN.

The results, shown in Figure 4-5, reveal averaged C_{AE33} values between 2.0 ± 0.5 at 880 nm and 2.3 ± 0.6 at 470 nm. Although the data exhibited high variability with a standard deviation of up to 0.6, there was no significant difference to establish a wavelength dependence of the C_{AE33} factor. Applying a statistical t-Student test to quantify the significance of the difference, we only observed a potentially significant distinction between the 470 nm and 880 nm values (with a p-value = 0.036). The test applied to all other wavelength pairs yields p > 0.05, indicating no evidence of a statistically significant difference. It is important to notice that the overall precision (unit-to-unit variability) of the AE33 is not wavelength dependent (Cuesta-Mosquera et al., 2021); hence, all wavelength dependent C_{AE33} presented in this part of the work fell within the relative error of ± 27% (considering the uncertainty of the MWAA equal to MAAP).

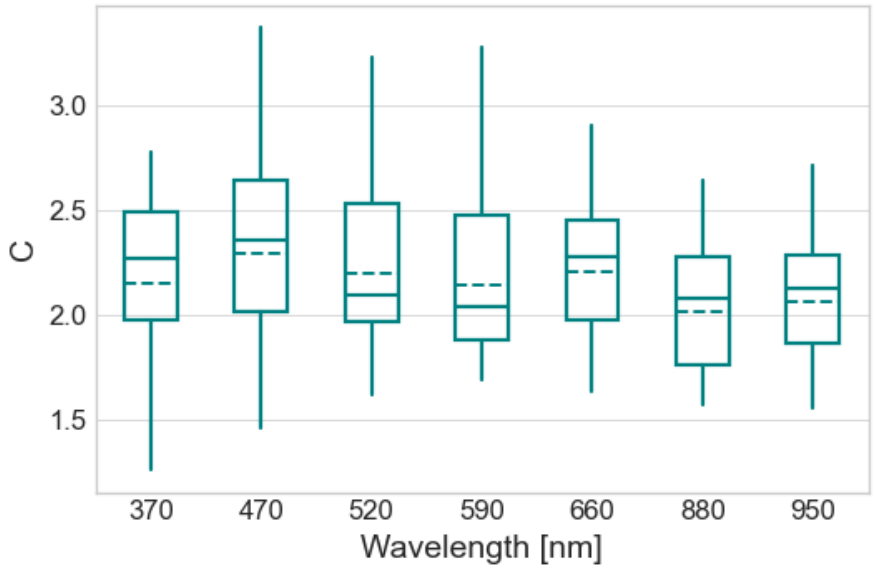

Figure 4-5: C_{AE33} dependence on aethalometer wavelengths for AE33 at CMN. C_{AE33} calculated from AE33 and MWAA measurements.

To date, only a limited number of studies have explored multi-wavelength absorption reference techniques for both models of aethalometer. In the case of the AE31 model, Bernardoni et al. (2021) and Ferrero et al. (2021) did not identify a significant wavelength dependence of the C factor. However, they noted improved agreement in the measured b_{abs} (λ) with AE31 and AE33 when a C(λ) correction was applied to both instruments. For the AE33 model, neither

Bernardoni et al. (2021) and Ferrero et al. (2021) observed a significant wavelength dependence when accounting for uncertainty. In contrast, Moschos et al. (2021) identified a decreasing trend from 2.5 at 370 nm to 2.3 at 880 nm for Swiss background conditions. Additionally, Yus-Díez et al. (2021) reported no significant dependence except in the case of aged aerosol where an increasing C with wavelength is observed with values in the range of 3.47 - 4.03.

4.2.5 Aethalometer model variability

When examining the AE31 model, it becomes apparent that the C_{AE31} were systematically lower than the C_{AE33}. First, the average C_{AE31} was 39% (3.2 $\pm$ 0.8) and 32% (4.1 $\pm$ 1.1) higher than C_{AE33} at CMN and JRC, respectively (Table 4-1). C_{AE31} also showed a wider distribution than C_{AE33} at both sides, with a relative standard deviation of 25-26%. The first contributor to a wide variability might be represented by the high uncertainty characterizing the absorption measurements of the AE31, quantified to be 35% (Zanatta et al., 2016), increasing the overall C_{AE31} uncertainty to 38% compared to 27% of C_{AE33}. Despite the higher uncertainty, the statistical test t-Student indicated a significant difference ($p << 0.05$) between C_{AE31} and C_{AE33} at CMN and JRC. However, this difference was not fund to be constant off-set, but observed a change as function of the season, at least at JRC. Figure 4-3 shows that monthly mean values of C_{AE33} and C_{AE31} did not follow the same trend remaining largely uncorrelated ($R^2 = 0.1$). As matter of fact, C_{AE31} was larger than C_{AE31} by 46-48% in the coldest and most polluted months of January and February, but only by 20% in June. Concerning the C_{AE31}-SSA relationship, it becomes evident that the C_{AE31} factor exhibits a decreasing trend within the range of SSAs from 0.5 to 0.9. This trend is consistent across all sites, with JRC showing a more pronounced effect compared to CMN. However, for SSAs exceeding 0.9 at CMN and 0.95 at JRC, there is a noticeable reversal, and the C_{AE31} factor begins to increase once again. Although a slight reduction in the C_{AE31} factor was observed consistently across all sites within the 0.5 to 0.9 SSA range, the specific starting point and extent of the increase varied among sites. Due to this behavior, C_{AE31} were not fitted to parametrize the cross sensitivity to scattering law proposed by Schmid et al. (2006) and used in Yus-Díez et al. (2021). Our analysis indicates a significant difference in performances between

the two aethalomer models; hence, each model should be corrected with an appropriate and dedicated C value. Past absorption coefficient data that were acquired with the AE31 model should not be corrected with C_{AE33} values and vice-versa. Moreover, C_{AE31} must not be derived from C_{AE33}-SSA parametrizations.

4.3 C DEPENDENCE ON MICROPHYSICAL PROPERTIES OF FRESHLY EMITTED BC IN LABORATORY STUDIES

Ambient observations provide the possibility to investigate the temporal and spatial variability of C values, under the realistic conditions of a varying sources, meteorology and atmospheric ageing. Chamber experiments, despite their shorter duration, allow reducing the number of variable and, in theory, facilitating the understanding of specific physical and chemical processes. The experiments carried out in the CESAM simulation chamber have been designed to study the variability of C_{AE33} as a function of the microphysical properties of BC. In this section, we focus on the measurements made during experiments in which the chamber was filled with freshly generated aerosol with different properties. The aerosol was generated with a mini-CAST burner (Moore et al., 2014) using five different combustion to form five types of cast soot aerosol (CS) with different compositions CS1 - CS5 and decreasing EC/OC as described in Section 3.5 and summarized in Table 3-4.

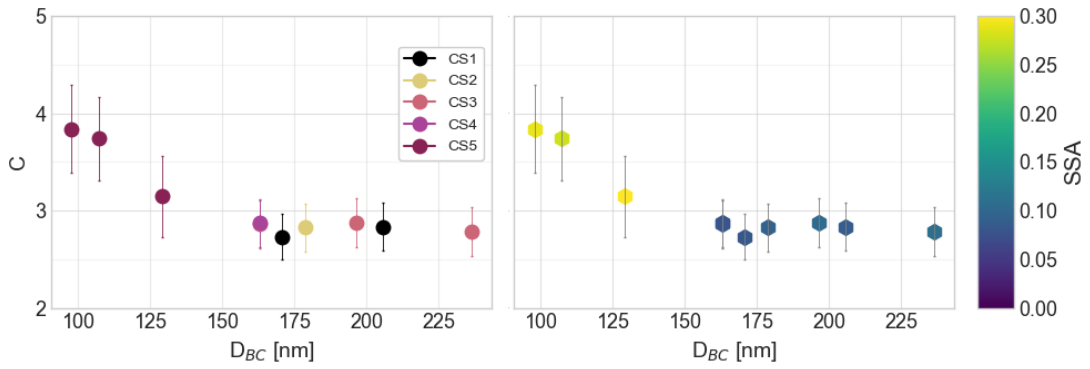

Figure 4-6: C dependence on particle size, in laboratory studies using different freshly emitted particles. On the left this dependence is compared with the BC type emitted (different composition with increasing organic content from CS1 to CS5). On the right it is compared with the optical properties of the particles described by the SSA.

For each experiment done we calculated C_{AE33} values comparing the aethalometer AE33 with the EMS as described in Section 3.5. We calculated the optical properties of the particles in terms of SSA from the ratio between the scattering coefficient measured with the nephelometer and the extinction measured with the CAPS. And evaluated the D_{BC} from the diameter corresponding to the peak of the number size distribution evaluated with the SMPS.

As shown in Figure 4-6, the C_{AE33} factor seems to depend on the microphysical properties of the particles. We obtained similar C_{AE33} values for the type CS1, CS2, CS3, CS4 (ranging from 2.73 to 2.87), and higher values up to 3.84 for CS5. However, it is difficult to constrain the property controlling this change. CS5 is the aerosol type with the lowest diameters (97.7-129 nm). It is possible that very small particles, are able to cause a higher multiple scattering effect by penetrating more deeply into the filter fibres. But CS5 is also the one with the highest organic content and the lowest EC content (almost 0). They are thus able to significantly scatter the radiation, as shown by the higher SSA in Figure 4-6 (right panel), increasing the multiple scattering. However, the relationship between C and SSA is not so obvious, as the experiment with the highest SSA does not have the highest C. The reason for the larger increase in the two smaller diameter experiments is probably a combination of effects related to the size and optical properties of the particles.

The results obtained in the chamber, suggest that the composition and diameter of the particles, which could not be distinguished in ambient measurements, can drastically change the C_{AE33} from 2.9 to 4. this difference, which corresponds to 35%, is very similar to that observed between CMN and JRC in ambient. It is therefore theoretically possible, not proven here, that very fresh, small particles with a high concentration of organic and inorganic components could justify higher values at JRC compared to CMN.

4.4 COMPARISON OF MASS CONCENTRATION MEASUREMENTS

The accurate quantification of black carbon mass concentration is a fundamental step for the quantification of its climatic impacts. As reported by Bond et al. (2013) and Petzold et al. (2013), there is a multitude of different techniques capable of providing BC mass concertation. However, as reported

by several works, the intra-technique precision (rBC/rBC, Laborde et al., 2012; EC/EC, Cavalli et al., 2016) and inter-technique precision (rBC/EC, Pileci et al., 2021; eBC/EC, Liu et al., 2022) of these techniques is subject to a high degree of variability. In this section we compared the mass concentration measurements of BC made with independent techniques during the measurement campaign in Barcelona in July 2021, as described in Section 3.3. High temporal resolution SP2 measurements of refractory BC mass concentration (m_{rBC}) were averaged over elemental carbon mass concentration (m_{EC}) measurements taken over three hour periods. As can be seen both from the time series and from the scatter plot in Figure 4-7, the two independent techniques produced highly correlated results (R^2 = 0.92) at both moderate (m_{EC} < 0.5 µg m^{-3}) and high (m_{EC} > 0.5 µg m^{-3}) concentrations. The high correlation indicated the establishment of a liner proportionality between m_{EC} and m_{rBC} and confirmed that both techniques quantified the same refractory and absorbing aerosol as found by Pileci et al. (2021), although with a different sensitivity. In fact, there was a considerable difference in the absolute rBC and EC mass concentration.

The average m_{rBC} was 0.5 µg/m^3 with a standard deviation of 0.3 µg/m^3 and affected by an instrumental uncertainty of ± 10% (Laborde et al., 2012b). Lower values were observed for m_{EC} (mean = 0.3 µg/m^3 and sd = 0.2 µg/m^3), which are associated with an overall uncertainty of ± 24% (Cavalli et al., 2016). Hence m_{EC} and m_{rBC} did not fell within the instrumental uncertainty range. As we can see from the slope of the linear fit in Figure 4-7, the SP2 overestimated m_{EC} by a factor of 1.75. Table 4-2 summarizes the results for each technique. The resulting ratio (m_{rBC}/m_{EC}) between the two measurements is on average 1.7 with a standard deviation of 0.3 and a median of 1.6. Other studies previously compared EC and rBC mass concentrations. Miyakawa et al. (2016) found high correlation and close agreement (within 7%) in ambient aerosols at an urban location. In contrast, Sharma et al. (2017) reported a factor of 3.1 in the Arctic, attributing the bias to filter loadings near the limit of quantification and charring bias causing EC mass overestimation. Finally, Pileci et al. (2021) analysed ambient measurements across several European sites, concluding that systematic discrepancies up to 50% were often linked to the BC source.

Table 4-2: Averaged m_{rBC} and m_{EC}, mean ratio m_{rBC}/m_{EC}, measured by the SP2, and the semi-continuous Sunset in Barcelona during the campaign in July 2021.

Mean (sd) m_{rBC} non corrected [µg/m³]	Mean (sd) m_{rBC} corrected [µg/m³]	Mean (sd) m_{EC} [µg/m³]	Mean (sd) Ratio m_{rBC}/m_{EC} [µg/m³]
0.4 (0.3)	0.5 (0.3)	0.3 (0.2)	1.7 (0.3)

Although it is difficult to differentiate between the factors controlling the performances of both techniques, hereafter we provide some potential explanations. Differences in the upper cut-off diameter for EC and rBC mass measurements are a potential source of discrepancy. In this work, EC measurements were performed with a cut-off of 2.5 µm, the rBC measurements have the highest detection limit around 500 nm and were corrected by extending the diameter range from 10 to 1000 nm (Section 2.2.3.4). If this were the main source of bias, we would observe higher values for EC than for rBC, for missing mass in the range between 1 and 2.5 µm.

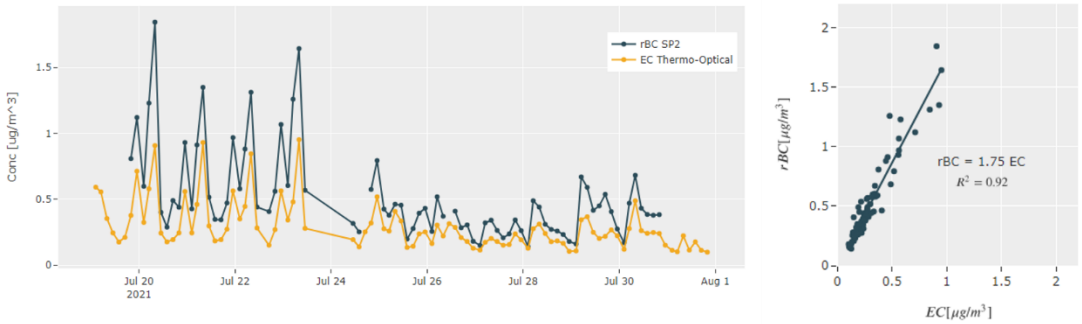

Figure 4-7: Comparison of rBC and EC mass concentration measurements done in the field campaign in Barcelona in July 2021. On the left the two time-series averaged over three hours, on the right the resulting scatterplot with the estimated slope.

Instead we observe higher values for the rBC. Another potential source of bias is an overestimated missing mass correction for rBC. The uncorrected values are lower than the corrected values, but still higher than the EC. Furthermore, there is no correlation between the values of the applied correction and the ratio. Issues with the thermal-optical techniques may introduce other uncertainties into this comparison. Underestimation of EC may occur in the separation of EC and OC components, influenced by factors such as filter

overloading with EC. This interference reduces the detection of pyrolytic carbon, resulting in a systematic low bias in the EC concentration. In addition, poor separation performance may occur due to low TC surface loading and low EC to TC mass ratios.

Our results show a difference more pronounced than some of the previous results with a percentage difference up to 70 %. This combined with the variability already shown in the absorption coefficient leads to very high uncertainties in the quantification of the MAC. Challenges include the lack of a traceable reference method, uncertainties in both techniques, and potential cross-correlations among various aerosol and BC properties.

4.5 IMPACT OF METROLOGY LIMITS ON EVALUATION OF BC OPTICAL PROPERTIES

In this section we underline with a specific example how important is the instrumental validation presented above to quantify the direct radiative forcing of BC. As described in the introduction, the key parameter used in models to estimate the radiative forcing of BC is the MAC. It is derived from the ratio between the absorption coefficient b_{abs}, often measured using the aethalometer corrected as described above, and the mass concentration that is derived in literature both with the SP2 (m_{rBC}) and the Sunset (m_{EC}) method. Taking the measurements in Barcelona as an example, we estimated the potential variability of MAC that can be derived from the same measurements by using different C values for correcting the aethalometer and adjusting the m_{rBC} to the m_{EC} with different factors.

In particular, we explored a set of different situations. In the first one (EX1- ACTRIS best; Table 4-3) we used the harmonization factor suggested by the ACTRIS network to correct the AE33 resulting in a C = 2.45, and the mean value found in Pileci et al. (2021) to adjust the m_{rBC} to the m_{EC} (0.92). This example is representative of what could be done when no reference technique is available for the absorption and no comparison EC-rBC can be done. EX2 (Literature absorption uncertainty; Table 4-3) represents the maximum variation possible due to rBC-EC factor variability. The C used is the one from ACTRIS, the rBC-EC ratio the highest and lowest (0.53-1.29) found in Pileci et al. (2021). EX3 (Literature absorption uncertainty; Table 4-3), we used the

highest and lowest C values (2.23-3.43) found in literature (Valentini et al., 2020; Ferrero et al., 2021; Bernardoni et al., 2021; Yus-Díez et al., 2021), and the mean rBC-EC ratio value (0.92; Pileci et al., 2021). The EX4 (EX4-This study in-situ; Table 4-3) was derived for the opposite situation, so when it is possible to compare both. The C value of 2.44 was derived by Yus-Díez et al. (2021) during the Barcelona campaign, while the rBC-EC factor (1.75) was value obtained in this work.

Table 4-3: Averaged mass absorption cross-section at 660 nm, measured in Barcelona by changing corrections applied to the aethalometer and the SP2. Evaluation of variability that results from C obtained in this study.

	EX1-Best ACTRIS	**EX2-Literature Mass uncertainty**		**EX3-Literature absorption uncertainty**		**EX4-This study In-situ uncertainty**	**EX5-This study Po-Valley uncertainty**	
C	2.45	2.45		2.23	3.43	2.44	2.3	3.1
m_{rBC}/m_{EC} ratio	0.92	0.53	1.29	0.92		1.75	0.92	
MAC [m^2/g]	8.97	5.2	12.85	9.86	6.4	17.13		
MAC difference from Best ACTRIS	0%	-42%	43%	10%	-29%	91%	-6%	27%

By using the correction factors of EX1, we obtain a "reference" MAC of 8.97 m^2/g (Table 4-3). As we can see in Table 4-3, changing the chosen parameters the MAC at 660 nm may increase from a minimum value of 5.2 m^2/g to a maximum of 17.13 m^2/g. The most pronounced fluctuations are observed due to different m_{rBC}/m_{EC} ratio found in literature and in this work, leading to fluctuation of ± 40% with respect to EX1. The variability of literature C values introduced a smaller bias, quantified to vary from -29% to +10% compared to EX1. These examples might be, however, not suitable or representative of specific ambient or sampling conditions. As a matter of fact, the use of in-situ specific correction factors leads to an overall estimation of +91% with respect with EU-reference. In the case of Po-Valley, the C correction at CMN would be in line with the EU-standard (-6%). However, in the Po-Valley background station of JRC, the C value would lead to an overestimation of absorption and MAC by 27% with respect to the EU-reference.

These results underline that instrumental inaccuracies and uncertainties have a direct impact on the ability of comparing daily, seasonal and multi-year trends across a monitoring network, potentially impacting the interpretation of BC phenomenology. It must be reminded that this degree of uncertainty is directly propagated to the products of global models and satellites, which are validated against the open-access database of monitoring networks.

5 RESULTS: ANTHROPOGENIC IMPACT ON URBAN SCALE

Research on BC in urban areas has attracted particular interest because of its potential role as a tracer of anthropogenic pollutants with adverse health effects. Although epidemiological studies have not found a clear association between BC and adverse health effects, there is evidence that the presence of other compounds condensed on these particles causes BC to lead to health problems when inhaled (WHO, 2021; Janssen et al., 2012). To date, there are no guidelines for the use of eBC in air quality regulations, but it is recognised that it would be a better tracer of combustion emissions rich in health-damaging compounds. Their monitoring and source identification can therefore provide important data for improved policies to reduce urban air pollution.

Characterising the properties of BC in urban environments, close to sources, is also crucial for climate models. By measuring the size distribution, size-resolved coating thickness and MAC in urban areas, it is possible to define their range of variability shortly after emission. This information, in turn, can be used to more accurately model and determine the evolution of BC properties (e.g. MAC) at a distance from the sources after long ageing. As shown in several works (e.g. Matsui, 2016, Matsui et al., 2018), all this information is crucial for a better estimation of the radiative effect of BC.

This chapter presents a study on black carbon in the urban environment. In the first part, its concentration and percentage contribution to submicron particulate matter are studied, as well as the contribution of its main sources at two sites, Milan and Bologna, in one of the most polluted areas in Europe, the Po Valley. A presentation of the measurement campaign and the methods used are summarised in Section 0. The second part analyses BC microphysical properties in two different urban environments, characterised by very different sources, air quality regulations and meteorological conditions. One is Barcelona in Europe and the other two are La Paz and El Alto in the Bolivian Andes in South America. Details about methods applied during the two campaigns are provided in Section 3.4.

5.1 BC AND ITS SOURCES VARIABILITY IN THE PO VALLEY

In this section, we present an analysis of the chemical composition of atmospheric particulate matter in the submicron fraction (PM1), focusing on the contribution of BC to total PM1 and the influence of liquid fuel combustion and solid fuel combustion on the resulting BClf and BCsf concentration. We will do this for the two urban measurement sites located in the Po Valley, Bologna and Milan in 2023. The contribution of BC to PM1 was calculated as the ratio of eBC over PM1. The latter was estimated in a simplified manner as the sum of the non-refractory component (NR-PM1) and the eBC concentration. The two eBC components were identified with the aethalometer source apportionment model described in Section 2.2.1.1, then applied at the two sites as described in Section 3.2.1.2 and 3.2.2.2.

5.1.1 BC contribution to PM1 mass concentration

The average values for NR-PM1 and eBC measured in Milan are 6.3 ± 6.2 μg/m³ and 0.9 ± 0.9 μg/m³ respectively over the year 2023. In Bologna we found an average and standard deviation NR-PM1 of 9.0 ± 8.0 μg/m³ and an eBC of 1.2 ± 0.9 μg/m³ for the same year. We obtained higher values in Bologna than in Milan. This is related to the characteristics of the site in Milan located in a parking inside a group of building in a traffic-controlled area of the city center, while Bologna site is directly exposed to heavy urban and highway traffic without building obstructions.

The two cities were characterized by a very similar average chemical composition. The percentage contribution of each compound to the total mass is shown in the pie charts in Figure 5-1. The organic material dominated the chemical composition at both sites with a value of 42%. This fraction contained both secondary and primary aerosols, produced by a variety of sources such as fossil fuel combustion (e.g. vehicular traffic, energy related activities), biomass combustion (burning of wood for domestic heating) or food cooking practices and many other different secondary formation processes (Hallquist et al., 2009; Via et al., 2021). At both sites, the most abundant component after organic aerosol is nitrate accounting for 24.8% and 23.2% of PM1 in Milan and Bologna respectively. This is followed by sulphates and ammonium with similar percentages of around 10-11%, BC with 11-12% and a negligible amount of

chloride (below 1%). These results are consistent with other previous studies conducted in Europe (Putaud et al., 2010) and Po Valley (Gilardoni et al., 2014; Paglione et al., 2020) and highlight the non-negligible presence of BC as a significant component of particulate matter in urban environments comparable to sulphate and ammonium.

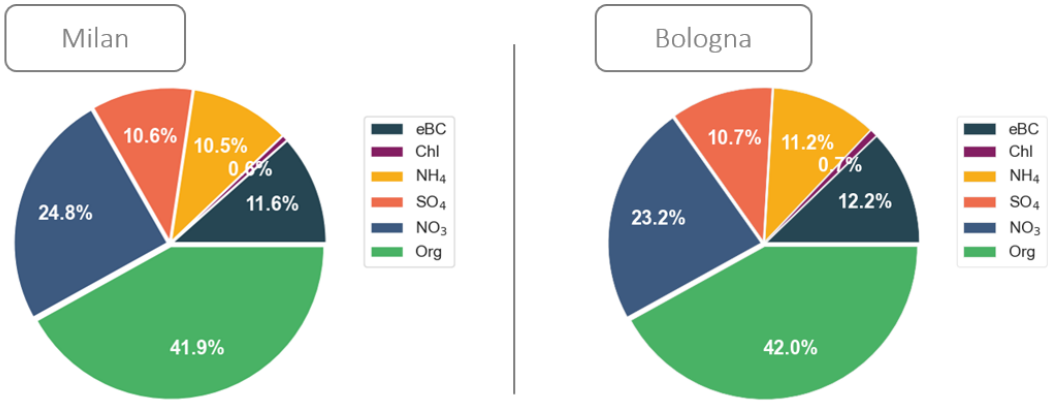

Figure 5-1: Fractional chemical composition of PM1 for two main cities in the Po Valley, Milan and Bologna, accounting for equivalent black carbon (eBC), Chlorine (Cl), ammonium (NH4), sulphate (SO4), Nitrate (NO3), organic matter (Org).

5.1.2 Contribution of liquid and solid fuel emissions to BC concentration

The total eBC mass concentration was subdivided into its main components, BClf from liquid fuel emissions (mainly traffic in the urban environment) and BCsf from solid fuel emissions (mainly related to biomass burning in particular from residential heating systems in the urban environment). BClf accounted for 58.7% and 63.2% of eBC mass in Milan and Bologna, respectively; with a minor but not negligible contribution of solid fuel combustion. These data indicate that BC from liquid fuel emissions dominates and traffic is the main source of BC in urban environments in the Po Valley.

This result is in line with what was observed in Savadkoohi et al. (2023), where the same method, but with different Ångström exponents (1.0 for AAElf and 2.0 for AAEsf), was applied to several European sites. Traffic was found to be the largest contributor in all of them. However, the percentage contribution of solid and liquid fuels is slightly different. The results of this work show a

higher contribution from solid fuels and appear more similar to suburban sites (BCsf account for 30-40%) than to urban sites (BCsf account for less than 30%), where less traffic and more potential sources of biomass burning are expected. We applied the same absorption Ångström exponents for the source apportionment at the Bologna and Milan dataset. This choice is supported by the similar chemical composition of PM1 at both sites. Although it must be considered that the choice of Ångström exponents may affect the source apportionment method (Zotter et al., 2017), we proceeded further to investigate the temporal variability of source influence at both sites on diurnal and seasonal scale.

5.1.2.1 *Diurnal variability*

We applied the source apportionment method with a diurnal resolution to investigate the hourly influence of liquid and solid burning on the BC concentrations at Milan and Bologna. The study of the diurnal variability suggested that the applied model is capable of splitting the two contributions fairly well. This variability is shown for both the Milan and Bologna sites in Figure 5-2. Both sites presented very similar pattern for both components, similar also to those reported in other studies (Mousavi et al., 2019; Paglione et al., 2020), in which a similar study was conducted in Milan and a source apportionment model based on AMS data was applied in Bologna to derive contribution and variability of traffic and biomass related compounds. BClf exhibited a diurnal pattern marked by two peaks during rush hours, specifically between 7–9 AM and 8–10 PM, aligning with peak vehicular traffic, confirming the efficient identification of liquid fuel combustion.

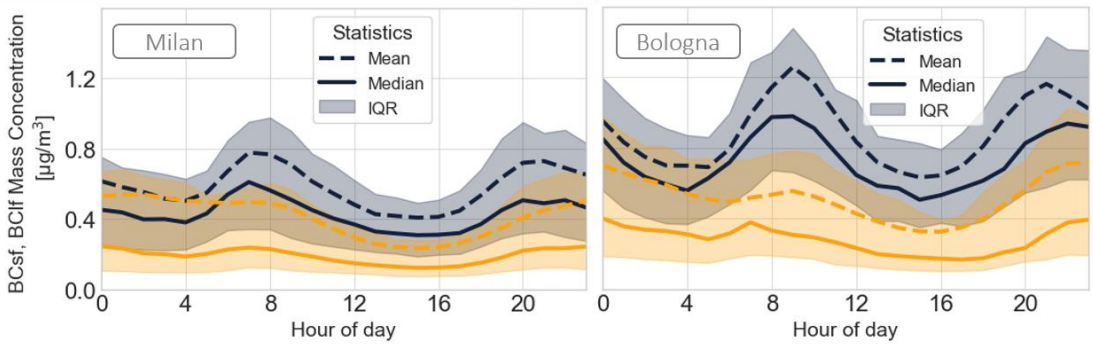

Figure 5-2: Diurnal variability of BClf and BCsf components in Milan and Bologna.

On the other hand, BCsf follows a daily cycle with a pronounced maximum during the night and a secondary peak in coincidence of traffic emissions. These patterns are however, not only influenced by a change in emission fluxes during the day, but also by atmospheric dilution controlled by the boundary layer reaching its maximum in the early afternoon. Hence, the minimum of absolute eBC and both of its components reached between 12:00 and 16:00 is mostly due to dilution. Otherwise, during night, a shallow boundary layer promotes pollutant accumulation near the ground at night, and the daily emission pattern from domestic heating (BCsf), which rises during the evening and night hours.

5.1.2.2 ***Seasonal variability***

Black carbon concentration in polluted continental regions undergo a strong seasonal variability, with higher concentration in winter compared to summer (Savadkoohi et al., 2023). Total eBC concentration was lower in summer-spring compared to winter-autumn, with an eBC mass concentration increase in winter compared to summer by a factor 1.8 in Bologna and 2.2 in Milan.

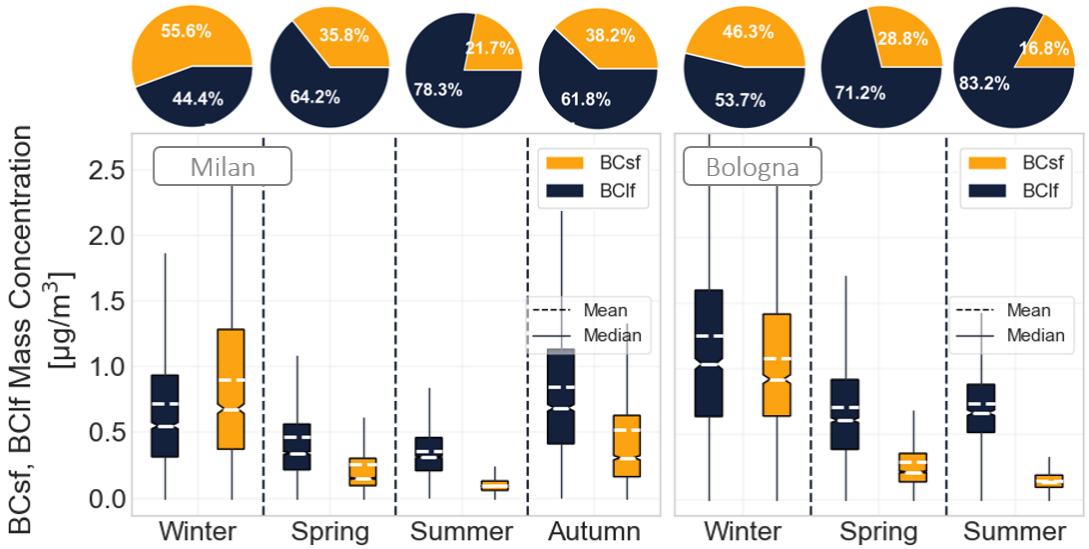

Figure 5-3: Boxplot representing the seasonal variability of two BC components, BCsf and BClf, in the two sites of Milan and Bologna.

This variation reflects the combination of a change in activities-sources, and the meteorological effect due to higher mixing layer usually observed in warmer periods, that enhance the dilution of pollutants locally emitted. The source apportionment model of the aethalometer was used in this work to verify the absolute and relative strength of biomass burning (BCsf) and fossil (BClf) fuels burning during various seasons at Milan and Bologna. Figure 5-3 and Table 5-1 summarizes the seasonal variability of both components in the two sites.

Table 5-1: Average and standard deviation values of BC components, BCsf and BClf, in different seasons in Milan and Bologna.

	MI		**BO**	
	BCsf [µg/m³] Avg. (SD)	BClf [µg/m³] Avg. (SD)	BCsf [µg/m³] Avg. (SD)	BClf [µg/m³] Avg. (SD)
Winter	0.9 (0.7)	0.7 (0.6)	1.1 (0.7)	1.3 (0.9)
Spring	0.3 (0.3)	0.5 (0.4)	0.3 (0.2)	0.7 (0.5)
Summer	0.1 (0.06)	0.4 (0.2)	0.15 (0.08)	0.7 (0.3)
Autumn	0.5 (0.6)	0.9 (0.6)		

BClf and BCsf have a very different variability. BClf decrease by a factor of 1.8 and 1.9 in Milan and Bologna respectively, following a decrease in work and school-university activities nearby the two sites. BCsf decrease instead by a much bigger factor of 7.3 and 9 in Bologna and Milan respectively. The observed decrease in this component is attributed to the complete loss of the primary source, i.e. heating systems in summer. With the elimination of this source, the remaining contributors may include outdoor cooking activities, which are more common in summer, and activities related to the disposal of agricultural waste by combustion.

Overall, this study shows how two different and distant urban cities, both being located within the Po Valley, display a very similar average aerosol composition. The black carbon component, while not dominant, is nonetheless significant with a contribution equal to inorganic components such as

sulphates and ammonium. The BC present is predominantly associated with urban traffic throughout most of the year, a source matched if not exceeded by biomass burning (mainly due to domestic heating) only in winter and especially during the night.

5.2 VARIABILITY OF MICROPHYSICAL PROPERTIES IN URBAN ENVIRONMENTS

In this section we explore the complex variability of rBC microphysical properties in urban environments that were found to be mainly affected by traffic sources and thus liquid fuel emissions. In particular, we use here results obtained in two campaigns in very different environments: a European metropolitan region on the Mediterranean Sea, the city of Barcelona, and two urban sites in the Bolivian Andes (La Paz and El Alto).

5.2.1 Barcelona

Barcelona is a European metropolitan city located on the Mediterranean Sea, characterized by local/regional recirculation patterns and sea breezes in summer associated with low rainfall. PM concentration at this location are mainly influenced by numerous local sources, regional recirculation patterns and dust outbreaks from North Africa (Ealo et al., 2016), but also by secondary aerosol particles which formation is promoted by low precipitation and high solar radiation (Rodríguez et al., 2002; Pérez et al., 2010; Querol et al., 2017).

5.2.1.1 *General characterization of BC in Barcelona*

During the intensive campaign conducted in BCN from 19 July to 31 July 2021, a mean m_{rBC} of 0.5 µg/m³ was observed, with a standard deviation of 0.4 µg/m³. This result lies in the range of m_{eBC} observations in Europe during summer (Savadkoohi et al., 2023), and is also comparable with the values of m_{eBC} (0.5-0.85 µg/m³) measured in summer in the Po valley, presented in the previous section. Nonetheless, eBC concentrations (from a MAAP instrument) are reported to increase towards autumn by one order of magnitude in BCN (3.6 µg/m³, Pérez et al., 2010). Concerning the rBC mass size distribution (Figure 5-4), the mass median diameter (MMD) obtained from the lognormal fit to the median distribution was 102 nm. This value is very close to traffic observations in other European cities such as Paris, London and Zurich (Laborde et al., 2013;

Liu et al., 2014; Motos et al., 2019). Hence our rBC appeared to have a typical small diameter of freshly emitted from traffic sources, compared to larger rBC emitted by ship-traffic (D_{rBC} ~ 500 nm; Zanatta et al., 2020) or biomass burning (D_{rBC} ~ 200 nm; Schwarz et al., 2006) or being aged on continental scale (D_{rBC} ~ 190-240 nm; Yuan et al., 2021).

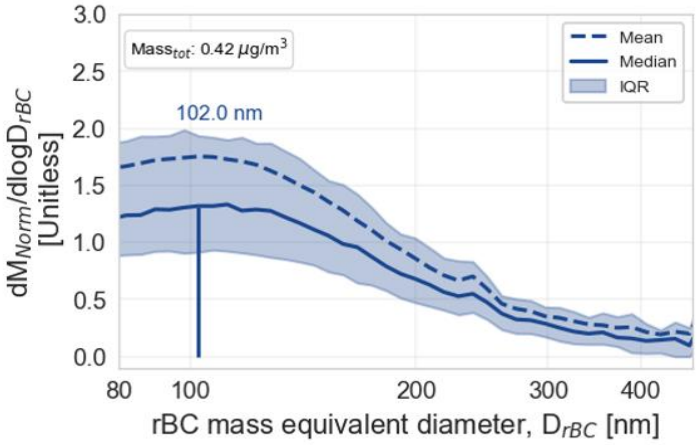

Figure 5-4: Average mass size distribution observed in BCN.

The procedure to derive the coating thickness, described in Section 2.2.3.3, was applied to all detected particles (D_{rBC} range of 80-500 nm; Figure 5-5) similar to Motos et al. (2019). However, we will describe only the results for the diameter range between 180 nm and 220 nm, where the coating thickness is expected not to be affected by the biases discussed in Section 2.2.3.4. Figure 5-5 shows the density plot of coating thickness in the chosen range of rBC cores (180 and 220 nm).

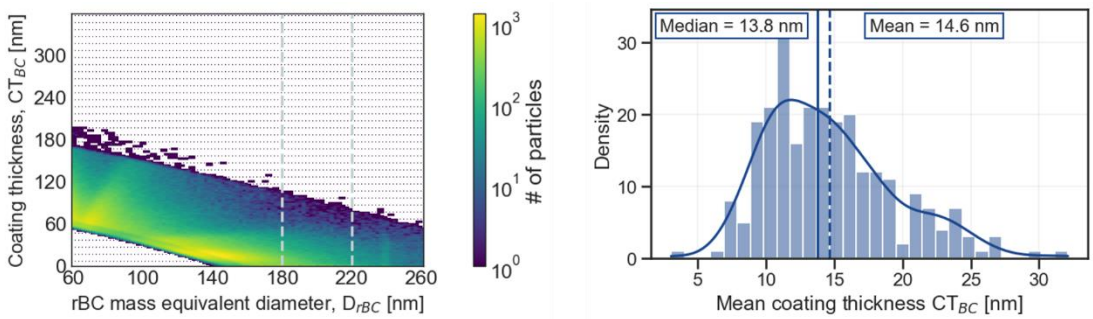

Figure 5-5: Coating thickness CT_{rBC} variability in BCN. On the left the variability of particle number with both coating thickness and rBC core diameter. On the right the density plot of hourly averaged coating thickness values only in the rBC core diameter range between 180 and 220 nm.

We observed a mean coating thickness of 15 nm and a standard deviation of 5 nm, with minimum and maximum values ranging from 0 nm to 30 nm, respectively. These values are relatively low, indicating a majority of predominantly fresh or poorly aged particles at this site, as expected for urban sites (Laborde et al., 2013; Ahlberg et al., 2023), where suspension time is too short to promote the formation of thick coatings (Matsui, 2016). It is important to notice that the thickness distribution shown in Figure 5-5 did not peak at 0, as observed in previous studies (e.g. Laborde et al., 2013), indicating that the majority of the rBC cores presented a non-null coating. Hence, coating formation might represent an important sink for volatile precursors in the city of BCN, where photo chemically induced nucleation particles make only a small contribution to the total particle number concentration (Dall'Osto et al., 2012).

5.2.1.2 *Diurnal cycle of rBC properties*

BCN temperatures undergo a daily increase with a maximum at mid-day, in coincidence with the maximum vertical extent of the surface mixing layer (Pérez et al., 2010; Pandolfi et al., 2013).

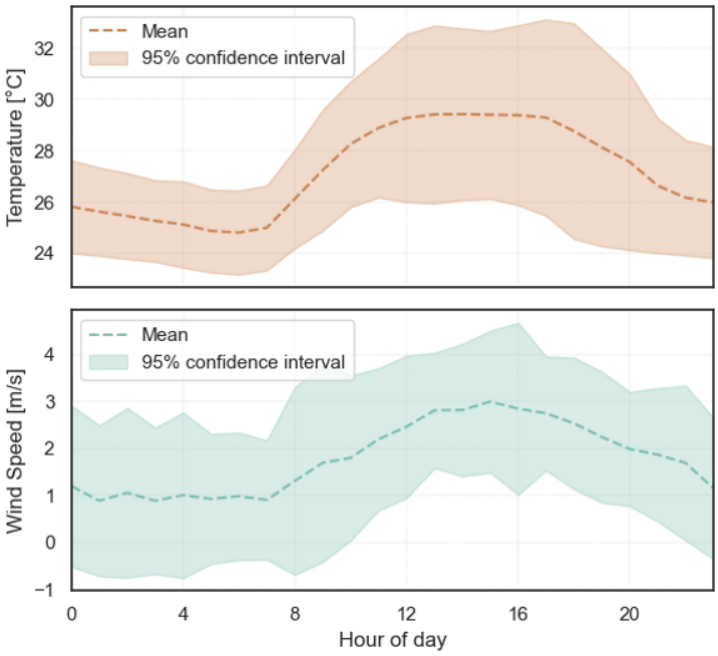

Figure 5-6: Diurnal variability of temperature and wind speed of the campaign conducted in BCN.

During the present summer study, atmospheric temperature reached its daily maximum between 12:00 and 16:00 (Figure 5-6), being approximately 10-12°C higher than autumn (Pandolfi et al., 2013). We can thus argue that the maximum dilution observed in BCN in summer 2021 occurred between 12:00 and 16:00, being potentially more intense than in the autumn season.

	Sun	Mon	Tue	Wed	Thu	Fri	Sat
12:00 AM	29 min	27 min 40 s	28 min 40 s	29 min	29 min 20 s	29 min 40 s	29 min
	30 min	29 min	30 min 20 s	31 min 20 s	31 min 40 s	31 min 20 s	30 min
02:00 AM	31 min 40 s	31 min 20 s	32 min 20 s	33 min	33 min 20 s	33 min 40 s	32 min 40 s
	31 min 20 s	30 min 20 s	31 min	31 min	31 min 20 s	32 min 40 s	32 min 40 s
04:00 AM	28 min	24 min 20 s	24 min 40 s	24 min 40 s	25 min	26 min 20 s	28 min 20 s
	25 min 40 s	22 min	21 min 20 s	21 min 40 s	22 min	22 min 40 s	24 min 40 s
06:00 AM	25 min 40 s	23 min 40 s	24 min	24 min	24 min	23 min 40 s	24 min 20 s
	23 min 40 s	33 min	34 min	33 min 40 s	33 min	31 min	23 min 40 s
08:00 AM	23 min 20 s	36 min 20 s	38 min 20 s	37 min 40 s	37 min 20 s	33 min 20 s	24 min
	24 min	33 min	35 min 20 s	34 min 40 s	34 min 40 s	30 min 40 s	25 min 20 s
10:00 AM	25 min 20 s	30 min	31 min 40 s	31 min 40 s	31 min 40 s	30 min	27 min
	26 min 20 s	30 min 40 s	31 min 20 s	31 min 40 s	31 min 40 s	31 min 20 s	28 min 40 s
12:00 PM	27 min	31 min	32 min	32 min	32 min 20 s	32 min	29 min 40 s
	28 min	30 min 40 s	31 min 20 s	32 min	32 min 20 s	32 min 40 s	30 min 20 s
02:00 PM	27 min 20 s	30 min 20 s	31 min	31 min 40 s	32 min	36 min	29 min
	26 min 40 s	30 min 40 s	31 min 40 s	32 min	32 min 20 s	36 min 40 s	27 min 40 s
04:00 PM	26 min 40 s	31 min	32 min 20 s	32 min 40 s	33 min	34 min 40 s	27 min 40 s
	27 min	33 min 40 s	35 min 20 s	35 min 40 s	36 min 40 s	36 min 40 s	28 min 40 s
06:00 PM	28 min 20 s	35 min	37 min	37 min 40 s	38 min 40 s	35 min	30 min 40 s
	29 min 40 s	32 min	33 min 40 s	34 min 40 s	35 min 40 s	32 min 40 s	31 min 40 s
08:00 PM	29 min 20 s	30 min	30 min 40 s	31 min 20 s	32 min	32 min	31 min 40 s
	27 min 40 s	28 min 20 s	28 min 40 s	29 min	29 min 40 s	30 min 40 s	30 min 40 s
10:00 PM	27 min 20 s	27 min 40 s	28 min	28 min 20 s	28 min 40 s	29 min 20 s	29 min 40 s
	27 min 40 s	28 min	28 min 20 s	29 min	29 min 20 s	28 min 40 s	29 min

Figure 5-7: Time required for travel 20 km in the metropolitan region of BCN, during different hours of the day and different days of the week. This refers to the year 2022 (Barcelona traffic report | TomTom Traffic Index, 2024).

The increase of wind speed in the afternoon similar to what previously reported for the city of BCN in autumn (Pérez et al., 2010), was followed by a minimum during the nighttime (00:00-04:00). Wind speed controls ventilation and thus dilution of atmospheric pollutants. Hence its daily cycle might efficiently affect

the concentration of BC in urban coastal environments (Pérez et al., 2010). Considering the influence of atmospheric dynamic on urban pollution as function of daytime, hereafter we discuss the black carbon properties according the daily cycle. The diurnal variability of rBC mass concentration is presented in Figure 5-8. Located in a predominantly residential area, the main source of black carbon (BC) at this site was road traffic as reported by previous studies (Pandolfi et al., 2016; Via et al., 2023).

The diurnal variability observed was therefore largely influenced by a combination of daily traffic variations, and boundary layer and wind variability. The Figure 5-7 shows that the peak traffic hours in this metropolitan region are 7 a.m. and 6 p.m., with a decrease in the central part of the day. The rush hour easily explain the m_{rBC} peaking in the morning up to the mean value of 1.03 µg/m^3 (Figure 5-8), when the dilution driven by the boundary layer (temperature proxy) and wind speed was at its daily minimum (Figure 5-8). However, a second daily peak of m_{rBC} was not observed in the late afternoon, as reported otherwise for eBC in autumn for Barcelona (Pérez et al., 2010). The increase dilution due to temperature above 30°C and maximum wind speed (2.5 m/s) might be responsible for the absence of a second peak in the afternoon in the correspondence of the second rush hour of the day (Figure 5-7).

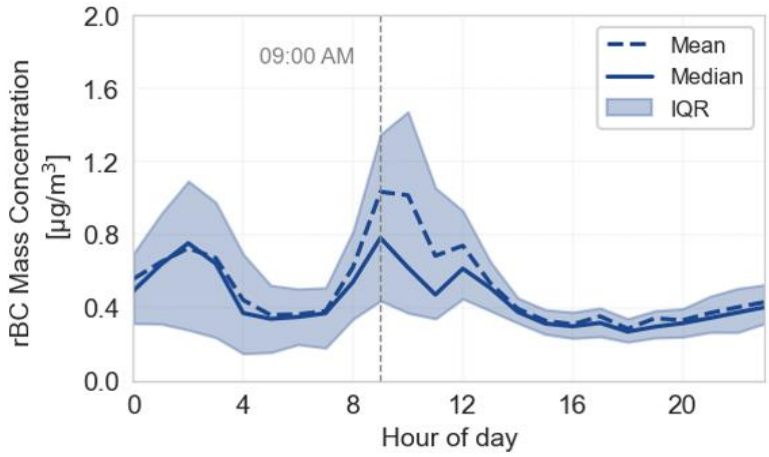

Figure 5-8: Diurnal variability of rBC mass concentration during the campaign in BCN.

With all due precautions, we can argue that wind-controlled dilution might completely counteract the increase of vehicular emission, reducing the overall impact on BC concertation. This process was presented already for coastal

urban environment (Pérez et al., 2010). Quit surprisingly, the second highest m_{rBC} (0.73 µg/m^3) was observed at night between 00:00 and 04.00. Although vehicular traffic was still relevant in the early morning (Figure 5-7), and regional recirculation and stagnation might contribute to increased level of anthropogenic aerosol particles during night (Rodríguez et al., 2002; Pérez et al., 2010), specific sources might arise during the BCN night. Dall'Osto et al. (2012) reported increasing sulfur content during night, which was mostly related with industrial activities and ship emission, and potentially contributed to the m_{rBC} night peak shown in Figure 5-8.

We also investigated the variation of coating thickness throughout the day. As illustrated in Figure 5-9, we observed lower values during the morning peak in concentration, intermediate values in the middle part of the day, and notably high values during the night. The lower values observed during rush hours can be attributed to a higher concentration of newly emitted particles. During the night the increase is even higher suggesting a different process or source compared to daytime. First, it is possible that while condensation of photochemical pollutants is the dominant mechanism acting during the day (Wei et al., 2023), coagulation resulting in thicker coating, more likely happen during the night. Second, sulfur-reach night emission might represent a distinct of coating precursors (Rodríguez et al., 2002; Pérez et al., 2010), potentially contributed to the m_{rBC} night peak shown in Figure 5-8.

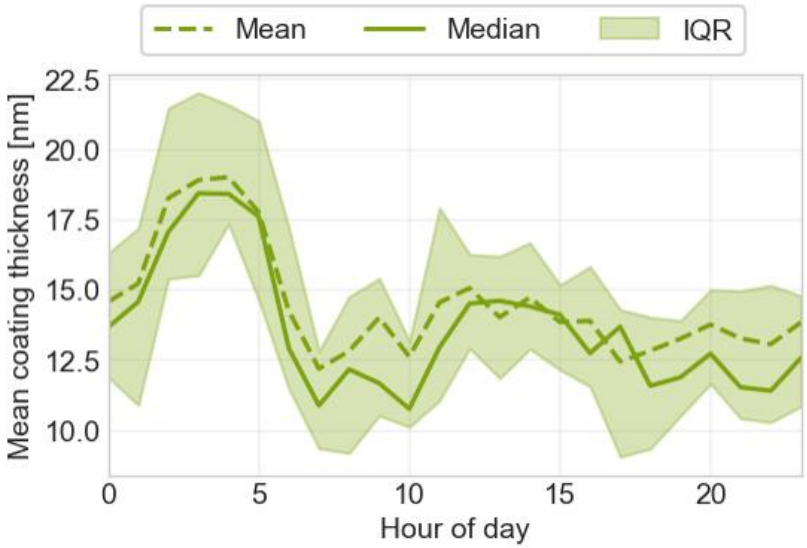

Figure 5-9: Diurnal variability of mean coating thickness in the site of BCN.

5.2.1.3 ***Optical properties***

The MAC (660 nm) was also derived in BCN obtaining an average value of 11 m^2/g, with a standard deviation of 2 m^2/g. This value was very similar to that obtained in Yus-Díez et al. (2022) by using EC as method for measuring the mass concentration (10.85 ± 3.02 m^2/g) at the same site, and to the average reported for other European background and urban sites (Laborde et al., 2013; Zanatta et al., 2016). The MAC enhancement (E_{abs}) was then calculated as the ratio of MAC over the reference MAC for uncoated BC particles (7.5 ± 1.2 m^2/g at 550 nm) adjusted to 660 nm (with an AAE = 1). The resulting absorption enhancement was 1.7 ± 0.4, comparable to the value calculated in Yus-Díez et al. (2022) at 660 nm (1.63 ± 0.54), but higher than those found by many other works (Liu et al., 2015; Zhang et al., 2018; Cappa et al., 2019). One of the reasons of this difference could be related to the choice of the reference MAC. The real reference MAC of uncoated particles could be higher in this site than the estimate used, since externally mixed BrC has a non-negligible impact on the MAC as observed in the same site by Yus-Díez et al. (2022). Taking into account this potential bias in the reference MAC results in lower E_{abs} (Liu et al., 2015; Zhang et al., 2018; Yus-Díez et al., 2022). Moreover, the size distribution could also play a role, since we observe here small particles, that could have a higher MAC (Zanatta et al., 2018).

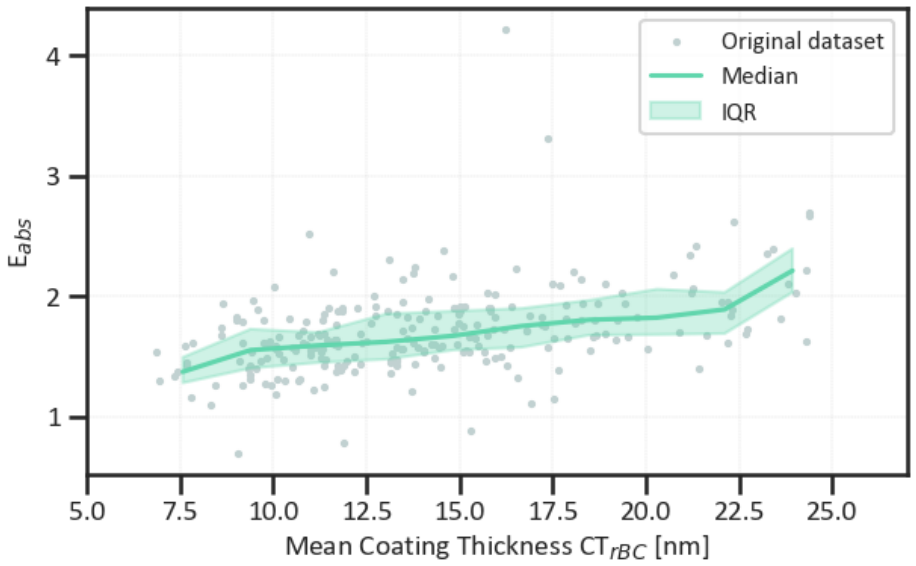

Figure 5-10: Scatterplot of hourly averaged E_{abs} and median binned E_{abs}, at 660 nm as a function of the mean coating thickness CT_{rBC} around rBC cores with diameter in the range 180-220 nm, in BCN.

This deviation from the absorption expected for bare BC particles is anyway due to the persistent presence of coating, even if low, as we can see in Figure 5-10, and reported by Yus-Díez et al. (2022). We then studied the relation between the mean coating thickness and the E_{abs}, by binning the E_{abs} values on mean coating thickness values. The median and IQR variability of E_{abs} as a function of the binned mean coating thickness is displayed in Figure 5-10. The E_{abs} showed an increase of about 60% in the small range of coating thickness values explored, and shows an almost linear relationship with the coating, confirming the expected dependency. However, the small range of coating thicknesses available did not allow a very detailed study of this dependence.

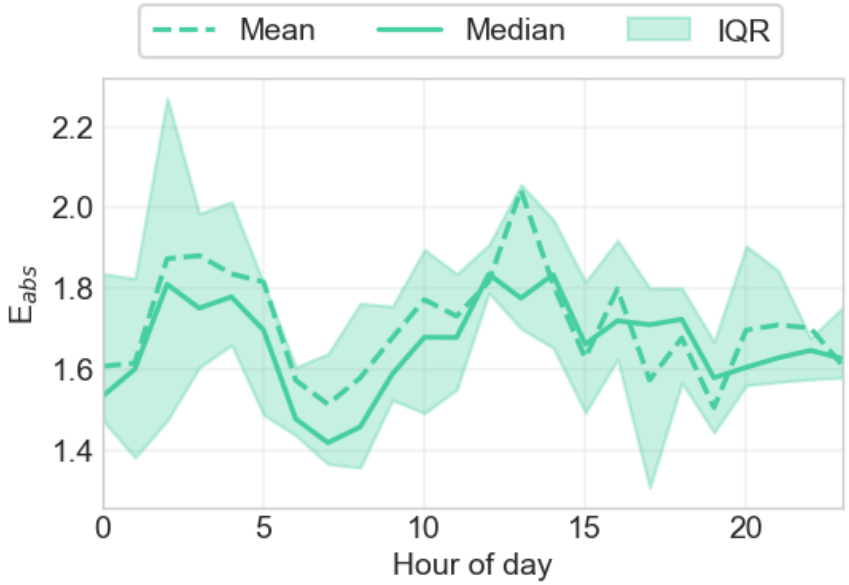

Figure 5-11: Diurnal variability of the E_{abs} at 660 nm derived in BCN.

We also studied the diurnal variability of the absorption enhancement, reported in Figure 5-11. The diurnal pattern of E_{abs} reflected well the variability observed in the coating thickness. We calculated smaller values (1.51 - 1.57) during the morning and evening rush hours, higher values (1.88 – 1.81) during the night and the central part of the day. It could be that different degrees of internal and external mixing, and a different coating composition determine different enhancement degrees (Liu et al., 2017; Luo et al., 2018; Yus-Díez et al., 2022). But this aspect needs more investigation to be better understood.

5.2.1.4 *BC properties during clean and polluted periods*

During the BCN campaign we observed two distinct meteorological phases: a period from 19 to 23 July, hereafter referred to as the "first period" (FP), and a "second period" (SP) from 24 to 31 July. The first period was characterized by drier conditions and prevailing winds from inland (north-northwest; Figure 5-12). From 24 July onwards, we observed an increased variability in wind directions, with the additional contribution from the sea (south-east sector; Figure 5-12) introducing moisture and precipitation events on 30-31 July.

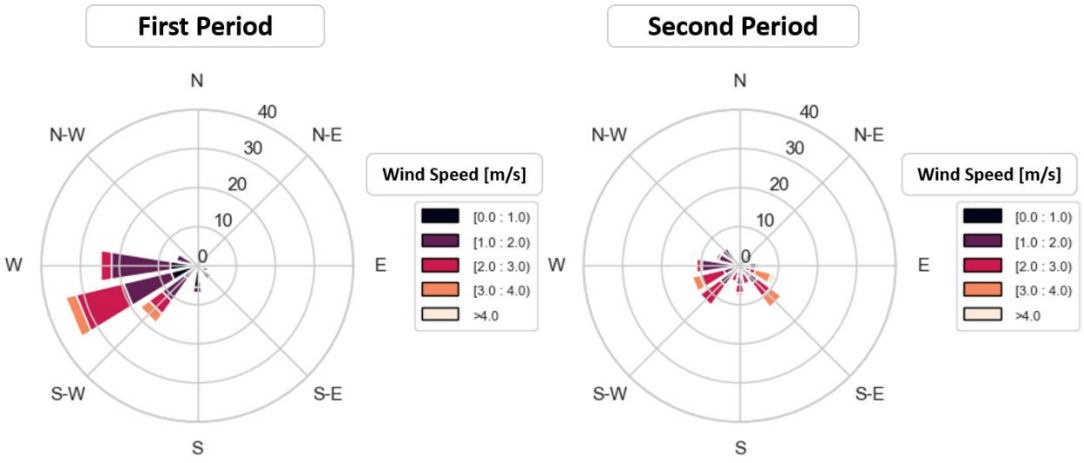

Figure 5-12: Wind roses during the campaign in BCN. With first period we refer to the first week of the campaign from 19-24 July 2018, with second period we refer to the period between 25-31 July.

The FP period was characterized by higher air pressure with a mean of 1005 mbar, a relative humidity of 67% ± 11% and a mean temperature of 28.4°C ± 2.3°C. In contrast, the SP was characterized by lower pressure (1002 ± 2 mbar), higher relative humidity (76 ± 9%) and lower temperature (26.0 ± 1.6°C). The average concentration decreased from 0.8 µg/m³ in the FP to 0.4 µg/m³ in the SP. Figure 5-13 shows a general decrease of the m_{rBC} baseline after 24 July 2021, but also the reduced occurrence and intensity of pollution events: four pollution events exceeding 4 µg/m³ of rBC mass concentration were observed in the first period. The stable conditions observed in FP might have facilitated the accumulation of pollutants, whereas unstable conditions in the SP, including rainfall and sea breeze, might have promoted aerosol removal and dilution. The wind rose (Figure 5-13), which shows the variation in m_{rBC} with

wind direction, supports this finding. Westerly winds from inland and from busy roads might transport BC and lead to enhanced m_{rBC}. In contrast, south-easterly winds from the sea were associated with lower concentrations. In addition, the southern direction showed high concentrations as it corresponds to the nearest busy roads. Although the concentration decreased significantly, the microphysical properties of rBC from the first to the second period remained within the instrumental uncertainty of the SP2.

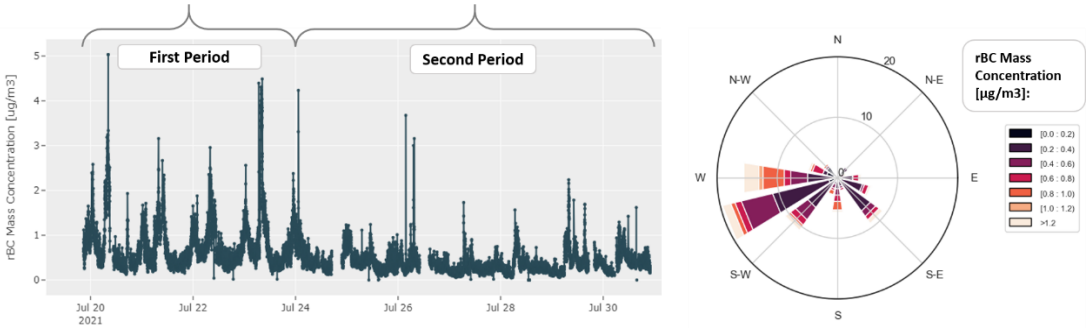

Figure 5-13: On the left rBC mass concentration times series (1 min resolution), with division in first and second periods. On the right variability of the concentration with wind direction.

The mass mean diameter increased from 98 nm in FP to 107 nm in the SP, while the coatings thickened from 12 nm in the FP to 16 nm in the SP. The variability of rBC properties during this campaign was further explored by studying specific cases characterized by opposite conditions. The first one addressed as high concentration (HC) case and the second one called low concentration (LC) case. In HC we included the two pronounced morning peak observed in the first period of the campaign (20 and 23 of July from 6:00 to 11:00), in LC we, instead, included two cases with low concentration and mainly south-easterly winds observed in the second period of the campaign (24 and 25 July from 10:00 to 19:00). Figure 5-14 well represents the differences in wind pattern in these two cases. The HC is characterized by low wind speed below 2 m/s and mainly from the west direction (hinterland, big highways), while the LC period is associated with south and south-easterly stronger sea breeze, with speeds higher than 4 m/s.

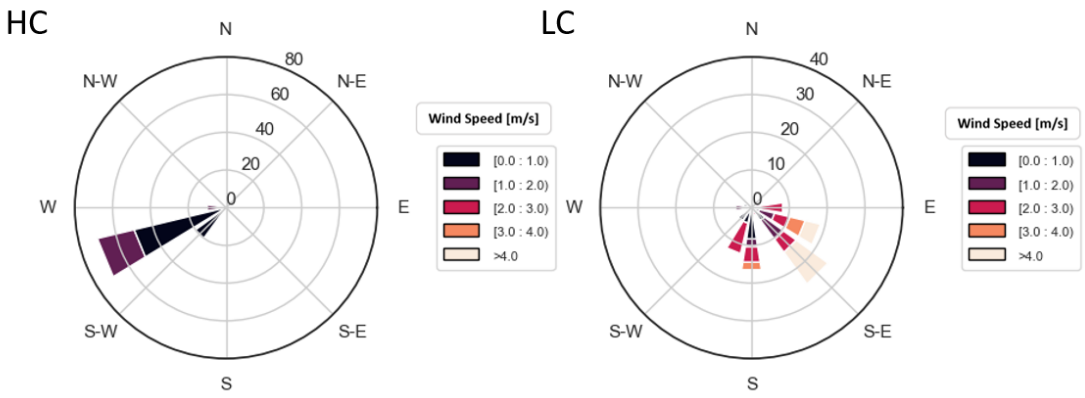

Figure 5-14: Wind roses during the 'high concentrations' (HC) and 'low concentrations' (LC) cases in BCN.

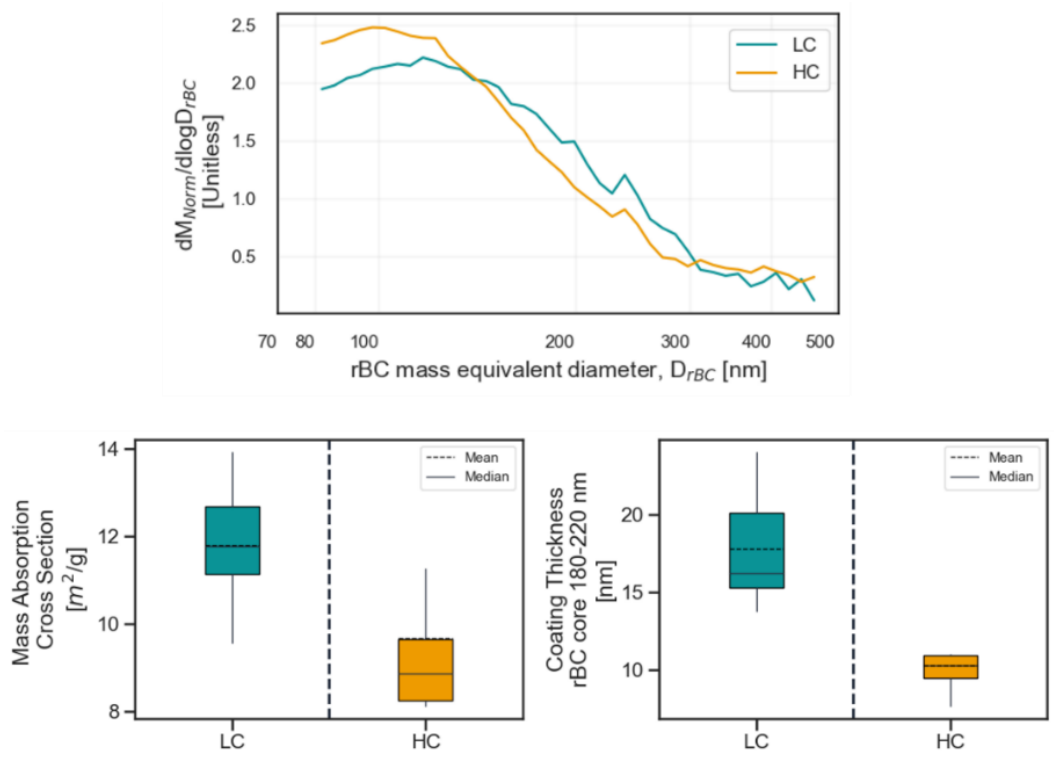

Figure 5-15: Variability of rBC properties derived by the SP2 during the campaign performed in BCN in July 2021. The values are divided in two distinct periods, LC containing two periods with south-easterly strong winds from the sea and HC representing two intense morning rush hours. Top panel: normalized mass size distribution or rBC particles. Bottom left panel: boxplot of mass absorption cross-section (MAC) at 660 nm of wavelength. Bottom right panel: coating thickness of rBC particles (CT_{rBC}) in the range of core diameter 180-220 nm.

Figure 5-15 and Table 5-2 summarize the rBC properties observed in the selected cases. The m_{rBC} concentration was substantially different with a mean for HC of 1.5±1.1 μg/m³ and for LC of 0.3±0.2 μg/m³, with an 80% decrease when strong winds are blowing from the sea. Concerning the mass size distributions in the two cases we observed (upper panel of Figure 5-15) that both of them were quite similar to other observation in urban sites close to traffic sources (Laborde et al., 2013; Krasowsky et al., 2018). The distribution corresponding to the LC period was slightly shifted towards larger diameter. The MMD was 103±6 nm in the HC period and 110±13 nm in the LC period, increasing of 7% (small compared to the uncertainty on the size distribution: 15%, Laborde et al., 2012). These two periods were thus influenced by the same BC sources.

Table 5-2: Summary of mean and standard deviation of rBC properties derived by the SP2 during the campaign performed in BCN in July 2021. The values are divided in two distinct periods, LC containing two periods with south-easterly strong winds and HC representing two intense morning rush hours.

	[rBC] μg/m³	**MMD nm**	**CT nm**	**MAC m²/g**
LC	0.3±0.2	110±13	18±5	12±1
HC	1.5±1.1	103±6	10±2	9.7±2.3

The parameters that differ the most are those related to the mixing state of the particles, the coating thickness and the MAC. The coating thickness was 10±2 nm in the HC period and 18±5 nm in the LC period. An increase of 80% was observed for periods with strong winds form the coast compared to morning traffic rush hours in periods with low weak winds. The similar but lower difference was observed in the MAC. The HC period was characterized by a mean MAC of 9.7±2.3 m^2/g and the LC period by a value of 12±1 m^2/g, showing an increase of 24%.

This result suggests that periods with air masses from the sea are associated in this season to a higher mixing of rBC particles resulting in higher absorption. A similar conclusion about the ageing of the aerosol particles reaching this site with easterly winds during summer was derived by Dall'Osto

et al. (2012), who found an increased accumulation mode in periods with similar wind pattern, compared to periods with air masses from south-west.

5.2.2 Urban sites in South America: La Paz and El Alto

La Paz (LP) and El Alto (EA) are two of Bolivia's fastest-growing cities at high altitude. Situated between 3200 and 4050 m above sea level, they are home to around 1.8 million people and form the second largest metropolitan area in the country. Air quality in this metropolitan area is strongly influenced by urbanization, particularly by sources such as traffic emissions, open burning of waste and biomass burning, although there are still no regulations on particulate concentrations. Despite their proximity, the considerable differences in altitude, topography and socio-economic activities between LP and EA result in different sources, dynamics and transport of particulate matter.

5.2.2.1 *Meteorological conditions during the campaign*

The campaign occurred during the transitional phase between the rainy and dry seasons, and at the beginning of the dry season. This temporal context is characterized by reduced temperatures compared to other periods of the year and minimal precipitation. At the LP station, precipitation rates data indicates rainfall only in few days: the 13th of April, 2018, at 4:00 the 28th of April, 2018, at 21:00, and the 3 and 5 May, 2018. Throughout the rest of the campaign, a precipitation rate of zero was observed.

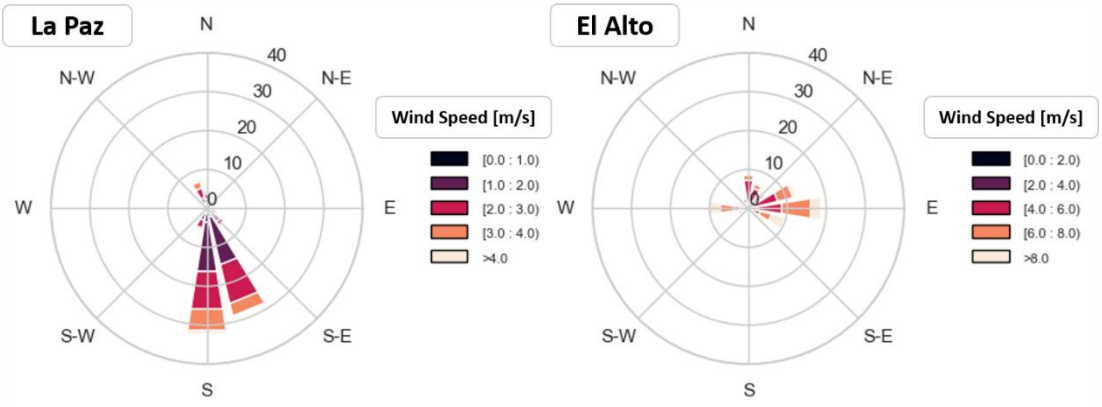

Figure 5-16: Wind roses for LP and EA, during the campaign.

The two urban stations exhibit distinct meteorological characteristics, distinguished by their geographical locations – one situated in a valley (LP) and the other on an Altiplano (EA), 425 m above LP. In LP, the average temperature stands at 12.2 °C, with a standard deviation of 4.2°C. Conversely, EA experiences a lower average temperature of 6.7 °C, with a higher standard deviation of 5.5°C. Nighttime temperatures drop to -6°C in EA, while they remain above 4°C in LP.

The prevailing wind patterns also contribute to the divergent climatic conditions. In LP, winds blow predominantly from the south-east, with an average speed of 2 m/s (with a standard deviation of 1.0). In EA, on the other hand, easterly winds prevail, but the directions are more scattered here (Figure 5-16), exhibiting an average speed of 5.3 m/s (with a standard deviation of 2.4).

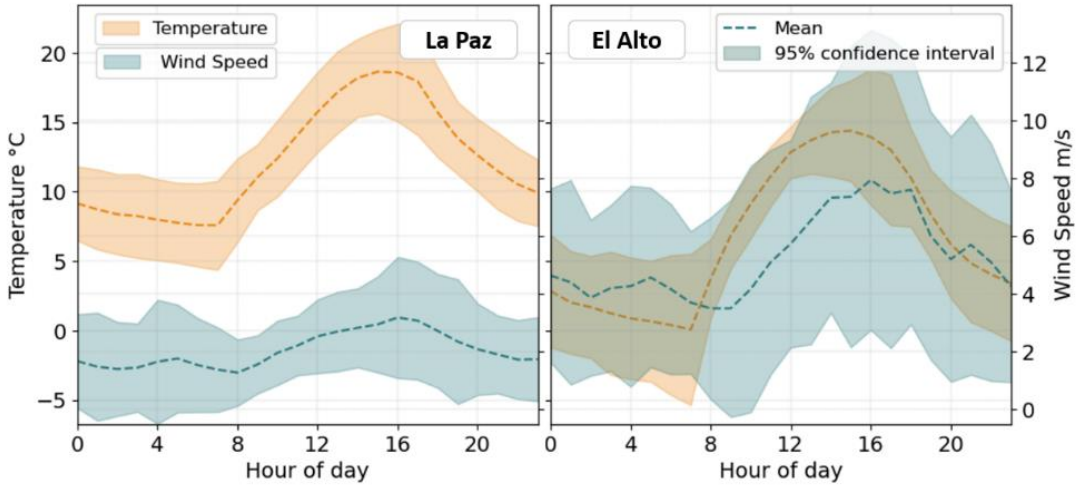

Figure 5-17: Diurnal profile of temperature and wind speed at the Bolivian urban sites.

The diurnal wind and temperature profiles show remarkable similarities in terms of hourly variability, but significant differences remain in absolute values. The temperature follows a clear pattern, rising from a minimum of 7.6°C at seven in the morning to a maximum of 18.6°C around 15:00. It then decreases in the afternoon, falling back to the morning minimum. During the night, the rate of decrease is more gradual, while the afternoon and morning periods are characterized by pronounced temperature variations (> 1°C/h). This observed trend is linked to the dynamics of solar radiation: the sun rises at around 6:40 am, reaches its maximum intensity at 12:30 pm and sets at 6:30 pm. EA reflects

this diurnal pattern, with identical times for temperature minima and maxima. However, the temperature range is more pronounced at this location, with a significant difference of 14.3°C between the minimum and maximum values, corresponding to an hourly variation of approximately 1.6°C. The wind patterns are slightly different. With a minimum around 8 a.m., the wind increases to its maximum speed at 4 p.m., before decreasing in the late afternoon. In EA, the wind speed increases from 3.5 m/s to 7.9 m/s, while in LP it increases from 1.3 m/s to 3.2 m/s.

5.2.2.2 *rBC mass concentration*

In this section we present the average variability of rBC mass concentrations in two urban high-altitude sites in the Bolivian Andes, LP (3600 m) and EA (4025 m).

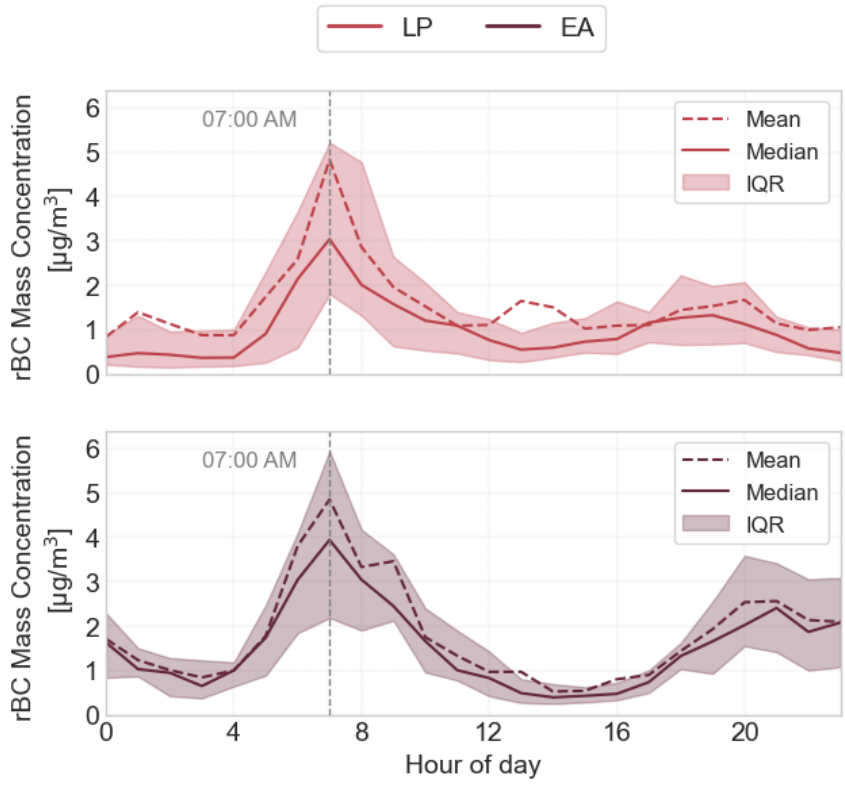

Figure 5-18: Diurnal variability of rBC mass concentration in the two urban sites of the Bolivian Andes: LP and EA.

The respective average m_{rBC} were 1.5 µg/m³ and 1.8 µg/m³. These values are lower than previous observations in two other high-altitude sites in South America. A daily mean m_{eBC} up to 5 µg/m³ was observed in Bogota (3152 m

a.s.l.) by Rincón-Riveros et al. (2020), while an average m_{eBC} of 2.34 μg/m^3 was obtained in Mexico City (2280 m a.s.l.) by Peralta et al. (2019), in the same season of our campaign. A decrease of 64-23% is found in our observations compared to these other cities. While an increase of 40-50% is observed compared to the values reported in previous sections in the Po valley. Considering that vehicular traffic, mainly from gasoline cars, is the main source of BC in this region (Wiedensohler et al., 2018; Mardoñez et al., 2023), with a secondary contribution from waste burning in EA, and that the combined population of the LP-EA conurbation is more than four times smaller than that of Bogota or Mexico City, the concentration measured here are remarkable.

Figure 5-18 illustrates the diurnal variations in average m_{rBC}. LP and EA share a similar pattern in mass concentrations, characterized by higher levels in the early morning and late afternoon or evening, and lower concentrations in the midday and nighttime. This pattern, typical of urban areas influenced by vehicular traffic, results from a combination of source variability and atmospheric conditions. Although detailed information on traffic evolution during the day is not available at these sites, we know that people usually move by personal petrol-powered vehicles and public transports, with main vehicles in order of importance constituted by car, mini-buses, motorbike, van, truck (INE, 2022). Moreover, it was estimated that nearly 440'000 people commute daily from the city of EA to the city of LP to work every day (Suárez-Alemán and Serebrisky, 2017; Garsous et al., 2019). This would imply a diurnal increase in traffic in the morning and in the late afternoon, and a different travel times in the two cities. From the variability of temperature and wind speed in Section 5.2.2.1 we can instead have a rough idea of the diurnal variability of the boundary layer height increasing when the sun is shining heating the atmosphere and decreasing when it set leading to lower temperatures. Peak concentrations in both cities coincide with minimum in boundary layer height during morning and evening rush hours. The subsequent decline is influenced mainly by changes in the height of the atmospheric boundary layer.

Both sites have a common morning peak around 07:00, slightly higher in EA (4.9 μg/m^3) than in LP (4.8 μg/m^3). However, the late afternoon and evening patterns are different. In LP, the second peak begins at around 16:00, peaks (1.7 μg/m^3) at 19:00 and reaches values close to the minimum at 22:00

(0.8-0.9 μg/m^3). In EA, the peak with a mean of 2.6 μg/m^3 begins an hour later, lasts until 21:00 and decreases to the minimum (0.8-0.9 μg/m^3) at 4:00. Not only the time variability is different in the evening but also the magnitude of the peak, with the one in EA 53% higher than that in LP. These variations are attributed to differences in boundary layer dynamics. EA, located on an open Altiplano, contrasts with LP, located in a valley, where the sun sets early and valley winds increase the dispersion of pollutants. In addition, people commute from LP to EA in the evening, so sources are likely to increase later on the Altiplano.

5.2.2.3 ***Size distributions***

This section focuses on the characterization of rBC-containing particles at the two Bolivian urban sites. Mass size distributions (dM/dlog(D_{rBC})) at LP and EA, normalized to mean total mass concentration ($Mass_{tot}$) for better comparability, are shown in Figure 5-19. The median and mean distributions were used to calculate the mass median diameter (MMD). This involved fitting the observations with a lognormal distribution (diameter range 10-1000 nm) and determining the diameter that equally divides the fitted distribution, ensuring the same total integral in each part.

The results for the mean and median size distributions show that the MMD for the median and mean distributions were 142-85 nm in LP and 187 nm in EA. The values for EA were slightly higher than values typically associated to urban environments, more consistent with a regional background site characterized by more aged BC (Ahlberg et al., 2023). The LP distribution was unique, with most mass in particles <150 nm, and the median distribution peaking below the minimum detectable diameter. Therefore, while the EA results were more reliable, with a significant fraction likely to be within the instrument's detection range, a large fraction is lost at LP, making the lognormal fit more uncertain and the MMD potentially overestimated. EA's distribution could be the result of fast aging in an urban polluted environment. LP's unique distribution, similar to few other observations close to sources, could be attributed to freshly emitted particles from vehicles (Krasowsky et al., 2018). Although both cities share vehicular traffic as a major aerosol source, their distributions differ significantly.

Possible explanations for the differences include secondary sources such as waste burning, which affects EA and is associated with larger sizes. However, since the source is not constant, significant temporal fluctuations in the distribution would be expected, which are not observed. Mardoñez et al. (2023) identify two types of traffic in the two cities, one due to emissions from petrol vehicles, which dominate in LP, and one due to diesel vehicles, which are present in comparable proportions in EA.

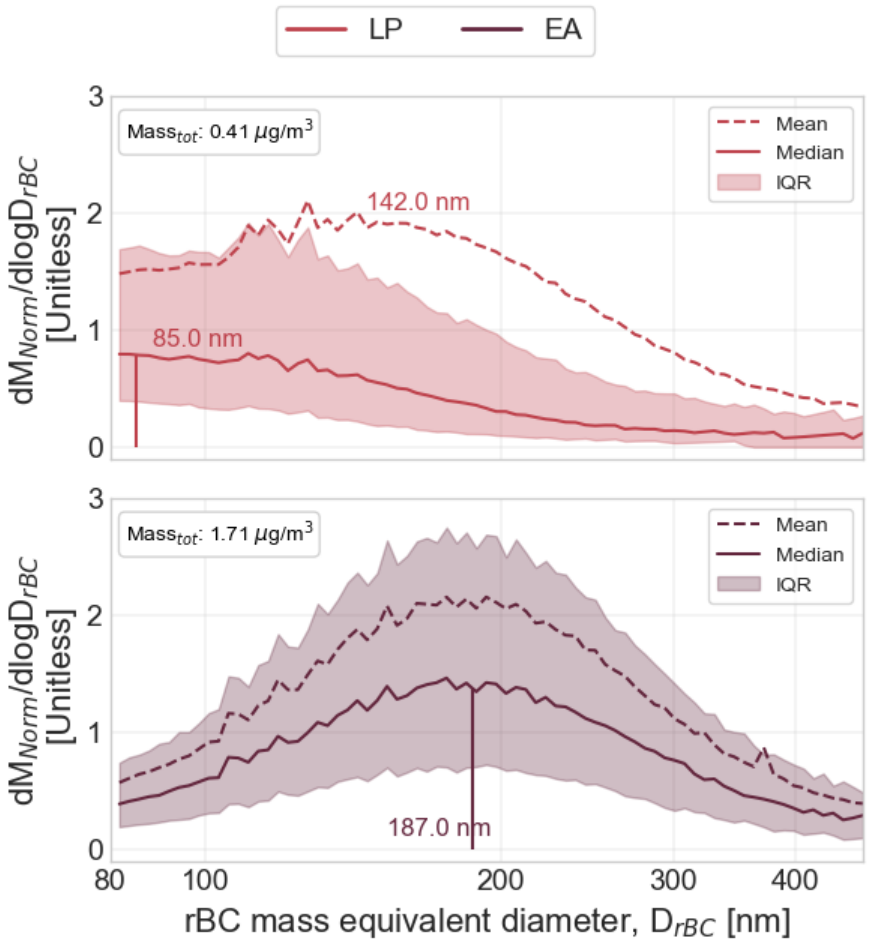

Figure 5-19: Average normalized mass size distributions of rBC cores in LP and EA.

This difference in sources could be a reason for the different distributions, as emissions from gasoline vehicles can produce particles with very different properties and even smaller sizes than those from diesel vehicles (Karjalainen et al., 2014), especially under such unique conditions. A more likely explanation for the different distributions could be the distance between the vehicular

sources to the sampling site. The LP station, located in the city center and closer to busy roads (<50 m), is likely to observe freshly emitted particles. In contrast, EA, located at least 500 m from the nearest busy road, is likely to observe partially aged particles due to coagulation and condensation, shifting the size distribution towards larger diameters. A more detailed analysis of the peculiarities of the LP distribution is presented in Modini et al. (in preparation).

5.2.2.4 ***Optical properties***

The mass absorption cross-section (MAC at 660 nm) was derived for the two sites of LP and EA (Figure 5-20). The resulting means and standard deviations are 11±9, 8±2 m^2/g for LP and EA, respectively. The values observed in LP are quite high compared to those expected in an urban site very close to direct traffic sources and also higher than those derived in the same site using EC measurements (MAC_{EC} = 7.6±1.7 m^2/g) instead of rBC (Mardoñez et al., 2024). This is probably a result of the instrument's constraints, particularly the restricted diameter range (80-460 nm). The mass size distribution at this site peaks at, or even below, the minimum measurable diameter. Although the mass values have been corrected for comparison with EC, this correction may not be entirely adequate to capture the full variability in true concentration. As a consequence, there is an underestimation of the mass concentration, leading to an overestimation of MAC.

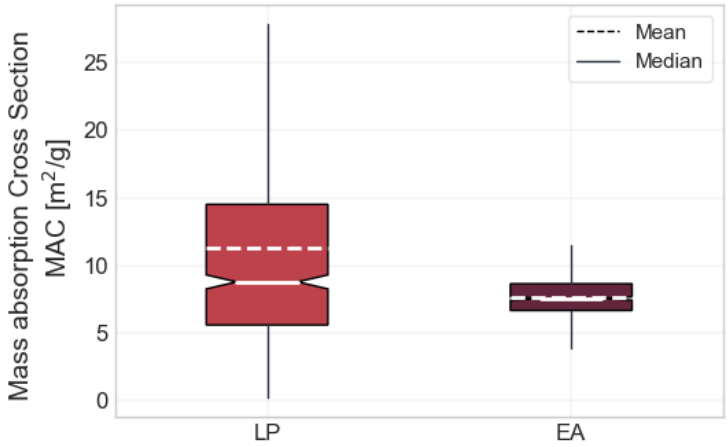

Figure 5-20: MAC boxplots in the urban Bolivian sites of LP and EA.

The median value equal to 8.8 m^2/g is probably more representative and less affected by outliers in this site, considering the variability it is also more comparable to the one obtained in EA. However, the values measured in EA align with expectations for an urban background location and are more consistent with those obtained using EC (MAC_{EC} = 7.7 ± 1.9 m^2/g) for measuring the mass concentration. It is also more comparable to that reported by Bond and Bergstrom (2006) for pure black carbon 7.5 ± 1.2 m^2/g not mixed with other compounds. This indicates that the particles observed at this site are mainly fresh soot, and their aging time is insufficient to develop a significant coating that would enhance absorption. The resulting absorption enhancement derived in EA is E_{abs} = 1.2 at 660 nm.

6 RESULTS: ANTHROPOGENIC IMPACT ON REGIONAL SCALE AND FREE TROPOSPHERE

As reported in the last IPCC report (2021), high mountain regions are particularly susceptible to climate changes, with a growing evidence of an enhanced rate of global warming, through many different mechanisms. As already described, BC directly warms the atmosphere by absorbing the radiation (Bond et al., 2013), with a more efficient radiative forcing when it is located above clouds rather than near the surface (Samset and Myhre, 2015), and it can decrease surface albedo after deposition on the cryosphere (Réveillet et al., 2022). Hence, mountain region is particularly vulnerable to positive forcers. López-Moreno et_al. (2014) found a positive trend between altitude and warming rate in the European mountain chains, the so called elevation dependent warming (EDW) might involve absorbing aerosol particles such as BC (Pepin et al., 2015). For this reason, it is very important to monitor BC concentrations, processes and properties at high altitude to better evaluate its impacts. Unfortunately, BC observations in high mountain regions, with state of the art techniques able to capture microphysical properties (such as SP2), are limited to few examples (e.g. Liu et al., 2010; Zhu et al., 2016; Tinorua et al., 2023).

Bolivian Andes are of particular interest with considerably elevated peaks up to 6,000 metres. This region is characterised by unique high-altitude urban areas such as LP and EA (4000 m), which with their 1.8 million inhabitants constitute a strong source of BC. As reported by few studies urban area in South America are characterized by high BC concentrations (Peralta et al., 2019; Rincón-Riveros et al., 2020) compared to most urban cities in Europe (Savadkoohi et al., 2023), due to the absence of policies for emission regulation. This high concentration, can in particular affect the cryosphere enhancing glaciers melting in the Andes (Molina et al., 2015; Gilardoni et al., 2022; Lapere et al., 2023). Although, some areas of South America are among the few in the world where there has been an increase in the optical thickness of the aerosol layer rather than a decrease between 2000 and 2019 (IPCC,

2021), a lack in atmospheric research and observations is registered here. Only fifteen WHO-GAW operational stations are present including global, regional and contributing network stations. The site of Chacaltaya, where this study was conducted, is one of the only two global stations in the whole South America, and the campaign whose results are reported in this chapter, was one of the very few in which an SP2 was used to measure the microphysical properties of black carbon in the area (Saturno et al., 2018), and the only one at a high mountain site. Among the most important effort in filling the knowledge and observational gap in southern America is represented by the SALTENA experiment, aimed to identify the sources, understand the formation mechanisms and transport, and characterise the properties of the atmospheric aerosol (Bianchi et al., 2022). In this context the use of the SP2 allowed to focus on characterising the properties of BC in a high-altitude environment.

The objectives of this study are to:

- Quantify the microphysical properties of BC at the Chacaltaya station
- Understand the relationship between microphysics and optical properties in the free troposphere
- Identify the main transport pathways and their impact on BC population in the free troposphere

6.1 AIR MASSES CHARACTERIZATION AT CHACALTAYA

In order to obtain accurate information on the origin of the air masses passing over Chacaltaya and sampled here, as well as the transport pathways to this site, the results of a previous study based on FLEXible PARTicle Dispersion-Weather Research and Forecasting model (FLEXPART-WRF) simulations were used (Aliaga et al., 2021). Specifically, 20000 particles per hour were released in a layer 20 m thick and extending over a distance of 2x2 km in the horizontal, centred on CHC, and their retro trajectory was studied for four days. The output variable of the model is the source-receptor relationship (SRR), expressed in units of seconds and depending on the location, the time of release (arrival at CHC), the time elapsed before release and the number of

particles present at the grid point considered. The output SRR dataset was then processed through a number of steps (e.g. log-polar grid transformation and grid cell pre-processing) before being subjected to cluster analysis using a k-means clustering algorithm. At the conclusion of this analysis, six primary transport pathways were identified representing the diverse air masses reaching CHC (Figure 6-1):

- 03_PW from the East: Originating from the Amazon basin and the eastern/south-eastern lowlands.
- 05_PW from South and Southeast: Extending from the south-eastern lowlands to the southern Altiplano.
- 07_PW from Southwest: Encompassing the Pacific Ocean, coastal area, western Altiplano, and LP–EA.
- 08_PW from West: Covering the western Altiplano, Lake Titicaca, and the coastal area.
- 11_PW from North and Northwest: Spanning the Amazon basin, western Altiplano, and coastal area.
- 12_PW from North: Originating in the Amazon basin.

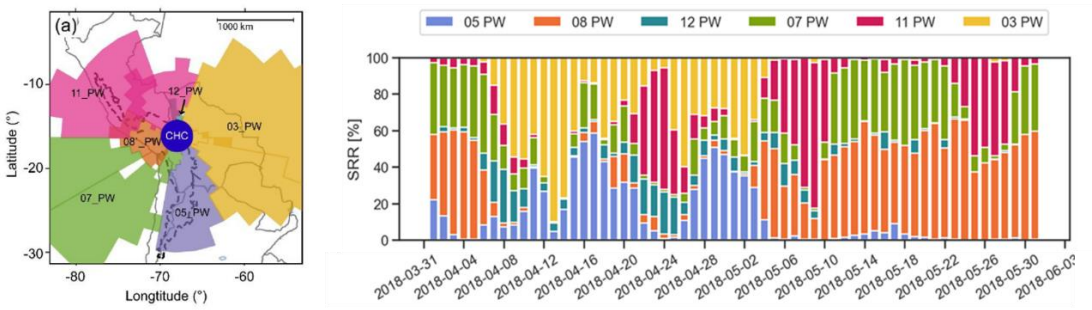

Figure 6-1: Geographical representation of air mass pathways reaching the site of Chacaltaya (Aliaga et al., 2021). Variability of pathway percentage contribution through the campaign.

The results of this study make it possible to also assess the influence from the surface and the free troposphere. During the six months of the study, it was observed that 76% of the air masses reaching CHC came from the free troposphere, but that influences from the pure free troposphere are very rare. Very often, even for short periods of four days, air masses are influenced by the surface or the first layer of the atmosphere within 1500 m above the

ground. These results were studied in detail during the campaign period in question in order to characterise the air masses in terms of their area of origin and the dominant influence of the free troposphere or the boundary layer.

6.1.1.1 *Identification of transport pathways*

We examined the variability of air mass pathways at the CHC site during the measurement campaign presented in this thesis, utilizing the SRR sets generated by Aliaga et al. (2021) as output. The corresponding analysis is illustrated in Figure 6-2, where the percentage of influence from each pathway is depicted for each day. The graph shows that each day is typically influenced by multiple pathways, with a single pathway rarely contributing more than 40%. To identify representative periods for each air mass trajectory and to reduce the simultaneous influence of several trajectories, we decided to group the air masses in three sectors.

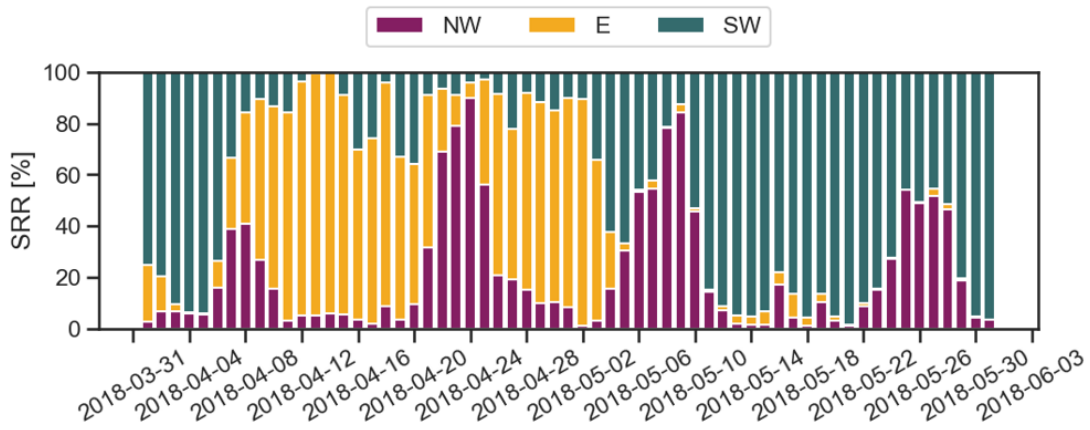

Figure 6-2: Variability of source-receptor relationship (SRR) percentages for the new sector division during the campaign at the Chacaltaya station. NW indicates the North Western sector; E, indicates the Eastern sector; SW indicates the South Western sector.

The first, labelled 'East' (E), was identified by combining sectors 03_PW and 05_PW, and includes the lowlands and the Amazon forest from the southeast to the northeast. The second, labelled 'North-West' (NW), was created by merging 12_PW with 11_PW and covers part of the Amazon basin and the Altiplano to the west. The final one, named 'South-West' (SW), was created by merging sections 07_PW and 08_PW and includes the metropolitan

region of LP-EA, part of the western Altiplano, Lake Titicaca and the Pacific coast. Shown in Figure 6-2 is the daily change in the percentage of the influence of each of macro-sector over the course of the campaign.

This grouping makes it possible to identify more clearly which sector is dominant on any given day. We then selected the days on which a single pathway accounted for more than 65% and identified them as representative of that sector. Using this criterion, 13 days were identified as representative of the East sector, 22 days were identified as representative of the South-West pathway and only 5 days were identified as representative of the North-West sector.

6.1.1.2 *Periods representative of free tropospheric conditions*

In addition, the model outputs allowed the derivation of the 'fractional contribution of free tropospheric air' to the air mass. That is to say, the percentage in time spent by each considered pathway at an altitude above 1500 m above ground level.

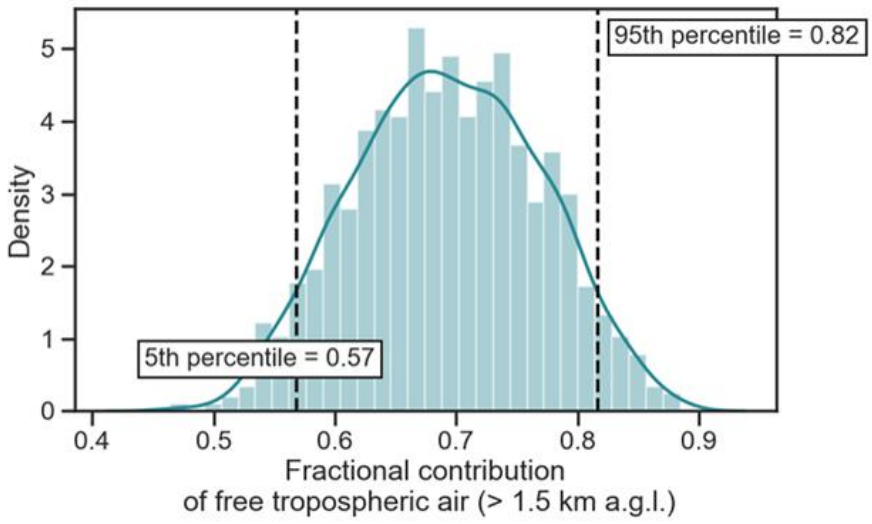

Figure 6-3: Histogram of the fractional contribution of free tropospheric air throughout the campaign at the Chacaltaya station. Boundary layer high defined at constant vertical distance of 1500 m from the ground.

The histogram in Figure 6-3 shows the fractional contribution of free tropospheric air during the entire campaign and highlights a predominant influence of the free troposphere at CHC, with a minimum contribution of at least 50%. At the same time, there are no examples where air masses are

completely unaffected by the planetary boundary layer. The fractional contribution of free tropospheric air rarely exceeds 90%, indicating that minimal but not negligible fraction of the air masses passed below 1500 m a.g.l.

On the basis of these results, we proceeded to identify distinct periods characterized by a predominant influence of the free troposphere, termed 'free tropospheric periods' (FT), and periods characterized by a maximal influence of the boundary layer, termed 'boundary layer periods' (BL). In the former category, we included periods with a fractional contribution of free tropospheric air above the 95th percentile of the distribution (0.82) and an rBC concentration value < 0.1 μg/m^3. In the latter category we included periods with a fraction of free tropospheric air below the 5th percentile of the distribution (< 0.57).

6.2 MICROPHYSICAL AVERAGE PROPERTIES OF BC IN A REMOTE SITE

6.2.1 Average rBC mass concentration

The rBC mass concentration was calculated here by using the SP2 measurements derived from the incandescence signal properly calibrated as detailed in Section 2.2.3.1 and corrected as described in Section 2.2.3.4. The average value of rBC mass concentration (m_{rBC}) measured in this site during the campaign was 0.11 μg/m^3, with a standard deviation of 0.18 μg/m^3. This value is similar to other SP2 observations in high altitude sites in Europe and Tibet (Zhu et al., 2016; Tinorua et al., 2023a) and very low compared to the Bolivia urban sites. We know from previous studies that the metropolitan region of LP-EA is the main source of BC at CHC (Wiedensohler et al., 2018; Bianchi et al., 2022). Considering the values in EA as representative for the average condition of the metropolitan area, the mean concentration in CHC was sixteen times lower than that in EA. This result is well informative about the typical difference in rBC mass concentration between a high mountain site and an urban one.

The diurnal profile of the rBC mass concentration (Figure 6-4) was also different in CHC, reversed compared to the one derived in EA. Very low values

were observed during the night until late morning. During the day from around 10:00 in the morning, the boundary layer height started to increase promoting the transport of pollutants to CHC while causing a dilution of the pollutants in EA. This resulted in an increase of the rBC mass concentration at CHC since night until a main peak at 12:00 (m_{rBC} = 0.35 µg/m^3). This peak occurred about 5 hours later than the morning peak at the urban sites being five time lower than the average in EA. This is consistent with previous observations of boundary layer variability over the metropolitan region and the transport of pollution to CHC (Wiedensohler et al., 2018).

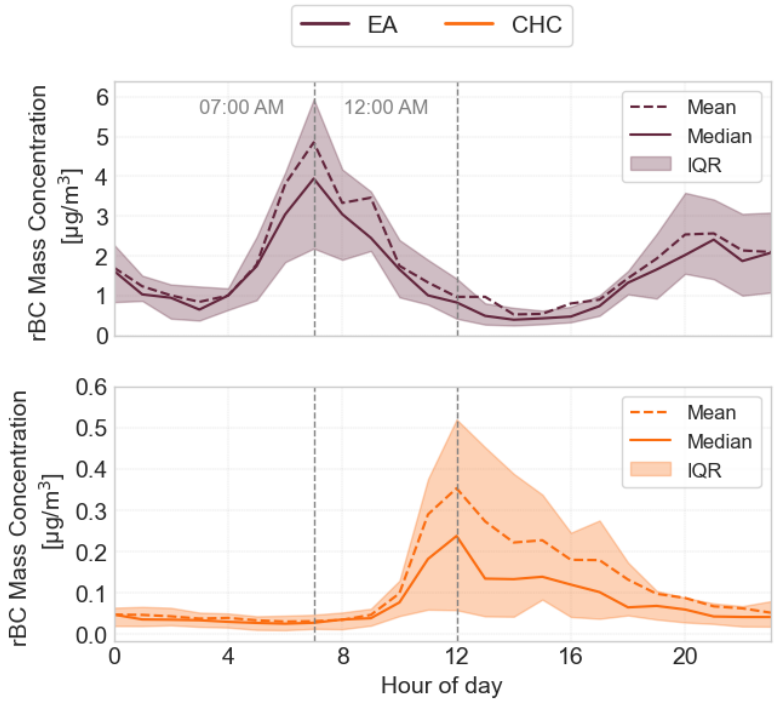

Figure 6-4: Diurnal variability of rBC mass concentration, measured by the SP2, in the site of Chacaltaya (CHC) compared to that observed in El Alto (EA).

Moreover, considering again the SRR sets of results from (Aliaga et al., 2021) for the time spent by each air mass at an altitude below 1500 m a.g.l, we found a similar pattern to that observed for the concentration as shown in Figure 6-5. This means that air masses observed in the central part of the day spent a longer time in the boundary layer where the BC produced in the metropolitan region was more likely to have accumulated.

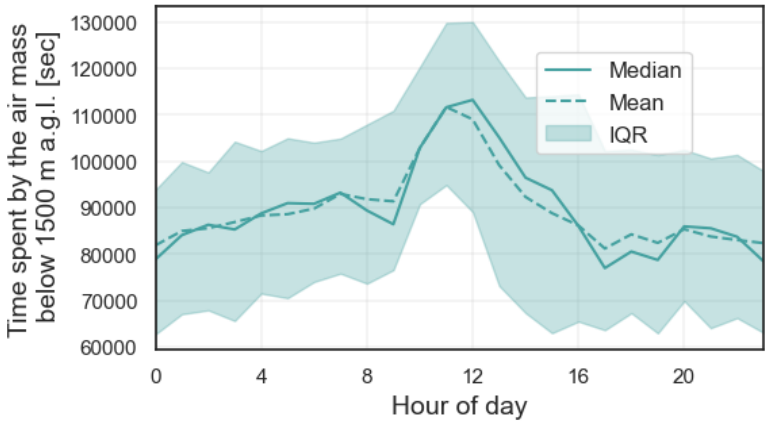

Figure 6-5: Diurnal variability of the time [sec] spent by the air masses arriving at this site, in the boundary layer (below 1500 m a.g.l.).

The transport of particles from the boundary layer and the metropolitan region of LP and EA was the dominant source of BC particles measured at CHC. Most of rBC was the result of anthropogenic sources placed in the metropolitan region but aged for at least few hours before being transported to the mountain top. We expect them to be much more aged than those measured in LP and EA. This site is a good location to study how the aging modifies the rBC properties during transport.

6.2.2 Size distributions

The SP2 was used to derive hourly mass size distribution as described in Section 1.1.2.2 for the entire campaign. The mean and median size distributions observed in CHC are compared to those measured in EA in Figure 6-6. The distributions were very similar to one another with a peak diameter of the median distribution equal to 171 nm in CHC and 187 nm in EA.

Particles observed in CHC were thus just slightly smaller than those measured in EA, but considering that the agreement in size distributions measured with the SP2 is expected to be 15%, this difference (~9%) does not seem to be significant. This is an additional confirmation that the particles observed in the two environments originate from a common source. Both of them are in agreement with particles emitted from aged traffic sources (Laborde et al., 2013), with no evidence of a strong impact form biomass burning that would result in larger particles (Schwarz et al., 2008). The similarity

of the size distributions showed above suggests that transport from urban to remote location occurred in the same way for particles of all sizes without significant removal mechanisms or intra-coagulation that may impact the rBC size distribution.

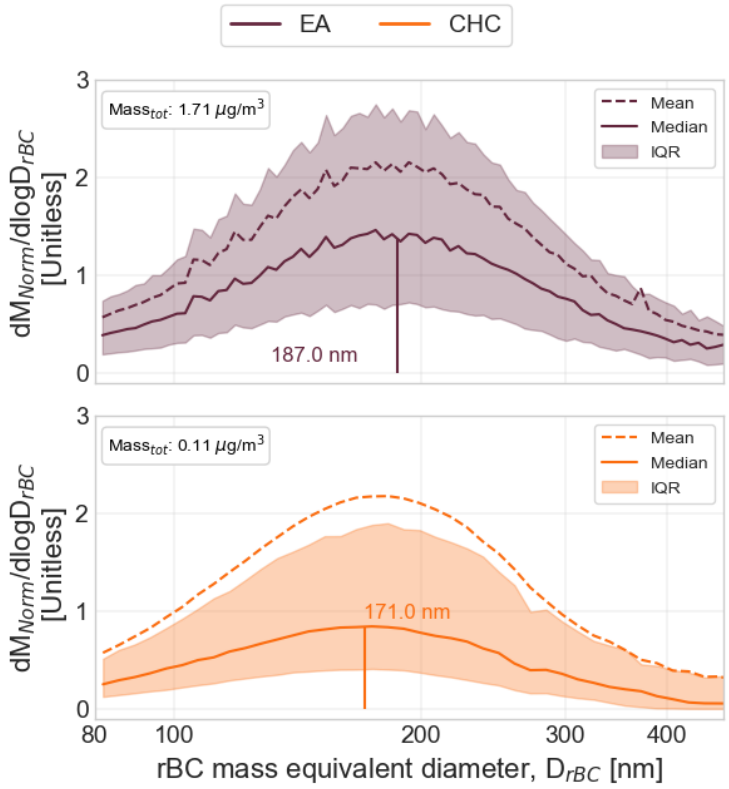

Figure 6-6: Mass size distribution measured by the SP2, normalized to the total mass measured in El Alto (EA) and Chacaltaya (CHC).

6.2.3 Coating thickness at Chacaltaya

At the CHC site, we also derived the coating thickness around BC-containing particles using the LEO-fit method detailed in Section 2.2.3.3. The purpose of this evaluation is to provide a quantitative and dimensionally resolved assessment of particle mixing levels. The range of BC core diameters over which we could perform this measurement was 180-220 nm. This range falls above the mass size distribution peak, allowing evaluation for only a small fraction of the BC-containing particles.

Figure 6-7 shows the variability of the coating thickness measured by the instrument for different diameters of rBC cores and the distribution of values obtained for diameters between 180 and 220 nm. Compared with the

results obtainend in BCN, at this mountain site we observed rBC cores with a thicker coating. In the urban site of BCN, we never observed particles with coatings thickness higher than 120 nm, while here we observe particles with coatings up to 300 nm. However, the distribution of hourly averaged coating thickness (Figure 6-7) indicated that the majority of rBC particles with cores in the 180-220 nm range seem to be uncoated.

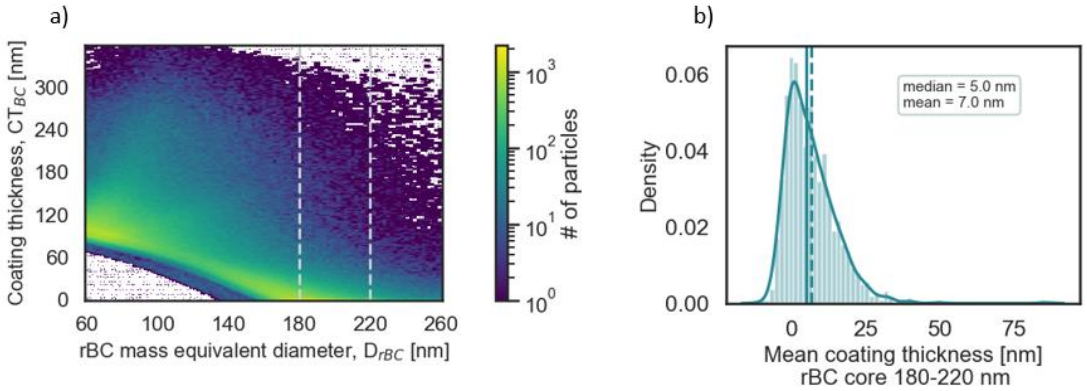

Figure 6-7: Left panel: Coating thickness as a function of rBC diameter for all measured particles. Right panel: density distribution of mean coating thickness derived for rBC cores with diameters in the range 180-220 nm, at the Chacaltaya station.

This result is rather surprising for a remote site like CHC, where we expected to measure mainly long-aged particles. Similar cases of thinly coated BC have been observed in the upper troposphere on the Swiss Alps, e.g. significantly lower in winter compared to summer at Jungfraujoch (Motos et al., 2020). In addition, very low coating thickness was observed downstream of a fire plume passing through clouds in Canada (Taylor et al., 2014). It has been hypothesized that the reduced coating thickness may be due to more effective removal of heavily coated particles in precipitating clouds. However, in the context of the campaign in CHC, this scenario seems unlikely given that it was carried out during the transition period with the dry season when not so frequent precipitations are present, and only a couple of days of precipitations were observed in the metropolitan region.

6.2.4 Optical properties

The optical properties of BC particles were estimated by calculating the MAC at 637 nm as described in Section 3.4.2.2. This was done to evaluate the radiative impact of the particles in this location and to assess potential differences with the urban sites. The MAC mean were 24±13 m^2/g, with a median of 21 m^2/g. These values are three times higher than those measured in the metropolitan region, and also vary high compared to the maximum values reported in Zanatta et al., (2016) at the mountain site of Puy de Dôme (17.3±1.71 m^2/g up to 19.9±1.68 m^2/g in summer), and to the highest measured by Tinorua et al., (2023) at Pic du Midi observatory.

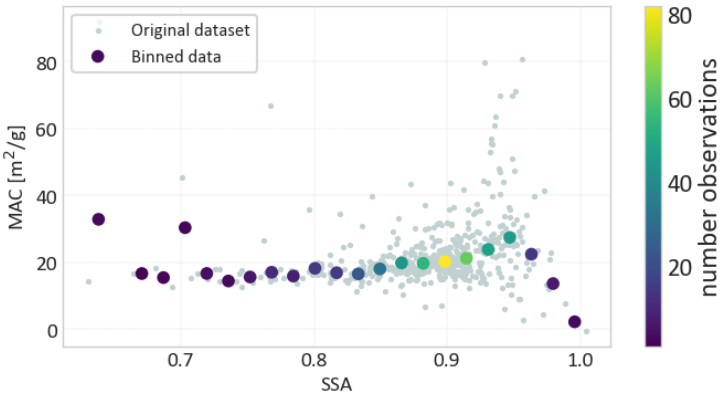

Figure 6-8: MAC (derived with rBC and MAAP at 637 nm) dependence on SSA (derived with MAAP and nephelometer).

As observed in BCN, the presence of coating would cause the radiation to interact more efficiently with rBC cores through the lensing effect, leading to an increase in the MAC. The high MAC values observed at CHC, however, cannot be explained by the lensing effect, due to the thin coatings. To exclude potential source of biases in these results, we checked the data quality of mass concentration measurements by comparing different techniques. The results obtained in this work using rBC mass concentration are well comparable to what is found by Mardonez et al. (2024) using EC mass concentration, excluding biases due to the SP2's mass correction applied. Considering the absorption coefficient, the MAAP instrument used in this study is considered to be a reference for absorption measurements, and subject to little

instrumental bias (Weingartner et al., 2003; Collaud Coen et al., 2010; Yus-Díez et al., 2021). However, a potential source of bias in absorption coefficient measurements with filter-based instruments is the presence of non-absorbing particles collected in the filter, which can be approximated with the single scattering albedo (SSA). While examining the variability of MAC with SSA in this site (Figure 6-8), we observe a tendency for MAC to increase at high SSA values. However, it's important to note that SSA values during the campaign are never exceptionally high. Additionally, this potential bias alone does not account for the consistently high MAC observed even at lower SSA values. In essence, this bias might contribute to positive peaks and outliers, especially during periods of very low concentrations. However, when excluding periods with concentrations below a certain threshold (e.g., < 0.01 μg/m^3), the results show only minimal deviations from the median obtained using all values (still 21 m^2/g in both cases with a reduced standard deviation of 8 m^2/g compared to 13 m^2/g).

Another potential source of bias at low BC concentrations is the presence of other absorbing components in the sample collected on the filter, specifically dust and organic material. The presence of organic matter could result in an overestimation of absorption, potentially up to 10%, as indicated by Zanatta et al. (2016). However, it's crucial to note that at these wavelengths, organic matter is not expected to be the dominant absorber. Regarding dust, it is unlikely to cause substantial differences in the measurements. If dust were a significant contributor, we would observe a notable impact on absorption and, consequently, a bias in the MAC also in EA, where a substantial percentage of dust in the total particulate matter was identified (Mardoñez et al., 2023).

In summary, we have no other reason than a substantial presence of highly aged particles at this location, to explain the heightened MAC measured at this site. It is thus plausible that the average coating value was subject to significant biases that affect its accuracy. As pointed out by Naseri et al. (2023), in addition to the limited detection range, the SP2 may underestimate the actual coating due to the assumptions required to apply LEO-fit. In this case, it's possible that the spherical core-shell assumption or the refractive indices used as input to Mie theory are significantly different from reality, leading to

an underestimation of the coating in this diameter range. By considering as representative for the site the median MAC value obtained after excluding periods with concentrations below 0.01 µg/m^3, the resulting absorption enhancement is E_{abs} = 3.2, upper limit of many ambient observations (Cappa et al., 2019).

6.3 INFLUENCE OF AIR TRANSPORT ON rBC PROPERTIES

6.3.1 Free tropospheric air masses

The potential evolution of rBC properties and their mixing state with the influence of the planetary boundary layer was studied by dividing the dataset into periods with free troposphere characteristics (FT) and periods significantly influenced by the boundary layer (BL), as described in Section 6.1.1.2. First, the periods identified as BL were characterised by much higher average concentrations than those identified as FT.

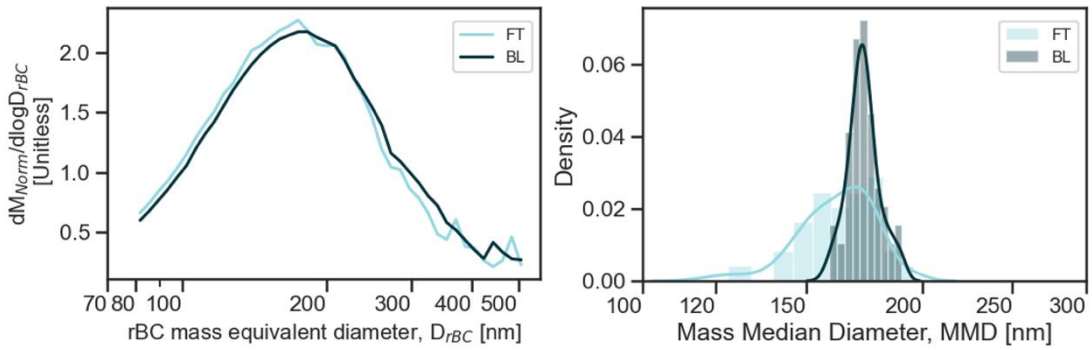

Figure 6-9: Variability of rBC size at Chacaltaya station during periods affected by boundary layer (BL) influence and free troposphere influence (FT). Left panel: normalized mass size distribution. Right panel: distribution of the mass median diameter (MMD).

The mean m_{rBC} value in BL periods (0.13 µg/m^3) was six times higher than that in FT periods (0.02 µg/m^3). This increase clearly shows the influence of direct sources on BC levels in a remote location via vertical transport modulated by the boundary layer dynamics, as observed at CHC by Wiedensohler et al. (2018). This vertical export, driven by mountain-valley circulation, was also reported as an efficient transport pathway of BC at high altitudes in the Chilean Andes (Lapere et al., 2023; Ruggeri et al., 2024).

However, these studies could not investigate other microphysical properties of BC such as size and mixing. The comparison between particle sizes in the two type of periods is shown in Figure 6-9, were both the size distributions and the histogram of hourly averaged MMD are reported. The size distributions are very similar with just a slight shift towards smaller diameters in FT period compared to BL period. This trend is confirmed by the density distributions of MMD, revealing a common mode around 170 nm. However, for FT periods the diameters have a wider variability, being more spread towards smaller values not observed in BL. It thus appears that even short time spent in the boundary layer, strongly modified the overall properties of FT-rBC, as confirmed by the similarity with the EA size distribution. None the less, the wider spread in MMD of FT-rBC might suggest the influence of different processes on the rBC size. As an example, the impact of cloud processing on D_{rBC} might be further investigated at the CHC site using a combination of back-trajectories, reanalysis data and CO measurements as proposed in Tinorua et al. (2023).

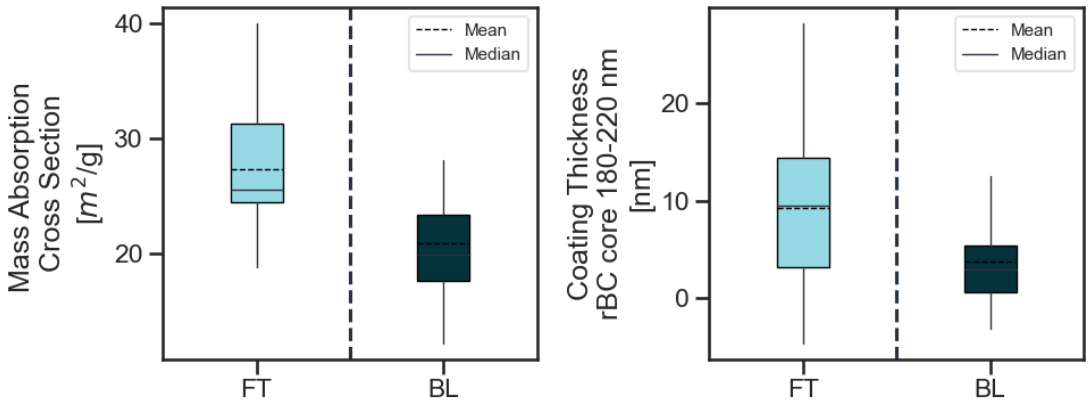

Figure 6-10: Coating thickness and mass absorption cross-section boxplots corresponding to FT and BL periods, at Chacaltaya.

Besides rBC diameter, the main difference between the two air masses was related to the mixing state of the particles. BL periods had a coating very close to 0 and a MAC very close the median derived for the whole campaign. The presence of null or thin coatings suggests the dominance of fresh rBC, externally mixed with other atmospheric material as expected in urban

environments (Laborde et al., 2013). FT periods have slightly higher values of coating (mean coating thickness of 9.2 nm) and a mean MAC of 27 m^2/g. Particles observed for free tropospheric periods seems thus to be more mixed than those observed during transport from the PBL. This is close to expectations since in the free troposphere we expect to measure particles that have been in suspension in the atmosphere for a longer time and are therefore subject to increased ageing.

Nonetheless, the coatings observed in FT at CHC remained thinner compared to continental Europe (Laborde et al., 2013) or the Arctic (Zanatta et al., 2018). The fact that an increase in MAC corresponds to an increase in coating is in line with the lensing effect described above. However, given the likely poor accuracy of the coating values, it is difficult to study the relationship between these variables in more depth. Looking at these results, summarized in Table 6-1, particles measured in the different type of air masses probably derive from similar sources, as the properties of the rBC cores do not show substantial differences. The main difference between FT and BL periods is that in former particles remained in suspension for a longer time, ageing more through mixing with other compounds and with a compaction of the internal core.

6.3.2 Air masses following different pathways

6.3.2.1 *Mass concentrations*

Three dominant horizontal pathways, not distinguished in FT and BL, followed by the air masses reaching Chacaltaya were identified as described in Section 6.1.1.1. The average rBC mass concentration varied depending on the pathway, as summarized in Table 6-1. The South-West sector was associated with the highest concentration as we can see in Figure 6-11. Not only the average and the median were the highest but also the lowest and highest percentiles. This result is consistent with the presence of the metropolitan region of LP-EA in the path followed by these air masses. From the diurnal profile (Figure 6-11) it is indeed evident the increase during the day up to 0.46 $\mu g/m^3$ at midday, and higher concentrations compared to other sectors even during the night (0.04 - 0.07 $\mu g/m^3$). On the other hand, the path involving the

east sector (E) has the lowest values, with a slight increase during the day, not exceeding 0.25 µg/m^3, and values ten times smaller during the night (0.017 - 0.027 µg/m^3). This sector was characterized by the presence of the Amazon basin and lowlands, where biomass burning emissions are systematic and has been shown to affect the melting rate of glaciers in the Andes (Magalhães et al., 2019). However, the low rBC concentration did not reflect any influence of major biomass burning emission in the Eastern sector. As matter of fact, this campaign occurred in the low of the biomass burning seasonal cycle, which is characterized by BC concertation peak between June and February (Artaxo et al., 2013).

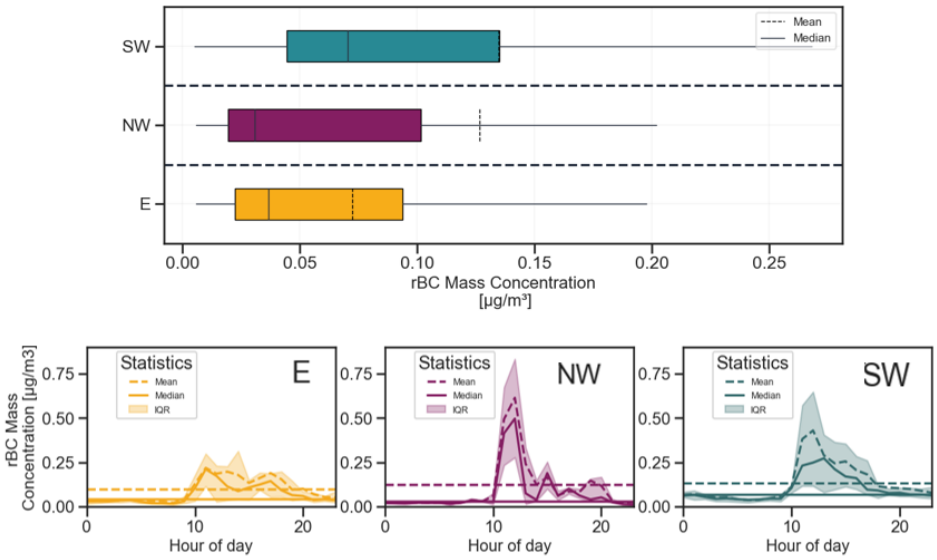

Figure 6-11: rBC mass concentrations measured at Chacaltaya for different air mass pathways coming from South-West (SW), North-West (NW) and East (E).

Finally, the northwest sector, which also includes part of the Amazon rainforest to the north and the Altiplano to the west, is characterized by intermediate and more variable concentrations than the other sectors. First, the large difference between mean (0.14 µg/m^3, similar to the SW mean) and median (0.03 µg/m^3, lower than E median) suggested the establishment of a clean background condition perturbed by intense pollution vents. From the diurnal variability (Figure 6-11) we can appreciate how night-time concentration was very low (0.008-0.022 µg/m^3), lower than the eastern sector, but then raised significantly

by two orders of magnitude for a few hours in the late morning up to 0.65 µg/m^3 (higher than the diurnal maximum of the SW sector). Hence, the sector NW was affected by extremely pristine and extremely polluted contributions, potentially reflecting mixed contributions from the clean eastern sector and the polluted SW sector. It must be considered that, the NW sector was also the one for which the lowest counting statistic with only 5 days of dominant influence.

6.3.2.2 *Particle population properties*

Figure 6-12 shows some of the microphysical properties of BC in the different sectors. In particular, we can see from Figure 6-12a and Figure 6-12b that there was no significant difference in the distributions of the mean hourly values of the mass median diameter and the mean distribution.

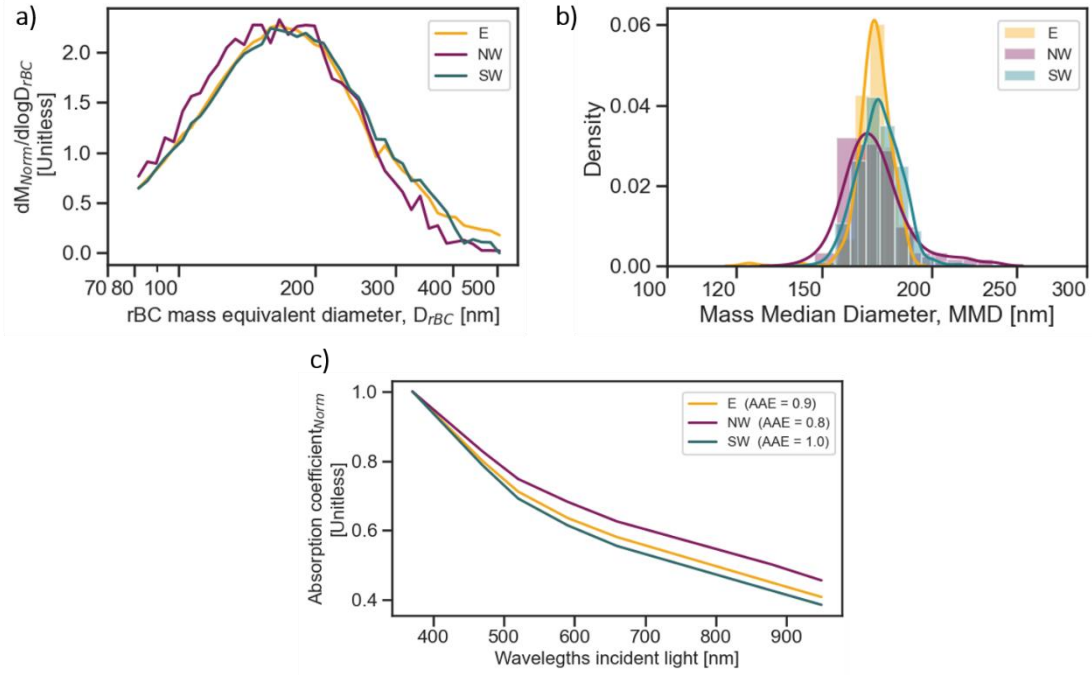

Figure 6-12: Variability of mean microphysical and optical properties of BC at Chacaltaya in the different sectors calculated on hourly time stamp. a) Normalized mass size distribution of rBC; b) Density distribution of mass median diameter (MMD); c) Spectral dependence of the absorption coefficient. Sectors: South-West (SW), North-West (NW), East (E).

Although the North West sector showed the widest distribution of MMD, the mean MMD from all sectors fell within 5 nm from 185 nm (NW) to 190 nm

(SW), not enough to be representative of different particle populations. Similarly, the spectral dependence of the absorption did not seem to show any substantial differences (Figure 6-12c). The resulting absorption exponent varied from 0.8 (NW) to 1.0 (SW), potentially related to more compact and aged particles (Liu et al., 2018) rather than soot produced from biomass burning (Zotter et al., 2017).

A slight difference can be observed in the mixing state of the particles shown in Figure 6-13 in terms of coating thickness and mass absorption cross-section. The NW sector was confirmed to have mixed influence leading to strong variability but also highest absolute means of both the MAC (24 m^2/g) and coating thickness (13 nm). The cleanest Amazonian sector (E), showed, on the contrary, thin mean coatings (2.5 nm) and the lowest mean MAC (21 m^2/g). The most polluted sector, intermediate mean values were observed (MAC = 22 m^2/g; CT = 7.2 nm). Overall, the MAC values for the different sectors fell within the MAC uncertainty of 18% propagated by the absorption coefficient uncertainty (MAAP; 15%; Müller et al., 2011) and rBC mass concentration uncertainty (SP2; 10%; Laborde et al., 2012). Otherwise, the coating thickness appeared to have a sector-to-sector variability higher than its instrumental uncertainty of 17% (Laborde et al., 2012b).

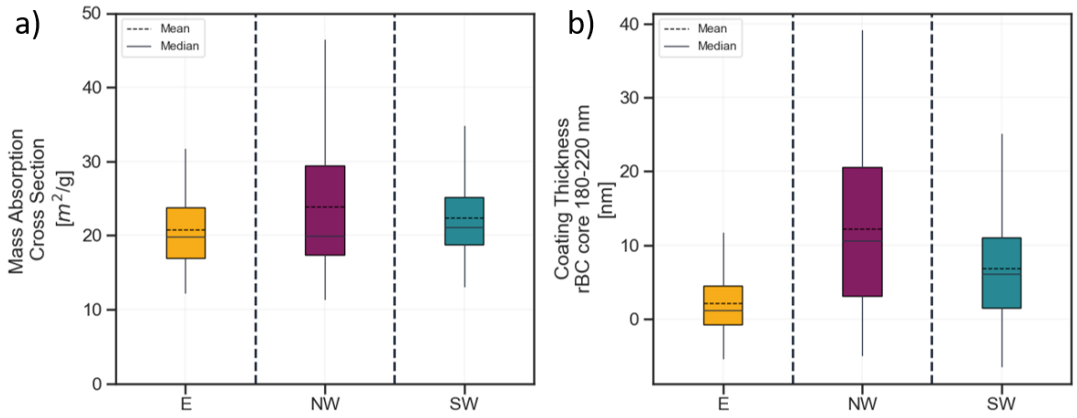

Figure 6-13: Boxplot of optical properties and mixing state of BC at Chacaltaya in the different sectors calculated on hourly time stamp. Left panel: mass absorption cross-section at a wavelength of 637 nm. Right panel: coating thickness for rBC cores with a diameter of 180-220 nm; Spectral dependence of the absorption coefficient. Sectors: South-West (SW), North-West (NW), East (E).

The similarity in properties observed in air masses that followed such different pathways, as well as the common shape of the diurnal profiles, suggest that the observed rBC particles may not have had such different sources during this campaign. While the eastern and northern sectors, dominated by the Amazon rainforest, could have been influenced by BC transport from biomass burning, it's important to note that this campaign took place during the transition between the rainy and dry seasons, a period less affected by such events. No substantial change towards larger particle diameters or higher AAE is observed, as would be expected in the presence of large biomass burning particle transport events. The primary source region for BC appears to be LP and EA, considering that other urban areas are at least 200 km away. During periods dominated by air masses from the east or northwest, pollution from this source region is likely to be diluted by cleaner air, resulting in lower concentrations.

Table 6-1: Summary of averaged and standard deviation values of main properties, for different air masses characteristics. Free tropospheric and boundary layer influenced air masses are summarized as well as air masses from different pathways East (E), North West (NW) and South West (SW).

	[rBC] μg/m^3	MMD nm	CT nm	MAC m^2/g
FT	0.02 ± 0.02	164 ± 14	9.2 ± 9.2	27.3 ± 5.4
BL	0.13 ± 0.15	173 ± 7	3.7 ± 4.9	20.9 ± 5.3
E	0.07 ± 0.08	172 ± 6	2 ± 4	20.8 ± 5.7
NW	0.13 ± 0.25	174 ± 15	12 ± 11	23.4 ± 8.7
SW	0.14 ± 0.19	175 ± 10	7 ± 7	22.1 ± 5.3

6.3.3 Contribution of volcanic emissions to coating formation on BC particles

The works of Aliaga et al. (2021) and Bianchi et al. (2022) show that the volcanic activity of the Sabancaya volcano in Peru had a visible impact on the aerosol properties measured at the CHC site during this measurement campaign. Moreno et al. (2023) in particular showed how the SO_4^{2-} concentration is dominated by volcanic activity at this site.

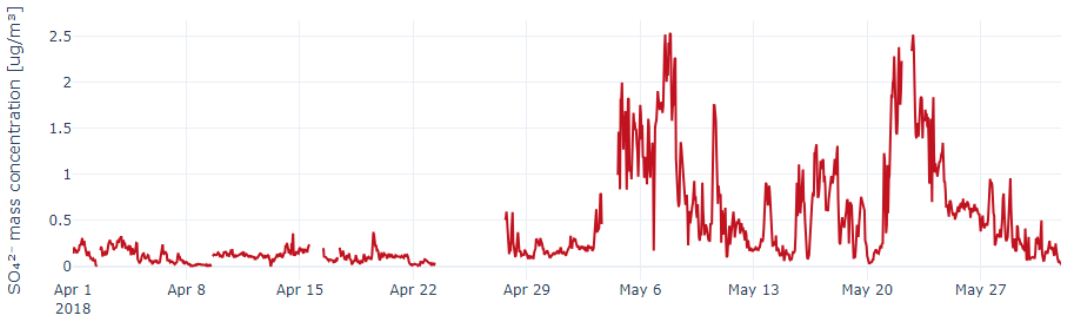

Figure 6-14: time series of the SO_4^{2-} mass concentration during the campaign.

With the aim to study if the volcanic activity could have had an impact on BC properties during our campaign, we looked through SO_4^{2-} variability for the presence of air impacted by volcanic activity, identified a parameter able to quantify this impact on the aerosol composition and properties and studied the variability of BC concentration and coating of BC-containing particles as a function of this parameter.

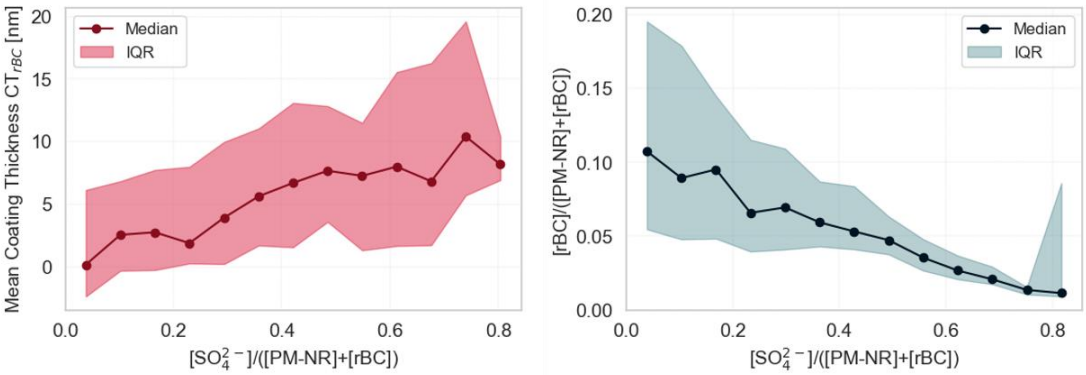

Figure 6-15: Scatterplots showing the dependence of the mean coating thickness and the rBC/([NR-PM]+[rBC]) ratio, on the $[SO_4^{2-}]$/([NR-PM]+[rBC]) ratio, under the influence of volcanic emission observed at Chacaltaya on May 2018.

As we can see from Figure 6-14, the impact of volcanic activity was clearly visible in the second part of the campaign when the concentrations of SO_4^{2-} shifted from being less than 0.5 µg/m^3 to 2.5 µg/m^3. As a parameter to represent this impact on the aerosol properties we calculated the ratio between SO_4^{2-} concentration and the total aerosol mass concentration, obtained as the sum between the total concentration of non-refractory material NR-PM

derived from the ACSM and the rBC mass concentration ([SO_4^{2-}]/([NR-PM]+[rBC])).

Figure 6-15 shows how this parameter correlated with the rBC mass concentration and coating thickness. The coating thickness increased with the relative concentration of SO_4^{2-} and decreased with the rBC relative concertation. This means that volcanic activity may influence the mixing state of rBC providing aerosol precursors such as SO_2 and sulphate aerosol SO_4^{2-} and SO_2, which can condense and coagulate with rBC particles. Hence, even if SO_4^{2-} is not recognized as a major component of black carbon coatings (Fierce et al., 2016; Zhang et al., 2018; Wang et al., 2019), volcanic emission might represent an important regional and punctual driver for BC ageing.

7 CONCLUSIONS

In this thesis I explored some of the challenges related to the quantification of BC impacts on the climate system, from the accuracy of measurement to the characterization of some properties and atmospheric processes in different environments.

First of all, I studied how to reduce the uncertainty in eBC observations. The measure of the absorption coefficient of aerosol particles is at date one of the sources of uncertainty in the evaluation of BC impact on climate. The aethalometer is the instrument most widely used to measure the absorption coefficient and its use is recommended by research infrastructures and global networks. It requires a parameter, C, to correct for the multiple scattering of the sampled particles on the filter tape. We calculated the C parameter by using two model of aethalometer (AE33, AE31) compared to different reference techniques (MAAP, EMS). We analysed the C variability in ambient conditions at different environments and through experiments in the CESAM simulation chamber. We obtained significantly different values in different sites, with an average of 2.3 ± 0.5 (SD) at the CMN mountain site of to a mean value of 3.1 ± 0.4 (SD) at the background polluted site of JRC. The C_{AE33} value at JRC regional background site was 35% higher than to the mountain top site. In ambient studies non-significant seasonal and wavelength dependence of the C_{AE33} was observed. C_{AE33} showed higher values at high SSA but the observations available were not enough to properly assess a clear relation. Chamber experiments allowed to explore the C variability with composition and size of freshly emitted particles, suggesting that the difference found between the background and the mountain top sites could be related to higher concentrations of small particles with a higher organic content. It was observed that the variability introduced by the aethalometer model was significant, with C_{AE31} values systematically higher and opposite relationship with SSA compared to C_{AE33}. These results reinforce the message that this corrective parameter can vary significantly from site to site, due to different properties of the collected particles. The use of a standardised value of C, which is necessary

in absence of a reference technique to derive it, can lead to a significant deviation in the absorption coefficient estimate. Moreover, clear recommendations for a reference technique to directly measure the BC mass concentration are still missing, and two of the most used techniques, the incandescence emission detection (m_{rBC}) and the thermo-optical analysis (m_{EC}) can differ for a factor up to 1.75. The combination of these two sources of uncertainty can induce a deviation in the MAC estimate up to 90%.

On the other hand, the monitoring and characterization of BC concentration and properties in different urban and remote environments is essential for an improvement of policy actions to reduce urban air pollution and to derive important information, needed in models for a better representation of BC ageing and a better quantification of BC radiative forcing.

I first focused on the analysis of eBC concentrations in two urban environments located in the European hot spot for climate and air quality: the Po Valley. Despite the stringent air quality policies in this area, the analysis revealed that eBC accounted for a significant proportion (11-12%) of submicron particulate matter, both in Milan and Bologna. This contribution was comparable to that of major inorganic components such as sulphate and ammonium. BC emissions were mainly associated to vehicular traffic (~75%) in both cities, in particular in summer, while in winter the contribution of biomass burning becomes nearly 50% of total eBC. This analysis is important to derive more efficient policy for air quality regulations. Reducing source-specific BC emissions as a function of the season can reduce people exposure to harmful compounds in the Po Valley. The first objective to reach in both cities should be the reduction of vehicular traffic with policies that promote the use of alternative means of transport such as public transport and cycling. However, measures to improve the efficiency of heating systems and favour cleaner energy choices can also be important in reducing emissions, particularly during the most polluted winter period, when the legal limits for particulate matter are most often reached and exceeded.

Some of the most important BC properties needed for a better modelling of BC life cycle and climate impact, the mass concentration, the mass size distribution and MMD, the coating thickness and the MAC, have been

studied in this work both in different urban areas and a remote mountain top site. The diurnal profiles of the BC mass concentrations significantly differ in different urban environments and at the mountain top. All urban environments were characterized by a typical bimodal pattern during the day, but the timing and the magnitude of the main peaks can significantly differ from city to city because of population habits, orography and meteorological conditions affecting the dilution and accumulation of particles. The mountain top site showed an inverted pattern due to the absence of local sources, and a reversed influence of the boundary layer variability, bringing pollutants thanks to valley breezes in early afternoon.

The size distributions can also differ significantly in different cities, reflecting the distance from sources and their variability. Sites located closer to major roads (<50 m) such as LP and BCN shows distributions more affected by smaller particles with the peak of the mass median distribution at 85 and 102 nm, respectively. While EA located at a longer distance from major roads > 250 m, and potentially affected by waste burning in addiction to traffic, shows larger particles with a peak of the distribution at 187 nm. The mountain top site shows instead a distribution very close to the one observed in EA, more representative for the background conditions of the whole metropolitan region, with a peak at a diameter of 171 nm. Particle size evolve quickly through aggregation of small particles in highly polluted urban environments, while no significant variation was observed during transport towards more clean environments. In CHC, slightly smaller particles were observed during free tropospheric conditions, suggesting a possible rearrangement of BC when remained longer in suspension. No significant diameter fluctuations were instead observed for air masses coming from different regions.

The coating thickness was also estimated in one of the urban sites, BCN and in the CHC mountain top site. Small coatings were observed both in the urban and in the mountain site with an averaged value of 14.6 nm and 7 nm respectively. The one in Barcelona is consistent with freshly emitted particles form traffic sources, while that in CHC is probably affected by biases in the method used to calculate it. However, a significant increase in the coating at CHC was observed when the site has been affected by volcanic activity.

Finally, the variability of optical properties represented by the MAC have been evaluated in all the sites. Values in the range 8-11 m^2/g were observed in the three urban sites. In LP and EA, lower values closer to the one reported for uncoated BC were observed, while BCN was characterised by a slight enhancement due to the presence of a non-negligible coating thickness. These properties can be significantly different in urban environments due to different meteorological conditions. Smaller particles with a lower absorption enhancement were observed during rush hours in BCN compared to periods cleaner with air masses from the sea. In CHC the value was surprisingly much higher up to 24 m^2/g, and this is probably due to the high level of mixing of these aged particles. It cannot be excluded that the exceptionally high MAC values calculated at CHC might derive from inconsistencies of SP2 values compared to potential eBC observations. Hence, the CHC MAC anomaly might be regarded as an excellent example to improve the repeatability of absorption and BC observations across monitoring networks. The MAC can be thus significantly different from urban to mountain top sites. Close to sources particles are more externally mixed with other compounds resulting in just a slight increase in the absorption compared to that of bare BC particles, while after a long aging, internal mixing become predominant inducing a strong absorption enhancement.

These results are important to highlight the need of a better characterization of BC properties in different urban environments, as they can vary significantly close to sources depending on the type of the source and the meteorological conditions. This characterization set the starting conditions in models for evaluating the subsequent BC life cycle and BC radiative forcing both close and far from the source. Moreover, the results in CHC show the high importance of deriving correct absorption enhancement in remote locations, where the degree of internal mixing can be very high. This can lead to huge impacts on BC radiative forcing regional estimate in these areas.

BIBLIOGRAPHY

Adachi, K. and Buseck, P. R.: Changes of ns-soot mixing states and shapes in an urban area during CalNex, J. Geophys. Res. Atmospheres, 118, 3723–3730, https://doi.org/10.1002/jgrd.50321, 2013.

Adachi, K., Chung, S. H., and Buseck, P. R.: Shapes of soot aerosol particles and implications for their effects on climate, J. Geophys. Res. Atmospheres, 115, https://doi.org/10.1029/2009JD012868, 2010.

Ahlberg, E., Ausmeel, S., Nilsson, L., Spanne, M., Pauraite, J., Klenø Nøjgaard, J., Bertò, M., Skov, H., Roldin, P., Kristensson, A., Swietlicki, E., and Eriksson, A.: Measurement report: Black carbon properties and concentrations in southern Sweden urban and rural air – the importance of long-range transport, Atmospheric Chem. Phys., 23, 3051–3064, https://doi.org/10.5194/acp-23-3051-2023, 2023.

Albrecht, B. A.: Aerosols, cloud microphysics, and fractional cloudiness, Science, 245, 1227–1230, https://doi.org/10.1126/science.245.4923.1227, 1989.

Alfaro, S. C., Lafon, S., Rajot, J. L., Formenti, P., Gaudichet, A., and Maillé, M.: Iron oxides and light absorption by pure desert dust: An experimental study, J. Geophys. Res. Atmospheres, 109, https://doi.org/10.1029/2003JD004374, 2004.

Aliaga, D., Sinclair, V. A., Andrade, M., Artaxo, P., Carbone, S., Kadantsev, E., Laj, P., Wiedensohler, A., Krejci, R., and Bianchi, F.: Identifying source regions of air masses sampled at the tropical high-altitude site of Chacaltaya using WRF-FLEXPART and cluster analysis, Atmospheric Chem. Phys., 21, 16453–16477, https://doi.org/10.5194/acp-21-16453-2021, 2021.

Anderson, T. L. and Ogren, J. A.: Determining Aerosol Radiative Properties Using the TSI 3563 Integrating Nephelometer, Aerosol Sci. Technol., 29, 57–69, https://doi.org/10.1080/02786829808965551, 1998.

Anderson, T. L., Covert, D. S., Marshall, S. F., Laucks, M. L., Charlson, R. J., Waggoner, A. P., Ogren, J. A., Caldow, R., Holm, R. L., Quant, F. R., Sem, G. J., Wiedensohler, A., Ahlquist, N. A., and Bates, T. S.: Performance Characteristics of a High-Sensitivity, Three-Wavelength, Total Scatter/Backscatter Nephelometer, J. Atmospheric Ocean. Technol., 13, 967–986, https://doi.org/10.1175/1520-0426(1996)013, 1996.

Anderson, T. L., Wu, Y., Chu, D. A., Schmid, B., Redemann, J., and Dubovik, O.: Testing the MODIS satellite retrieval of aerosol fine-mode fraction, J. Geophys. Res. Atmospheres, 110, https://doi.org/10.1029/2005JD005978, 2005.

Andrade, M., Zaratti, F., Forno, R., Gutiérrez, R., Moreno, I., Velarde, F., Ávila, F., Roca, M., Sánchez, M. F., Laj, P., Jaffrezo, J. L., Ginot, P., Sellegri, K., Ramonet, M., Laurent, O., Weinhold, K., Wiedensohler, A., Krejci, R., Bonasoni, P., Cristofanelli, P., Whiteman, D., Vimeux, F., Dommergue, A., and Magand, O.: Set to work of a new climate monitoring station in the central andes of Bolivia: the Gaw/Chacaltaya station, Rev. Boliv. Física, 26, 06–15, 2015.

Barcelona traffic report | TomTom Traffic Index: https://www.tomtom.com/traffic-index/barcelona-traffic/, last access: 11 January 2024.

Anon: Parque Automotor, INE, n.d.

Artaxo, P., Rizzo, L., F. de Brito, J., Barbosa, H., Arana, A., Sena, E., Cirino, G., Bastos, W., Martin, S., and Andreae, M.: Atmospheric aerosols in Amazonia and land use change: From natural biogenic to biomass burning conditions, Faraday Discuss., 165, 203–35, https://doi.org/10.1039/c3fd00052d, 2013.

Atkinson, J. D., Murray, B. J., Woodhouse, M. T., Whale, T. F., Baustian, K. J., Carslaw, K. S., Dobbie, S., O'Sullivan, D., and Malkin, T. L.: The importance of feldspar for ice nucleation by mineral dust in mixed-phase clouds, Nature, 498, 355–358, https://doi.org/10.1038/nature12278, 2013.

Backman, J., Schmeisser, L., Virkkula, A., Ogren, J. A., Asmi, E., Starkweather, S., Sharma, S., Eleftheriadis, K., Uttal, T., Jefferson, A., Bergin, M., Makshtas, A., Tunved, P., and Fiebig, M.: On Aethalometer measurement uncertainties and an instrument correction factor for the Arctic, Atmospheric Meas. Tech., 10, 5039–5062, https://doi.org/10.5194/amt-10-5039-2017, 2017.

Bauer, S. E., Bausch, A., Nazarenko, L., Tsigaridis, K., Xu, B., Edwards, R., Bisiaux, M., and McConnell, J.: Historical and future black carbon deposition on the three ice caps: Ice core measurements and model simulations from 1850 to 2100, J. Geophys. Res. Atmospheres, 118, 7948–7961, https://doi.org/10.1002/jgrd.50612, 2013.

Baumgardner, D., Popovicheva, O., Allan, J., Bernardoni, V., Cao, J., Cavalli, F., Cozic, J., Diapouli, E., Eleftheriadis, K., Genberg, P. J., Gonzalez, C., Gysel, M., John, A., Kirchstetter, T. W., Kuhlbusch, T. a. J., Laborde, M., Lack, D., Müller, T.,

Niessner, R., Petzold, A., Piazzalunga, A., Putaud, J. P., Schwarz, J., Sheridan, P., Subramanian, R., Swietlicki, E., Valli, G., Vecchi, R., and Viana, M.: Soot reference materials for instrument calibration and intercomparisons: a workshop summary with recommendations, Atmospheric Meas. Tech., 5, 1869–1887, https://doi.org/10.5194/amt-5-1869-2012, 2012.

Baynard, T., Lovejoy, E. R., Pettersson, A., Brown, S. S., Lack, D., Osthoff, H., Massoli, P., Ciciora, S., Dube, W. P., and Ravishankara, A. R.: Design and Application of a Pulsed Cavity Ring-Down Aerosol Extinction Spectrometer for Field Measurements, Aerosol Sci. Technol., 41, 447–462, https://doi.org/10.1080/02786820701222801, 2007.

Becerril-Valle, M., Coz, E., Prévôt, A. S. H., Močnik, G., Pandis, S. N., Sánchez de la Campa, A. M., Alastuey, A., Díaz, E., Pérez, R. M., and Artíñano, B.: Characterization of atmospheric black carbon and co-pollutants in urban and rural areas of Spain, Atmos. Environ., 169, 36–53, https://doi.org/10.1016/j.atmosenv.2017.09.014, 2017.

Bellouin, N.: Aerosols: Role in Climate Change, in: Encyclopedia of Atmospheric Sciences: Second Edition, 76–85, https://doi.org/10.1016/B978-0-12-382225-3.00054-2, 2014.

Bergstrom, R. W., Russell, P. B., and Hignett, P.: Wavelength Dependence of the Absorption of Black Carbon Particles: Predictions and Results from the TARFOX Experiment and Implications for the Aerosol Single Scattering Albedo, J. Atmospheric Sci., 59, 567–577, https://doi.org/10.1175/1520-0469(2002)059, 2002.

Bergstrom, R. W., Pilewskie, P., Russell, P. B., Redemann, J., Bond, T. C., Quinn, P. K., and Sierau, B.: Spectral absorption properties of atmospheric aerosols, Atmospheric Chem. Phys., 7, 5937–5943, https://doi.org/10.5194/acp-7-5937-2007, 2007.

Bernardoni, V., Ferrero, L., Bolzacchini, E., Forello, A. C., Gregorič, A., Massabò, D., Močnik, G., Prati, P., Rigler, M., Santagostini, L., Soldan, F., Valentini, S., Valli, G., and Vecchi, R.: Determination of Aethalometer multiple-scattering enhancement parameters and impact on source apportionment during the winter 2017/18 EMEP/ACTRIS/COLOSSAL campaign in Milan, Atmospheric Meas. Tech., 14, 2919–2940, https://doi.org/10.5194/amt-14-2919-2021, 2021.

Bianchi, F., Sinclair, V. A., Aliaga, D., Zha, Q., Scholz, W., Wu, C., Heikkinen, L., Modini, R., Partoll, E., Velarde, F., Moreno, I., Gramlich, Y., Huang, W., Koenig, A. M., Leiminger, M., Enroth, J., Peräkylä, O., Marinoni, A., Xuemeng, C., Blacutt, L., Forno, R., Gutierrez, R., Ginot, P., Uzu, G., Facchini, M. C., Gilardoni, S., Gysel-Beer, M., Cai, R., Petäjä, T., Rinaldi, M., Saathoff, H., Sellegri, K., Worsnop, D., Artaxo, P., Hansel, A., Kulmala, M., Wiedensohler, A., Laj, P., Krejci, R., Carbone, S., Andrade, M., and Mohr, C.: The SALTENA Experiment: Comprehensive Observations of Aerosol Sources, Formation, and Processes in the South American Andes, Bull. Am. Meteorol. Soc., 103, E212–E229, https://doi.org/10.1175/BAMS-D-20-0187.1, 2022.

Birch, M. E. and Cary, R. A.: Elemental Carbon-Based Method for Monitoring Occupational Exposures to Particulate Diesel Exhaust, Aerosol Sci. Technol., 25, 221–241, https://doi.org/10.1080/02786829608965393, 1996.

Bisiaux, M. M., Edwards, R., McConnell, J. R., Albert, M. R., Anschütz, H., Neumann, T. A., Isaksson, E., and Penner, J. E.: Variability of black carbon deposition to the East Antarctic Plateau, AD 1800–2000, Aerosols/Field Measurements/Troposphere/Chemistry (chemical composition and reactions), https://doi.org/10.5194/acpd-11-31091-2011, 2011.

Bohren, C. F. and Huffman, D. R.: Absorption and Scattering of Light by Small Particles, 544 pp., 1998.

Bond, T. C. and Bergstrom, R. W.: Light Absorption by Carbonaceous Particles: An Investigative Review, Aerosol Sci. Technol., 40, 27–67, https://doi.org/10.1080/02786820500421521, 2006.

Bond, T. C., Anderson, T. L., and Campbell, D.: Calibration and Intercomparison of Filter-Based Measurements of Visible Light Absorption by Aerosols, Aerosol Sci. Technol., 30, 582–600, https://doi.org/10.1080/027868299304435, 1999.

Bond, T. C., Habib, G., and Bergstrom, R. W.: Limitations in the enhancement of visible light absorption due to mixing state, J. Geophys. Res. Atmospheres, 111, https://doi.org/10.1029/2006JD007315, 2006.

Bond, T. C., Doherty, S. J., Fahey, D. W., Forster, P. M., Berntsen, T., DeAngelo, B. J., Flanner, M. G., Ghan, S., Kärcher, B., Koch, D., Kinne, S., Kondo, Y., Quinn, P. K., Sarofim, M. C., Schultz, M. G., Schulz, M., Venkataraman, C., Zhang, H., Zhang, S., Bellouin, N., Guttikunda, S. K., Hopke, P. K., Jacobson, M. Z., Kaiser, J. W., Klimont, Z., Lohmann, U., Schwarz, J. P., Shindell, D., Storelvmo, T., Warren, S.

G., and Zender, C. S.: Bounding the role of black carbon in the climate system: A scientific assessment, J. Geophys. Res. Atmospheres, 118, 5380–5552, https://doi.org/10.1002/jgrd.50171, 2013.

Bozzo, A., Remy, S., Benedetti, A., Flemming, J., Bechtold, P., Rodwell, M., and Morcrette, J.-J.: Implementation of a CAMS-based aerosol climatology in the IFS, 2017.

Cachier, H., Brémond, M.-P., and Buat-Ménard, P.: Carbonaceous aerosols from different tropical biomass burning sources, Nature, 340, 371–373, https://doi.org/10.1038/340371a0, 1989.

Cappa, C. D., Onasch, T. B., Massoli, P., Worsnop, D. R., Bates, T. S., Cross, E. S., Davidovits, P., Hakala, J., Hayden, K. L., Jobson, B. T., Kolesar, K. R., Lack, D. A., Lerner, B. M., Li, S.-M., Mellon, D., Nuaaman, I., Olfert, J. S., Petäjä, T., Quinn, P. K., Song, C., Subramanian, R., Williams, E. J., and Zaveri, R. A.: Radiative absorption enhancements due to the mixing state of atmospheric black carbon, Science, 337, 1078–1081, https://doi.org/10.1126/science.1223447, 2012.

Cappa, C. D., Zhang, X., Russell, L. M., Collier, S., Lee, A. K. Y., Chen, C.-L., Betha, R., Chen, S., Liu, J., Price, D. J., Sanchez, K. J., McMeeking, G. R., Williams, L. R., Onasch, T. B., Worsnop, D. R., Abbatt, J., and Zhang, Q.: Light Absorption by Ambient Black and Brown Carbon and its Dependence on Black Carbon Coating State for Two California, USA, Cities in Winter and Summer, J. Geophys. Res. Atmospheres, 124, 1550–1577, https://doi.org/10.1029/2018JD029501, 2019.

Cavalli, F., Viana, M., Yttri, K. E., Genberg, J., and Putaud, J.-P.: Toward a standardised thermal-optical protocol for measuring atmospheric organic and elemental carbon: the EUSAAR protocol, Atmospheric Meas. Tech., 3, 79–89, https://doi.org/10.5194/amt-3-79-2010, 2010.

Cavalli, F., Alastuey, A., Areskoug, H., Ceburnis, D., Čech, J., Genberg, J., Harrison, R. M., Jaffrezo, J. L., Kiss, G., Laj, P., Mihalopoulos, N., Perez, N., Quincey, P., Schwarz, J., Sellegri, K., Spindler, G., Swietlicki, E., Theodosi, C., Yttri, K. E., Aas, W., and Putaud, J. P.: A European aerosol phenomenology -4: Harmonized concentrations of carbonaceous aerosol at 10 regional background sites across Europe, Atmos. Environ., 144, 133–145, https://doi.org/10.1016/j.atmosenv.2016.07.050, 2016.

Chakrabarty, R. K. and Heinson, W. R.: Scaling Laws for Light Absorption Enhancement Due to Nonrefractory Coating of Atmospheric Black Carbon Aerosol, Phys. Rev. Lett., 121, 218701, https://doi.org/10.1103/PhysRevLett.121.218701, 2018.

Chen, D., Cui, H., Zhao, Y., Yin, L., Lu, Y., and Wang, Q.: A two-year study of carbonaceous aerosols in ambient PM2.5 at a regional background site for western Yangtze River Delta, China, Atmospheric Res., 183, 351–361, https://doi.org/10.1016/j.atmosres.2016.09.004, 2017.

Chen, G., Wang, J., Wang, Y., Wang, J., Jin, Y., Cheng, Y., Yin, Y., Liao, H., Ding, A., Wang, S., Hao, J., and Liu, C.: An Aerosol Optical Module With Observation-Constrained Black Carbon Properties for Global Climate Models, Journal of Advances in Modeling Earth Systems, 15, e2022MS003501, https://doi.org/10.1029/2022MS003501, 2023.

China, S., Mazzoleni, C., Gorkowski, K., Aiken, A. C., and Dubey, M. K.: Morphology and mixing state of individual freshly emitted wildfire carbonaceous particles, Nat. Commun., 4, 2122, https://doi.org/10.1038/ncomms3122, 2013.

China, S., Scarnato, B., Owen, R. C., Zhang, B., Ampadu, M. T., Kumar, S., Dzepina, K., Dziobak, M. P., Fialho, P., Perlinger, J. A., Hueber, J., Helmig, D., Mazzoleni, L. R., and Mazzoleni, C.: Morphology and mixing state of aged soot particles at a remote marine free troposphere site: Implications for optical properties, Geophys. Res. Lett., 42, 1243–1250, https://doi.org/10.1002/2014GL062404, 2015.

Chow, J. C., Watson, J. G., Pritchett, L. C., Pierson, W. R., Frazier, C. A., and Purcell, R. G.: The dri thermal/optical reflectance carbon analysis system: description, evaluation and applications in U.S. Air quality studies, Atmospheric Environ. Part Gen. Top., 27, 1185–1201, https://doi.org/10.1016/0960-1686(93)90245-T, 1993.

Chow, J. C., Watson, J. G., Chen, L.-W. A., Chang, M. C. O., Robinson, N. F., Trimble, D., and Kohl, S.: The IMPROVE_A Temperature Protocol for Thermal/Optical Carbon Analysis: Maintaining Consistency with a Long-Term Database, J. Air Waste Manag. Assoc., 57, 1014–1023, https://doi.org/10.3155/1047-3289.57.9.1014, 2007.

Chung, S. H. and Seinfeld, J. H.: Global distribution and climate forcing of carbonaceous aerosols, J. Geophys. Res. Atmospheres, 107, AAC 14-1-AAC 14-33, https://doi.org/10.1029/2001JD001397, 2002.

Clarke, A., McNaughton, C., Kapustin, V., Shinozuka, Y., Howell, S., Dibb, J., Zhou, J., Anderson, B., Brekhovskikh, V., Turner, H., and Pinkerton, M.: Biomass burning and pollution aerosol over North America: Organic components and their influence on spectral optical properties and humidification response, J. Geophys. Res. Atmospheres, 112, https://doi.org/10.1029/2006JD007777, 2007.

Collaud Coen, M., Weingartner, E., Apituley, A., Ceburnis, D., Fierz-Schmidhauser, R., Flentje, H., Henzing, J. S., Jennings, S. G., Moerman, M., Petzold, A., Schmid, O., and Baltensperger, U.: Minimizing light absorption measurement artifacts of the Aethalometer: evaluation of five correction algorithms, Atmospheric Meas. Tech., 3, 457–474, https://doi.org/10.5194/amt-3-457-2010, 2010.

Corbin, J. C., Pieber, S. M., Czech, H., Zanatta, M., Jakobi, G., Massabò, D., Orasche, J., El Haddad, I., Mensah, A. A., Stengel, B., Drinovec, L., Mocnik, G., Zimmermann, R., Prévôt, A. S. H., and Gysel, M.: Brown and Black Carbon Emitted by a Marine Engine Operated on Heavy Fuel Oil and Distillate Fuels: Optical Properties, Size Distributions, and Emission Factors, J. Geophys. Res. Atmospheres, 123, 6175–6195, https://doi.org/10.1029/2017JD027818, 2018.

Corbin, J. C., Czech, H., Massabò, D., de Mongeot, F. B., Jakobi, G., Liu, F., Lobo, P., Mennucci, C., Mensah, A. A., Orasche, J., Pieber, S. M., Prévôt, A. S. H., Stengel, B., Tay, L.-L., Zanatta, M., Zimmermann, R., El Haddad, I., and Gysel, M.: Infrared-absorbing carbonaceous tar can dominate light absorption by marine-engine exhaust, Npj Clim. Atmospheric Sci., 2, 1–10, https://doi.org/10.1038/s41612-019-0069-5, 2019.

Cristofanelli, P., Brattich, E., Decesari, S., Landi, T. C., Maione, M., Putero, D., Tositti, L., and Bonasoni, P.: High-Mountain Atmospheric Research: The Italian Mt. Cimone WMO/GAW Global Station, 1st ed. 2018 edizione., Springer, 239 pp., 2017.

Cuesta-Mosquera, A., Močnik, G., Drinovec, L., Müller, T., Pfeifer, S., Minguillón, M. C., Briel, B., Buckley, P., Dudoitis, V., Fernández-García, J., Fernández-Amado, M., Ferreira De Brito, J., Riffault, V., Flentje, H., Heffernan, E., Kalivitis, N., Kalogridis, A.-C., Keernik, H., Marmureanu, L., Luoma, K., Marinoni, A., Pikridas,

M., Schauer, G., Serfozo, N., Servomaa, H., Titos, G., Yus-Díez, J., Zioła, N., and Wiedensohler, A.: Intercomparison and characterization of 23 Aethalometers under laboratory and ambient air conditions: procedures and unit-to-unit variabilities, Atmospheric Meas. Tech., 14, 3195–3216, https://doi.org/10.5194/amt-14-3195-2021, 2021.

Cui, X., Wang, X., Yang, L., Chen, B., Chen, J., Andersson, A., and Gustafsson, Ö.: Radiative absorption enhancement from coatings on black carbon aerosols, Sci. Total Environ., 551–552, 51–56, https://doi.org/10.1016/j.scitotenv.2016.02.026, 2016.

Dahlkötter, F., Gysel, M., Sauer, D., Minikin, A., Baumann, R., Seifert, P., Ansmann, A., Fromm, M., Voigt, C., and Weinzierl, B.: The Pagami Creek smoke plume after long-range transport to the upper troposphere over Europe – aerosol properties and black carbon mixing state, Atmospheric Chem. Phys., 14, 6111–6137, https://doi.org/10.5194/acp-14-6111-2014, 2014.

Dalirian, M., Ylisirniö, A., Buchholz, A., Schlesinger, D., Ström, J., Virtanen, A., and Riipinen, I.: Cloud droplet activation of black carbon particles coated with organic compounds of varying solubility, Atmospheric Chem. Phys., 18, 12477–12489, https://doi.org/10.5194/acp-18-12477-2018, 2018.

Dall'Osto, M., Beddows, D. C. S., Pey, J., Rodriguez, S., Alastuey, A., Harrison, R. M., and Querol, X.: Urban aerosol size distributions over the Mediterranean city of Barcelona, NE Spain, Atmospheric Chem. Phys., 12, 10693–10707, https://doi.org/10.5194/acp-12-10693-2012, 2012.

DeMott, P. J., Prenni, A. J., Liu, X., Kreidenweis, S. M., Petters, M. D., Twohy, C. H., Richardson, M. S., Eidhammer, T., and Rogers, D. C.: Predicting global atmospheric ice nuclei distributions and their impacts on climate, Proc. Natl. Acad. Sci., 107, 11217–11222, https://doi.org/10.1073/pnas.0910818107, 2010.

Di Biagio, C., Formenti, P., Cazaunau, M., Pangui, E., Marchand, N., and Doussin, J.-F.: Aethalometer multiple scattering correction C_{ref} for mineral dust aerosols, Atmospheric Meas. Tech., 10, 2923–2939, https://doi.org/10.5194/amt-10-2923-2017, 2017.

Diehl, K., Quick, C., Matthias-Maser, S., Mitra, S. K., and Jaenicke, R.: The ice nucleating ability of pollen: Part I: Laboratory studies in deposition and condensation freezing modes, Atmos Res, 58, 75–87, https://doi.org/10.1016/S0169-8095(01)00091-6, 2001.

Ding, S., Zhao, D., He, C., Huang, M., He, H., Tian, P., Liu, Q., Bi, K., Yu, C., Pitt, J., Chen, Y., Ma, X., Chen, Y., Jia, X., Kong, S., Wu, J., Hu, D., Hu, K., Ding, D., and Liu, D.: Observed Interactions Between Black Carbon and Hydrometeor During Wet Scavenging in Mixed-Phase Clouds, Geophys. Res. Lett., 46, 8453–8463, https://doi.org/10.1029/2019GL083171, 2019.

Dusek, U., Frank, G. P., Hildebrandt, L., Curtius, J., Schneider, J., Walter, S., Chand, D., Drewnick, F., Hings, S., Jung, D., Borrmann, S., and Andreae, M. O.: Size Matters More Than Chemistry for Cloud-Nucleating Ability of Aerosol Particles, Science, 312, 1375–1378, https://doi.org/10.1126/science.1125261, 2006.

Ealo, M., Alastuey, A., Ripoll, A., Pérez, N., Minguillón, M. C., Querol, X., and Pandolfi, M.: Detection of Saharan dust and biomass burning events using near-real-time intensive aerosol optical properties in the north-western Mediterranean, Atmospheric Chem. Phys., 16, 12567–12586, https://doi.org/10.5194/acp-16-12567-2016, 2016.

Feingold, G.: Modeling of the first indirect effect: Analysis of measurement requirements, Geophys. Res. Lett., 30, https://doi.org/10.1029/2003GL017967, 2003.

Ferrero, L., Bernardoni, V., Santagostini, L., Cogliati, S., Soldan, F., Valentini, S., Massabò, D., Močnik, G., Gregorič, A., Rigler, M., Prati, P., Bigogno, A., Losi, N., Valli, G., Vecchi, R., and Bolzacchini, E.: Consistent determination of the heating rate of light-absorbing aerosol using wavelength- and time-dependent Aethalometer multiple-scattering correction, Sci. Total Environ., 791, undefined-undefined, https://doi.org/10.1016/j.scitotenv.2021.148277, 2021.

Fierce, L., Riemer, N., and Bond, T. C.: Explaining variance in black carbon's aging timescale, Atmospheric Chem. Phys., 15, 3173–3191, https://doi.org/10.5194/acp-15-3173-2015, 2015.

Fierce, L., Bond, T. C., Bauer, S. E., Mena, F., and Riemer, N.: Black carbon absorption at the global scale is affected by particle-scale diversity in composition, Nat. Commun., 7, 12361, https://doi.org/10.1038/ncomms12361, 2016.

Flagan, R. C.: History of Electrical Aerosol Measurements, Aerosol Sci. Technol., 28, 301–380, https://doi.org/10.1080/02786829808965530, 1998.

Freedman, D. and Diaconis, P.: On the histogram as a density estimator:L 2 theory, Z. Wahrscheinlichkeitstheorie Verwandte Geb., 57, 453–476, https://doi.org/10.1007/BF01025868, 1981.

Fröhlich-Nowoisky, J., Kampf, C. J., Weber, B., Huffman, J. A., Pöhlker, C., Andreae, M. O., Lang-Yona, N., Burrows, S. M., Gunthe, S. S., Elbert, W., Su, H., Hoor, P., Thines, E., Hoffmann, T., Després, V. R., and Pöschl, U.: Bioaerosols in the Earth system: Climate, health, and ecosystem interactions, Atmospheric Res., 182, 346–376, https://doi.org/10.1016/j.atmosres.2016.07.018, 2016.

Fuchs, N. A. and Fuks, N. A.: The Mechanics of Aerosols, Dover Publications, 460 pp., 1964.

Fung, K.: Particulate Carbon Speciation by MnO_2 Oxidation, Aerosol Sci. Technol., 12, 122–127, https://doi.org/10.1080/02786829008959332, 1990.

Gao, R. S., Schwarz, J. P., Kelly, K. K., Fahey, D. W., Watts, L. A., Thompson, T. L., Spackman, J. R., Slowik, J. G., Cross, E. S., Han, J.-H., Davidovits, P., Onasch, T. B., and Worsnop, D. R.: A Novel Method for Estimating Light-Scattering Properties of Soot Aerosols Using a Modified Single-Particle Soot Photometer, Aerosol Sci. Technol., 41, 125–135, https://doi.org/10.1080/02786820601118398, 2007.

Garsous, G., Suárez-Alemán, A., and Serebrisky, T.: Cable cars in urban transport: Travel time savings from La Paz-El Alto (Bolivia), Transp. Policy, 75, 171–182, 2019.

Gilardoni, S., Massoli, P., Giulianelli, L., Rinaldi, M., Paglione, M., Pollini, F., Lanconelli, C., Poluzzi, V., Carbone, S., Hillamo, R., Russell, L. M., Facchini, M. C., and Fuzzi, S.: Fog scavenging of organic and inorganic aerosol in the Po Valley, Atmospheric Chem. Phys., 14, 6967–6981, https://doi.org/10.5194/acp-14-6967-2014, 2014.

Gilardoni, S., Di Mauro, B., and Bonasoni, P.: Black carbon, organic carbon, and mineral dust in South American tropical glaciers: A review, Glob. Planet. Change, 213, 103837, https://doi.org/10.1016/j.gloplacha.2022.103837, 2022.

Gliß, J., Mortier, A., Schulz, M., Andrews, E., Balkanski, Y., Bauer, S. E., Benedictow, A. M. K., Bian, H., Checa-Garcia, R., Chin, M., Ginoux, P., Griesfeller, J. J., Heckel, A., Kipling, Z., Kirkevåg, A., Kokkola, H., Laj, P., Le Sager, P., Lund, M. T., Lund Myhre, C., Matsui, H., Myhre, G., Neubauer, D., van Noije, T., North, P., Olivié, D. J. L., Rémy, S., Sogacheva, L., Takemura, T., Tsigaridis, K., and Tsyro, S. G.: AeroCom phase III multi-model evaluation of the aerosol life cycle and

optical properties using ground- and space-based remote sensing as well as surface in situ observations, Atmospheric Chem. Phys., 21, 87–128, https://doi.org/10.5194/acp-21-87-2021, 2021.

Gong, X., Zhang, C., Chen, H., Nizkorodov, S. A., Chen, J., and Yang, X.: Size distribution and mixing state of black carbon particles during a heavy air pollution episode in Shanghai, Atmospheric Chem. Phys., 16, 5399–5411, https://doi.org/10.5194/acp-16-5399-2016, 2016.

Gundel, L. A., Dod, R. L., Rosen, H., and Novakov, T.: The relationship between optical attenuation and black carbon concentration for ambient and source particles, Sci. Total Environ., 36, 197–202, https://doi.org/10.1016/0048-9697(84)90266-3, 1984.

Gysel, M., Laborde, M., Olfert, J. S., Subramanian, R., and Gröhn, A. J.: Effective density of Aquadag and fullerene soot black carbon reference materials used for SP2 calibration, Atmospheric Meas. Tech., 4, 2851–2858, https://doi.org/10.5194/amt-4-2851-2011, 2011.

Hallquist, M., Wenger, J. C., Baltensperger, U., Rudich, Y., Simpson, D., Claeys, M., Dommen, J., Donahue, N. M., George, C., Goldstein, A. H., Hamilton, J. F., Herrmann, H., Hoffmann, T., Iinuma, Y., Jang, M., Jenkin, M. E., Jimenez, J. L., Kiendler-Scharr, A., Maenhaut, W., McFiggans, G., Mentel, T. F., Monod, A., Prévôt, A. S. H., Seinfeld, J. H., Surratt, J. D., Szmigielski, R., and Wildt, J.: The formation, properties and impact of secondary organic aerosol: current and emerging issues, Atmospheric Chem. Phys., 9, 5155–5236, https://doi.org/10.5194/acp-9-5155-2009, 2009.

Han, C., Li, S.-M., Liu, P., and Lee, P.: Size Dependence of the Physical Characteristics of Particles Containing Refractory Black Carbon in Diesel Vehicle Exhaust, Environ. Sci. Technol., 53, 137–145, https://doi.org/10.1021/acs.est.8b04603, 2019.

Hänel, G.: Radiation budget of the boundary layer: Part II. Simultaneous measurement of mean solar volume absorption and extinction coefficients of particles, Beitr Phys Atmos, 60, 241–247, 1987.

Hansen, A. D. A., Rosen, H., and Novakov, T.: The aethalometer - An instrument for the real-time measurement of optical absorption by aerosol particles, Sci. Total Environ., 36, 191–196, 1984.

Hansen, J., Sato, M., and Ruedy, R.: Radiative forcing and climate response, J. Geophys. Res. Atmospheres, 102, 6831–6864, https://doi.org/10.1029/96JD03436, 1997.

Haynes, B. S. and Wagner, H. Gg.: Soot formation, Prog. Energy Combust. Sci., 7, 229–273, https://doi.org/10.1016/0360-1285(81)90001-0, 1981.

Haywood, J. M. and Shine, K. P.: The effect of anthropogenic sulfate and soot aerosol on the clear sky planetary radiation budget, Geophys. Res. Lett., 22, 603–606, https://doi.org/10.1029/95GL00075, 1995.

He, C., Liou, K.-N., Takano, Y., Zhang, R., Levy Zamora, M., Yang, P., Li, Q., and Leung, L. R.: Variation of the radiative properties during black carbon aging: theoretical and experimental intercomparison, Atmospheric Chem. Phys., 15, 11967–11980, https://doi.org/10.5194/acp-15-11967-2015, 2015.

Healy, R. M., Wang, J. M., Jeong, C.-H., Lee, A. K. Y., Willis, M. D., Jaroudi, E., Zimmerman, N., Hilker, N., Murphy, M., Eckhardt, S., Stohl, A., Abbatt, J. P. D., Wenger, J. C., and Evans, G. J.: Light-absorbing properties of ambient black carbon and brown carbon from fossil fuel and biomass burning sources, J. Geophys. Res. Atmospheres, 120, 6619–6633, https://doi.org/10.1002/2015JD023382, 2015.

Hinds, W. C. and Zhu, Y.: Aerosol Technology: Properties, Behavior, and Measurement of Airborne Particles, John Wiley & Sons, 452 pp., 2022.

Hyvärinen, A.-P., Vakkari, V., Laakso, L., Hooda, R. K., Sharma, V. P., Panwar, T. S., Beukes, J. P., van Zyl, P. G., Josipovic, M., Garland, R. M., Andreae, M. O., Pöschl, U., and Petzold, A.: Correction for a measurement artifact of the Multi-Angle Absorption Photometer (MAAP) at high black carbon mass concentration levels, Atmospheric Meas. Tech., 6, 81–90, https://doi.org/10.5194/amt-6-81-2013, 2013.

Intergovernmental Panel On Climate Change: Climate Change 2021 – The Physical Science Basis: Working Group I Contribution to the Sixth Assessment Report of the Intergovernmental Panel on Climate Change, 1st ed., Cambridge University Press, https://doi.org/10.1017/9781009157896, 2023.

Jacobson, M. Z.: Strong radiative heating due to the mixing state of black carbon in atmospheric aerosols, Nature, 409, 695–697, https://doi.org/10.1038/35055518, 2001.

Jacobson, M. Z.: Air Pollution and Global Warming: History, Science, and Solutions, Cambridge University Press, 397 pp., 2012.

Janssen, N. A., Gerlofs-Nijland, M. E., Lanki, T., Salonen, R. O., Cassee, F., Hoek, G., Fischer, P., Brunekreef, B., and Krzyzanowski, M.: Health effects of black carbon, World Health Organization. Regional Office for Europe, 2012.

Jiang, J., Aksoyoglu, S., El-Haddad, I., Ciarelli, G., Denier Van Der Gon, H. A. C., Canonaco, F., Gilardoni, S., Paglione, M., Minguillón, M. C., Favez, O., Zhang, Y., Marchand, N., Hao, L., Virtanen, A., Florou, K., O'Dowd, C., Ovadnevaite, J., Baltensperger, U., and Prévôt, A. S. H.: Sources of organic aerosols in Europe: A modelling study using CAMxwith modified volatility basis set scheme, Aerosols/Atmospheric Modelling/Troposphere/Chemistry (chemical composition and reactions), https://doi.org/10.5194/acp-2019-468, 2019.

Kahn, R. A., Andrews, E., Brock, C. A., Chin, M., Feingold, G., Gettelman, A., Levy, R. C., Murphy, D. M., Nenes, A., Pierce, J. R., Popp, T., Redemann, J., Sayer, A. M., da Silva, A. M., Sogacheva, L., and Stier, P.: Reducing Aerosol Forcing Uncertainty by Combining Models With Satellite and Within-The-Atmosphere Observations: A Three-Way Street, Rev. Geophys., 61, e2022RG000796, https://doi.org/10.1029/2022RG000796, 2023.

Kanji, Z. A., Welti, A., Corbin, J. C., and Mensah, A. A.: Black Carbon Particles Do Not Matter for Immersion Mode Ice Nucleation, Geophys. Res. Lett., 47, e2019GL086764, https://doi.org/10.1029/2019GL086764, 2020.

Karanasiou, A., Panteliadis, P., Perez, N., Minguillón, M. C., Pandolfi, M., Titos, G., Viana, M., Moreno, T., Querol, X., and Alastuey, A.: Evaluation of the Semi-Continuous OCEC analyzer performance with the EUSAAR2 protocol, Sci. Total Environ., 747, 141266, https://doi.org/10.1016/j.scitotenv.2020.141266, 2020.

Karjalainen, P., Pirjola, L., Heikkilä, J., Lähde, T., Tzamkiozis, T., Ntziachristos, L., Keskinen, J., and Rönkkö, T.: Exhaust particles of modern gasoline vehicles: A laboratory and an on-road study, Atmos. Environ., 97, 262–270, https://doi.org/10.1016/j.atmosenv.2014.08.025, 2014.

Kim, H.-R., Yu, S., Oh, J., Kim, K.-H., Lee, J.-H., Moniruzzaman, M., Kim, H. K., and Yun, S.-T.: Nitrate contamination and subsequent hydrogeochemical processes of shallow groundwater in agro-livestock farming districts in South Korea, Agric. Ecosyst. Environ., 273, 50–61, https://doi.org/10.1016/j.agee.2018.12.010, 2019.

Kirchstetter, T. W., Novakov, T., and Hobbs, P. V.: Evidence that the spectral dependence of light absorption by aerosols is affected by organic carbon, J. Geophys. Res. Atmospheres, 109, 2004JD004999, https://doi.org/10.1029/2004JD004999, 2004.

Koch, D., Schulz, M., Kinne, S., McNaughton, C., Spackman, J. R., Balkanski, Y., Bauer, S., Berntsen, T., Bond, T. C., Boucher, O., Chin, M., Clarke, A., De Luca, N., Dentener, F., Diehl, T., Dubovik, O., Easter, R., Fahey, D. W., Feichter, J., Fillmore, D., Freitag, S., Ghan, S., Ginoux, P., Gong, S., Horowitz, L., Iversen, T., Kirkev&aring, G, A., Klimont, Z., Kondo, Y., Krol, M., Liu, X., Miller, R., Montanaro, V., Moteki, N., Myhre, G., Penner, J. E., Perlwitz, J., Pitari, G., Reddy, S., Sahu, L., Sakamoto, H., Schuster, G., Schwarz, J. P., Seland, Ø., Stier, P., Takegawa, N., Takemura, T., Textor, C., van Aardenne, J. A., and Zhao, Y.: Evaluation of black carbon estimations in global aerosol models, Atmospheric Chem. Phys., 9, 9001–9026, https://doi.org/10.5194/acp-9-9001-2009, 2009.

Koop, T., Luo, B., Tsias, A., and Peter, T.: Water activity as the determinant for homogeneous ice nucleation in aqueous solutions, Nature, 406, 611–614, https://doi.org/10.1038/35020537, 2000.

Koren, I., Kaufman, Y. J., Remer, L. A., and Martins, J. V.: Measurement of the Effect of Amazon Smoke on Inhibition of Cloud Formation, Science, 303, 1342–1345, https://doi.org/10.1126/science.1089424, 2004.

Krasowsky, T. S., McMeeking, G. R., Sioutas, C., and Ban-Weiss, G.: Characterizing the evolution of physical properties and mixing state of black carbon particles: from near a major highway to the broader urban plume in Los Angeles, Atmospheric Chem. Phys., 18, 11991–12010, https://doi.org/10.5194/acp-18-11991-2018, 2018.

Krecl, P., Johansson, C., Targino, A. C., Ström, J., and Burman, L.: Trends in black carbon and size-resolved particle number concentrations and vehicle emission factors under real-world conditions, Atmos. Environ., 165, 155–168, https://doi.org/10.1016/j.atmosenv.2017.06.036, 2017.

Kuwata, M., Kondo, Y., and Takegawa, N.: Critical condensed mass for activation of black carbon as cloud condensation nuclei in Tokyo, J. Geophys. Res. Atmospheres, 114, https://doi.org/10.1029/2009JD012086, 2009.

Laborde, M., Mertes, P., Zieger, P., Dommen, J., Baltensperger, U., and Gysel, M.: Sensitivity of the Single Particle Soot Photometer to different black carbon

types, Atmospheric Meas. Tech., 5, 1031–1043, https://doi.org/10.5194/amt-5-1031-2012, 2012a.

Laborde, M., Schnaiter, M., Linke, C., Saathoff, H., Naumann, K.-H., Möhler, O., Berlenz, S., Wagner, U., Taylor, J. W., Liu, D., Flynn, M., Allan, J. D., Coe, H., Heimerl, K., Dahlkötter, F., Weinzierl, B., Wollny, A. G., Zanatta, M., Cozic, J., Laj, P., Hitzenberger, R., Schwarz, J. P., and Gysel, M.: Single Particle Soot Photometer intercomparison at the AIDA chamber, Atmospheric Meas. Tech., 5, 3077–3097, https://doi.org/10.5194/amt-5-3077-2012, 2012b.

Laborde, M., Crippa, M., Tritscher, T., Jurányi, Z., Decarlo, P. F., Temime-Roussel, B., Marchand, N., Eckhardt, S., Stohl, A., Baltensperger, U., Prévôt, A. S. H., Weingartner, E., and Gysel, M.: Black carbon physical properties and mixing state in the European megacity Paris, Atmospheric Chem. Phys., 13, 5831–5856, https://doi.org/10.5194/acp-13-5831-2013, 2013.

Lack, D. A. and Cappa, C. D.: Impact of brown and clear carbon on light absorption enhancement, single scatter albedo and absorption wavelength dependence of black carbon, Atmospheric Chem. Phys., 10, 4207–4220, https://doi.org/10.5194/acp-10-4207-2010, 2010.

Lack, D. A., Cappa, C. D., Cross, E. S., Massoli, P., Ahern, A. T., Davidovits, P., and Onasch, T. B.: Absorption Enhancement of Coated Absorbing Aerosols: Validation of the Photo-Acoustic Technique for Measuring the Enhancement, Aerosol Sci. Technol., 43, 1006–1012, https://doi.org/10.1080/02786820903117932, 2009.

Laj, P., Bigi, A., Rose, C., Andrews, E., Lund Myhre, C., Collaud Coen, M., Lin, Y., Wiedensohler, A., Schulz, M., Ogren, J. A., Fiebig, M., Gliß, J., Mortier, A., Pandolfi, M., Petäja, T., Kim, S.-W., Aas, W., Putaud, J.-P., Mayol-Bracero, O., Keywood, M., Labrador, L., Aalto, P., Ahlberg, E., Alados Arboledas, L., Alastuey, A., Andrade, M., Artíñano, B., Ausmeel, S., Arsov, T., Asmi, E., Backman, J., Baltensperger, U., Bastian, S., Bath, O., Beukes, J. P., Brem, B. T., Bukowiecki, N., Conil, S., Couret, C., Day, D., Dayantolis, W., Degorska, A., Eleftheriadis, K., Fetfatzis, P., Favez, O., Flentje, H., Gini, M. I., Gregorič, A., Gysel-Beer, M., Hallar, A. G., Hand, J., Hoffer, A., Hueglin, C., Hooda, R. K., Hyvärinen, A., Kalapov, I., Kalivitis, N., Kasper-Giebl, A., Kim, J. E., Kouvarakis, G., Kranjc, I., Krejci, R., Kulmala, M., Labuschagne, C., Lee, H.-J., Lihavainen, H., Lin, N.-H., Löschau, G., Luoma, K., Marinoni, A., Martins Dos Santos, S., Meinhardt, F., Merkel, M., Metzger, J.-M., Mihalopoulos, N., Nguyen, N. A., Ondracek, J., Pérez, N.,

Perrone, M. R., Petit, J.-E., Picard, D., Pichon, J.-M., Pont, V., Prats, N., Prenni, A., Reisen, F., Romano, S., Sellegri, K., Sharma, S., Schauer, G., Sheridan, P., Sherman, J. P., Schütze, M., Schwerin, A., Sohmer, R., Sorribas, M., Steinbacher, M., Sun, J., Titos, G., et al.: A global analysis of climate-relevant aerosol properties retrieved from the network of Global Atmosphere Watch (GAW) near-surface observatories, Atmospheric Meas. Tech., 13, 4353–4392, https://doi.org/10.5194/amt-13-4353-2020, 2020.

Lamarque, J.-F., Bond, T. C., Eyring, V., Granier, C., Heil, A., Klimont, Z., Lee, D., Liousse, C., Mieville, A., Owen, B., Schultz, M. G., Shindell, D., Smith, S. J., Stehfest, E., Van Aardenne, J., Cooper, O. R., Kainuma, M., Mahowald, N., McConnell, J. R., Naik, V., Riahi, K., and van Vuuren, D. P.: Historical (1850–2000) gridded anthropogenic and biomass burning emissions of reactive gases and aerosols: methodology and application, Atmospheric Chem. Phys., 10, 7017–7039, https://doi.org/10.5194/acp-10-7017-2010, 2010.

Laothawornkitkul, J., Taylor, J. E., Paul, N. D., and Hewitt, C. N.: Biogenic volatile organic compounds in the Earth system, New Phytol., 183, 27–51, https://doi.org/10.1111/j.1469-8137.2009.02859.x, 2009.

Lapere, R., Huneeus, N., Mailler, S., Menut, L., and Couvidat, F.: Meteorological export and deposition fluxes of black carbon on glaciers of the central Chilean Andes, Atmospheric Chem. Phys., 23, 1749–1768, https://doi.org/10.5194/acp-23-1749-2023, 2023.

Lee, A. K. Y., Rivellini, L.-H., Chen, C.-L., Liu, J., Price, D. J., Betha, R., Russell, L. M., Zhang, X., and Cappa, C. D.: Influences of Primary Emission and Secondary Coating Formation on the Particle Diversity and Mixing State of Black Carbon Particles, Environ. Sci. Technol., 53, 9429–9438, https://doi.org/10.1021/acs.est.9b03064, 2019.

Lewis, K., Arnott, W. P., Moosmüller, H., and Wold, C. E.: Strong spectral variation of biomass smoke light absorption and single scattering albedo observed with a novel dual-wavelength photoacoustic instrument, J. Geophys. Res. Atmospheres, 113, https://doi.org/10.1029/2007JD009699, 2008.

Li, W., Shao, L., Zhang, D., Ro, C.-U., Hu, M., Bi, X., Geng, H., Matsuki, A., Niu, H., and Chen, J.: A review of single aerosol particle studies in the atmosphere of East Asia: morphology, mixing state, source, and heterogeneous reactions, J. Clean. Prod., 112, 1330–1349, https://doi.org/10.1016/j.jclepro.2015.04.050, 2016.

Liousse, C., Cachier, H., and Jennings, S. G.: Optical and thermal measurements of black carbon aerosol content in different environments: Variation of the specific attenuation cross-section, sigma (σ), Atmospheric Environ. Part Gen. Top., 27, 1203–1211, https://doi.org/10.1016/0960-1686(93)90246-U, 1993.

Liu, C., Chung, C. E., Yin, Y., and Schnaiter, M.: The absorption Ångström exponent of black carbon: from numerical aspects, Atmospheric Chem. Phys., 18, 6259–6273, https://doi.org/10.5194/acp-18-6259-2018, 2018.

Liu, D., Flynn, M., Gysel, M., Targino, A., Crawford, I., Bower, K., Choularton, T., Jurányi, Z., Steinbacher, M., Hüglin, C., Curtius, J., Kampus, M., Petzold, A., Weingartner, E., Baltensperger, U., and Coe, H.: Single particle characterization of black carbon aerosols at a tropospheric alpine site in Switzerland, Atmospheric Chem. Phys., 10, 7389–7407, https://doi.org/10.5194/acp-10-7389-2010, 2010.

Liu, D., Allan, J. D., Young, D. E., Coe, H., Beddows, D., Fleming, Z. L., Flynn, M. J., Gallagher, M. W., Harrison, R. M., Lee, J., Prevot, A. S. H., Taylor, J. W., Yin, J., Williams, P. I., and Zotter, P.: Size distribution, mixing state and source apportionment of black carbon aerosol in London during wintertime, Atmospheric Chem. Phys., 14, 10061–10084, https://doi.org/10.5194/acp-14-10061-2014, 2014.

Liu, D., Whitehead, J., Alfarra, M. R., Reyes-Villegas, E., Spracklen, D. V., Reddington, C. L., Kong, S., Williams, P. I., Ting, Y.-C., Haslett, S., Taylor, J. W., Flynn, M. J., Morgan, W. T., McFiggans, G., Coe, H., and Allan, J. D.: Black-carbon absorption enhancement in the atmosphere determined by particle mixing state, Nat. Geosci., 10, 184–188, https://doi.org/10.1038/ngeo2901, 2017.

Liu, D., Joshi, R., Wang, J., Yu, C., Allan, J. D., Coe, H., Flynn, M. J., Xie, C., Lee, J., Squires, F., Kotthaus, S., Grimmond, S., Ge, X., Sun, Y., and Fu, P.: Contrasting physical properties of black carbon in urban Beijing between winter and summer, Atmospheric Chem. Phys., 19, 6749–6769, https://doi.org/10.5194/acp-19-6749-2019, 2019.

Liu, F., Yon, J., Fuentes, A., Lobo, P., Smallwood, G. J., and Corbin, J. C.: Review of recent literature on the light absorption properties of black carbon: Refractive index, mass absorption cross section, and absorption function, Aerosol Sci. Technol., 54, 33–51, https://doi.org/10.1080/02786826.2019.1676878, 2020.

Liu, L. and Mishchenko, M. I.: Scattering and Radiative Properties of Morphologically Complex Carbonaceous Aerosols: A Systematic Modeling Study, Remote Sens., 10, 1634, https://doi.org/10.3390/rs10101634, 2018.

Liu, S., Aiken, A. C., Gorkowski, K., Dubey, M. K., Cappa, C. D., Williams, L. R., Herndon, S. C., Massoli, P., Fortner, E. C., Chhabra, P. S., Brooks, W. A., Onasch, T. B., Jayne, J. T., Worsnop, D. R., China, S., Sharma, N., Mazzoleni, C., Xu, L., Ng, N. L., Liu, D., Allan, J. D., Lee, J. D., Fleming, Z. L., Mohr, C., Zotter, P., Szidat, S., and Prévôt, A. S. H.: Enhanced light absorption by mixed source black and brown carbon particles in UK winter, Nat. Commun., 6, 8435, https://doi.org/10.1038/ncomms9435, 2015.

Liu, X., Zheng, M., Liu, Y., Jin, Y., Liu, J., Zhang, B., Yang, X., Wu, Y., Zhang, T., Xiang, Y., Liu, B., and Yan, C.: Intercomparison of equivalent black carbon (eBC) and elemental carbon (EC) concentrations with three-year continuous measurement in Beijing, China, Environ. Res., 209, 112791, https://doi.org/10.1016/j.envres.2022.112791, 2022.

López-Moreno, J. I., Fontaneda, S., Bazo, J., Revuelto, J., Azorin-Molina, C., Valero-Garcés, B., Morán-Tejeda, E., Vicente-Serrano, S. M., Zubieta, R., and Alejo-Cochachín, J.: Recent glacier retreat and climate trends in Cordillera Huaytapallana, Peru, Glob. Planet. Change, 112, 1–11, https://doi.org/10.1016/j.gloplacha.2013.10.010, 2014.

Luo, J., Zhang, Y., Wang, F., and Zhang, Q.: Effects of brown coatings on the absorption enhancement of black carbon: a numerical investigation, Atmospheric Chem. Phys., 18, 16897–16914, https://doi.org/10.5194/acp-18-16897-2018, 2018.

Luoma, K., Virkkula, A., Aalto, P., Lehtipalo, K., Petäjä, T., and Kulmala, M.: Effects of different correction algorithms on absorption coefficient – a comparison of three optical absorption photometers at a boreal forest site, Atmospheric Meas. Tech., 14, 6419–6441, https://doi.org/10.5194/amt-14-6419-2021, 2021.

Magalhães, N. de, Evangelista, H., Condom, T., Rabatel, A., and Ginot, P.: Amazonian Biomass Burning Enhances Tropical Andean Glaciers Melting, Sci. Rep., 9, 16914, https://doi.org/10.1038/s41598-019-53284-1, 2019.

Mahrt, F., Marcolli, C., David, R. O., Grönquist, P., Barthazy Meier, E. J., Lohmann, U., and Kanji, Z. A.: Ice nucleation abilities of soot particles determined with the

Horizontal Ice Nucleation Chamber, Atmospheric Chem. Phys., 18, 13363–13392, https://doi.org/10.5194/acp-18-13363-2018, 2018.

Mann, G. W., Carslaw, K. S., Reddington, C. L., Pringle, K. J., Schulz, M., Asmi, A., Spracklen, D. V., Ridley, D. A., Woodhouse, M. T., Lee, L. A., Zhang, K., Ghan, S. J., Easter, R. C., Liu, X., Stier, P., Lee, Y. H., Adams, P. J., Tost, H., Lelieveld, J., Bauer, S. E., Tsigaridis, K., van Noije, T. P. C., Strunk, A., Vignati, E., Bellouin, N., Dalvi, M., Johnson, C. E., Bergman, T., Kokkola, H., von Salzen, K., Yu, F., Luo, G., Petzold, A., Heintzenberg, J., Clarke, A., Ogren, J. A., Gras, J., Baltensperger, U., Kaminski, U., Jennings, S. G., O'Dowd, C. D., Harrison, R. M., Beddows, D. C. S., Kulmala, M., Viisanen, Y., Ulevicius, V., Mihalopoulos, N., Zdimal, V., Fiebig, M., Hansson, H.-C., Swietlicki, E., and Henzing, J. S.: Intercomparison and evaluation of global aerosol microphysical properties among AeroCom models of a range of complexity, Atmospheric Chemistry and Physics, 14, 4679–4713, https://doi.org/10.5194/acp-14-4679-2014, 2014.

Mardoñez, V., Pandolfi, M., Borlaza, L. J. S., Jaffrezo, J.-L., Alastuey, A., Besombes, J.-L., Moreno R., I., Perez, N., Močnik, G., Ginot, P., Krejci, R., Chrastny, V., Wiedensohler, A., Laj, P., Andrade, M., and Uzu, G.: Source apportionment study on particulate air pollution in two high-altitude Bolivian cities: La Paz and El Alto, Atmospheric Chem. Phys., 23, 10325–10347, https://doi.org/10.5194/acp-23-10325-2023, 2023.

Marinoni, A., Cristofanelli, P., Calzolari, F., Roccato, F., Bonafè, U., and Bonasoni, P.: Continuous measurements of aerosol physical parameters at the Mt. Cimone GAW Station (2165 m asl, Italy), Sci. Total Environ., 391, 241–251, https://doi.org/10.1016/j.scitotenv.2007.10.004, 2008.

Masiello, C. A.: New directions in black carbon organic geochemistry, Mar. Chem., 92, 201–213, https://doi.org/10.1016/j.marchem.2004.06.043, 2004.

Massabò, D., Bernardoni, V., Bove, M. C., Brunengo, A., Cuccia, E., Piazzalunga, A., Prati, P., Valli, G., and Vecchi, R.: A multi-wavelength optical set-up for the characterization of carbonaceous particulate matter, J. Aerosol Sci., 60, 34–46, https://doi.org/10.1016/j.jaerosci.2013.02.006, 2013.

Massoli, P., Murphy, D. M., Lack, D. A., Baynard, T., Brock, C. A., and Lovejoy, E. R.: Uncertainty in Light Scattering Measurements by TSI Nephelometer: Results from Laboratory Studies and Implications for Ambient Measurements, Aerosol

Sci. Technol., 43, 1064–1074, https://doi.org/10.1080/02786820903156542, 2009.

Massoli, P., Kebabian, P. L., Onasch, T. B., Hills, F. B., and Freedman, A.: Aerosol Light Extinction Measurements by Cavity Attenuated Phase Shift (CAPS) Spectroscopy: Laboratory Validation and Field Deployment of a Compact Aerosol Particle Extinction Monitor, Aerosol Sci. Technol., 44, 428–435, https://doi.org/10.1080/02786821003716599, 2010.

Matsui, H.: Black carbon simulations using a size- and mixing-state-resolved three-dimensional model: 2. Aging timescale and its impact over East Asia, J. Geophys. Res. Atmospheres, 121, 1808–1821, https://doi.org/10.1002/2015JD023999, 2016.

Matsui, H.: Black carbon simulations using a size- and mixing-state-resolved three-dimensional model: 1. Radiative effects and their uncertainties, Journal of Geophysical Research: Atmospheres, 121, 1793–1807, https://doi.org/10.1002/2015JD023998, 2016b.

Matsui, H., Koike, M., Kondo, Y., Moteki, N., Fast, J. D., and Zaveri, R. A.: Development and validation of a black carbon mixing state resolved three-dimensional model: Aging processes and radiative impact, J. Geophys. Res. Atmospheres, 118, 2304–2326, https://doi.org/10.1029/2012JD018446, 2013.

Matsui, H., Hamilton, D. S., and Mahowald, N. M.: Black carbon radiative effects highly sensitive to emitted particle size when resolving mixing-state diversity, Nat. Commun., 9, 3446, https://doi.org/10.1038/s41467-018-05635-1, 2018.

Matsui, H. and Mahowald, N.: Development of a global aerosol model using a two-dimensional sectional method: 2. Evaluation and sensitivity simulations, Journal of Advances in Modeling Earth Systems, 9, 1887–1920, https://doi.org/10.1002/2017MS000937, 2017.

McMeeking, G. R., Fortner, E., Onasch, T. B., Taylor, J. W., Flynn, M., Coe, H., and Kreidenweis, S. M.: Impacts of nonrefractory material on light absorption by aerosols emitted from biomass burning, J. Geophys. Res. Atmospheres, 119, 12,272-12,286, https://doi.org/10.1002/2014JD021750, 2014.

McMurry, P. H.: A review of atmospheric aerosol measurements&, Atmos. Environ., 2000.

Medalia, A. I. and Heckman, F. A.: Morphology of aggregates—II. Size and shape factors of carbon black aggregates from electron microscopy, Carbon, 7, 567–582, https://doi.org/10.1016/0008-6223(69)90029-3, 1969.

Michelsen, H. A., Schulz, C., Smallwood, G. J., and Will, S.: Laser-induced incandescence: Particulate diagnostics for combustion, atmospheric, and industrial applications, Prog. Energy Combust. Sci., 51, 2–48, https://doi.org/10.1016/j.pecs.2015.07.001, 2015.

Mikhailov, E. F., Mironova, S., Mironov, G., Vlasenko, S., Panov, A., Chi, X., Walter, D., Carbone, S., Artaxo, P., Heimann, M., Lavric, J., Pöschl, U., and Andreae, M. O.: Long-term measurements (2010–2014) of carbonaceous aerosol and carbon monoxide at the Zotino Tall Tower Observatory (ZOTTO) in central Siberia, Atmospheric Chem. Phys., 17, 14365–14392, https://doi.org/10.5194/acp-17-14365-2017, 2017.

Miyakawa, T., Kanaya, Y., Komazaki, Y., Taketani, F., Pan, X., Irwin, M., and Symonds, J.: Intercomparison between a single particle soot photometer and evolved gas analysis in an industrial area in Japan: Implications for the consistency of soot aerosol mass concentration measurements, Atmos. Environ., 127, 14–21, https://doi.org/10.1016/j.atmosenv.2015.12.018, 2016.

Miyakawa, T., Oshima, N., Taketani, F., Komazaki, Y., Yoshino, A., Takami, A., Kondo, Y., and Kanaya, Y.: Alteration of the size distributions and mixing states of black carbon through transport in the boundary layer in east Asia, Atmospheric Chem. Phys., 17, 5851–5864, https://doi.org/10.5194/acp-17-5851-2017, 2017.

Miyazaki, Y., Kondo, Y., K. Sahu, L., Imaru, J., Fukushima, N., and Kano, M.: Performance of a newly designed continuous soot monitoring system (COSMOS), J. Environ. Monit., 10, 1195–1201, https://doi.org/10.1039/B806957C, 2008.

Modini, R. L., Corbin, J. C., Brem, B. T., Irwin, M., Bertò, M., Pileci, R. E., Fetfatzis, P., Eleftheriadis, K., Henzing, B., Moerman, M. M., Liu, F., Müller, T., and Gysel-Beer, M.: Detailed characterization of the CAPS single-scattering albedo monitor (CAPS PMssa) as a field-deployable instrument for measuring aerosol light absorption with the extinction-minus-scattering method, Atmospheric Meas. Tech., 14, 819–851, https://doi.org/10.5194/amt-14-819-2021, 2021.

Moffet, R. C., O'Brien, R. E., Alpert, P. A., Kelly, S. T., Pham, D. Q., Gilles, M. K., Knopf, D. A., and Laskin, A.: Morphology and mixing of black carbon particles collected in central California during the CARES field study, Atmospheric Chem. Phys., 16, 14515–14525, https://doi.org/10.5194/acp-16-14515-2016, 2016.

Molina, L. T., Gallardo, L., Andrade, M., Baumgardner, D., Borbor-Córdova, M., Bórquez, R., Casassa, G., Cereceda-Balic, F., Dawidowski, L., Garreaud, R., Huneeus, N., Lambert, F., McCarty, J. l., Mc Phee, J., Mena-Carrasco, M., Raga, G. b., Schmitt, C., and Schwarz, J. p.: Pollution and its Impacts on the South American Cryosphere, Earths Future, 3, 345–369, https://doi.org/10.1002/2015EF000311, 2015.

Monteiro Dos Santos, D. A., Brito, J. F., Godoy, J. M., and Artaxo, P.: Ambient concentrations and insights on organic and elemental carbon dynamics in São Paulo, Brazil, Atmos. Environ., 144, 226–233, https://doi.org/10.1016/j.atmosenv.2016.08.081, 2016.

Moore, R. H., Ziemba, L. D., Dutcher, D., Beyersdorf, A. J., Chan, K., Crumeyrolle, S., Raymond, T. M., Thornhill, K. L., Winstead, E. L., and Anderson, B. E.: Mapping the Operation of the Miniature Combustion Aerosol Standard (Mini-CAST) Soot Generator, Aerosol Sci. Technol., 48, 467–479, https://doi.org/10.1080/02786826.2014.890694, 2014.

Moosmüller, H., Chakrabarty, R. K., and Arnott, W. P.: Aerosol light absorption and its measurement: A review, J. Quant. Spectrosc. Radiat. Transf., 110, 844–878, https://doi.org/10.1016/j.jqsrt.2009.02.035, 2009.

Moreno, C. I., Krejci, R., Jaffrezo, J.-L., Uzu, G., Alastuey, A., Andrade, M. F., Mardóñez, V., Koenig, A. M., Aliaga, D., Mohr, C., Ticona, L., Velarde, F., Blacutt, L., Forno, R., Whiteman, D. N., Wiedensohler, A., Ginot, P., and Laj, P.: Tropical tropospheric aerosol sources and chemical composition observed at high-altitude in the Bolivian Andes, Aerosols/Field Measurements/Troposphere/Chemistry (chemical composition and reactions), https://doi.org/10.5194/egusphere-2023-1298, 2023.

Moschos, V., Gysel-Beer, M., Modini, R. L., Corbin, J. C., Massabò, D., Costa, C., Danelli, S. G., Vlachou, A., Daellenbach, K. R., Szidat, S., Prati, P., Prévôt, A. S. H., Baltensperger, U., and El Haddad, I.: Source-specific light absorption by carbonaceous components in the complex aerosol matrix from yearly filter-based measurements, Atmospheric Chem. Phys., 21, 12809–12833, https://doi.org/10.5194/acp-21-12809-2021, 2021.

Moteki, N. and Kondo, Y.: Effects of Mixing State on Black Carbon Measurements by Laser-Induced Incandescence, Aerosol Sci. Technol., 41, 398–417, https://doi.org/10.1080/02786820701199728, 2007.

Moteki, N. and Kondo, Y.: Dependence of Laser-Induced Incandescence on Physical Properties of Black Carbon Aerosols: Measurements and Theoretical Interpretation, Aerosol Sci. Technol., 44, 663–675, https://doi.org/10.1080/02786826.2010.484450, 2010.

Moteki, N., Kondo, Y., Oshima, N., Takegawa, N., Koike, M., Kita, K., Matsui, H., and Kajino, M.: Size dependence of wet removal of black carbon aerosols during transport from the boundary layer to the free troposphere, Geophys. Res. Lett., 39, https://doi.org/10.1029/2012GL052034, 2012.

Motos, G., Schmale, J., Corbin, J. C., Zanatta, M., Baltensperger, U., and Gysel-Beer, M.: Droplet activation behaviour of atmospheric black carbon particles in fog as a function of their size and mixing state, Atmospheric Chem. Phys., 19, 2183–2207, https://doi.org/10.5194/acp-19-2183-2019, 2019.

Motos, G., Corbin, J. C., Schmale, J., Modini, R. L., Bertò, M., Kupiszewski, P., Baltensperger, U., and Gysel-Beer, M.: Black Carbon Aerosols in the Lower Free Troposphere are Heavily Coated in Summer but Largely Uncoated in Winter at Jungfraujoch in the Swiss Alps, Geophys. Res. Lett., 47, e2020GL088011, https://doi.org/10.1029/2020GL088011, 2020.

Mousavi, A., Sowlat, M. H., Lovett, C., Rauber, M., Szidat, S., Boffi, R., Borgini, A., De Marco, C., Ruprecht, A. A., and Sioutas, C.: Source apportionment of black carbon (BC) from fossil fuel and biomass burning in metropolitan Milan, Italy, Atmos. Environ., 203, 252–261, https://doi.org/10.1016/j.atmosenv.2019.02.009, 2019.

Müller, T., Henzing, J. S., de Leeuw, G., Wiedensohler, A., Alastuey, A., Angelov, H., Bizjak, M., Collaud Coen, M., Engström, J. E., Gruening, C., Hillamo, R., Hoffer, A., Imre, K., Ivanow, P., Jennings, G., Sun, J. Y., Kalivitis, N., Karlsson, H., Komppula, M., Laj, P., Li, S.-M., Lunder, C., Marinoni, A., Martins dos Santos, S., Moerman, M., Nowak, A., Ogren, J. A., Petzold, A., Pichon, J. M., Rodriquez, S., Sharma, S., Sheridan, P. J., Teinilä, K., Tuch, T., Viana, M., Virkkula, A., Weingartner, E., Wilhelm, R., and Wang, Y. Q.: Characterization and intercomparison of aerosol absorption photometers: result of two intercomparison workshops, Atmospheric Meas. Tech., 4, 245–268, https://doi.org/10.5194/amt-4-245-2011, 2011.

Murray, B. J., Carslaw, K. S., and Field, P. R.: Opinion: Cloud-phase climate feedback and the importance of ice-nucleating particles, Atmospheric Chem. Phys., 21, 665–679, https://doi.org/10.5194/acp-21-665-2021, 2021.

Naseri, A., Corbin, J., and Olfert, J.: Comparison of the LEO and CPMA-SP2 techniques for black-carbon mixing-state measurements, Aerosols/In Situ Measurement/Validation and Intercomparisons, https://doi.org/10.5194/egusphere-2023-2216, 2023.

Novakov, T., Ramanathan, V., Hansen, J. E., Kirchstetter, T. W., Sato, M., Sinton, J. E., and Sathaye, J. A.: Large historical changes of fossil-fuel black carbon aerosols, Geophys. Res. Lett., 30, https://doi.org/10.1029/2002GL016345, 2003.

Ogren, J. A. and Charlson, R. J.: Elemental carbon in the atmosphere: cycle and lifetime, Tellus B, 35B, 241–254, https://doi.org/10.1111/j.1600-0889.1983.tb00027.x, 1983.

Ohata, S., Moteki, N., Mori, T., Koike, M., and Kondo, Y.: A key process controlling the wet removal of aerosols: new observational evidence, Sci. Rep., 6, 34113, https://doi.org/10.1038/srep34113, 2016.

Ohata, S., Mori, T., Kondo, Y., Sharma, S., Hyvärinen, A., Andrews, E., Tunved, P., Asmi, E., Backman, J., Servomaa, H., Veber, D., Eleftheriadis, K., Vratolis, S., Krejci, R., Zieger, P., Koike, M., Kanaya, Y., Yoshida, A., Moteki, N., Zhao, Y., Tobo, Y., Matsushita, J., and Oshima, N.: Estimates of mass absorption cross sections of black carbon for filter-based absorption photometers in the Arctic, Atmospheric Meas. Tech., 14, 6723–6748, https://doi.org/10.5194/amt-14-6723-2021, 2021.

Ouf, F.-X., Bourrous, S., Fauvel, S., Kort, A., Lintis, L., Nuvoli, J., and Yon, J.: True density of combustion emitted particles: A comparison of results highlighting the influence of the organic contents, J. Aerosol Sci., 134, 1–13, https://doi.org/10.1016/j.jaerosci.2019.04.007, 2019.

Paglione, M., Gilardoni, S., Rinaldi, M., Decesari, S., Zanca, N., Sandrini, S., Giulianelli, L., Bacco, D., Ferrari, S., Poluzzi, V., Scotto, F., Trentini, A., Poulain, L., Herrmann, H., Wiedensohler, A., Canonaco, F., Prévôt, A. S. H., Massoli, P., Carbone, C., Facchini, M. C., and Fuzzi, S.: The impact of biomass burning and aqueous-phase processing on air quality: a multi-year source apportionment study in the Po Valley, Italy, Atmospheric Chem. Phys., 20, 1233–1254, https://doi.org/10.5194/acp-20-1233-2020, 2020.

Pandolfi, M., Martucci, G., Querol, X., Alastuey, A., Wilsenack, F., Frey, S., O'Dowd, C. D., and Dall'Osto, M.: Continuous atmospheric boundary layer observations in the coastal urban area of Barcelona during SAPUSS, Atmospheric Chem. Phys., 13, 4983–4996, https://doi.org/10.5194/acp-13-4983-2013, 2013.

Pandolfi, M., Alastuey, A., Pérez, N., Reche, C., Castro, I., Shatalov, V., and Querol, X.: Trends analysis of PM source contributions and chemical tracers in NE Spain during 2004–2014: a multi-exponential approach, Atmospheric Chem. Phys., 16, 11787–11805, https://doi.org/10.5194/acp-16-11787-2016, 2016.

Panopoulou, A., Liakakou, E., Sauvage, S., Gros, V., Locoge, N., Stavroulas, I., Bonsang, B., Gerasopoulos, E., and Mihalopoulos, N.: Yearlong measurements of monoterpenes and isoprene in a Mediterranean city (Athens): Natural vs anthropogenic origin, Atmos. Environ., 243, 117803, https://doi.org/10.1016/j.atmosenv.2020.117803, 2020.

Park, R. J., Kim, M. J., Jeong, J. I., Youn, D., and Kim, S.: A contribution of brown carbon aerosol to the aerosol light absorption and its radiative forcing in East Asia, Atmos. Environ., 44, 1414–1421, https://doi.org/10.1016/j.atmosenv.2010.01.042, 2010.

Pawlyta, M. and Hercman, H.: Transmission electron microscopy (TEM) as a tool for identification of combustion products: Application to black layers in speleothems, Ann. Soc. Geol. Pol., 86, https://doi.org/10.14241/asgp.2016.004, 2016.

Peng, J., Hu, M., Guo, S., Du, Z., Zheng, J., Shang, D., Levy Zamora, M., Zeng, L., Shao, M., Wu, Y.-S., Zheng, J., Wang, Y., Glen, C. R., Collins, D. R., Molina, M. J., and Zhang, R.: Markedly enhanced absorption and direct radiative forcing of black carbon under polluted urban environments, Proc. Natl. Acad. Sci., 113, 4266–4271, https://doi.org/10.1073/pnas.1602310113, 2016.

Pepin, N., Bradley, R. S., Diaz, H. F., Baraer, M., Caceres, E. B., Forsythe, N., Fowler, H., Greenwood, G., Hashmi, M. Z., Liu, X. D., Miller, J. R., Ning, L., Ohmura, A., Palazzi, E., Rangwala, I., Schöner, W., Severskiy, I., Shahgedanova, M., Wang, M. B., Williamson, S. N., Yang, D. Q., and Mountain Research Initiative EDW Working Group: Elevation-dependent warming in mountain regions of the world, Nat. Clim. Change, 5, 424–430, https://doi.org/10.1038/nclimate2563, 2015.

Peralta, O., Ortínez-Alvarez, A., Basaldud, R., Santiago, N., Alvarez-Ospina, H., de la Cruz, K., Barrera, V., de la Luz Espinosa, M., Saavedra, I., Castro, T., Martínez-Arroyo, A., Páramo, V. H., Ruíz-Suárez, L. G., Vazquez-Galvez, F. A., and Gavilán, A.: Atmospheric black carbon concentrations in Mexico, Atmospheric Res., 230, 104626, https://doi.org/10.1016/j.atmosres.2019.104626, 2019.

Pérez, N., Pey, J., Cusack, M., Reche, C., Querol, X., Alastuey, A., and Viana, M.: Variability of Particle Number, Black Carbon, and PM10, PM2.5, and PM1 Levels and Speciation: Influence of Road Traffic Emissions on Urban Air Quality, Aerosol Sci. Technol., 44, 487–499, https://doi.org/10.1080/02786821003758286, 2010.

Petzold, A. and Schönlinner, M.: Multi-angle absorption photometry - A new method for the measurement of aerosol light absorption and atmospheric black carbon, J. Aerosol Sci., 35, 421–441, https://doi.org/10.1016/j.jaerosci.2003.09.005, 2004.

Petzold, A., Kopp, C., and Niessner, R.: The dependence of the specific attenuation cross-section on black carbon mass fraction and particle size, Atmos. Environ., 31, 661–672, https://doi.org/10.1016/S1352-2310(96)00245-2, 1997.

Petzold, A., Schloesser, H., Sheridan, P. J., Arnott, W. P., Ogren, J. A., and Virkkula, A.: Evaluation of multiangle absorption photometry for measuring aerosol light absorption, Aerosol Sci. Technol., 39, 40–51, https://doi.org/10.1080/027868290901945, 2005.

Petzold, A., Ogren, J. A., Fiebig, M., Laj, P., Li, S.-M., Baltensperger, U., Holzer-Popp, T., Kinne, S., Pappalardo, G., Sugimoto, N., Wehrli, C., Wiedensohler, A., and Zhang, X.-Y.: Recommendations for reporting "black carbon" measurements, Atmospheric Chem. Phys., 13, 8365–8379, https://doi.org/10.5194/acp-13-8365-2013, 2013.

Pileci, R. E., Modini, R. L., Bertò, M., Yuan, J., Corbin, J. C., Marinoni, A., Henzing, B., Moerman, M. M., Putaud, J. P., Spindler, G., Wehner, B., Müller, T., Tuch, T., Trentini, A., Zanatta, M., Baltensperger, U., and Gysel-Beer, M.: Comparison of co-located refractory black carbon (rBC) and elemental carbon (EC) mass concentration measurements during field campaigns at several European sites, Atmospheric Meas. Tech., 14, 1379–1403, https://doi.org/10.5194/amt-14-1379-2021, 2021.

Pruppacher, H. R., Klett, J. D., and Wang, P. K.: Microphysics of Clouds and Precipitation, Aerosol Sci. Technol., 28, 381–382, https://doi.org/10.1080/02786829808965531, 1998.

Putaud, J.-P., Van Dingenen, R., Alastuey, A., Bauer, H., Birmili, W., Cyrys, J., Flentje, H., Fuzzi, S., Gehrig, R., Hansson, H. C., Harrison, R. M., Herrmann, H., Hitzenberger, R., Hüglin, C., Jones, A. M., Kasper-Giebl, A., Kiss, G., Kousa, A., Kuhlbusch, T. A. J., Löschau, G., Maenhaut, W., Molnar, A., Moreno, T., Pekkanen, J., Perrino, C., Pitz, M., Puxbaum, H., Querol, X., Rodriguez, S., Salma, I., Schwarz, J., Smolik, J., Schneider, J., Spindler, G., ten Brink, H., Tursic, J., Viana, M., Wiedensohler, A., and Raes, F.: A European aerosol phenomenology – 3: Physical and chemical characteristics of particulate matter from 60 rural, urban, and kerbside sites across Europe, Atmos. Environ., 44, 1308–1320, https://doi.org/10.1016/j.atmosenv.2009.12.011, 2010.

Qiu, C., Khalizov, A. F., and Zhang, R.: Soot Aging from OH-Initiated Oxidation of Toluene, Environ. Sci. Technol., 46, 9464–9472, https://doi.org/10.1021/es301883y, 2012.

Querol, X., Gangoiti, G., Mantilla, E., Alastuey, A., Minguillón, M. C., Amato, F., Reche, C., Viana, M., Moreno, T., Karanasiou, A., Rivas, I., Pérez, N., Ripoll, A., Brines, M., Ealo, M., Pandolfi, M., Lee, H.-K., Eun, H.-R., Park, Y.-H., Escudero, M., Beddows, D., Harrison, R. M., Bertrand, A., Marchand, N., Lyasota, A., Codina, B., Olid, M., Udina, M., Jiménez-Esteve, B., Soler, M. R., Alonso, L., Millán, M., and Ahn, K.-H.: Phenomenology of high-ozone episodes in NE Spain, Atmospheric Chem. Phys., 17, 2817–2838, https://doi.org/10.5194/acp-17-2817-2017, 2017.

Ramanathan, V., Cess, R. D., Harrison, E. F., Minnis, P., Barkstrom, B. R., Ahmad, E., and Hartmann, D.: Cloud-radiative forcing and climate: results from the Earth radiation budget experiment, Science, 243, 57–63, https://doi.org/10.1126/science.243.4887.57, 1989.

Réveillet, M., Dumont, M., Gascoin, S., Lafaysse, M., Nabat, P., Ribes, A., Nheili, R., Tuzet, F., Ménégoz, M., Morin, S., Picard, G., and Ginoux, P.: Black carbon and dust alter the response of mountain snow cover under climate change, Nat. Commun., 13, 5279, https://doi.org/10.1038/s41467-022-32501-y, 2022.

Riemer, N., West, M., Zaveri, R., and Easter, R.: Estimating black carbon aging time-scales with a particle-resolved aerosol model, J. Aerosol Sci., 41, 143–158, https://doi.org/10.1016/j.jaerosci.2009.08.009, 2010.

Riemer, N., Ault, A. P., West, M., Craig, R. L., and Curtis, J. H.: Aerosol Mixing State: Measurements, Modeling, and Impacts, Rev. Geophys., 57, 187–249, https://doi.org/10.1029/2018RG000615, 2019.

Rincón-Riveros, J. M., Rincón-Caro, M. A., Sullivan, A. P., Mendez-Espinosa, J. F., Belalcazar, L. C., Quirama Aguilar, M., and Morales Betancourt, R.: Long-term brown carbon and smoke tracer observations in Bogotá, Colombia: association with medium-range transport of biomass burning plumes, Atmospheric Chem. Phys., 20, 7459–7472, https://doi.org/10.5194/acp-20-7459-2020, 2020.

Rodríguez, S., Querol, X., Alastuey, A., and Plana, F.: Sources and processes affecting levels and composition of atmospheric aerosol in the western Mediterranean, J. Geophys. Res. Atmospheres, 107, AAC 12-1-AAC 12-14, https://doi.org/10.1029/2001JD001488, 2002.

Romshoo, B., Pöhlker, M., Wiedensohler, A., Pfeifer, S., Saturno, J., Nowak, A., Ciupek, K., Quincey, P., Vasilatou, K., Ess, M. N., Gini, M., Eleftheriadis, K., Robins, C., Gaie-Levrel, F., and Müller, T.: Importance of size representation and morphology in modelling optical properties of black carbon: comparison between laboratory measurements and model simulations, Atmospheric Meas. Tech., 15, 6965–6989, https://doi.org/10.5194/amt-15-6965-2022, 2022.

Rosen, H., Hansen, A. D., Gundel, L., and Novakov, T.: Identification of the optically absorbing component in urban aerosols, Appl. Opt., 17, 3859–3861, https://doi.org/10.1364/AO.17.003859, 1978.

Ruggeri, M. F., Bolaño-Ortiz, T., and Cereceda-Balic, F.: Atmospheric black carbon in a key location of the Chilean Central Andes: Identifying patterns, sources, and potential impacts, Atmos. Environ., 318, 120273, https://doi.org/10.1016/j.atmosenv.2023.120273, 2024.

Samset, B. H. and Myhre, G.: Climate response to externally mixed black carbon as a function of altitude, J. Geophys. Res. Atmospheres, 120, 2913–2927, https://doi.org/10.1002/2014JD022849, 2015.

Samset, B. H., Stjern, C. W., Andrews, E., Kahn, R. A., Myhre, G., Schulz, M., and Schuster, G. L.: Aerosol Absorption: Progress Towards Global and Regional Constraints, Curr. Clim. Change Rep., 4, 65–83, https://doi.org/10.1007/s40641-018-0091-4, 2018.

Sandradewi, J., Prévôt, A. S. H., Szidat, S., Perron, N., Alfarra, M. R., Lanz, V. A., Weingartner, E., and Baltensperger, U.: Using Aerosol Light Absorption

Measurements for the Quantitative Determination of Wood Burning and Traffic Emission Contributions to Particulate Matter, Environ. Sci. Technol., 42, 3316–3323, https://doi.org/10.1021/es702253m, 2008.

Saturno, J., Pöhlker, C., Massabò, D., Brito, J., Carbone, S., Cheng, Y., Chi, X., Ditas, F., Hrabě de Angelis, I., Morán-Zuloaga, D., Pöhlker, M. L., Rizzo, L. V., Walter, D., Wang, Q., Artaxo, P., Prati, P., and Andreae, M. O.: Comparison of different Aethalometer correction schemes and a reference multi-wavelength absorption technique for ambient aerosol data, Atmospheric Meas. Tech., 10, 2837–2850, https://doi.org/10.5194/amt-10-2837-2017, 2017.

Saturno, J., Holanda, B. A., Pöhlker, C., Ditas, F., Wang, Q., Moran-Zuloaga, D., Brito, J., Carbone, S., Cheng, Y., Chi, X., Ditas, J., Hoffmann, T., Hrabe de Angelis, I., Könemann, T., Lavrič, J. V., Ma, N., Ming, J., Paulsen, H., Pöhlker, M. L., Rizzo, L. V., Schlag, P., Su, H., Walter, D., Wolff, S., Zhang, Y., Artaxo, P., Pöschl, U., and Andreae, M. O.: Black and brown carbon over central Amazonia: long-term aerosol measurements at the ATTO site, Atmospheric Chem. Phys., 18, 12817–12843, https://doi.org/10.5194/acp-18-12817-2018, 2018.

Savadkoohi, M., Pandolfi, M., Reche, C., Niemi, J. V., Mooibroek, D., Titos, G., Green, D. C., Tremper, A. H., Hueglin, C., Liakakou, E., Mihalopoulos, N., Stavroulas, I., Artiñano, B., Coz, E., Alados-Arboledas, L., Beddows, D., Riffault, V., De Brito, J. F., Bastian, S., Baudic, A., Colombi, C., Costabile, F., Chazeau, B., Marchand, N., Gómez-Amo, J. L., Estellés, V., Matos, V., van der Gaag, E., Gille, G., Luoma, K., Manninen, H. E., Norman, M., Silvergren, S., Petit, J.-E., Putaud, J.-P., Rattigan, O. V., Timonen, H., Tuch, T., Merkel, M., Weinhold, K., Vratolis, S., Vasilescu, J., Favez, O., Harrison, R. M., Laj, P., Wiedensohler, A., Hopke, P. K., Petäjä, T., Alastuey, A., and Querol, X.: The variability of mass concentrations and source apportionment analysis of equivalent black carbon across urban Europe, Environ. Int., 178, 108081, https://doi.org/10.1016/j.envint.2023.108081, 2023.

Scarnato, B. V., Vahidinia, S., Richard, D. T., and Kirchstetter, T. W.: Effects of internal mixing and aggregate morphology on optical properties of black carbon using a discrete dipole approximation model, Atmospheric Chem. Phys., 13, 5089–5101, https://doi.org/10.5194/acp-13-5089-2013, 2013.

Schmid, O., Artaxo, P., Arnott, W. P., Chand, D., Gatti, L. V., Frank, G. P., Hoffer, A., Schnaiter, M., and Andreae, M. O.: Spectral light absorption by ambient aerosols influenced by biomass burning in the Amazon Basin. I: Comparison

and field calibration of absorption measurement techniques, Atmospheric Chem. Phys., 6, 3443–3462, https://doi.org/10.5194/acp-6-3443-2006, 2006.

Schulz, M., Textor, C., Kinne, S., Balkanski, Y., Bauer, S., Berntsen, T., Berglen, T., Boucher, O., Dentener, F., Guibert, S., Isaksen, I. S. A., Iversen, T., Koch, D., Kirkevåg, A., Liu, X., Montanaro, V., Myhre, G., Penner, J. E., Pitari, G., Reddy, S., Seland, Ø., Stier, P., and Takemura, T.: Radiative forcing by aerosols as derived from the AeroCom present-day and pre-industrial simulations, Atmospheric Chem. Phys., 6, 5225–5246, https://doi.org/10.5194/acp-6-5225-2006, 2006.

Schwarz, J. P., Gao, R. S., Fahey, D. W., Thomson, D. S., Watts, L. A., Wilson, J. C., Reeves, J. M., Darbeheshti, M., Baumgardner, D. G., Kok, G. L., Chung, S. H., Schulz, M., Hendricks, J., Lauer, A., Kärcher, B., Slowik, J. G., Rosenlof, K. H., Thompson, T. L., Langford, A. O., Loewenstein, M., and Aikin, K. C.: Single-particle measurements of midlatitude black carbon and light-scattering aerosols from the boundary layer to the lower stratosphere, J. Geophys. Res. Atmospheres, 111, https://doi.org/10.1029/2006JD007076, 2006.

Schwarz, J. P., Gao, R. S., Spackman, J. R., Watts, L. A., Thomson, D. S., Fahey, D. W., Ryerson, T. B., Peischl, J., Holloway, J. S., Trainer, M., Frost, G. J., Baynard, T., Lack, D. A., de Gouw, J. A., Warneke, C., and Del Negro, L. A.: Measurement of the mixing state, mass, and optical size of individual black carbon particles in urban and biomass burning emissions, Geophys. Res. Lett., 35, https://doi.org/10.1029/2008GL033968, 2008.

Schwarz, J. P., Spackman, J. R., Gao, R. S., Perring, A. E., Cross, E., Onasch, T. B., Ahern, A., Wrobel, W., Davidovits, P., Olfert, J., Dubey, M. K., Mazzoleni, C., and Fahey, D. W.: The Detection Efficiency of the Single Particle Soot Photometer, Aerosol Sci. Technol., 44, 612–628, https://doi.org/10.1080/02786826.2010.481298, 2010.

Schwarz, J. P., Perring, A. E., Markovic, M. Z., Gao, R. S., Ohata, S., Langridge, J., Law, D., McLaughlin, R., and Fahey, D. W.: Technique and theoretical approach for quantifying the hygroscopicity of black-carbon-containing aerosol using a single particle soot photometer, J. Aerosol Sci., 81, 110–126, https://doi.org/10.1016/j.jaerosci.2014.11.009, 2015.

Sciare, J., Favez, O., Sarda-Estève, R., Oikonomou, K., Cachier, H., and Kazan, V.: Long-term observations of carbonaceous aerosols in the Austral Ocean atmosphere: Evidence of a biogenic marine organic source, J. Geophys. Res. Atmospheres, 114, https://doi.org/10.1029/2009JD011998, 2009.

Sedlacek III, A. J., Lewis, E. R., Kleinman, L., Xu, J., and Zhang, Q.: Determination of and evidence for non-core-shell structure of particles containing black carbon using the Single-Particle Soot Photometer (SP2), Geophys. Res. Lett., 39, https://doi.org/10.1029/2012GL050905, 2012.

Segura, S., Estellés, V., Titos, G., Lyamani, H., Utrillas, M. P., Zotter, P., Prévôt, A. S. H., Močnik, G., Alados-Arboledas, L., and Martínez-Lozano, J. A.: Determination and analysis of in situ spectral aerosol optical properties by a multi-instrumental approach, Atmospheric Meas. Tech., 7, 2373–2387, https://doi.org/10.5194/amt-7-2373-2014, 2014.

Seinfeld, J. H. and Pandis, S. N.: Atmospheric Chemistry and Physics: From Air Pollution to Climate Change, John Wiley & Sons, 1146 pp., 2016.

Sharma, S., Lavoué, D., Cachier, H., Barrie, L. A., and Gong, S. L.: Long-term trends of the black carbon concentrations in the Canadian Arctic, J. Geophys. Res. Atmospheres, 109, https://doi.org/10.1029/2003JD004331, 2004.

Sharma, S., Leaitch, W. R., Huang, L., Veber, D., Kolonjari, F., Zhang, W., Hanna, S. J., Bertram, A. K., and Ogren, J. A.: An evaluation of three methods for measuring black carbon in Alert, Canada, Atmospheric Chem. Phys., 17, 15225–15243, https://doi.org/10.5194/acp-17-15225-2017, 2017.

Sharma, S. K., Mandal, T. K., Banoo, R., Rai, A., and Rani, M.: Long-Term Variation in Carbonaceous Components of PM2.5 from 2012 to 2021 in Delhi, Bull. Environ. Contam. Toxicol., 109, 502–510, https://doi.org/10.1007/s00128-022-03506-6, 2022.

Shiraiwa, M., Kondo, Y., Iwamoto, T., and Kita, K.: Amplification of Light Absorption of Black Carbon by Organic Coating, Aerosol Sci. Technol., 44, 46–54, https://doi.org/10.1080/02786820903357686, 2010.

Skeie, R. B., Berntsen, T. K., Myhre, G., Tanaka, K., Kvalevåg, M. M., and Hoyle, C. R.: Anthropogenic radiative forcing time series from pre-industrial times until 2010, Atmospheric Chem. Phys., 11, 11827–11857, https://doi.org/10.5194/acp-11-11827-2011, 2011.

Smith, M. L.: Naturalistic Research, Pers. Guid. J., 59, 585–589, https://doi.org/10.1002/j.2164-4918.1981.tb00623.x, 1981.

Solomon, A., Feingold, G., and Shupe, M. D.: The role of ice nuclei recycling in the maintenance of cloud ice in Arctic mixed-phase stratocumulus,

Atmospheric Chem. Phys., 15, 10631–10643, https://doi.org/10.5194/acp-15-10631-2015, 2015.

Spurny, K. R.: Methods of Aerosol Measurement before the 1960s, Aerosol Sci. Technol., 29, 329–349, https://doi.org/10.1080/02786829808965573, 1998.

Srivastava, D., Vu, T. V., Tong, S., Shi, Z., and Harrison, R. M.: Formation of secondary organic aerosols from anthropogenic precursors in laboratory studies, Npj Clim. Atmospheric Sci., 5, 1–30, https://doi.org/10.1038/s41612-022-00238-6, 2022.

Stephens, M., Turner, N., and Sandberg, J.: Particle identification by laser-induced incandescence in a solid-state laser cavity, Appl. Opt., 42, 3726, https://doi.org/10.1364/AO.42.003726, 2003.

[Stocker, T.F., D. Qin, G.-K. Plattner, M. Tignor, S.K. Allen, J. Boschung, A. Nauels, Y. Xia, V. Bex and P.M. Midgley (eds.)]: IPCC, 2013: Climate Change 2013: The Physical Science Basis. Contribution of Working Group I to the Fifth Assessment Report of the Intergovernmental Panel on Climate Change, n.d.

Sturges, H. A.: The Choice of a Class Interval, J. Am. Stat. Assoc., 21, 65–66, https://doi.org/10.1080/01621459.1926.10502161, 1926.

Suárez-Alemán, A. and Serebrisky, T.: ¿Los teleféricos como alternativa de transporte urbano?: Ahorros de tiempo en el sistema de teleférico urbano más grande del mundo: La Paz-El Alto (Bolivia), IDB Publ., https://doi.org/10.18235/0000789, 2017.

Sun, H., Biedermann, L., and Bond, T. C.: Color of brown carbon: A model for ultraviolet and visible light absorption by organic carbon aerosol, Geophys. Res. Lett., 34, https://doi.org/10.1029/2007GL029797, 2007.

Taylor, J. W., Allan, J. D., Allen, G., Coe, H., Williams, P. I., Flynn, M. J., Le Breton, M., Muller, J. B. A., Percival, C. J., Oram, D., Forster, G., Lee, J. D., Rickard, A. R., Parrington, M., and Palmer, P. I.: Size-dependent wet removal of black carbon in Canadian biomass burning plumes, Atmospheric Chem. Phys., 14, 13755–13771, https://doi.org/10.5194/acp-14-13755-2014, 2014.

Taylor, J. W., Allan, J. D., Liu, D., Flynn, M., Weber, R., Zhang, X., Lefer, B. L., Grossberg, N., Flynn, J., and Coe, H.: Assessment of the sensitivity of core / shell parameters derived using the single-particle soot photometer to density and refractive index, Atmospheric Meas. Tech., 8, 1701–1718, https://doi.org/10.5194/amt-8-1701-2015, 2015.

Thornhill, G. D., Collins, W. J., Kramer, R. J., Olivié, D., Skeie, R. B., O'Connor, F. M., Abraham, N. L., Checa-Garcia, R., Bauer, S. E., Deushi, M., Emmons, L. K., Forster, P. M., Horowitz, L. W., Johnson, B., Keeble, J., Lamarque, J.-F., Michou, M., Mills, M. J., Mulcahy, J. P., Myhre, G., Nabat, P., Naik, V., Oshima, N., Schulz, M., Smith, C. J., Takemura, T., Tilmes, S., Wu, T., Zeng, G., and Zhang, J.: Effective radiative forcing from emissions of reactive gases and aerosols – a multi-model comparison, Atmospheric Chem. Phys., 21, 853–874, https://doi.org/10.5194/acp-21-853-2021, 2021.

Tinorua, S., Denjean, C., Nabat, P., Bourrianne, T., Pont, V., Gheusi, F., and Leclerc, E.: Two-year measurements of Black Carbon properties at the high-altitude mountain site of Pic du Midi Observatory in the French Pyrenees, Aerosols/Field Measurements/Troposphere/Physics (physical properties and processes), https://doi.org/10.5194/egusphere-2023-570, 2023a.

Tinorua, S., Denjean, C., Nabat, P., Bourrianne, T., Pont, V., Gheusi, F., and Leclerc, E.: Two-year measurements of Black Carbon properties at the high-altitude mountain site of Pic du Midi Observatory in the French Pyrenees, Aerosols/Field Measurements/Troposphere/Physics (physical properties and processes), https://doi.org/10.5194/egusphere-2023-570, 2023b.

Tosca, M. G., Diner, D. J., Garay, M. J., and Kalashnikova, O. V.: Human-caused fires limit convection in tropical Africa: First temporal observations and attribution, Geophys. Res. Lett., 42, 6492–6501, https://doi.org/10.1002/2015GL065063, 2015.

Twomey, S.: The nuclei of natural cloud formation part II: The supersaturation in natural clouds and the variation of cloud droplet concentration, Geofis. Pura E Appl., 43, 243–249, https://doi.org/10.1007/BF01993560, 1959.

Ueda, S., Nakayama, T., Taketani, F., Adachi, K., Matsuki, A., Iwamoto, Y., Sadanaga, Y., and Matsumi, Y.: Light absorption and morphological properties of soot-containing aerosols observed at an East Asian outflow site, Noto Peninsula, Japan, Atmospheric Chem. Phys., 16, 2525–2541, https://doi.org/10.5194/acp-16-2525-2016, 2016.

Ullrich, R., Hoose, C., Möhler, O., Niemand, M., Wagner, R., Höhler, K., Hiranuma, N., Saathoff, H., and Leisner, T.: A New Ice Nucleation Active Site Parameterization for Desert Dust and Soot, J. Atmospheric Sci., 74, 699–717, https://doi.org/10.1175/JAS-D-16-0074.1, 2017.

Valentini, S., Barnaba, F., Bernardoni, V., Calzolai, G., Costabile, F., Di Liberto, L., Forello, A. C., Gobbi, G. P., Gualtieri, M., Lucarelli, F., Nava, S., Petralia, E., Valli, G., Wiedensohler, A., and Vecchi, R.: Classifying aerosol particles through the combination of optical and physical-chemical properties: Results from a wintertime campaign in Rome (Italy), Atmospheric Res., 235, 104799, https://doi.org/10.1016/j.atmosres.2019.104799, 2020.

Van de hulst, H. C. (Ed.): Front Matter, in: Multiple Light Scattering, Academic Press, iii, https://doi.org/10.1016/B978-0-12-710701-1.50001-X, 1980.

Vergara-Temprado, J., Holden, M. A., Orton, T. R., O'Sullivan, D., Umo, N. S., Browse, J., Reddington, C., Baeza-Romero, M. T., Jones, J. M., Lea-Langton, A., Williams, A., Carslaw, K. S., and Murray, B. J.: Is Black Carbon an Unimportant Ice-Nucleating Particle in Mixed-Phase Clouds?, J. Geophys. Res. Atmospheres, 123, 4273–4283, https://doi.org/10.1002/2017JD027831, 2018.

Via, M., Minguillón, M. C., Reche, C., Querol, X., and Alastuey, A.: Increase in secondary organic aerosol in an urban environment, Atmospheric Chem. Phys., 21, 8323–8339, https://doi.org/10.5194/acp-21-8323-2021, 2021.

Via, M., Yus-Díez, J., Canonaco, F., Petit, J.-E., Hopke, P., Reche, C., Pandolfi, M., Ivančič, M., Rigler, M., Prevôt, A. S. H., Querol, X., Alastuey, A., and Minguillón, M. C.: Towards a better understanding of fine PM sources: Online and offline datasets combination in a single PMF, Environ. Int., 177, 108006, https://doi.org/10.1016/j.envint.2023.108006, 2023.

Virkkula, A., Chi, X., Ding, A., Shen, Y., Nie, W., Qi, X., Zheng, L., Huang, X., Xie, Y., Wang, J., Petäjä, T., and Kulmala, M.: On the interpretation of the loading correction of the aethalometer, Atmospheric Meas. Tech., 8, 4415–4427, https://doi.org/10.5194/amt-8-4415-2015, 2015.

Wang, C.-C., Lee, P.-H., Kumar, M., Huang, Y.-T., Sung, S., and Lin, J.-G.: Simultaneous partial nitrification, anaerobic ammonium oxidation and denitrification (SNAD) in a full-scale landfill-leachate treatment plant, J. Hazard. Mater., 175, 622–628, https://doi.org/10.1016/j.jhazmat.2009.10.052, 2010.

Wang, J., Doussin, J. F., Perrier, S., Perraudin, E., Katrib, Y., Pangui, E., and Picquet-Varrault, B.: Design of a new multi-phase experimental simulation chamber for atmospheric photosmog, aerosol and cloud chemistry research, Atmospheric Meas. Tech., 4, 2465–2494, https://doi.org/10.5194/amt-4-2465-2011, 2011.

Wang, J., Liu, D., Ge, X., Wu, Y., Shen, F., Chen, M., Zhao, J., Xie, C., Wang, Q., Xu, W., Zhang, J., Hu, J., Allan, J., Joshi, R., Fu, P., Coe, H., and Sun, Y.: Characterization of black carbon-containing fine particles in Beijing during wintertime, Atmospheric Chem. Phys., 19, 447–458, https://doi.org/10.5194/acp-19-447-2019, 2019.

Wei, J., Niu, Y.-B., Tang, M.-X., Peng, Y., Cao, L.-M., He, L.-Y., and Huang, X.-F.: Characterizing formation mechanisms of secondary aerosols on black carbon in a megacity in South China, Sci. Total Environ., 859, 160290, https://doi.org/10.1016/j.scitotenv.2022.160290, 2023.

Weingartner, E., Burtscher, H., and Baltensperger, U.: Hygroscopic properties of carbon and diesel soot particles, Atmos. Environ., 31, 2311–2327, https://doi.org/10.1016/S1352-2310(97)00023-X, 1997.

Weingartner, E., Saathoff, H., Schnaiter, M., Streit, N., Bitnar, B., and Baltensperger, U.: Absorption of light by soot particles: determination of the absorption coefficient by means of aethalometers, J. Aerosol Sci., 34, 1445–1463, https://doi.org/10.1016/S0021-8502(03)00359-8, 2003.

WHO: WHO global air quality guidelines: particulate matter (PM2.5 and PM10), ozone, nitrogen dioxide, sulfur dioxide and carbon monoxide., World Health Organization, 2021.

Wiedensohler, A., Andrade, M., Weinhold, K., Müller, T., Birmili, W., Velarde, F., Moreno, I., Forno, R., Sanchez, M. F., Laj, P., Ginot, P., Whiteman, D. N., Krejci, R., Sellegri, K., and Reichler, T.: Black carbon emission and transport mechanisms to the free troposphere at the La Paz/El Alto (Bolivia) metropolitan area based on the Day of Census (2012), Atmos. Environ., 194, 158–169, https://doi.org/10.1016/j.atmosenv.2018.09.032, 2018.

Winkler, P.: The growth of atmospheric aerosol particles as a function of the relative humidity—II. An improved concept of mixed nuclei, J. Aerosol Sci., 4, 373–387, https://doi.org/10.1016/0021-8502(73)90027-X, 1973.

Wu, Y., Cheng, T., Liu, D., Allan, J. D., Zheng, L., and Chen, H.: Light Absorption Enhancement of Black Carbon Aerosol Constrained by Particle Morphology, Environ. Sci. Technol., 52, 6912–6919, https://doi.org/10.1021/acs.est.8b00636, 2018.

Yang, M., Howell, S. G., Zhuang, J., and Huebert, B. J.: Attribution of aerosol light absorption to black carbon, brown carbon, and dust in China – interpretations

of atmospheric measurements during EAST-AIRE, Atmospheric Chem. Phys., 9, 2035–2050, https://doi.org/10.5194/acp-9-2035-2009, 2009.

Yuan, J., Modini, R. L., Zanatta, M., Herber, A. B., Müller, T., Wehner, B., Poulain, L., Tuch, T., Baltensperger, U., and Gysel-Beer, M.: Variability in the mass absorption cross section of black carbon (BC) aerosols is driven by BC internal mixing state at a central European background site (Melpitz, Germany) in winter, Atmospheric Chem. Phys., 21, 635–655, https://doi.org/10.5194/acp-21-635-2021, 2021.

Yus-Díez, J., Bernardoni, V., Močnik, G., Alastuey, A., Ciniglia, D., Ivančič, M., Querol, X., Perez, N., Reche, C., Rigler, M., Vecchi, R., Valentini, S., and Pandolfi, M.: Determination of the multiple-scattering correction factor and its cross-sensitivity to scattering and wavelength dependence for different AE33 Aethalometer filter tapes: a multi-instrumental approach, Atmospheric Meas. Tech., 14, 6335–6355, https://doi.org/10.5194/amt-14-6335-2021, 2021.

Yus-Díez, J., Via, M., Alastuey, A., Karanasiou, A., Minguillón, M. C., Perez, N., Querol, X., Reche, C., Ivančič, M., Rigler, M., and Pandolfi, M.: Absorption enhancement of black carbon particles in a Mediterranean city and countryside: effect of particulate matter chemistry, ageing and trend analysis, Atmospheric Chem. Phys., 22, 8439–8456, https://doi.org/10.5194/acp-22-8439-2022, 2022.

Zanatta, M., Gysel, M., Bukowiecki, N., Müller, T., Weingartner, E., Areskoug, H., Fiebig, M., Yttri, K. E., Mihalopoulos, N., Kouvarakis, G., Beddows, D., Harrison, R. M., Cavalli, F., Putaud, J. P., Spindler, G., Wiedensohler, A., Alastuey, A., Pandolfi, M., Sellegri, K., Swietlicki, E., Jaffrezo, J. L., Baltensperger, U., and Laj, P.: A European aerosol phenomenology-5: Climatology of black carbon optical properties at 9 regional background sites across Europe, Atmos. Environ., 145, 346–364, https://doi.org/10.1016/j.atmosenv.2016.09.035, 2016.

Zanatta, M., Laj, P., Gysel, M., Baltensperger, U., Vratolis, S., Eleftheriadis, K., Kondo, Y., Dubuisson, P., Winiarek, V., Kazadzis, S., Tunved, P., and Jacobi, H.-W.: Effects of mixing state on optical and radiative properties of black carbon in the European Arctic, Atmospheric Chem. Phys., 18, 14037–14057, https://doi.org/10.5194/acp-18-14037-2018, 2018.

Zanatta, M., Bozem, H., Köllner, F., Schneider, J., Kunkel, D., Hoor, P., Faria, J. de, Petzold, A., Bundke, U., Hayden, K., Staebler, R. M., Schulz, H., and Herber, A. B.: Airborne survey of trace gases and aerosols over the Southern Baltic Sea: from

clean marine boundary layer to shipping corridor effect, 72, 1695349, https://doi.org/10.1080/16000889.2019.1695349, 2020.

Zanatta, M., Mertes, S., Jourdan, O., Dupuy, R., Järvinen, E., Schnaiter, M., Eppers, O., Schneider, J., Jurányi, Z., and Herber, A.: Airborne investigation of black carbon interaction with low-level, persistent, mixed-phase clouds in the Arctic summer, Atmospheric Chem. Phys., 23, 7955–7973, https://doi.org/10.5194/acp-23-7955-2023, 2023.

Zeng, L., Tan, T., Zhao, G., Du, Z., Hu, S., Shang, D., and Hu, M.: Overestimation of black carbon light absorption due to mixing state heterogeneity, Npj Clim. Atmospheric Sci., 7, 1–8, https://doi.org/10.1038/s41612-023-00535-8, 2024.

Zhai, J., Yang, X., Li, L., Bai, B., Liu, P., Huang, Y., Fu, T.-M., Zhu, L., Zeng, Z., Tao, S., Lu, X., Ye, X., Wang, X., Wang, L., and Chen, J.: Absorption Enhancement of Black Carbon Aerosols Constrained by Mixing-State Heterogeneity, Environ. Sci. Technol., 56, 1586–1593, https://doi.org/10.1021/acs.est.1c06180, 2022.

Zhang, Y., Favez, O., Canonaco, F., Liu, D., Močnik, G., Amodeo, T., Sciare, J., Prévôt, A. S. H., Gros, V., and Albinet, A.: Evidence of major secondary organic aerosol contribution to lensing effect black carbon absorption enhancement, Npj Clim. Atmospheric Sci., 1, 1–8, https://doi.org/10.1038/s41612-018-0056-2, 2018.

Zhu, C.-S., Cao, J.-J., Xu, B.-Q., Huang, R.-J., Wang, P., Ho, K.-F., Shen, Z.-X., Liu, S.-X., Han, Y.-M., Tie, X.-X., Zhao, Z.-Z., and Chen, L.-W. A.: Black Carbon Aerosols at Mt. Muztagh Ata, a High-Altitude Location in the Western Tibetan Plateau, Aerosol Air Qual. Res., 16, 752–763, https://doi.org/10.4209/aaqr.2015.04.0255, 2016.

Zotter, P., Herich, H., Gysel, M., El-Haddad, I., Zhang, Y., Močnik, G., Hüglin, C., Baltensperger, U., Szidat, S., and Prévôt, A. S. H.: Evaluation of the absorption Ångström exponents for traffic and wood burning in the Aethalometer-based source apportionment using radiocarbon measurements of ambient aerosol, Atmospheric Chem. Phys., 17, 4229–4249, https://doi.org/10.5194/acp-17-4229-2017, 2017.